



HAL
open science

Bio-inspired waveforms and processing

Anthony Torre

► **To cite this version:**

Anthony Torre. Bio-inspired waveforms and processing. Signal and Image Processing. Ecole nationale supérieure Mines-Télécom Atlantique, 2024. English. NNT : 2024IMTA0448 . tel-04918775

HAL Id: tel-04918775

<https://theses.hal.science/tel-04918775v1>

Submitted on 29 Jan 2025

HAL is a multi-disciplinary open access archive for the deposit and dissemination of scientific research documents, whether they are published or not. The documents may come from teaching and research institutions in France or abroad, or from public or private research centers.

L'archive ouverte pluridisciplinaire **HAL**, est destinée au dépôt et à la diffusion de documents scientifiques de niveau recherche, publiés ou non, émanant des établissements d'enseignement et de recherche français ou étrangers, des laboratoires publics ou privés.

THÈSE DE DOCTORAT DE

L'ÉCOLE NATIONALE SUPÉRIEURE
MINES-TÉLÉCOM ATLANTIQUE BRETAGNE
PAYS DE LA LOIRE – IMT ATLANTIQUE

ÉCOLE DOCTORALE N° 648
Sciences pour l'Ingénieur et le Numérique
Spécialité : *Signal, Image, Vision*

Par

Anthony TORRE

Bio-inspired waveforms and processing

Formes d'ondes et traitements bio-inspirés

Thèse présentée et soutenue à l'ONERA, Palaiseau, France, le 19 Décembre 2024

Unité de recherche : MATS-DEMR, ONERA / Lab-STICC, CNRS

Thèse N° : 2024IMTA0448

Rapporteurs avant soutenance :

Alessio BALLERI Professeur, Université de Cranfield, Royaume-Uni
Laurent FERRO-FAMIL Professeur, ISAE-SUPAERO

Composition du Jury :

Présidente :	Atika RIVENQ	Professeur, Université de Valenciennes
Examineurs :	Alessio BALLERI	Professeur, Université de Cranfield, Royaume-Uni
	Laurent FERRO-FAMIL	Professeur, ISAE-SUPAERO
Directeur de thèse :	Thierry CHONAVEL	Professeur, IMT Atlantique
Co-encadrants :	Abigael TAYLOR	Ingénieur de recherche, ONERA (Encadrant)
	Dominique POULLIN	Ingénieur de recherche, ONERA (Encadrant)

Invité :

Abdeljalil AISSA EL BEY Professeur, IMT Atlantique

I am Batman.

Batman

ACKNOWLEDGEMENT

Une thèse, c'est certes trois ans de travaux, mais également trois ans de rencontres et de partage avec des personnes de tous horizons, tant sur le plan professionnel que personnel. Il est donc venu le temps, non pas des cathédrales, mais des remerciements.

Rien de tout cela n'existerait sans eux, je remercie tout d'abord mon équipe encadrante : Thierry, Abi et Dodo. Merci à vous trois de m'avoir fait confiance dès le début, que ce soit pour le stage (je ne t'oublie pas Fred, merci aussi) comme pour la thèse. Merci à Thierry de m'avoir suivi tout du long avec mes histoires de radar chauve-souris. Tu as toujours soutenu mes idées, sauf peut-être quand il s'agissait de mon humour, qui t'a maintes fois embêté, aussi bien dans mes présentations que dans mon manuscrit. Qui plus est, tu as toujours une myriade d'idées, un peu trop pour une thèse, mais j'aurais aimé pouvoir toutes les explorer. Abi et Dodo, mes senseis, aussi bien en radar qu'en rangement de bureau... Merci du fond du cœur pour tout. Le petit Anthony qui est rentré en stage, sûr de ne pas faire de thèse, est bien content d'avoir changé d'avis. Même si vous ne lisez pas toujours mes titres de diapos, j'ai passé de super moments tout au long de ma thèse que ce soit pour les vannes douteuses d'Abi ou quand on embêtait Dodo. Vous êtes des encadrants en or et je referais une thèse avec vous tous les jours.

Je tiens ensuite à remercier tous les membres du jury qui ont accepté d'évaluer mon travail Atika Rivenq, Abdeljallil Aissa El Bey, Alessio Balleri et Laurent Ferro-Famil. Merci aux rapporteurs Laurent Ferro-Famil et Alessio Balleri. A special thanks to you Alessio, you have quickly become a reference in my work on bio-inspired radar and I am very grateful to have you on my jury. Je remercie également Abdeljallil et Israel qui m'ont suivi en tant que membres de mon CSI pendant ces trois années.

Je remercie maintenant ceux sans qui une partie de ces travaux n'aurait pas été possible. Merci à Raimund Specht et Matthias Götsche qui ont accepté que j'utilise les signaux de chauves-souris enregistrés et mis à disposition sur leur site. Merci à Milan et Pierre d'avoir permis à ma petite forme d'onde bio-inspirée de traquer des avions avec HYCAM. Merci également à Daniel et Nicolas pour les essais BABI. Les résultats ne font pas partie du manuscrit malheureusement, mais je les utiliserais à bon escient pour d'autres papiers. Et pour les données NOSTRA-ROS qui m'ont permis de tester le CuSum sur données réelles, je remercie Jean-Philippe Molinié, Nicolas Gonçalves et Michel Menelle

Un grand merci à l'équipe MATS (vive le traitement du signal !) et tous ses membres pour m'avoir accueilli. Mention spéciale à la team doctorant, les anciens comme les nouveaux. Merci à Marilisa, avec qui j'ai partagé mon bureau et de nombreux fous rires. Pardon pour toutes ces

frayeurs, volontaires ou non. Merci aux voisins Huy et Pierre, de un an mes aînés, et bonne chance à Simon pour les trois années à venir !

Trois années de thèse, ce sont aussi trois finales avec l'équipe de foot ONERA dont deux gagnées, ainsi qu'une première place au championnat d'hiver. Avec un tel palmarès, je ne peux que remercier toute l'équipe pour tous ces bons moments footballistiques et espérer en vivre beaucoup d'autres.

Je n'oublie pas non plus les frères, Guillaume et Thomas, toujours présents pour geeker. En trois ans, on en a poncé des jeux et on ne compte plus tous les bons moments passés ensemble. Je lève ensuite mon verre à l'équipe qui sait toujours où se garer, Cécile, Madeleine, Charles, Alex, Pierre et Quentin. À tous ces bons moments, ces vacances et bien plus encore depuis le lycée et pour encore longtemps je l'espère. Merci à Amélie, la douce brune qui partage ma vie. Merci de supporter mes taquineries et ma double vie de Batman. Et la boquette Disney, elle est où ?! Tout doux Hélène, tout doux... Merci à vous tous, pour tous ces moments depuis les Arts, cœur sur vous ! On a encore plein de bêtises à faire avec la grande blonde, tant de repas léger à préparer avec Mam's et des voyages à organiser pour aller voir les expats des pays froids (n'est-ce pas DD et Pocket ?). Spéciale dédicace à Julia, Tom et Mathis qui verront eux aussi la lumière au bout du tunnel de la thèse un jour. Petite dédicace à la 151-113. Il y a un désormais un docteur dans la plus pinée des fam's.

Enfin, par qui finir si ce n'est par ceux à qui je dois tout. Merci à mes parents, mon frère et mes sœurs. Je vous aime.

Tout le monde a participé à cette thèse d'une manière ou d'une autre. Un grand merci à tous !

Table of Contents

Acknowledgement	i
Table of Contents	iii
List of Figures	vii
List of Tables	xiii
Acronyms	xv
Notations	xvii
Résumé en Français	xix
1 Introduction	1
1.1 Context and Objectives	1
1.2 Contributions	2
1.3 Thesis Layout	3
1.4 Publications	4
2 Radar and Bats for Beginners	5
2.1 The World of Radar	5
2.1.1 Generalities and Basic Principles	5
2.1.2 Radar Waveforms	8
2.1.3 Radar Processing	9
2.2 The World of Bats	19
2.2.1 Introduction to Bats and Echolocation	19
2.2.2 Bats Waveforms	22
2.2.3 Bats Processing	24
2.3 Conclusion	29
3 From Bats to Radar	31

TABLE OF CONTENTS

3.1	Becoming a Bat	31
3.1.1	Listen to the Bats	31
3.1.2	A Function to Mimic them all	34
3.2	First Steps as a Radar Waveform	38
3.2.1	The Parsons Waveform: a Function with Curves	38
3.2.2	Behaviour towards Classical Radar Processing	39
3.2.3	The Cramér-Rao Lower Bat Bound	45
3.3	Real Data Experiments	51
3.3.1	Experiment Framework	51
3.3.2	Data Processing	52
3.3.3	Data Analysis	56
3.4	Conclusion	59
4	The Parsons Waveform in a Radar Framework	61
4.1	MultisBatic Application	61
4.1.1	The Multistatic Principle	61
4.1.2	A Simulated Multistatic Environment	63
4.1.3	Radar Processing and Evaluation	64
4.1.4	Simulation Results	66
4.1.5	Discussion	71
4.2	Doppler Estimation	73
4.2.1	The Concept	73
4.2.2	Simulations and Results	75
4.3	Conclusion	77
5	The CuSum: an Algorithm to Detect the Presence of an Unknown Signal	79
5.1	Story of an Algorithm	79
5.1.1	CuSum begins	79
5.1.2	CuSum and Radar	81
5.2	Behind the Sum	82
5.2.1	Statistical Framework	82
5.2.2	Signal Distribution in the Radar Framework	84
5.3	Everything has a Beginning and an End	87
5.3.1	The CuSum Logic for Pulse Detection	87
5.3.2	Thresholds settings	89
5.3.3	Performance indicators	91
5.4	CuSum at Work	93
5.4.1	Simulations	93

5.4.2	Real Data	97
5.5	A Bias in the Estimator	101
5.5.1	Empirical estimator	101
5.5.2	Alternative estimators	102
5.5.3	Comparison of the estimators	104
5.5.4	Improved CuSum	105
5.6	Conclusion	107
6	Conclusion	109
6.1	Conclusion	109
6.2	Perspectives	110
	Appendices	113
A	Doppler Invariance	115
B	FSST and Ridges Extraction	117
C	Amplitude Modulation and GMM	119
D	CRLB Additional Ressources	121
E	CuSum Appendices	123
E.1	Complex Signal Distribution	123
E.2	Noise Distribution	123
E.3	Noisy Signal Distribution	125
E.4	Towards a 2D-CuSum?	128
	Bibliography	131

List of Figures

1	Principe du radar.	xxi
2	Exemples de formes d'ondes radar classiques : a) le chirp et b) HFM. Les impulsions ont une durée $T = 10\mu\text{s}$ et une largeur de bande $B = 100\text{MHz}$. Sur chaque sous-figure, le graphe de gauche représente le spectre (représentation en fonction des fréquences), tandis que celui de droite montre un spectrogramme (une représentation Temps-Fréquence). La fréquence d'échantillonnage est de $F_s = 500\text{MHz}$	xxi
3	Sortie du traitement retard-Doppler pour deux cibles simulées avec un train d'impulsions composé de chirp. Une cible est statique à un retard de $\tau = 20\mu\text{s}$, tandis que la seconde est mobile, à un retard de $\tau = 50\mu\text{s}$ et présente un doppler de $\nu_d = 1\text{kHz}$	xxii
4	Schéma illustratif du principe d'écholocation.	xxiii
5	Catégories principales des signaux d'écholocation (extrait de [13], CC BY-NC-SA 3.0).	xxiii
6	Séquence de chasse d'une chauve-souris émettant a) des signaux FM et b) une autre émettant des signaux CF (extrait de [13], CC BY-NC-SA 3.0).	xxiv
7	Authentique séquence de chasse de <i>Nyctalus noctula</i> [14]. Le train d'impulsions comprend 25 impulsions échantillonnées à 250kHz.	xxiv
8	Fréquences instantanées de fonctions de Parsons avec différentes courbures ($\frac{f_0}{f_1} = 3$ avec $f_0 = 60\text{kHz}$, $f_1 = 20\text{kHz}$ et $T = 20\text{ms}$).	xxvi
9	Sortie de compression d'impulsion en utilisant a) le filtre adapté et b) le filtre désadapté ($T = 50\mu\text{s}$, $B = 100\text{MHz}$).	xxvii
10	CLRB et RMSE sur le retard τ , pour un train d'impulsion en fonction du SNR ($T = 50\mu\text{s}$, $B = 100\text{MHz}$, $T_r = 10T$, $N_p = 10$ impulsions).	xxix
11	Cartes distance-Doppler de l'avion pour les différentes formes d'ondes et un traitement distance par filtre adapté (MF).	xxx
12	Environnement multistatique simulé vu à travers les fréquences instantanées des formes d'ondes considérées ($B = 100\text{MHz}$, $T = 50\mu\text{s}$).	xxxi

13	Exemple de sortie du CuSum pour une impulsion. Les paramètres τ_i et η_i représentent respectivement les instants associés à un point de changement et les seuils utilisés pour les valider.	xxxii
2.1	Overview of the radar framework.	6
2.2	Example of classical radar waveforms with a duration of $T = 10\mu\text{s}$ and a bandwidth of $B = 100\text{MHz}$. For both subfigures, the left plot displays the spectrum (representation as function of the frequencies), while the right plot is the spectrogram (Time-Frequency response). The sampling frequency is of $F_s = 500\text{MHz}$. . .	9
2.3	Illustrative scheme of the information received with a radar illuminating two distinct targets with a chirp. The two reflected signals, $r_1(t)$ and $r_2(t)$, are received with different delays, τ and τ' , and the second one presents a Doppler shift, ν_d , due to the radial velocity of the target.	9
2.4	Matched filter output for a noiseless chirp ($T = 10\mu\text{s}$, $B = 100\text{MHz}$) with no delay.	11
2.5	Two-target discrimination situation with a chirp ($T = 10\mu\text{s}$, $B = 100\text{MHz}$).	12
2.6	The sidelobes problematic with the MF for a chirp ($T = 10\mu\text{s}$, $B = 100\text{MHz}$).	12
2.7	MF and MMF output for a chirp ($T = 10\mu\text{s}$, $B = 100\text{MHz}$). The PSLR is optimised in the left figure, while the ISLR is optimised in the right one ($K_q = N = 5001$ samples, $\beta_q = 2\text{dB}$ for both filters). Zoom on the mainlobe are added to illustrate the LPG effect for the ISLR optimisation with controlled (2.26) and uncontrolled (2.24) LPG.	15
2.8	Example of the Ambiguity Function of a chirp ($T = 10\mu\text{s}$, $B = 100\text{MHz}$). The upper plot is the zero-Doppler cut, while the left plot is the zero-Delay cut.	16
2.9	Example of the Ambiguity Function of a HFM waveform ($T = 10\mu\text{s}$, $B = 100\text{MHz}$). The upper plot is the zero-Doppler cut, while the left plot is the zero-Delay cut.	17
2.10	Representative scheme of a chirp pulse train.	18
2.11	Output of the Range-Doppler processing for two simulated targets with a chirp pulse train. One target is stationary at a delay of $\tau = 20\mu\text{s}$, while the second is at a delay of $\tau = 50\mu\text{s}$ with a Doppler of $\nu_d = 1\text{kHz}$	19
2.12	The worldwide distribution of bat species and their diet explained by Professor Batty. Bats can be found in the green areas.	20
2.13	Overview of the echolocation hunting framework.	21
2.14	Example of species with different "antennas". The common noctule, on the left, emits ultrasounds through its mouth, whereas the greater horseshoe bat emits through its noseleaf.	21
2.15	Main categories of bat echolocation pulses (From [13], CC BY-NC-SA 3.0).	23

2.16	Echolocation sequence of a FM (a) and CF (b) bats emitted during prey pursuit (From [13], CC BY-NC-SA 3.0).	24
2.17	Anatomical point of view of Batty's ear.	25
2.18	Overview of the cochlear block and its output as modelled by the SCAT. Butterworth filter hyperbolically spaced are implemented and the envelope-smoothing process is skipped in this case.	25
2.19	Descriptive scheme of the temporal block mechanism.	26
2.20	Pulse of a greater horseshoe bat [61].	28
2.21	Example of the amplitude modulation observable in bat echolocation with real signals.	29
3.1	Spectrogram of authentic hunting sequences from three different bat species recorded in Germany by Raimund Specht [14][64][65]. The pulse trains are sampled at 250kHz and contain respectively 25, 40 and 26 pulses.	32
3.2	Spectrogram of the first and thirteenth pulse of the <i>Nyctalus noctula</i> hunting sequence [14]. The pulse duration is greatly reduced as the bat approaches a target while the bandwidth broadens. The PRI, which can be observed in figures 3.1(a) to 3.1(c), decreases as well. Moreover, the quasi-constant frequency portion is eliminated to get a more linearly frequency modulated signal. This indicates the switch between the Doppler and target characteristics estimation process and the will to improve the range resolution.	34
3.3	Result of the harmonic isolation through the application of the FSST and a ridge extraction algorithm on the first pulse of the common noctule signal [14]. The IF of each harmonic is superimposed with black lines.	35
3.4	Instantaneous frequencies of Parsons functions with varying curvatures ($\frac{f_0}{f_1} = 3$ with $f_0 = 60\text{kHz}$, $f_1 = 20\text{kHz}$ and $T = 20\text{ms}$).	36
3.5	The mimicking of bat signals achieved with the Parsons function.	37
3.6	Comparisons between the flexibility of the HFM and Parson functions.	38
3.7	Comparison of auto-correlations between the Chirp, HFM and Parsons waveforms ($T = 50\mu\text{s}$, $B = 100\text{MHz}$).	39
3.8	Behaviour comparison between the Chirp, HFM and Parsons waveforms processed by the MMF for the optimisation of the ISLR ($T = 50\mu\text{s}$, $B = 100\text{MHz}$, $K_q = N = 25,001$ samples, $\beta_q = 2\text{dB}$). The legend is the same for both figures but not displayed in the second one for a better readability.	40
3.9	Comparison between the spectrum of the presented waveforms and the spectrum of their MMFs ($T = 50\mu\text{s}$, $B = 100\text{MHz}$).	41
3.10	Doppler cut of the AF for the Parsons waveform ($T = 50\mu\text{s}$, $B = 100\text{MHz}$, $a = 1$).	44
3.11	Ambiguity Functions of various waveforms ($T = 50\mu\text{s}$, $B = 100\text{MHz}$).	44

3.12	CLRB for delay τ for a unique pulse as a function of SNR for various waveforms.	49
3.13	CLRB and RMSE for delay τ , for a single pulse and Monte-Carlo simulations results with different waveforms as function of the SNR.	50
3.14	CLRB and RMSE for delay τ , for pulse train of various waveforms as function of the SNR ($T_r = 10T$, $N_p = 10$).	51
3.15	Conditions of the real experiments. The interpulse in the right figure is not representative of the true parameter to ensure a better visualisation.	52
3.16	Trajectory of the Airbus A-320 (Hex code 440128) in red with the position of HYCAM and Orly. Image obtained with Google Earth Pro.	53
3.17	Received data for the Airbus A-320 with two of the emitted waveforms.	54
3.18	Range-Doppler maps of the aircraft for a Parsons waveform ($a = 0.01$).	55
3.19	Range-Doppler maps of the aircraft for a Parsons waveform ($a = 0.01$) after clutter rejection.	55
3.20	Range-Doppler maps of the aircraft for the different waveforms after clutter rejection.	56
3.21	Range-Doppler maps of the aircraft computed with the MMF for the Parsons waveforms after clutter rejection.	57
3.22	Range cut of the aircraft response for the Parsons waveforms.	58
3.23	Observation of the response linked to the reactor of the aircraft.	58
4.1	Scheme of a multistatic radar configuration. Each radar emits a distinct signal, which is then reflected back by the target in varying directions. Consequently, each arrow represents a back-scattered signal, which complicates the reception for each radar.	62
4.2	The simulated multistatic environment through the instantaneous frequencies of the considered waveforms ($B = 100\text{MHz}$, $T = 50\mu\text{s}$) [79].	64
4.3	Auto-correlation (left) and cross-correlation of up- and down-chirps ($T = 50\mu\text{s}$, $B = 100\text{MHz}$). Here, isolation corresponds to the maximum cross-correlation. . .	66
4.4	(a) Evolution of the isolation level between a Parsons function and other chirp-based waveforms ($B = 100\text{MHz}$, $T = 50\mu\text{s}$). (b) Illustration of the cross-correlation behaviour of $\wedge - \setminus$ and $\wedge - \nearrow$ pairs.	67
4.5	(a) Isolation levels summarised in Table 4.1 for the Parsons down-sweep. (b) Isolation level for two pair of waveforms $\wedge - \setminus$ and $\setminus - \setminus$ for varying BT and a ($B = 100\text{MHz}$, $T \in [10; 100]\mu\text{s}$, $a \in [0; 11]$).	69
4.6	Comparison between the spectrum of the investigated waveforms and the spectrum of their MMFs.	69

4.7	Outputs of the Matched Filter and Mismatched Filter minimising the ISL criterion for the Parsons down-sweep ($a = 3.12$). A zoom on the mainlobe illustrates the widening of the mainlobe operated with the MMF (LPG compensated) [79]. . . .	70
4.8	Doppler mismatch loss results with different waveforms of the set. The Parsons up-sweep and the down-chirp (\nearrow and \searrow) are not represented but the results are similar to that of their inverted versions [79].	72
4.9	Illustration of the hyperbolically arranged filters in the cochlear block (one tenth of the filters are represented for clarity). The output of the cochlear block is given for a Parsons waveform ($B = 100\text{MHz}$, $T = 50\mu\text{s}$ and $a = 0.1$) and its echo delayed by $\tau = 50\mu\text{s}$	74
4.10	Comparison between the cochlear spectrum and the Fourier spectrum. The output of the cochlear block is given for a Parsons waveform ($B = 100\text{MHz}$, $T = 50\mu\text{s}$ and $a = 0.1$) and its echo delayed by $\tau = 50\mu\text{s}$	74
4.11	Doppler estimators based on the cochlear spectrum of a signal and its echo. . . .	75
4.12	Results of the Monte-Carlo simulations for the Doppler estimation. The true Doppler is $\nu_d = 70\text{kHz}$	76
5.1	Example of a real hunting sequence from <i>Nyctalus Noctula</i> [14]. This illustrates the kind of signal that have been investigated and the need to extract each pulse for relevant parameters estimation.	80
5.2	Example of a real hunting sequence from <i>Nyctalus Noctula</i> [14] where the first pulses are detected and can be extracted thanks to the CuSum algorithm (for the sake of clarity, the subsequent detections are not shown in this illustration). The black vertical lines represent the estimated onset and end of each pulse.	81
5.3	Example of the CuSum result for the detection of a single change point located at $\tau = 100$	84
5.4	CuSum outputs for the deterministic case without (top) and with (bottom) the AIC penalty for the detection of the beginning of a chirp located at $\tau = 1000$ samples. The left column represents a low SNR case, while the right column depicts a high SNR case.	86
5.5	Spectrogram of a Parsons waveform ($B = 10\text{MHz}$, $T = 25\mu\text{s}$ and $a = 5.10^{-3}$). . .	88
5.6	CuSum output on a pulse train (SNR= 0dB).	88
5.7	Minimum threshold setting for two values of α	90
5.8	Linear approximation of the CuSum output under the noise only hypothesis (H_0). . .	91
5.9	Minimum threshold application in the case of a false alarm and a true detection. . .	92
5.10	Maximum threshold application in the case of a true detection.	92
5.11	Spectrograms of a Chirp and a Parsons pulse with the first set of parameters ($B_1 = 26,73\text{MHz}$ and $T_1 = 19,66\mu\text{s}$).	93

5.12	Results of the Monte-Carlo simulations for the estimated FAR $\hat{\alpha}$	94
5.13	Results of the Monte-Carlo simulations for the mean delays of detection as a function of the SNR.	95
5.14	Results of the Monte-Carlo simulations for the RMSE as a function of the SNR.	96
5.15	Spectrogram of pulses 8 to 13.	97
5.16	Results of the Monte-Carlo simulations with various performance indicators as function of the SNR for the 13 real pulse trains.	98
5.17	Spectrograms of NOSTRA-ROS radar signals received at different moment of the day.	99
5.18	Results of the CuSum algorithm on the first signal.	100
5.19	Results of the CuSum algorithm on the second filtered signal.	101
5.20	Estimation of the amplitude ν as a function of the SNR = $10 \log_{10} \left(\frac{\nu^2}{\sigma_0^2} \right)$ (MC= 100 simulations).	104
5.21	KS test for different estimates of amplitude (MC= 100 simulations).	105
5.22	Illustration of the improvements made with the enhanced CuSum algorithm compared to previous work in [101].	106
5.23	Number of missed detection with different window sizes (ws) as function of SNR (MC= 100 simulations) [103].	107
6.1	Batman logo made of Parsons waveforms.	111
B.1	Results of the FSST process to separate two harmonics.	118
C.1	Approximation of a real bat envelope [14] with a GMM.	120
E.1	Verification of the compatibility between a Rayleigh distribution and a noise vector distribution.	124
E.2	Monte-Carlo simulation for a noise vector. Results of the KS tests for real part, imaginary part and magnitude.	125
E.3	Illustration of the behaviour of the Rice distribution as function of the SNR with KS tests (Monte-Carlo simulation with 1000 trials).	128
E.4	FSST processing of the third NOSTRA-ROS signal in order to extract the pulsating constant frequencies.	129
E.5	Illustration of the 2D-CuSum results.	129

List of Tables

1	Paramètres d'émission.	xxix
3.1	ISLRs and PSLRs calculated from the MF and MMF outputs of the different waveforms. The positive values obtained for the ISLRs of the HFM and the first Parsons waveforms are due to the sidelobes energy being superior to that of the mainlobe.	41
3.2	Emission parameters.	52
4.1	Isolation levels for different pair of waveforms. The third column represents the isolation level between a pair (s_i, s_j) . The fourth and fifth columns account respectively for the isolation level between the pair (q_i, s_j) and (s_i, q_j) , where q_i and q_j are the MMF of the corresponding waveform [79].	68
4.2	ISLRs and PSLRs calculated from the MF and MMF outputs of the different waveforms [79].	70
5.1	Parameters of the pulse trains.	97
5.2	Bias evolution of the estimators of ν [103].	105

ACRONYMS

- AF** Ambiguity Function. ix, xvii, xviii, 15, 16, 41–46, 48
- AIC** Akaike Information Criterion. xi, xvii, xviii, 85, 86
- CDF** Cumulative Distribution Function. xvii, xviii, 104
- CF** Constant Frequency. vii, ix, xvii, xviii, xxiii, xxiv, 22–24, 27, 28, 39, 74
- CLRB** Cramér-Rao Lower Bounds. vii, x, xvii, xviii, xxviii, xxix, 31, 43, 45, 49–51, 57, 59
- CuSum** Cumulative Sum. viii, xi, xii, xvii, xviii, xx, xxxi–xxxiv, 2, 33, 34, 36, 79–82, 84–91, 93–101, 105–107, 109, 110, 123, 128, 129
- EC-Threshold** Empirical Constant Threshold. xvii, xviii, 89, 94
- ECA** Extensive Cancellation Algorithm. xvii, xviii, 54, 55
- FAR** False Alarm Rate. xii, xvii, xviii, 91, 94, 97, 98
- FM** Frequency Modulated. vii, ix, xvii, xviii, xxiii, xxiv, 22–24, 27, 28, 39, 73
- FSST** Fourier Synchronsqueezed Transform. xvii, xviii, 34, 128
- GLLR** Generalised Log-Likelihood Ratio. xvii, xviii, 83, 85
- GMM** Gaussian Mixture Model. xii, xvii, xviii, 119, 120
- HFM** Hyperbolic Frequency Modulation. vii–ix, xiii, xvii, xviii, xxi, xxvi–xxviii, 8, 9, 15–17, 34, 38–41, 43–45, 49, 50, 59, 116, 121
- IF** Instantaneous Frequency. ix, xvii, xviii, 8, 33, 35, 36, 117
- ILLR** Instantaneous Log-Likelihood Ratio. xvii, xviii, 83–87
- ISLR** Integrated Side Lobe Ratio. viii, ix, xiii, xvii, xviii, 11–15, 40, 41
- KS** Kolmogorov-Smirnov. xii, xvii, xviii, 104, 105, 124, 125, 127, 128

LFM Linear Frequency Modulation. xvii, xviii, 8, 63

LLR Log-Likelihood Ratio. xvii, xviii, 83

LPG Loss-in-Processing Gain. viii, xi, xvii, xviii, 14, 15, 64, 70, 71

MC Monte-Carlo. xii, xvii, xviii, 104, 105, 107

MF Matched Filter. vii, viii, xiii, xvii, xviii, xxx, 10–15, 40, 41, 49, 50, 53, 55, 73

ML Maximum Likelihood. xvii, xviii, 83, 85, 119

MMF Mismatched Filter. viii–xi, xiii, xvii, xviii, xxvi, 12–15, 40, 41, 53, 55–57, 64, 65, 68–72, 110

MTBFA Mean Time Between False Alarm. xvii, xviii, 91, 94

PDF Probabiliy Density Function. xvii, xviii, 83, 84, 86, 126, 127

PLFM Piecewise Linear Frequency Modulation. xvii, xviii, 62, 63

PRF Pulse Repetition Frequency. xvii, xviii, 17

PRI Pulse Repetition Interval. ix, xvii, xviii, xxii, xxix, 17, 19, 33, 34, 52, 82, 93, 96–98, 106

PSLR Peak-to-Side Lobe Ratio. xiii, xvii, xviii, 11–15, 40, 41

QCF Quasi-Constant Frequency. xvii, xviii, xxiii, 22, 73, 76

RMSE Root Mean Squared Error. vii, x, xii, xvii, xviii, xxviii, xxix, 36, 37, 43, 49–51, 93, 96, 98

RR Rayleigh-Rice. xvii, xviii, 86, 89, 93, 95

SCAT Spectrogram Correlation and Transformation. ix, xvii, xviii, xxxi, 24–27, 61, 73, 77, 110

SNR Signal-to-Noise Ratio. vii, x–xii, xvii, xviii, xxii, xxviii, xxix, xxxiii, xxxiv, 10, 13, 14, 45, 49–51, 85, 86, 88, 93–98, 101–107, 110, 124, 126, 127

TOA Time of Arrival. xvii, xviii, 81, 100

NOTATIONS

Operator

\cdot^*	Conjugate.
\cdot^H	Hermitian transpose.
\cdot^T	Transpose.
$\hat{\cdot}$	Estimate.
$\mathbb{E}[\cdot]$	Expected value.

Radar

A_r	Target amplitude.
B	Bandwidth.
F_s	Sampling frequency.
K_q	Length of the Mismatched filter.
N_p	Number of pulses.
R_0	Initial range.
R	Range.
T_r	Pulse Repetition Interval.
T	Pulse duration.
Λ_q	Convolution matrix.
β_q	Loss-in-processing gain in dB.
$\chi(\tau, \nu_d)$	Ambiguity function.
ν_d	Doppler shift frequency.
τ_0	Initial delay.
τ	Delay.
$\varphi(t)$	Phase.
a	Parsons curvature parameter.
c	Speed of light in the vacuum.

$f(t)$	Instantaneous frequency.
f_0	Starting frequency.
f_1	Ending frequency.
f_c	Carrier frequency.
q	Mismatched filter.
$r(t)$	Received signal.
$u(t)$	Baseband signal.
v_r	Radial velocity.
$w(t)$	Noise.
$y(t)$	Compressed signal.

CuSum

I_k	k-th order modified Bessel function.
K	Number of samples (maximum threshold definition).
L	Number of noise series.
M	Number of samples.
N	Number of samples (received data).
α	False Alarm Rate.
η	Threshold.
μ	Mean.
ν	Signal amplitude.
σ^2	Variance.
τ	Change point.
$g[n]$	Generalized Log-Likelihood Ratio.
$r[N]$	Magnitude of the received data.
$s[n]$	Instantaneous Log-Likelihood Ratio.

RÉSUMÉ EN FRANÇAIS

Contexte

Héritage de la première moitié du XX^e siècle et en particulier de la Seconde Guerre mondiale [1], la technologie du radar s'est largement développée et se décline désormais dans de nombreuses applications. En effet, les systèmes radars sont utilisés aussi bien pour la surveillance météorologique, que le contrôle du trafic aérien ou encore la surveillance spatiale [2]. Ainsi, et comme toutes les technologies, le radar doit évoluer pour faire face à diverses problématiques.

Parmi ces problématiques, on retrouve notamment la congestion du spectre électromagnétique [3]. En effet, les applications du radar étant multiples, il occupe une partie non négligeable du spectre électromagnétique. De plus, cette ressource est également utilisée par d'autres services, comme ceux de communications ou encore de diffusions audiovisuelles par exemple. Le spectre électromagnétique se retrouve donc fortement encombré et la situation ne fait qu'empirer avec les années, le nombre d'utilisateurs et les besoins en bande des différents services ne cessant d'augmenter. Cela conduit à une cohabitation nécessaire au sein des bandes spectrales, tout en atténuant les interférences. À cela s'ajoute le besoin intemporel d'améliorer, ou du moins de maintenir, les performances des radars.

Les difficultés mentionnées ci-dessus nécessitent la création et l'optimisation de nouvelles formes d'ondes radar. Généralement regroupée sous l'appellation diversité des formes d'ondes [4], la recherche de nouvelles formes d'ondes pour les applications radar est un vaste sujet de recherche. En effet, la diversité des formes d'ondes peut englober aussi bien la conception de systèmes joint radar-communications [5], que la recherche de formes d'ondes valables pour des utilisations MIMO (Multiple Input Multiple Output) [6] ou encore les approches biomimétiques, sujet de cette thèse.

Le biomimétisme consiste à s'inspirer du vivant pour trouver des solutions technologiques à nos problématiques. Dans le domaine des formes d'ondes, les chauves-souris ont commencé leurs recherches quelques millions d'années avant nous afin de perfectionner une fascinante capacité : l'écholocation. En émettant des signaux ultrasonores, elles sont capables de naviguer et de chasser dans des environnements variés, qu'il s'agisse de milieux ouverts ou complètement encombrés, et ce, sans se gêner entre elles [7]. Le catalogue des formes d'ondes existantes parmi les différentes espèces de chauves-souris en fait un exemple remarquable d'adaptation et une source d'inspiration. L'analogie flagrante avec le radar a d'ailleurs fait de l'écholocation une source d'étude pour des applications en radar et sonar [8][9][10].

L'objectif de cette thèse est donc d'étudier les formes d'ondes des chauves-souris afin de proposer une forme d'onde bio-inspirée adaptée pour des applications radars.

Organisation de la thèse

Cette thèse est divisée en six chapitres. Le chapitre 1 introduit la thèse, son contexte et les contributions apportées.

Avec le chapitre 2, les bases du monde du radar sont introduites et expliquées afin de comprendre les travaux présentés. S'ensuit une description du monde des chauves-souris permettant de comprendre le principe d'écholocation et d'introduire les références sur le sujet.

Le chapitre 3 est dédié à l'objectif principal de cette thèse : la proposition d'une forme d'onde bio-inspirée. Après introduction de notre forme d'onde bio-inspirée, une étude et des discussions sur ses capacités par rapport au traitement radar et d'autres formes d'ondes existantes sont présentées. L'analyse de données réelles vient clôturer le chapitre.

La viabilité de la forme d'onde bio-inspirée ainsi validée, le chapitre 4 présente deux cas d'utilisation de cette dernière. Le premier exemple d'application, décrit l'apport de la forme d'onde bio-inspirée dans un cadre multistatique, en réponse au problème de gestion du spectre. Le second exemple est un travail exploratoire sur l'estimation de l'effet Doppler grâce à la forme d'onde bio-inspirée et un traitement lui aussi bio-inspiré.

Le chapitre 5 expose un travail supplémentaire sur un algorithme de détection de changement. Initialement proposé pour l'analyse des signaux de chauves-souris, l'algorithme du CuSum (Cumulative Sum en anglais, pour somme cumulative) a été dérivé pour la détection de signaux radars inconnus.

Enfin, le chapitre 6 conclut ce manuscrit et présente des pistes pour de futures recherches.

Synthèse des Travaux

Les Bases du Radar

Pour comprendre ce qui suit, qu'il s'agisse de ce résumé ou du manuscrit dans son entièreté, le principe du radar doit être compris. Un radar, acronyme en anglais de RAdio Detection And Ranging, est un système qui transmet des ondes électromagnétiques afin de détecter et localiser des cibles. Le signal transmis, $s(t)$, se propage à la vitesse de la lumière dans l'espace jusqu'à ce qu'il soit réfléchi par une cible. Le signal réfléchi, $r(t)$, correspondant à une version bruitée, atténuée et retardée du signal original, $s(t)$, est analysé par le radar afin de déterminer la distance de la cible, R , ou encore sa vitesse grâce à l'effet Doppler¹, ν_d . Le schéma présenté en figure 1 illustre ce principe.

1. L'effet Doppler traduit la différence entre la fréquence reçue et la fréquence émise.

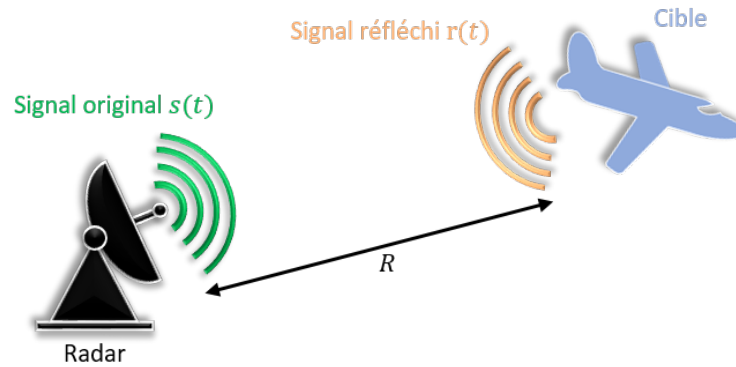


Figure 1: Principe du radar.

Les signaux envoyés par un radar sont appelés des formes d'ondes. Dans cette thèse, la forme d'onde bio-inspirée proposée est comparée à deux autres formes d'ondes couramment utilisées dans le domaine du radar. La première est le chirp [11], la forme d'onde la plus utilisée en radar. Elle est décrite comme une modulation linéaire de fréquence avec une amplitude constante et un spectre relativement plat. La seconde forme d'onde est la modulation de fréquence hyperbolique (désignée par l'acronyme HFM pour Hyperbolic Frequency Modulated). Cette dernière, souvent utilisée pour décrire les signaux de chauves-souris [8], désigne des formes d'ondes hyperboliques et présentant donc une certaine courbure dans leur fréquence instantanée. Les figures 2(a) et 2(b) permettent de visualiser les deux signaux présentés.

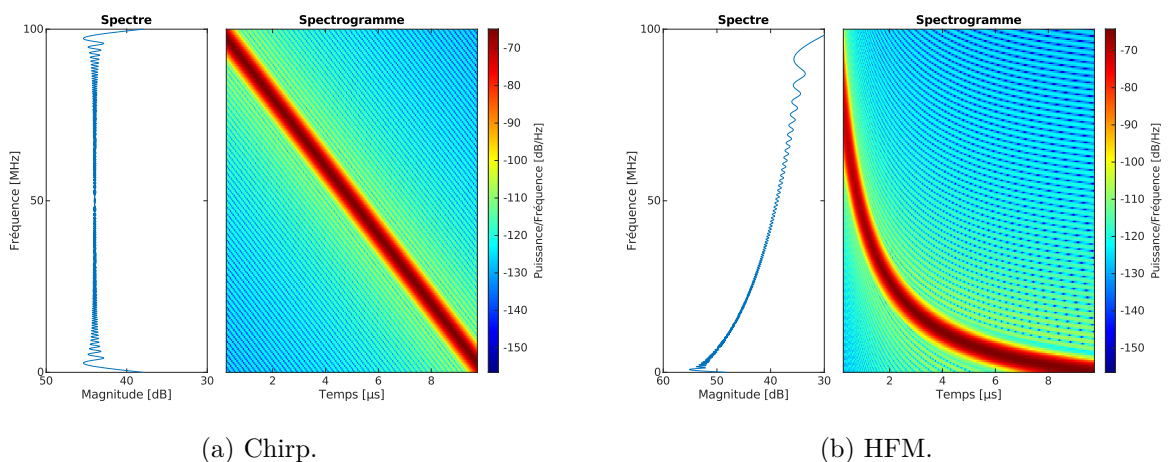


Figure 2: Exemples de formes d'ondes radar classiques : a) le chirp et b) HFM. Les impulsions ont une durée $T = 10\mu\text{s}$ et une largeur de bande $B = 100\text{MHz}$. Sur chaque sous-figure, le graphe de gauche représente le spectre (représentation en fonction des fréquences), tandis que celui de droite montre un spectrogramme (une représentation Temps-Fréquence). La fréquence d'échantillonnage est de $F_s = 500\text{MHz}$.

Un radar transmettant plus d'une impulsion, on considère ce qui s'appelle un train d'impulsions. Chaque signal est alors séparé du suivant par une durée, T_r , appelée la Période de Répétition des Impulsions (PRI). Afin d'analyser le train d'impulsions réfléchis, le traitement du signal en radar passe d'abord par une compression d'impulsion en retard (ou distance, les deux étant liés comme montré au chapitre 2). Pour réaliser cette compression, le filtre adapté (Matched Filter en anglais) est souvent utilisé [11]. Le filtre adapté est apprécié car il maximise le rapport signal à bruit de la cible (ou SNR pour Signal-To-Noise Ratio en anglais)². Le signal de référence est donc corrélé avec le signal reçu pour mesurer la similarité entre les deux signaux. Le filtre adapté permet ainsi de déterminer le retard entre les deux et ainsi la distance de la cible. La compression Doppler par transformée de Fourier permet ensuite de déterminer la fréquence Doppler de la cible et sa vitesse. En combinant ces compressions, on obtient alors des cartes retard-Doppler (ou distance-Doppler), comme celle donnée en figure 3.

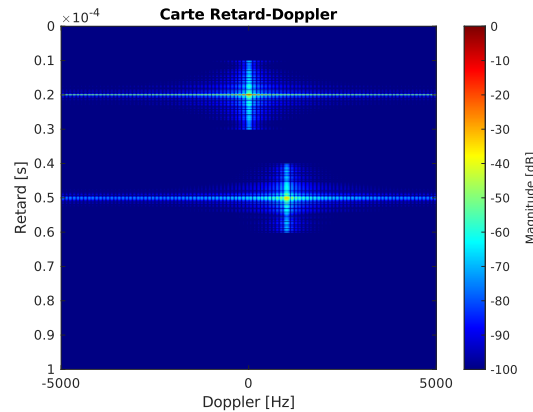


Figure 3: Sortie du traitement retard-Doppler pour deux cibles simulées avec un train d'impulsions composé de chirp. Une cible est statique à un retard de $\tau = 20\mu\text{s}$, tandis que la seconde est mobile, à un retard de $\tau = 50\mu\text{s}$ et présente un doppler de $\nu_d = 1\text{kHz}$.

Les Chauves-souris et l'Écholocation

Les chauves-souris et leur capacité d'écholocation sont au cœur de cette thèse. Ces mammifères capables de voler ont en effet acquis la capacité de naviguer en utilisant des ondes ultrasonores. Ce sonar biologique fonctionne en émettant des signaux sonores à haute fréquence entre 20kHz et 100kHz, voire plus, à travers la bouche ou le nez selon les espèces. À l'image du radar et comme le montre le schéma en figure 4, les chauves-souris analysent les signaux reçus pour s'orienter mais surtout pour chasser.

². Le rapport signal à bruit est le rapport entre la puissance du signal et celle du bruit, souvent exprimé en décibels (dB). Il indique la qualité du signal étudié. Plus le SNR est bas, plus le signal est altéré par le bruit et inversement.

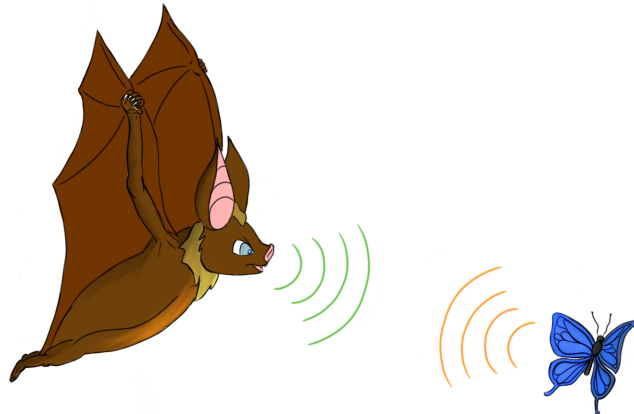


Figure 4: Schéma illustratif du principe d'écholocation.

Ce qui rend l'écholocation encore plus intéressante dans notre cas, c'est la diversité des formes d'ondes observées chez les chauves-souris. Tout d'abord, les signaux utilisés par les chauves-souris peuvent être classés en deux types : les signaux à bande étroite et les signaux à large bande [12][13]. D'une part, les formes d'ondes à bande étroite désignent soit des signaux à fréquence quasi constante (QCF pour Quasi-Constant Frequency) avec une légère modulation de fréquence, soit des signaux à fréquence constante (CF pour Constant Frequency) avec des portions de quelques kHz modulées en fréquence au début et à la fin. D'autre part, les signaux à large bande désignent les signaux avec des modulations décroissantes de fréquence et une grande largeur de bande (FM pour Frequency Modulated). La figure 5 résume ces différentes catégories.

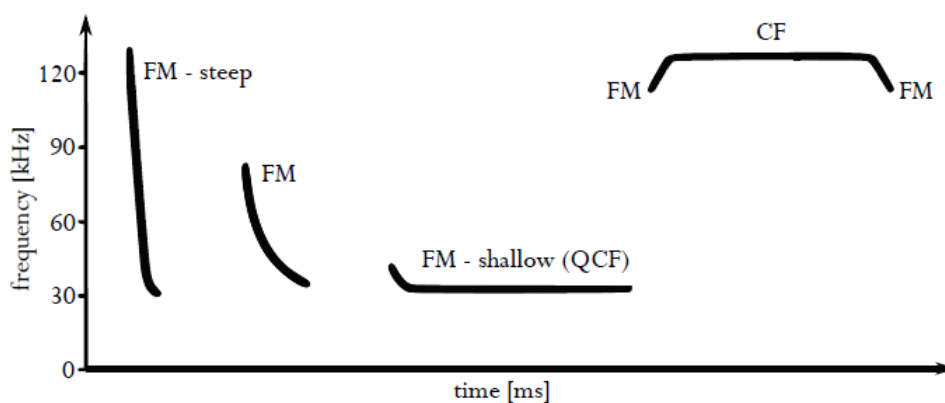


Figure 5: Catégories principales des signaux d'écholocation (extrait de [13], CC BY-NC-SA 3.0).

Chaque espèce dispose donc de son propre langage, adapté à son environnement, sa méthode de chasse et à ses proies favorites [7]. Qui plus est, les chauves-souris possèdent un contrôle

remarquable de leurs paramètres d'émission. Elles peuvent en effet faire varier la durée, la largeur de bande, la durée entre les impulsions et même la courbure de la fréquence instantanée de leurs formes d'ondes. Cette flexibilité est particulièrement visible lorsqu'elles chassent, comme illustré sur les schémas de la figure 6. Il s'agit d'exemples de séquence de chasse pour deux espèces de chauves-souris différentes, où trois phases peuvent être délimitées. La première, la phase de recherche, correspond à la période durant laquelle la chauve-souris scanne son environnement à la recherche d'une proie potentielle. Dès qu'une cible a été détectée, la chauve-souris passe en phase d'approche. Les paramètres d'émission sont alors modifiés pour éviter toute superposition entre signaux émis et reçus, en diminuant lentement l'intervalle entre les impulsions et leur durée. Enfin, la phase terminale, souvent appelée buzz final, précède la capture, réussie ou non.

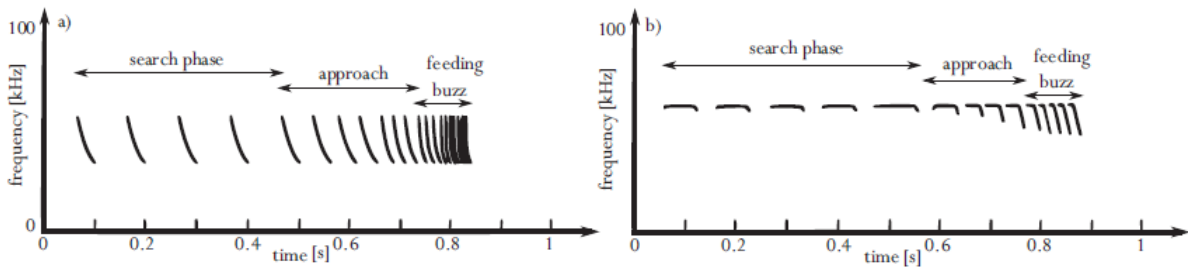


Figure 6: Séquence de chasse d'une chauve-souris émettant a) des signaux FM et b) une autre émettant des signaux CF (extrait de [13], CC BY-NC-SA 3.0).

Afin de trouver la forme d'onde bio-inspirée capable de correctement mimer les signaux de chauves-souris, une analyse de la littérature et de signaux réels a été menée. La figure 7 montre le spectrogramme d'un des signaux étudiés, une séquence de chasse d'une espèce spécifique de chauve-souris : la noctule commune (*Nyctalus noctula*). On remarque donc sur la figure 7,

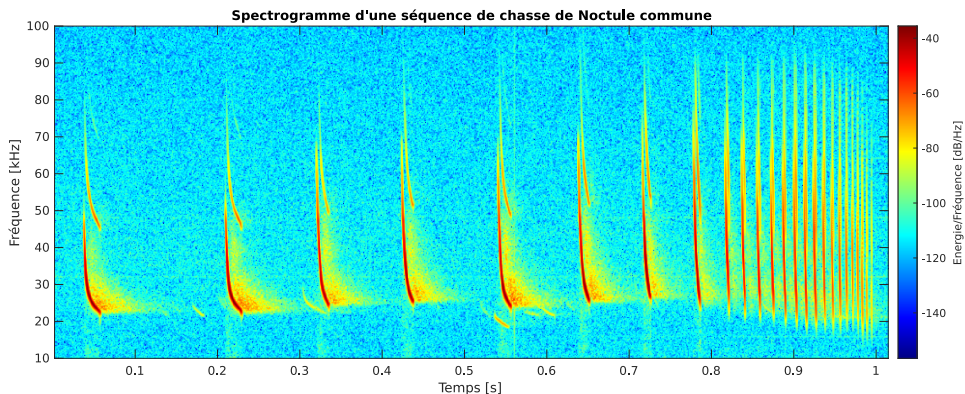


Figure 7: Authentique séquence de chasse de *Nyctalus noctula* [14]. Le train d'impulsions comprend 25 impulsions échantillonnées à 250kHz.

les phases de chasse ainsi que la flexibilité dans la création des impulsions mentionnées plus haut. Cette chauve-souris insectivore a pour habitude de chasser en milieu ouvert en émettant des signaux à bande relativement étroite et de durée assez longue, entre 8 et 25ms [7]. Après détection d'une proie potentielle, les impulsions deviennent plutôt large bande, balayant de manière décroissante une bande d'environ 40kHz [7][15]. Une impulsion contient souvent deux à trois harmoniques, le premier étant le plus énergétique.

Une étude préliminaire de ces signaux a permis d'en extraire les paramètres temporels et fréquentiels, puis de les approximer avec la fonction mathématique la plus appropriée. C'est ainsi que la fonction exponentielle-2 décroissante, désignée par la fonction de Parsons dans la suite, a été proposée pour décrire les signaux de chauves-souris. Étudiée avec sept autres fonctions mathématiques dans [16] pour identifier les espèces de chauves-souris selon leurs signaux, cette fonction était l'une des meilleures pour représenter les formes d'ondes de chauves-souris. La fonction de Parsons décrit la fréquence instantanée et le signal transmis avec les équations suivantes :

$$f(t) = \frac{f_0}{f_0 - af_1} \left[(f_0 - f_1) \left(\frac{af_1}{f_0} \right)^{\frac{t}{T}} + (1 - a)f_1 \right], \quad (1)$$

$$u(t) = \frac{1}{\sqrt{T}} \text{Rect} \left\{ \frac{t}{T} \right\} e^{\frac{2i\pi f_0}{f_0 - af_1} \left[\lambda \beta^{\frac{t}{T}} + (1-a)f_1 t \right]}, \quad (2)$$

où $\lambda = \frac{(f_0 - f_1)T}{\ln(\beta)}$ et $\beta = \frac{af_1}{f_0}$ avec f_0 la fréquence de début, f_1 la fréquence de fin et T la durée d'impulsion. Le terme $\text{Rect} \left\{ \frac{t}{T} \right\}$ est la fonction porte définie par

$$\text{Rect}\{t\} = \begin{cases} 1 & \text{pour } -\frac{1}{2} \leq t \leq \frac{1}{2} \\ 0 & \text{sinon} \end{cases}. \quad (3)$$

La particularité de la fonction de Parsons réside dans le paramètre a , qui permet d'ajuster la courbure hyperbolique du signal. Ce paramètre de décroissance s'accompagne de certaines conditions (on considère $f_0 > f_1$) [16] :

- ✎ $a = 0$, la courbe temps-fréquence décrit une composante verticale modulée fréquentiellement suivie d'une composante à fréquence constante.
- ✎ $a < \frac{f_0}{f_1}$, le balayage fréquentiel est convexe et approxime un chirp quand a se rapproche du rapport $\frac{f_0}{f_1}$.
- ✎ $a > \frac{f_0}{f_1}$, le balayage fréquentiel est concave.

La figure 8 illustre le comportement de la fonction de Parsons selon les différentes conditions citées. Ainsi, la fonction de Parsons permet, via le paramètre a , de définir une infinité de formes d'ondes à paramètres temporels et fréquentiels fixés. De plus, une étude d'ajustement de courbe

a permis de reproduire synthétiquement les signaux de la noctule commune avec la fonction de Parsons, et ce avec un fort degré de précision.

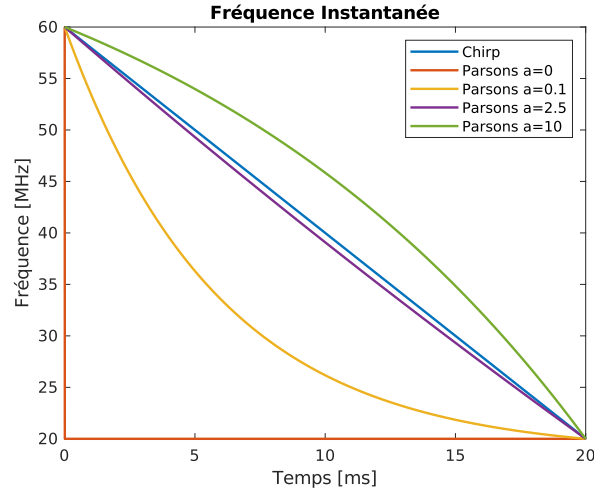


Figure 8: Fréquences instantanées de fonctions de Parsons avec différentes courbures ($\frac{f_0}{f_1} = 3$ avec $f_0 = 60\text{kHz}$, $f_1 = 20\text{kHz}$ et $T = 20\text{ms}$).

Forme d'Onde Bio-inspirée et Radar

La fonction de Parsons se retrouve ainsi propulsée comme candidate potentielle pour être une forme d'onde bio-inspirée en vue d'application radar. Mais pour cela, il a fallu évaluer sa réponse au traitement radar classique ainsi que ses performances.

La première étape a consisté dans la comparaison des sorties du filtre adapté pour la fonction de Parsons, le chirp et la fonction HFM. La figure 9(a) permet d'observer les différentes sorties et ainsi de noter que les fonctions hyperboliques, aussi bien les formes d'ondes de Parsons que HFM, ont, de manière générale, des niveaux de lobes secondaires plus élevés. Le lobe principal apparaît également plus large. Ce résultat est connu, notamment dans la littérature liée aux chauves-souris, et est attribué à la présence plus ou moins forte d'une portion à fréquence constante selon la courbure du signal. Pour ces mammifères volants, les modulations constantes sont plus adaptées à la détection et à l'estimation du Doppler, alors que les modulations fréquentielles sont, elles, nécessaires pour une estimation précise de la distance [17][18]. Néanmoins, on peut noter la flexibilité de la fonction de Parsons en réponse au filtre adapté. Le paramètre a permet donc une certaine adaptabilité comparable à celle des chauves-souris.

Concernant le niveau des lobes secondaires, cela peut poser problème dans un cadre radar, notamment en présence de cibles avec une faible réponse qui pourraient ainsi être masquées par une cible plus forte. Dans une telle situation, il est possible d'utiliser le filtre désadapté (ou MMF pour MisMatched Filter en anglais)[19]. Ce filtre s'obtient en résolvant un problème

d'optimisation qui, dans notre cas, consiste à réduire le niveau des lobes secondaires. Une fois le filtre calculé, la figure 9(b) est obtenue. Le niveau des lobes secondaires pour chacune des formes d'ondes a ainsi été diminué, la fonction de Parsons pouvant même obtenir des niveaux similaires à ceux du chirp. Une perte de 2dB est toutefois observable au niveau du lobe principal mais elle est simplement due à l'une des conditions à respecter pour résoudre le problème d'optimisation. Les détails sont disponibles dans les chapitres 2 et 3.

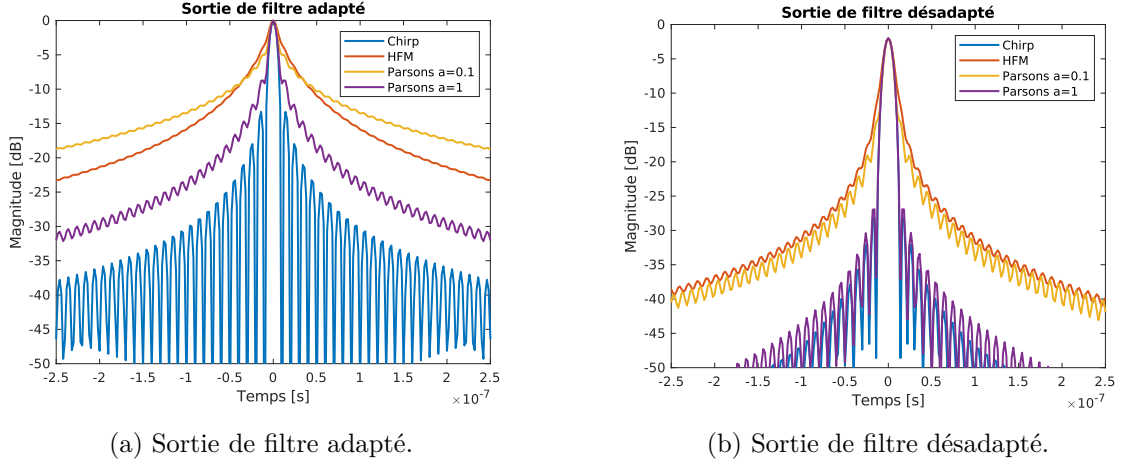


Figure 9: Sortie de compression d'impulsion en utilisant a) le filtre adapté et b) le filtre désadapté ($T = 50\mu\text{s}$, $B = 100\text{MHz}$).

L'étape suivante de cette étude a été d'évaluer la fonction d'ambiguïté de notre forme d'onde bio-inspirée. La fonction d'ambiguïté, notée $\chi(\tau, \nu_d)$, est un autre outil classique en radar qui permet de quantifier l'impact de la vitesse d'une cible et donc du Doppler sur la sortie du filtre adapté pour une forme d'onde donnée. Elle est fonction du retard, τ , et du Doppler, ν_d . Les formules théoriques de la fonction d'ambiguïté pour le chirp et la fonction HFM sont disponibles dans la littérature [11][20]. Concernant la fonction de Parsons, les calculs ont donc été menés pour fournir la fonction d'ambiguïté théorique. L'équation finale est la suivante :

$$\chi(\tau, \nu_d) = \frac{1}{\ln \beta} e^{\frac{-2i\pi f_0}{f_0 - a f_1} (1-a) f_1 \tau} \left[\left(\beta^{\frac{T-\tau}{T}} \right)^{\alpha_2 + 1} E_{-\alpha_2} \left(-\alpha_1 \beta^{\frac{T-\tau}{T}} \right) - E_{-\alpha_2}(-\alpha_1) \right]. \quad (4)$$

où $\lambda = \frac{(f_0 - f_1)T}{\ln(\beta)}$, $\beta = \frac{a f_1}{f_0}$, $\alpha_1 = \frac{2i\pi f_0}{f_0 - a f_1} \lambda \left(1 - \beta^{\frac{\tau}{T}} \right)$ et $\alpha_2 = 2i\pi \nu_d \frac{T}{\ln \beta} - 1$. La fonction $E_\alpha(z) = z^{\alpha-1} \int_z^\infty \frac{e^{-t}}{t^\alpha} dt$ représente la fonction exponentielle intégrale complexe et est définie pour $a, z \in \mathcal{C}, z \neq 0$ [21]. Les calculs théoriques ont été validés par simulation et il a été observé que la tolérance au Doppler de la fonction de Parsons peut être contrôlée via le paramètre a . Encore une fois, les détails des calculs sont présentés dans le chapitre 3 avec des figures illustrant les résultats.

La fonction d'ambiguïté ainsi introduite, le lien peut être fait avec les bornes de Cramér-Rao (ou CLRB pour Cramér-Rao Lower Bounds en anglais)[22]. Ces bornes définissent une limite inférieure sur la variance d'un estimateur non biaisé. En d'autres termes, cela permet d'évaluer la précision sur l'estimation du retard et du Doppler avec une forme d'onde donnée. Les bornes de Cramér-Rao sont dérivées de la matrice d'information de Fisher [22][23], comme suit :

$$CRLB(\tau) = -\frac{\mathbf{J}_{AF}(2, 2)}{\text{SNR} \det(\mathbf{J}_{AF})}, \quad (5)$$

$$CRLB(\nu_d) = -\frac{\mathbf{J}_{AF}(1, 1)}{\text{SNR} \det(\mathbf{J}_{AF})}, \quad (6)$$

où SNR représente le rapport signal à bruit et \mathbf{J}_{AF} est la matrice de la dérivée seconde de la norme carrée de la fonction d'ambiguïté décrite comme :

$$\mathbf{J}_{AF} = \left(\begin{array}{cc} \frac{\partial^2 |\chi(\tau, \nu_d)|^2}{\partial \tau^2} & \frac{\partial^2 |\chi(\tau, \nu_d)|^2}{\partial \tau \partial \nu_d} \\ \frac{\partial^2 |\chi(\tau, \nu_d)|^2}{\partial \nu_d \partial \tau} & \frac{\partial^2 |\chi(\tau, \nu_d)|^2}{\partial \nu_d^2} \end{array} \right) \Bigg|_{\tau, \nu_d=0} \quad (7)$$

Comme pour la fonction d'ambiguïté, les bornes du chirp et de la fonction HFM sont fournies dans la littérature [20][22] et les calculs pour la fonction de Parsons ont donc été effectués en suivant la logique décrite dans [20]. Détaillés dans le chapitre 3, ils permettent de définir la matrice suivante :

$$\mathbf{J}_{AF, Parsons} = \left(\begin{array}{cc} \frac{8\pi^2 f_0^2 \lambda^2 (\beta-1)}{T^2 (f_0 - a f_1)^2} \left[\beta - 1 - \frac{\ln(\beta)}{2} (\beta + 1) \right] + \frac{2}{T^2} & \left[2\lambda\beta - \left(\frac{2}{\ln(\beta)} + 1 \right) (\beta - 1)\lambda \right] \\ \frac{4\pi^2 f_0}{(f_0 - a f_1)} & -\frac{2}{3} \pi^2 T^2 \\ \left[2\lambda\beta - \left(\frac{2}{\ln(\beta)} + 1 \right) (\beta - 1)\lambda \right] & \end{array} \right) \Bigg|_{\tau, \nu_d=0} \quad (8)$$

Les bornes ainsi calculées, des simulations de Monte-Carlo ont été effectuées pour valider le comportement à un SNR ≥ 15 dB. La racine de l'erreur quadratique moyenne (ou RMSE pour Root Mean Square Error en anglais) sur l'estimation du retard avec le filtre adapté a donc été mesurée pour les différentes formes d'ondes. Les résultats présentés sur la figure 10 montrent les bornes de Cramér-Rao en pointillés, accompagnées des erreurs mesurées. La précision observée est visiblement proche des bornes pour chaque forme d'onde à fort SNR. De plus, les capacités d'estimation de la fonction de Parsons sont très satisfaisantes et peuvent même s'approcher de celles du chirp. La flexibilité de la forme d'onde bio-inspirée est également encore observable dans la différence entre bornes selon la valeur du paramètre a . D'autres bornes peuvent être considérées pour compléter l'étude et valider le comportement des mesures pour des SNR ≤ 15 dB, telle que la borne de Ziv-Zakai [24]. Pour plus d'informations, se référer au chapitre 3.

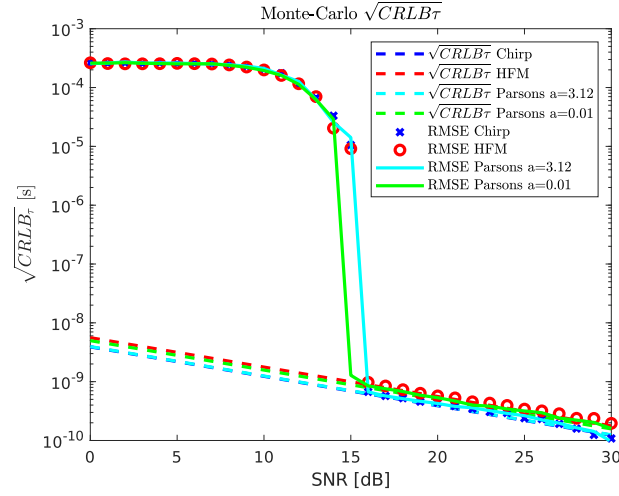


Figure 10: CLRБ et RMSE sur le retard τ , pour un train d'impulsion en fonction du SNR ($T = 50\mu\text{s}$, $B = 100\text{MHz}$, $T_r = 10T$, $N_p = 10$ impulsions).

Afin de compléter l'étude de validité de la forme d'onde bio-inspirée en tant que forme d'onde radar, une étude expérimentale a été menée. Le radar HYCAM [25][26], situé à l'ONERA Palaiseau, a été utilisé pour émettre des signaux réels afin de traquer des avions quittant l'aéroport d'Orly. L'exemple étudié dans ce manuscrit concerne un Airbus A320 quittant Orly le 31 Mai 2024. Des signaux entremêlés, trois fonctions de Parsons et un chirp servant de référence, ont été envoyés successivement avec les paramètres présentés dans la table 1.

Paramètres	Value
Largeur de bande B	20MHz
Fréquence d'échantillonnage F_s	25MHz
Durée d'impulsion T	5 μs
Durée interpulse T_p	50 μs
PRI T_r	200 μs
Paramètre a	[0.01, 0.1, 1]

Table 1: Paramètres d'émission.

Après traitement des données, les cartes distance-Doppler (Range-Doppler en anglais) comme celles présentées sur les figures 11(a) à 11(d) sont obtenues. Il est alors possible de suivre la trajectoire de l'avion à l'aide des différentes formes d'ondes et la fonction de Parsons se montre très efficace. Les mêmes résultats ont été obtenus en utilisant le filtre désadapté pour la compression distance afin de réduire le niveau des lobes secondaires pour les données avec les fonctions de Parsons.

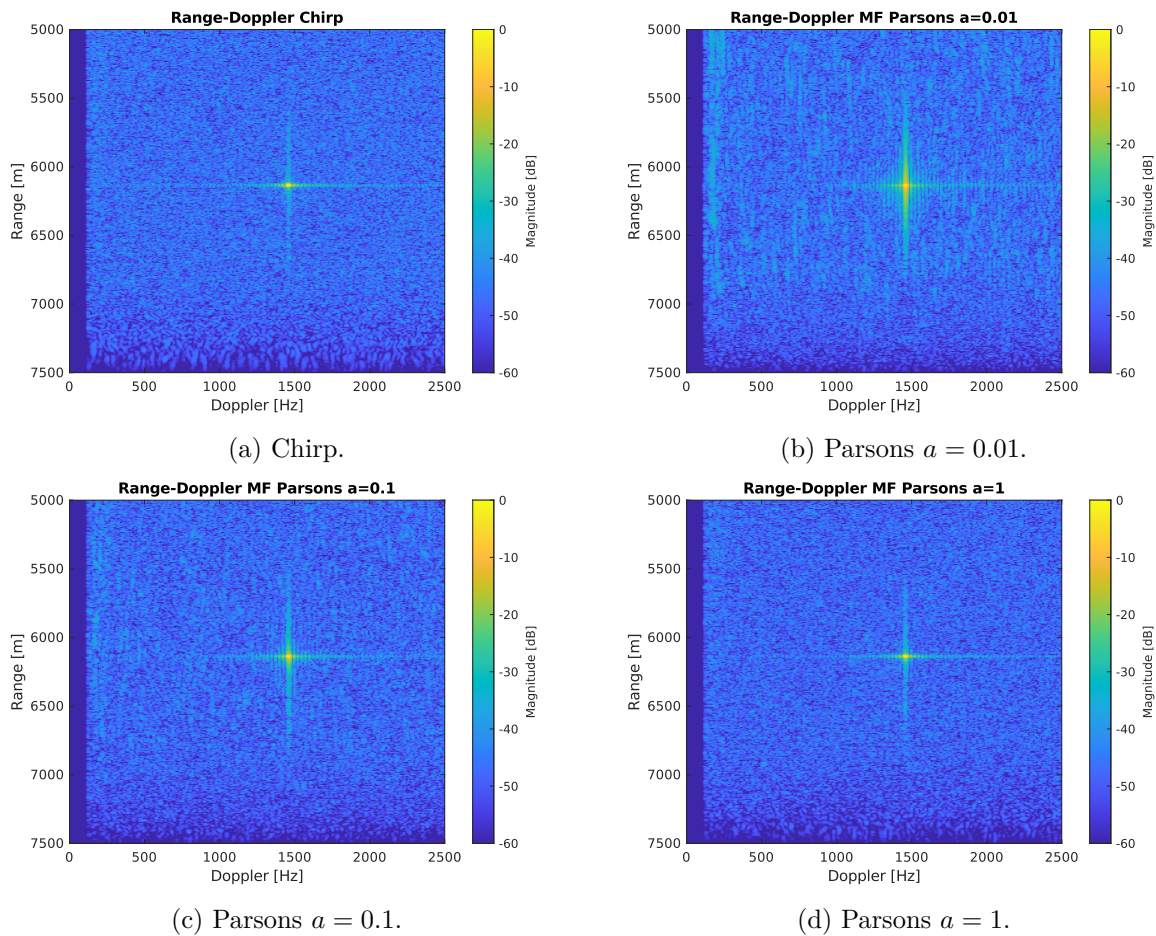


Figure 11: Cartes distance-Doppler de l'avion pour les différentes formes d'ondes et un traitement distance par filtre adapté (MF).

Cadre d'Application Radar

Une fois la forme d'onde bio-inspirée validée en tant que forme d'onde radar potentielle, son implémentation dans deux cadres précis d'applications radar a été étudiée.

Le premier cas répond directement à la problématique de gestion de spectre en considérant une application multistatique. Dans le cas d'un système radar multistatique, plusieurs radars opèrent dans une zone de couverture partagée et, qui plus est, sur la même bande de fréquence dans le cadre étudié. En conséquence, chaque radar doit composer avec les signaux directs et réfléchis des voisins, compliquant la réception et nécessitant la mitigation des interférences. L'objectif avec la fonction de Parsons était d'augmenter la diversité de formes d'ondes et la complexité d'un système multistatique initialement prévu pour trois radars/formes d'ondes [6]. La figure 12 présente l'environnement simulé dans lequel deux fonctions de Parsons ont été ajoutées.

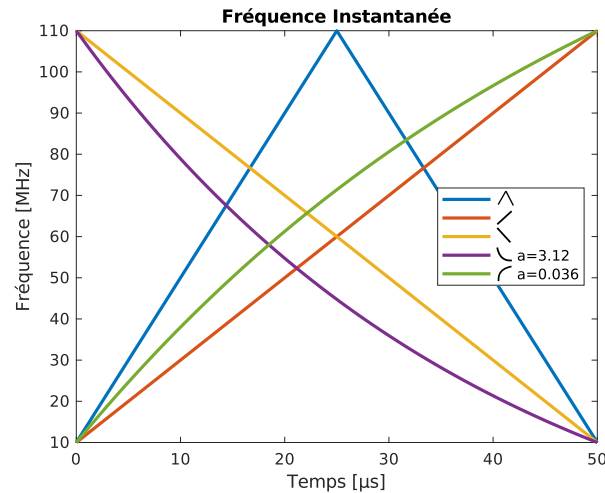


Figure 12: Environnement multistatique simulé vu à travers les fréquences instantanées des formes d'ondes considérées ($B = 100\text{MHz}$, $T = 50\mu\text{s}$).

Afin de vérifier l'implémentation de la forme d'onde bio-inspirée, le niveau d'isolation a été évalué. Ce niveau d'isolation reflète le niveau d'interférence observé dans les corrélations entre les différents signaux. Les résultats ont montré que la fonction de Parsons offrait d'excellents niveaux d'isolation et était donc valide dans un cadre multistatique. L'utilisation du filtre désadapté a également été testée pour gérer le niveau de lobes secondaires sans pour autant impacter négativement le niveau d'isolation.

Dans un second travail exploratoire, la fonction de Parsons a été utilisée pour estimer le Doppler dans les signaux reçus. Pour ce faire, le récepteur Spectrogram Correlation And Transformation (SCAT) [27] a été implémenté. Il s'agit d'un modèle monaural (relatif à une oreille) du système auditif d'une chauve-souris capable de reproduire le traitement réalisé par cette dernière. L'objectif était donc de combiner une forme d'onde bio-inspirée et un traitement bio-inspiré afin de profiter du caractère hyperbolique de ces signaux pour estimer le Doppler d'une cible, à l'image de ce que font certaines espèces de chauves-souris [17][28]. Les premiers résultats sont intéressants, car, avec l'utilisation d'une banque de filtres (l'une des composantes du modèle SCAT), il est possible d'analyser le spectre reçu pour voir les différences avec le spectre émis et d'extraire une information Doppler. Ce travail n'en étant qu'à ses débuts, de plus amples études sont néanmoins nécessaires.

Un Algorithme de Détection de Changement : le CuSum

Présenté au chapitre 5, l'algorithme de somme cumulative (CuSum) désigne un algorithme de détection de changement très apprécié dans la littérature pour sa simplicité et sa vitesse

de traitement [29][30]. Dans cette thèse, l'algorithme a initialement été adapté pour isoler les impulsions dans les signaux de chasses réels de chauves-souris et s'est révélé très efficace. Compte tenu des résultats obtenus et du peu de littérature sur son utilisation dans le domaine radar, un développement de l'algorithme pour des applications radar a été effectué. L'algorithme a donc été réadapté et amélioré pour la détection de signaux radar inconnus. L'objectif consiste à détecter le début et la fin d'impulsions inconnues, ce qui pourrait être profitable pour l'analyse de bandes spectrales d'intérêt afin de connaître l'occupation. Cela s'inscrit dans la problématique de gestion de spectre.

Pour comprendre le principe de l'algorithme, considérons un signal contenant des impulsions noyées dans du bruit. L'objectif du CuSum est d'identifier les moments où la probabilité de distribution de notre signal change en observant les changements dans la moyenne et la variance du signal en question. Deux hypothèses sont alors possibles :

H_0 : Seul le bruit est présent.

H_1 : Le signal est présent.

Chacune de ces hypothèses peut être associée à un modèle statistique. L'algorithme effectue alors une somme des rapports de vraisemblance instantanée liés aux probabilités des modèles choisis et aux paramètres estimés à partir du signal (moyenne et variance). L'utilisation de seuils permet ensuite de déterminer le début et la fin des impulsions présentes dans le signal. Le résultat classique obtenu avec le CuSum dans le cadre de la thèse est illustré en figure 13.

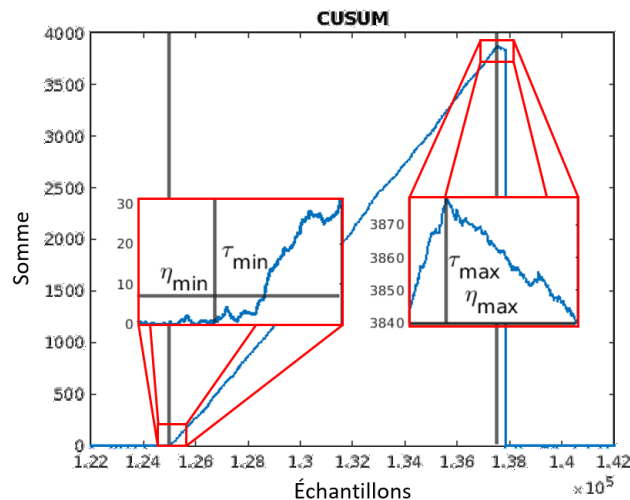


Figure 13: Exemple de sortie du CuSum pour une impulsion. Les paramètres τ_i et η_i représentent respectivement les instants associés à un point de changement et les seuils utilisés pour les valider.

La majeure partie des travaux sur le CuSum présentés dans cette thèse ont été effectués en considérant un modèle de distribution Rayleigh-Rice [31][32]. Des analyses sur des données simulées mais également réelles ont permis de montrer l'efficacité de l'algorithme en terme de détection et d'extraction de paramètres. Une limite a toutefois été mise en exergue notamment avec des signaux réels assez encombrés où l'algorithme peine à séparer les signaux d'intérêt. Des premiers travaux pour résoudre ce problème sont mentionnés en appendice D. Une version améliorée de l'algorithme a aussi été proposée afin de corriger un biais sur un des estimateurs utilisés. La distribution de Rayleigh-Rice étant également utilisée en imagerie médicale, la littérature sur le sujet [33] a permis de corriger le biais sur l'estimateur de notre algorithme et ainsi d'augmenter les performances de détection/estimation à faible SNR.

Conclusion

Conclusions

L'objectif de cette thèse était de proposer une forme d'onde bio-inspirée en vue d'applications radar. Cette recherche de forme d'onde s'inscrivait également dans un contexte de congestion du spectre électromagnétique.

Après une étude de l'écholocation des chauves-souris et de la création de leurs signaux, une solution a été proposée pour imiter de manière effective leurs formes d'ondes grâce à la fonction de Parsons. La flexibilité obtenue avec le paramètre a permet de recréer avec une certaine précision certains signaux de chauves-souris et de valider le côté bio-inspirée du projet.

Cette nouvelle forme d'onde bio-inspirée a bien sûr été évaluée vis-à-vis de ses capacités radar. Le traitement radar classique combiné à une analyse comparative avec d'autres formes d'ondes radars ont validé le potentiel de la fonction de Parsons en tant que forme d'onde radar. La fonction d'ambiguïté et les bornes de Cramér-Rao ont été calculées pour cette fonction. Que ce soit sur données simulées comme réelles, la fonction de Parsons a ainsi montré de notables capacités de précision en estimation distance et une certaine efficacité pour des applications radar. De plus, l'application de la fonction de Parsons dans un cadre multistatique s'est montrée appropriée au vu des résultats de simulations. La forme d'onde bio-inspirée ainsi proposée peut être considérée comme une solution à la problématique de gestion du spectre électromagnétique, tout en maintenant des performances radars appréciables. En supplément, un traitement bio-inspiré a été brièvement étudié pour estimer le Doppler grâce à la fonction de Parsons.

Concernant un résultat subsidiaire, le CuSum, un algorithme de détection de changement, a été implémenté. Initialement choisi et adapté pour la segmentation des signaux de chauves-souris, les résultats intéressants obtenus avec l'algorithme ont amené à une étude approfondie du CuSum en vue d'applications radars, notamment pour la détection de signaux inconnus. Ses performances ont ainsi été évaluées à travers des simulations et des essais sur signaux réels. Le

CuSum permet ainsi d'identifier le début et la fin d'impulsions radars inconnues.

Perspectives

Les perspectives après cette thèse sont nombreuses, en voici donc une liste non exhaustive.

- ✪ L'étude de l'impact des harmoniques présents dans les signaux de chauves-souris. Ces harmoniques pourraient effectivement servir dans le rejet du clutter [34] ou la suppression d'ambiguïté [35].
- ✪ L'étude de la modulation d'amplitude. Les radars ne sont pas encore adaptés pour une telle modulation mais cela pourrait peut-être avoir un intérêt pour la reconnaissance de cible, à l'image de ce que font les chauves-souris.
- ✪ Approfondir les approches cognitives. Acquérir le contrôle des paramètres d'émission en temps réel qui caractérise les séquences de chasse des chauves-souris pourrait être avantageux dans certains cas. En particulier, comprendre comment leur cerveau traite l'information et améliorer le SCAT [27] permettrait d'autres approches pour le traitement du signal.
- ✪ L'optimisation de la forme d'onde bio-inspirée. La fonction de Parsons est loin d'être l'unique solution, des améliorations sont possibles que ce soit vis-à-vis du niveau de lobes secondaires ou même de sa définition mathématique. Le choix du paramètre a pourrait également être optimisé selon la situation, rejoignant ainsi le point précédent.
- ✪ Concernant le CuSum, les travaux sont loin d'être terminés. Les limitations observées avec les signaux congestionnés à faible SNR ont montré que d'autres versions de l'algorithme sont à explorer, comme la version Temps-Fréquence. Les définitions des seuils ou encore le choix des modèles de distributions nécessitent également des recherches approfondies.

INTRODUCTION

1.1 Context and Objectives

Legacy of the first half of the 20th century and particularly of the Second World War [1], radar technology has since been extensively developed and extended to various areas of application. In fact, the use of radar systems ranges from weather monitoring, air traffic control, automotive safety to space monitoring and, of course, surveillance for defence and security. Nevertheless, radar, like any technology, is not immune to the need to evolve in order to face issues on several aspects.

One of the main problematic encountered by the radar community in the past decades concerns the electromagnetic spectrum congestion [3]. Radar, with its wide range of applications, occupies a non-negligible part of the electromagnetic spectrum. Yet this resource is also the playground for communications or radio and television broadcasting. The electromagnetic spectrum is thus highly congested and the situation is not improving over the years, as the number of users is increasing along with the need for greater bandwidth for each of these services. This leads to an inevitable cohabitation within frequency bands, which implies either the mitigation of interference or solutions to coexist. Another timeless challenge is the constant desire to improve the performances of radar systems, including a greater resolution, a better clutter rejection, an improved radar coverage or Doppler estimation.

The aforementioned issues highlight the necessity to design and optimise new radar waveforms. Generically called waveform diversity [4], the investigation of new radar waveforms has been a broad research topic in recent years. It can cover the search for cooperative and multifunctional systems such as joint radar-communication systems [5], the design of valuable waveforms at fixed parameters for Multiple Input Multiple Output (MIMO) applications [6] or biomimicry, the latter being the focus of this thesis.

Biomimicry is synonymous with Nature, and the complex world of waveform design has been effectively studied for millions of years by bats to build their fascinating ability of echolocation. By emitting sophisticated ultrasonic sounds, bats are able to navigate and hunt in various environments, from open to highly cluttered spaces, without interfering with each others [7]. The catalogue of their waveforms is a remarkable example of adaptation and a source of inspiration. Because the analogy between radar and bats is quite obvious, bat echolocation has often been

studied for radar and sonar applications [8][9][10].

The objective of this thesis is thus to study bat waveforms in order to propose a bio-inspired waveform design for radar applications along with the appropriate processing.

1.2 Contributions

The term 'biomimicry' literally stands for imitation of life¹. In order to accurately replicate bat waveforms, the study of their signals and their parameters of emission was the first step. The goal was to understand how bats design their waveform to correctly adapt to their environment but also their hunting behaviour. The literature about bat echolocation is extensive and the paths to begin the thesis were as numerous as interesting. After a comprehensive review of the literature, we narrowed down the possibilities to finally find a valuable strategy to mimic bat waveforms. This involved deriving a mathematical function from the literature on bats and subsequently proposing the waveform for radar applications.

Obviously, this approach is not self-sufficient and the preliminary bibliography work for the search of a waveform led to its radar performance assessment. A comparison was made between the bio-inspired waveform and classical radar waveforms with the usual radar processing. In particular, the Ambiguity Function and Cramér-Rao Lower Bounds associated to the new waveform have been calculated in order to evaluate its accuracy in terms of delay and Doppler estimation, which appeared rather satisfying. Beyond simulations, the bio-inspired waveform was tested in a real experiment to check its true capabilities and the newly acquired flexibility in waveform design.

The next step of this research was to insert the bio-inspired waveform into a concrete radar framework with the objective of asserting its potential as a radar waveform. A first study on a multistatic application has thus been carried out. The objective was to observe the behaviour of the bio-inspired waveform in such a framework and to validate its use to broaden the waveform diversity. Therefore, the waveform was confronted with an already investigated set of waveforms. The isolation level between the bio-inspired function and the other waveforms as well as the Doppler mismatch loss were then evaluated.

Because the objectives of the thesis were both the proposition of a waveform and its processing, a bio-inspired processing known in bat literature has also been studied. This supplementary work thus concerned the implementation of the waveform together with the right processing, both bio-inspired, in order to realise Doppler estimation.

The final result presented in this thesis is an additional work derived from the preliminary investigation on bat waveforms. It is an adaptation of a well-known change point detection algorithm: the Cumulative Sum (CuSum) algorithm. Firstly implemented as a tool to help separate

1. For the distinguished Hellenist $\beta\iota\omicron\varsigma=bios$ for life and $\mu\acute{\iota}\mu\eta\sigma\iota\varsigma=mimesis$ for imitation.

pulses in real bat signal, the algorithm attracted our attention for many reasons. The literature regarding its application in the radar domain was scarce and the possibilities for unknown radar signal detection were really interesting. Therefore, the algorithm has been implemented and enhanced to detect unknown radar signals.

1.3 Thesis Layout

This thesis is divided into six chapters.

Chapter 1 has already begun and is almost finished (keep going, it gets better), since it is the classic introduction and the overall presentation of the thesis.

Following this introduction, Chapter 2 starts with an overview of the world of radar for beginners. It describes the fundamentals needed to clearly understand the work pursued during the thesis in the radar domain. Because this thesis is about biomimicry, the second part of the chapter 2 is thus dedicated to the other important half of this work: bats. In a similar logic, the objective is to understand the basics behind the bat echolocation, and to review the literature (or at least a part), which supports this work.

Chapter 3 is devoted to the main goal of this thesis: the proposition of a bio-inspired waveform. Where does it come from? what are its advantages?... many questions that may find an answer in this chapter. The initial section of this chapter contains discussions about the capabilities of the novel bio-inspired waveform and comparisons with other radar waveforms. The calculation of the bio-inspired waveform Ambiguity Function and its Cramér-Rao Lower Bounds enrich the discussion. It is followed by actual experimental measurements of the bio-inspired waveform.

The bio-inspired waveform described and analysed, Chapter 4 presents two cases of study. Firstly, the proposed bio-inspired waveform is implemented in a concrete multistatic radar framework and observations are made to check if it can widen the radar waveform diversity. A second section describes an adapted processing technique, which is bio-inspired itself, implemented to estimate the Doppler effect thanks to our bio-inspired waveform. It validates the use of the novel bio-inspired waveform as a radar waveform.


Chapter 5 presents a supplementary work. A change point detection algorithm, initially used to study bat signals at the beginning of this thesis, is derived in order to detect unknown radar signals.

Finally, the conclusion of this thesis is presented in Chapter 6, along with a glimpse into potential future works.


1.4 Publications


The following list summarises the publications issued from the work presented in this thesis. Ask me for autograph versions.


- **National Conference Article**

 Anthony Torre, Abigael Taylor, Dominique Poullin, Thierry Chonavel. *Formes d'ondes bio-inspirées : de la chauve-souris au radar*. GRETSI 2023, Aug 2023, Grenoble, France.

- **International Conference Article**

 Anthony Torre, Abigael Taylor, Dominique Poullin, Thierry Chonavel. *Parameters Extraction of Unknown Radar Signals Using Change Point Detection*. RADAR 2023: IEEE International Radar conference, Nov 2023, Sydney, Australia.

 Anthony Torre, Abigael Taylor, Dominique Poullin, Thierry Chonavel. *Improved Change Point Detection via Bias Reduction in Parameters Estimation*. 2024 32nd European Signal Processing Conference (EUSIPCO), Lyon, France, 2024.

 Anthony Torre, Abigael Taylor, Dominique Poullin, Thierry Chonavel. *Bioinspired Waveform in a Multistatic Configuration*. RADAR 2024: IEEE International Radar conference, Oct. 2024, Rennes, France.

- **Journal Article (in preparation)**

 Anthony Torre, Abigael Taylor, Dominique Poullin, Thierry Chonavel. *Bioinspired Waveform and Processing for Radar Applications*. IET Radar, Sonar and Navigation.

RADAR AND BATS FOR BEGINNERS

Welcome to both the apprentice and the master in this introductory and informative chapter about radar and bats. It does not matter if you are unaware of the specificities of bats or if you wish to check your knowledge about radar processing, this chapter will describe all the fundamentals needed to clearly understand the work pursued in this thesis. The first section introduces the world of radar with a clear definition of the basic principles behind this technology. It is followed by a description of the classical waveforms transmitted by the radar along with the overall signal processing used to extract the information of interest. The second part of the chapter then brings you into the world of bats, to the discovery of these cute little mammals and their fascinating echolocation ability. After a brief introduction to the basis of the echolocation, the subject of this thesis, their waveforms will be presented. A documented analysis of their sonar capacities and their biological processing is provided before concluding this introductory chapter on both radar and bats.

2.1 The World of Radar

2.1.1 Generalities and Basic Principles

RAdio Detection And Ranging, commonly referred to as RADAR, designates a system that transmits electromagnetic waves in order to detect and localise targets by processing the back-scattered signal. Radar is complementary to optical sensors because it can process information about a target under circumstances where optical imaging reaches its limits. Indeed, radar can see through the darkness of the night, adverse weather conditions like fog or rain, and at very long distances. The story behind the development of the radar technology is often reduced to the research prior and during the World War II, but the idea of radar detection can be traced back to the late 19th century and the early 20th century. Demonstrations and experiments conducted at this time showed the potential of an electromagnetic system, later on called radar [2]. Nowadays, the technological advances have allowed such an evolution that radar systems are ubiquitous. In fact, even though the first radar that comes to mind is often the one that sentences you to a fine for speeding, they can have many uses as shown in the following non-exhaustive list [2]:

✈ Ground-based radar [36] devoted to the detection of airborne and spaceborne targets but

also missiles in a battle field, or vehicles.

- ✦ Air traffic control [37] to monitor air navigation, to provide information to pilots, to prevent collisions or to support landing manoeuvres.
- ✦ Embedded radar [38], which can be found in aircrafts, ships or satellites with various purposes (weather monitoring, surveillance, navigation, ...).
- ✦ Automotive radar [39] to assist drivers as parking aid or collision avoidance system.
- ✦ Through-the-wall [40] and around-the-corner [41][42] radars for the detection and localisation of static or moving targets behind solid walls and in complex urban environment.

The history of radar put aside, let's try to better understand how this technology works. To help the comprehension, the scheme in figure 2.1 illustrates the following description.

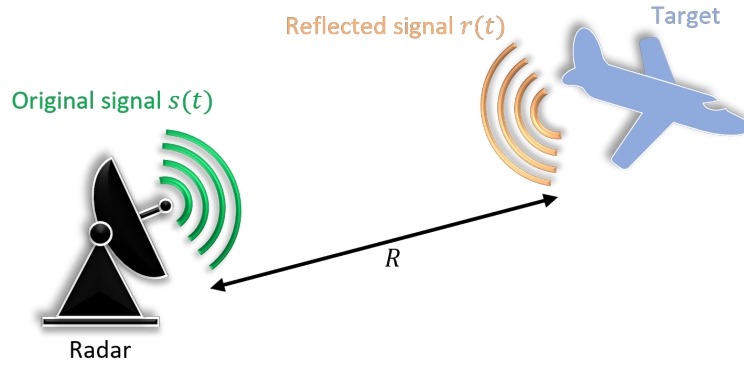


Figure 2.1: Overview of the radar framework.

Firstly, the radar sends an electromagnetic wave $s(t)$ through an antenna. This signal is often a narrow band-pass signal [11] described by the equation

$$s(t) = u(t)e^{2i\pi f_c t}. \quad (2.1)$$

It is composed of a baseband signal $u(t)$ and the carrier signal, which shifts the baseband component at a carrier frequency f_c used to transmit the signal in the desired electromagnetic band. Then, the emitted signal will propagate through space with a velocity equal to the speed of light $c \approx 3 \times 10^8 \text{ m.s}^{-1}$ until it encounters a potential target at a distance R , the target range, as illustrated with the plane in the scheme 2.1. The signal is then reflected back to the radar to be further processed. The received signal, denoted by $r(t)$, corresponds to a noisy, attenuated and delayed version of the original signal, $s(t)$, expressed as follows:

$$r(t) = A_r u(t - \tau(t)) e^{2i\pi f_c (t - \tau(t))} + w(t), \quad (2.2)$$

where $w(t)$ is an additive white Gaussian noise, while $\tau(t)$ represents the target delay and A_r is the target amplitude. The returning echo can be used to determine the position and the velocity of the target. The delay $\tau(t)$ is in fact the time needed for the signal to travel the two-way path between the radar and the target. However, it depends on time as it is influenced by the relative motion between the radar and the target, which has a radial velocity v_r . For a target with constant radial velocity, this delay can be expressed with a first order approximation as

$$\tau(t) = \tau_0 + \frac{2v_r}{c}t, \quad (2.3)$$

where τ_0 is the initial delay corresponding to [11]

$$\tau_0 = \frac{2R_0}{c}, \quad (2.4)$$

with R_0 the initial range. Note that the factor 2 is due to the fact that the signal travels the distance twice. The delay $\tau(t)$ thus described can be assimilated to a contraction/dilatation of the back-scattered signal, which affects both the baseband and the carrier part of the signal. When injected in (2.2), the received signal becomes

$$\begin{aligned} r(t) &= A_r u \left(t - \frac{2v_r}{c}t - \tau_0 \right) e^{2i\pi f_c(t - \frac{2v_r}{c}t - \tau_0)} + w(t) \\ &= A_r u \left(\left(1 - \frac{2v_r}{c} \right) t - \tau_0 \right) e^{2i\pi f_c t} e^{-2i\pi f_c \left(\frac{2v_r}{c} \right) t} e^{-2i\pi f_c \tau_0} + w(t). \end{aligned} \quad (2.5)$$

Because the radial velocity v_r is assumed much smaller than the speed of light, the impact of the delay on the baseband signal is generally neglected [11]. The factor $\left(1 - \frac{2v_r}{c} \right)$ causes a time contraction/dilatation in the time domain, but as the ratio $\frac{2v_r}{c} \ll 1$, it is considered negligible on the duration of the pulse in many radar applications and the delay can be reduced to the definition (2.4). However, the impact of v_r on the carrier signal is not negligible and causes a Doppler shift ν_d given by

$$\nu_d = -\frac{2v_r}{c} f_c. \quad (2.6)$$

The received signal can finally be approximated as

$$r(t) = A_r u(t - \tau_0) e^{2i\pi f_c(t - \tau_0)} e^{2i\pi \nu_d t} + w(t). \quad (2.7)$$

The first objective of the radar is to process the returning signal in order to conclude about the target presence. Thanks to the delay and Doppler shift information, the range and velocity of the target can then be extracted or at least estimated with the right processing. But before describing the classic radar processing, the next section will consider the radar waveforms used to convey these information.

2.1.2 Radar Waveforms

The major topic of this thesis being the study of radar waveforms, this section is dedicated to classic radar waveforms. Each will be described by the corresponding baseband signal, $u(t)$, written as

$$u(t) = \frac{\text{Rect}\left\{\frac{t}{T}\right\}}{\sqrt{T}} e^{i\varphi(t)}, \quad (2.8)$$

where T is the pulse duration and $\varphi(t)$ is the phase. The term $\text{Rect}\left\{\frac{t}{T}\right\}$ is the rectangular function defined by

$$\text{Rect}\{t\} = \begin{cases} 1 & \text{for } -\frac{1}{2} \leq t \leq \frac{1}{2} \\ 0 & \text{otherwise} \end{cases}. \quad (2.9)$$

The Instantaneous Frequency (IF), $f(t)$, which represents the evolution of the frequency as function of time t , will also be provided. It is obtained by deriving the phase of the baseband signal

$$f(t) = \frac{1}{2\pi} \frac{d\varphi(t)}{dt}. \quad (2.10)$$

One of the first signal to be considered is the chirp, which is the most widely used waveform in radar systems. It is defined as a Linear Frequency Modulation (LFM) with a constant amplitude and a relatively flat spectrum. Its instantaneous frequency and the transmitted signal are given by [11]

$$f(t) = f_0 + 2\gamma t, \text{ where } \gamma = \frac{-B}{2T}, \quad (2.11)$$

$$u(t) = \frac{\text{Rect}\left\{\frac{t}{T}\right\}}{\sqrt{T}} e^{2i\pi f_0 t} e^{2i\pi\gamma t^2}, \quad (2.12)$$

where B is the bandwidth and f_0 is the starting frequency. Figure 2.2(a) gives an example of a chirp following this definition, where the linear behaviour is clearly visible along with the flat spectrum.

Another radar waveform examined in this thesis is the Hyperbolic Frequency Modulated (HFM) signal. It has often been used to describe bat signals [8] due to its hyperbolic behaviour, which resembles the curvature of the bat signals. Moreover, its Doppler tolerance in sonar but also in radar detecting high-velocity targets with large time-bandwidth product [43][44] has frequently been investigated. The instantaneous frequency and the resulting transmitted signal of the HFM are expressed as

$$f(t) = \frac{f_0}{1 + \kappa t}, \text{ where } \kappa = \frac{f_0 - f_1}{f_1 T}, \quad (2.13)$$

$$s(t) = \frac{1}{\sqrt{T}} \text{Rect}\left\{\frac{t}{T}\right\} e^{2i\pi\alpha_n \ln(1+\kappa t)}, \quad (2.14)$$

where f_0 and f_1 represent respectively the starting and ending frequencies and $\alpha_h = \frac{f_0}{\kappa}$. The figure 2.2(b) illustrates the behaviour of this function.

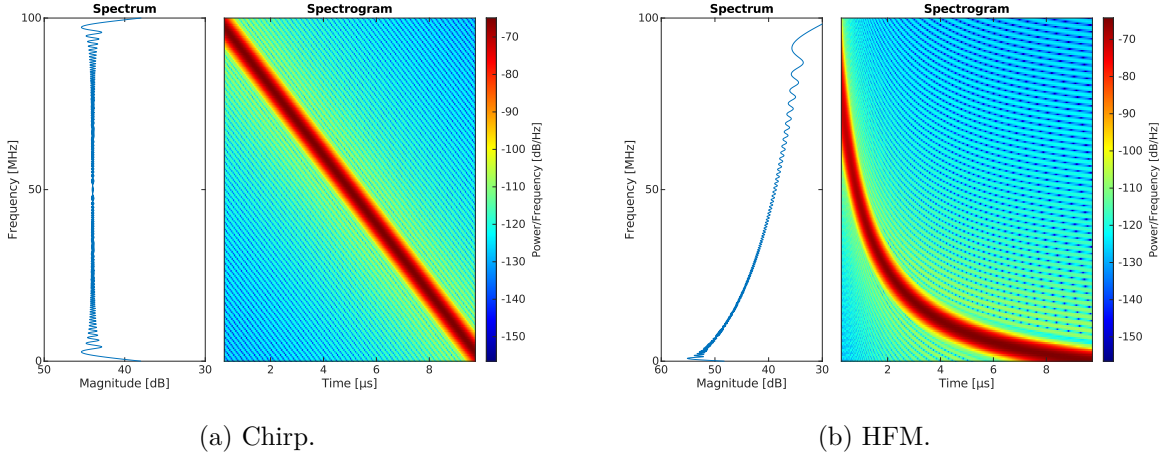


Figure 2.2: Example of classical radar waveforms with a duration of $T = 10\mu\text{s}$ and a bandwidth of $B = 100\text{MHz}$. For both subfigures, the left plot displays the spectrum (representation as function of the frequencies), while the right plot is the spectrogram (Time-Frequency response). The sampling frequency is of $F_s = 500\text{MHz}$.

2.1.3 Radar Processing

The previous sections have described basic radar concepts and illustrated two of the most common radar waveforms. Nevertheless, one question remains: what about the processing of the received information and particularly, how to deal with the delay τ and Doppler information ν_d recapitulated in figure 2.3?

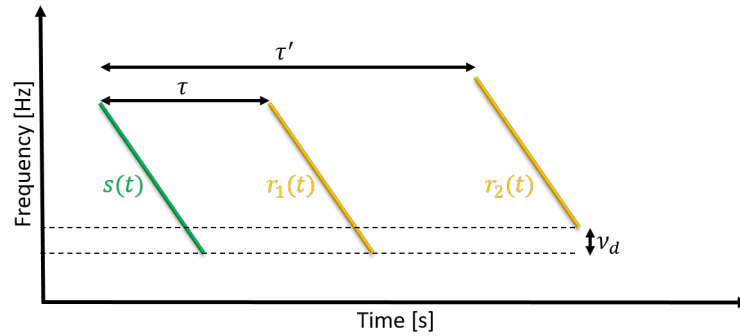


Figure 2.3: Illustrative scheme of the information received with a radar illuminating two distinct targets with a chirp. The two reflected signals, $r_1(t)$ and $r_2(t)$, are received with different delays, τ and τ' , and the second one presents a Doppler shift, ν_d , due to the radial velocity of the target.

The Matched Filter

The following discussion focuses exclusively on the delay, with the Doppler information addressed subsequently in the context of range-Doppler processing. After receiving the back-scattered signal, the analysis in the radar framework is often provided by the matched filter (MF). In radar processing, the matched filter is appreciated as it maximises the Signal-to-Noise Ratio (SNR)¹ at the target delay [11], hence enabling the detection and localisation of a potential target. In other words, for a target with delay τ_0 , it maximises the ratio between the signal energy and the noise energy as follows:

$$\hat{\tau} = \arg \max_{\tau} \frac{|\int_{\mathbb{R}} u(t - \tau_0)h(\tau - t)dt|^2}{\mathbb{E} \left[|\int_{\mathbb{R}} w(t)h(\tau - t)dt|^2 \right]}, \quad (2.15)$$

where h is a filter and $\mathbb{E}[\cdot]$ the expectation operator. It can be demonstrated that for a white noise, the solution to this optimisation problem is the matched filter [11]

$$h(t) = Cu^*(-t), \quad (2.16)$$

where C is an arbitrary constant, generally equal to 1. Note that as $u^*(-t)$ is not causal, a shifted version $u^*(T - t)$, where T is the pulse duration, is generally considered instead in practice. Moreover, the MF being defined, it now has to be applied for the different possible delays. Therefore, the output of the matched filter can be seen as the convolution of the received signal with this optimal filter, which for a noiseless signal is also the autocorrelation of the waveform. In the hypothesis where no Doppler shifts are observed, the output compressed signal y can be written as

$$\begin{aligned} y(\tau) &= (r * h)(\tau) \\ &= A_r \int_{-\infty}^{+\infty} u(t - \tau_0)h(\tau - t)dt + \int_{-\infty}^{+\infty} w(t)h(\tau - t)dt \\ &= A_r \int_{-\infty}^{+\infty} u(t - \tau_0)u^*(t - \tau)dt + \int_{-\infty}^{+\infty} w(t)u^*(t - \tau)dt. \end{aligned} \quad (2.17)$$

From the Cauchy-Schwarz inequality, the first integral is maximum for $\tau = \tau_0$. Figure 2.4(a) gives an example of the output of the matched filter for $\tau_0 = 0$ in the case of a chirp, while figure 2.4(b) emphasises the particularities of such output with a zoom. The MF output is centred at $\tau_0 = 0$. The first particularity to be mentioned is the difference between the mainlobe and the sidelobes. The mainlobe corresponds to the higher peak of the compression output and indicates

1. The Signal-to-Noise Ratio (SNR) is the ratio between the signal power and the noise power often expressed in decibels (dB). It indicates the quality of the studied signal in the discussions here. The lower the SNR, the more corrupted by noise is the signal and inversely.

where the target lies, whereas the sidelobes designate all the remaining lobes of the compression output.

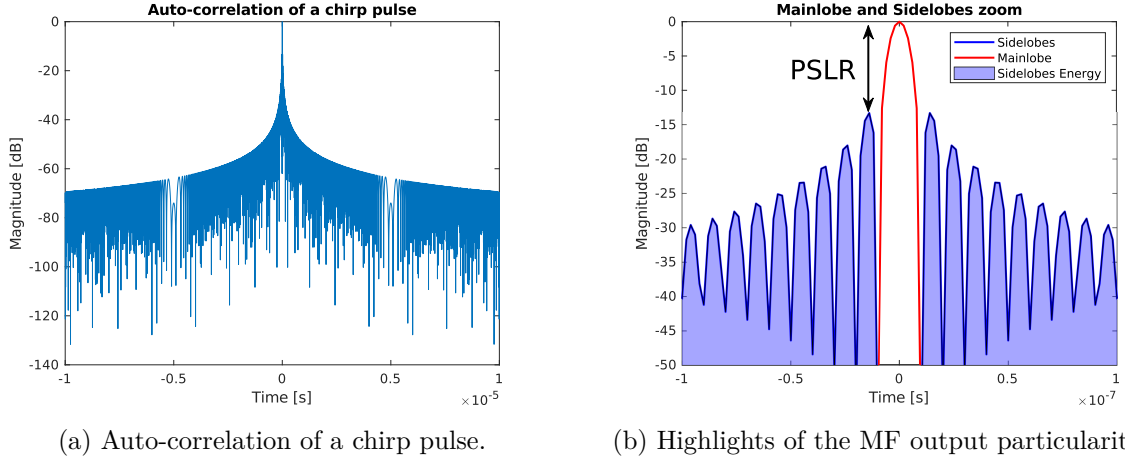


Figure 2.4: Matched filter output for a noiseless chirp ($T = 10\mu\text{s}$, $B = 100\text{MHz}$) with no delay.

Furthermore, two common criteria on the sidelobes behaviour can be defined [5]. On one hand, the Integrated Sidelobe Ratio (ISLR) is described as the ratio of the energy of all the sidelobes, the blue region in figure 2.4(b), to the energy of the mainlobe. It indicates the minimum level under which targets of the same level could mask a target with a weaker response. On the other hand, the Peak-to-Sidelobe Level Ratio (PSLR) is identified as the ratio between the energy of the first highest sidelobe and the energy of the mainlobe. It provides indication on the possible masking of a weak target by close and stronger targets. For the chirp, the values of ISLR and PSLR are commonly of -10dB and -13.5dB . The width of the mainlobe is also of significance, as it impacts the range resolution. The range resolution determines the ability to resolve close targets with identical levels. Therefore, the thinner the mainlobe, the easier is the target discrimination. As a reference, the chirp usually has a mainlobe width defined as the inverse of the bandwidth at -3dB ,

$$\Delta\tau = \frac{1}{B}. \quad (2.18)$$

This leads to a range resolution defined by the next equation:

$$\Delta_R = \frac{c}{2B}. \quad (2.19)$$

The range resolution issue is depicted in figures 2.5(a) and 2.5(b), where targets are separated respectively by a relative delay greater and lower than the range resolution. In the first case, the targets can be resolved, whereas in the second case it is impossible to discriminate the two targets due to the merging of the mainlobes.

It is common use to perform matched filtering to maximise the target Signal-to-Noise Ratio

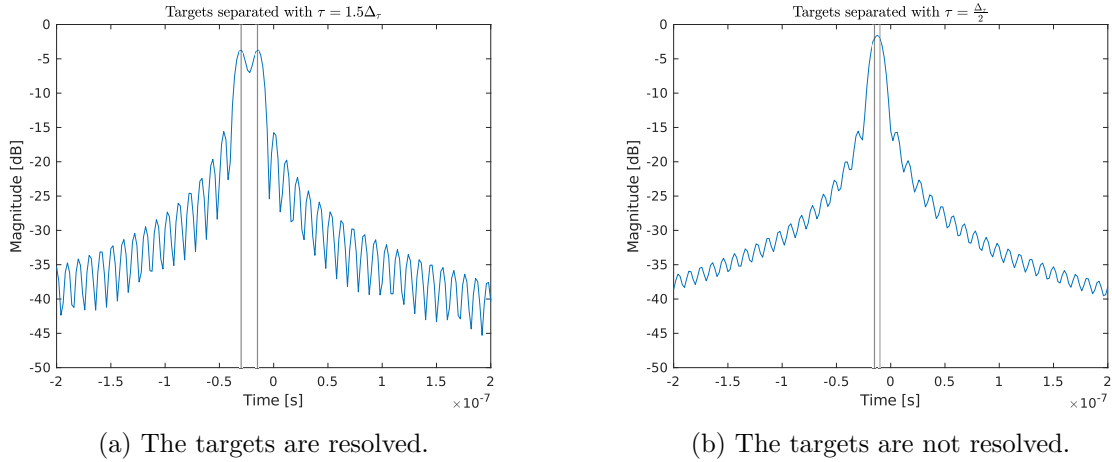


Figure 2.5: Two-target discrimination situation with a chirp ($T = 10\mu\text{s}$, $B = 100\text{MHz}$).

[11] and thus to determine the range of a target. However, the MF has a downside as it creates high sidelobes which can mask the main lobe of a weak target response as illustrated in figure 2.6(a). One can apply a weighting window to the signal, such as the Hamming window [4], to reduce sidelobes level at the expense of the mainlobe broadening and thus a degradation of targets discrimination capacities. This windowing is depicted in figure 2.6(b) for a chirp. The ISLR and the PSLR have successfully been reduced to -32dB and -43dB . However, this is followed by a broadening of the mainlobe by a factor of 1.5 (measured 3dB below the peak of the mainlobe). Another solution to mitigate these sidelobes is the use of a Mismatched Filter (MMF) [19] described in the next paragraph.

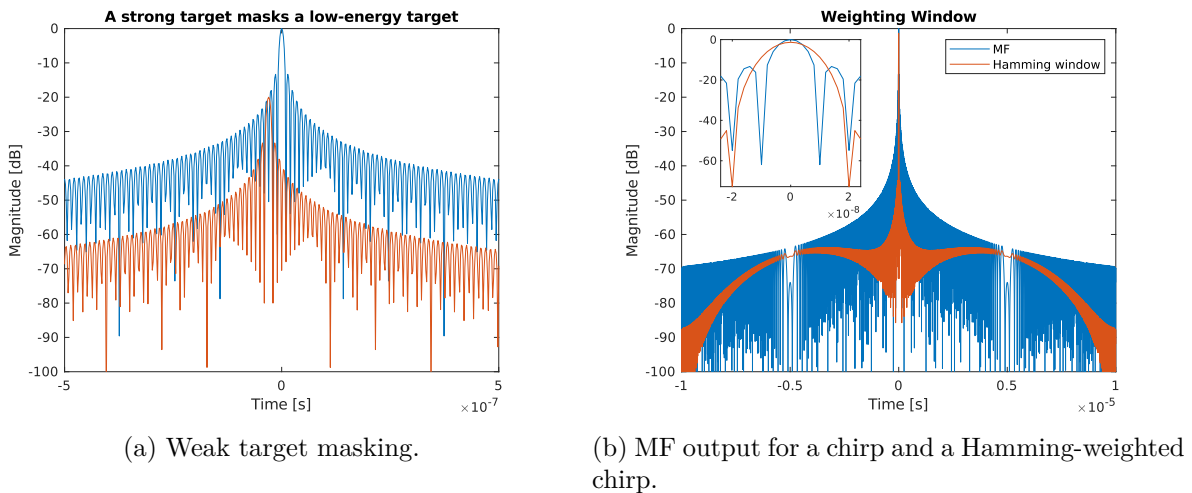


Figure 2.6: The sidelobes problematic with the MF for a chirp ($T = 10\mu\text{s}$, $B = 100\text{MHz}$).

The Mismatched Filter

The MMF can be defined as the solution of a minimisation problem [19]. Consider a signal, \mathbf{s} , of N samples defined by

$$\mathbf{s} = [s_1 \ s_2 \ \dots \ s_N]^T, \quad (2.20)$$

where $.^T$ is the transpose operator. We note \mathbf{q} the MMF of length $K_q \geq N$. The range compression that the received signal undergoes with this filter is expressed by [19]

$$\mathbf{y} = \mathbf{\Lambda}_q^*(\mathbf{s})\mathbf{q},$$

$$\begin{pmatrix} y_1 \\ \vdots \\ \vdots \\ \vdots \\ \vdots \\ \vdots \\ \vdots \\ y_{K_q+N-1} \end{pmatrix} = \begin{pmatrix} s_N & 0 & \dots & \dots & 0 \\ \vdots & \ddots & \ddots & & \vdots \\ s_2 & \dots & s_N & \ddots & \vdots \\ s_1 & \ddots & \vdots & \ddots & 0 \\ 0 & \ddots & s_2 & \dots & s_N \\ \vdots & \ddots & s_1 & \ddots & \vdots \\ \vdots & & \ddots & \ddots & s_2 \\ 0 & \dots & \dots & 0 & s_1 \end{pmatrix} \begin{pmatrix} q_1 \\ \vdots \\ \vdots \\ \vdots \\ \vdots \\ q_{K_q} \end{pmatrix}, \quad (2.21)$$

where $\mathbf{\Lambda}_q$ is a convolution matrix of size $(K_q + N - 1) \times K_q$. If the filter is chosen as $\mathbf{q} = \mathbf{s}$, then the classic MF is obtained². The goal with the MMF is to optimise a criterion other than the SNR. Several options are possible. The most common one is the optimisation of the PSLR, but the MMF can also optimise criteria such as the ISLR. In the first case, the MMF tries to minimise the ratio between the energy of the first highest sidelobe and the energy of the mainlobe. In the second case, the MMF aims to minimise the ratio between the energy of all the sidelobes to the energy of the mainlobe. Both options lead to the objective function defined by

$$f_{obj}(\mathbf{q}) = \|\mathbf{F}\mathbf{y}\|_p^2, \quad (2.22)$$

where \mathbf{F} is a diagonal matrix of ones except for some zero values which correspond to the mainlobe positions, and $\|\cdot\|_p^2$ defines the l_p norm of a vector. For the PSLR criterion, $p = \infty$, which means that only the largest sidelobe is taken into account, while for the ISLR criterion, $p = 2$, in order to get the total energy of the sidelobes. For the ISLR objective, the optimisation

2. The MF is obtained with $q = s$ instead of $q = s^*$ as in (2.16) due to the presence of the conjugate transpose on the convolution matrix, $\mathbf{\Lambda}_q$, in (2.21).

problem to be solved writes [19]:

$$\begin{aligned} \min_{\mathbf{q}} \quad & \|\mathbf{F}\mathbf{y}\|_2^2, \\ \text{s.t.} \quad & \mathbf{s}^H \mathbf{q} = \mathbf{s}^H \mathbf{s}, \end{aligned} \quad (2.23)$$

where the constraint is added to discard the trivial null solution and \cdot^H is the Hermitian transpose or conjugate transpose. For the ISLR criterion, this minimisation problem has an analytic solution obtained by applying the method of Lagrange multipliers [19]. It is expressed as

$$\mathbf{q}(\mathbf{s}, \mathbf{M}_\Lambda) = \frac{(\mathbf{s}^H \mathbf{s}) \mathbf{M}_\Lambda^{-1} \mathbf{s}}{\mathbf{s}^H \mathbf{M}_\Lambda^{-1} \mathbf{s}}, \quad (2.24)$$

where $\mathbf{M}_\Lambda = \mathbf{\Lambda}_q^T(\mathbf{s}) \mathbf{F} \mathbf{\Lambda}_q^*(\mathbf{s})$. Note that this analytical solution provides an optimal sidelobe level but comes with an uncontrolled Loss-in-Processing Gain (LPG). The LPG is defined as the ratio between the SNR obtained with the MMF and the optimal SNR obtained with the MF, expressed in dB:

$$\text{LPG} = 10 \log_{10} \left(\frac{|\mathbf{q}^H \mathbf{s}|^2}{(\mathbf{q}^H \mathbf{q})(\mathbf{s}^H \mathbf{s})} \right) \leq 0. \quad (2.25)$$

In order to mitigate such a loss, a second constraint can be added to the minimisation problem [19]:

$$\min_{\mathbf{q}} \quad \|\mathbf{F}\mathbf{y}\|_2^2, \quad (2.26a)$$

$$\text{s.t.} \quad \mathbf{s}^H \mathbf{q} = \mathbf{s}^H \mathbf{s}, \quad (2.26b)$$

$$\mathbf{q}^H \mathbf{q} \leq 10^{\frac{\beta_q}{10}} \mathbf{s}^H \mathbf{s}, \quad (2.26c)$$

where β_q is a positive constant. It can be checked that in (2.26), β_q represents an upper bound for the LPG. Indeed:

$$\text{LPG} = 10 \log_{10} \left(\frac{|\mathbf{q}^H \mathbf{s}|^2}{(\mathbf{q}^H \mathbf{q})(\mathbf{s}^H \mathbf{s})} \right) = 10 \log_{10} \left(\frac{\mathbf{s}^H \mathbf{s}}{\mathbf{q}^H \mathbf{q}} \right) \leq \beta_q, \quad (2.27)$$

where the second equality results from (2.26b) and the inequality from (2.26c). Figures 2.7(a) and 2.7(b) illustrate the improvement made on the PSLR and ISLR for a chirp with the MMF compared to a classic MF. In figure 2.7(a), the PSLR has been reduced to -64.9dB , while the ISLR is now of -33.8dB . In figure 2.7(b), the optimisation of the ISLR gives an improved ratio of -24.8dB with a PSLR of -26.8dB with the controlled LPG. In comparison, the MMF with uncontrolled LPG gives an ISLR and a PSLR of -26.5dB and -29.1dB respectively, which seems better at first sight but comes with a non-negligible LPG of -18dB . With such a loss, the target could be masked or simply missed at detection, hence the constraint (2.26c). It can be noted

that the MMF induces an increase of the mainlobe by a factor of 1.5 for the PSLR optimisation and 1.2 for the ISLR optimisation with the actual settings.

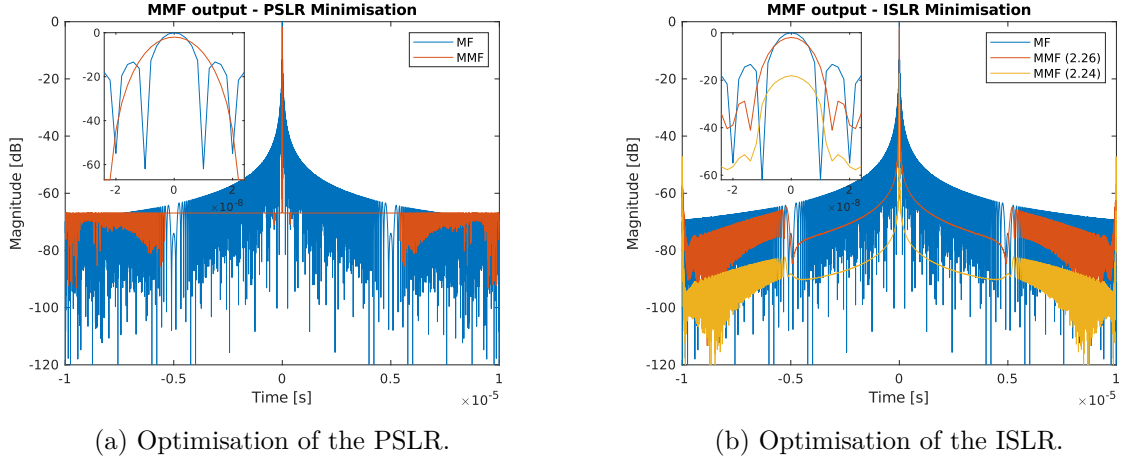


Figure 2.7: MF and MMF output for a chirp ($T = 10\mu\text{s}$, $B = 100\text{MHz}$). The PSLR is optimised in the left figure, while the ISLR is optimised in the right one ($K_q = N = 5001$ samples, $\beta_q = 2\text{dB}$ for both filters). Zoom on the mainlobe are added to illustrate the LPG effect for the ISLR optimisation with controlled (2.26) and uncontrolled (2.24) LPG.

The Ambiguity Function

Previously, the target was assumed to be stationary, and only the delay was subjected to investigation. But as mentioned earlier, the received signal is affected by the radial velocity, v_r , between the target and the radar. This causes a Doppler shift, ν_d , which hinders the response of the matched filter optimised for the zero-Doppler case. To take the Doppler effect into consideration, it is possible to make use of another fundamental tool in the processing of radar signals: the Ambiguity Function (AF). The AF enables the analysis of the impact of the target velocity on the output of the matched filter for a given waveform. The Ambiguity Function thus represents the time-frequency response of the matched filter for a received signal with delay τ and Doppler ν_d . It is defined as [11]

$$\chi(\tau, \nu_d) = \int_{-\infty}^{+\infty} u(t)u^*(t + \tau)e^{2i\pi\nu_d t} dt. \quad (2.28)$$

Figures 2.8 and 2.9 give an example for the chirp and the HFM waveforms with the zero-Delay and zero-Doppler cuts associated. In each case, the zero-Doppler cut, $\chi(\tau, 0)$, is equivalent to the definition of the matched filter (2.17). Concerning the sign of the Doppler frequency, a positive Doppler is synonymous of an approaching target, whereas a negative Doppler indicates a target moving away.

A comparison of figures 2.8 and 2.9 reveals a clear correlation between the behaviour of the ambiguity function and the considered waveform. In the case of a chirp, the appreciated target detection capacity at every possible delay and Doppler comes with a delay-Doppler coupling marked by the diagonal ridge in figure 2.8. For a given Doppler shift, the peak response is shifted from its true delay value [11]. This ridge can be modelled by the following equation:

$$\tau_{shift} = \frac{\nu_d}{2\gamma}. \tag{2.29}$$

The chirp is therefore characterised as robust to the Doppler effect or in other words, as Doppler tolerant [11]. Compared to the linear behaviour of the chirp AF, the AF for the HFM has more of a bow tie pattern, as the sidelobe level increases with the Doppler. Furthermore, the mainlobe peak height observes a tendency to decrease. Therefore, the HFM waveform appears less robust to Doppler at narrowband due to this behaviour. Nevertheless, it can be demonstrated (see Appendix A) that in a wideband³ situation, the HFM waveform becomes Doppler invariant [43][44], which is optimal for applications where the targets present relatively high velocity.

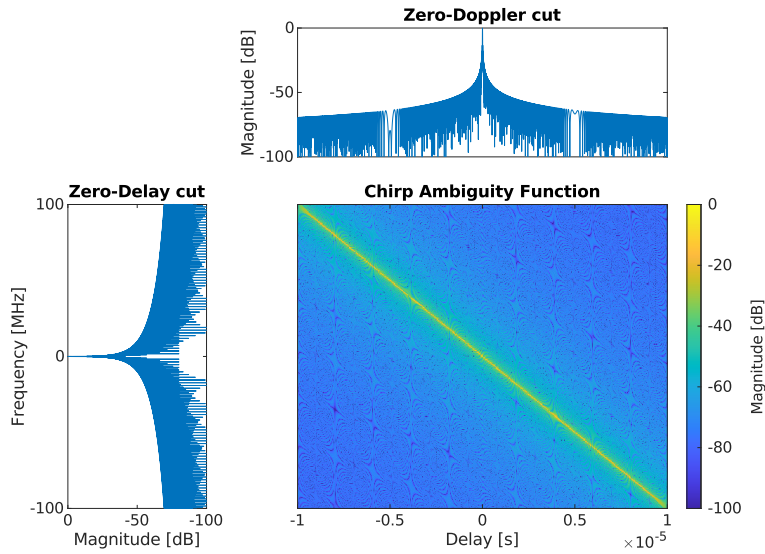


Figure 2.8: Example of the Ambiguity Function of a chirp ($T = 10\mu\text{s}$, $B = 100\text{MHz}$). The upper plot is the zero-Doppler cut, while the left plot is the zero-Delay cut.

In light of the aforementioned discussion, the Ambiguity Function assumes great importance in characterising the suitability of a given waveform for radar application. However, while the AF enable the analysis of the Doppler effect on a considered waveform, it does not assist in

3. In contrast to the narrowband case, the wideband hypothesis suggests a large time-bandwidth product BT . Under this assumption, the Doppler effect is no longer regarded as a simple frequency shift but rather as a compression or expansion of the transmitted signal.

retrieving the Doppler shift ν_d , and thus the velocity of a specific target. This issue is addressed in the next paragraph with the final radar processing technique to be examined in order to become the perfect little radarist.

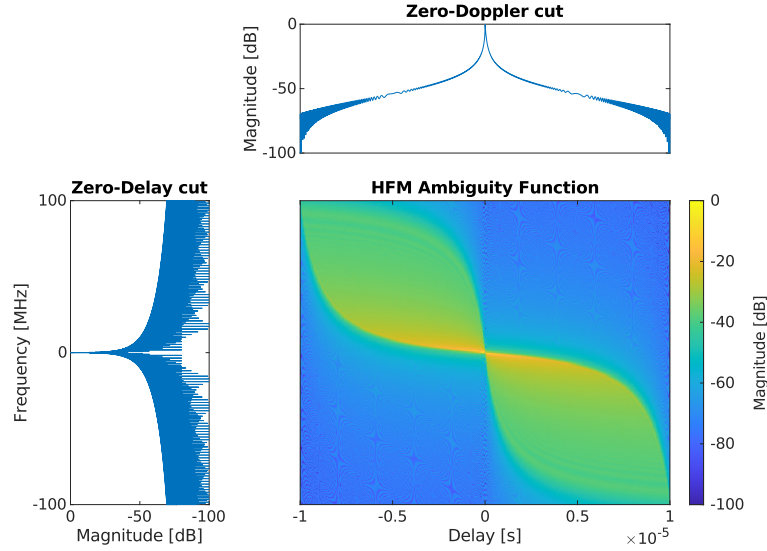


Figure 2.9: Example of the Ambiguity Function of a HFM waveform ($T = 10\mu\text{s}$, $B = 100\text{MHz}$). The upper plot is the zero-Doppler cut, while the left plot is the zero-Delay cut.

The Range-Doppler Processing

In order to enhance the Doppler resolution, a radar does not transmit only one pulse but periodically transmits, with a certain Pulse Repetition Interval (PRI) T_r , repeated identical pulses. This leads to a coherent train of N_p pulses expressed by

$$u_{N_p}(t) = \frac{1}{\sqrt{N_p}} \sum_{n=0}^{N_p-1} u(t - nT_r). \quad (2.30)$$

Figure 2.10 illustrates this repeated emission scheme with a sequence of chirp pulses. The resulting improved Doppler resolution is given by [11]

$$\Delta_{\nu_d} = \frac{1}{N_p T_r}. \quad (2.31)$$

Nevertheless, the associated Pulse Repetition Frequency (PRF), the inverse of the PRI, must be chosen wisely to avoid range ambiguity. If the PRF is too large, the echo of a pulse n might arrive after or in between the transmission of the next pulse $n + 1$, leading to a target that appears closer than it actually is. Such an error in localisation can be avoided if the desired

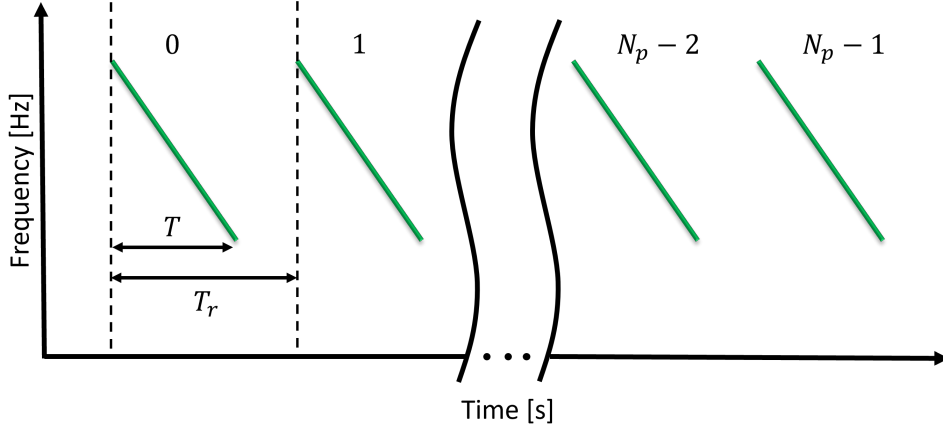


Figure 2.10: Representative scheme of a chirp pulse train.

delay\range values are less than the delay\range ambiguity, which are expressed as

$$\tau_{ambig} = T_r \text{ or } R_{ambig} = \frac{cT_r}{2} = \frac{c}{2\text{PRF}}. \quad (2.32)$$

Similarly, ambiguities can occur along the Doppler axis at interval defined by

$$\nu_{ambig} = \text{PRF}. \quad (2.33)$$

With train pulses, the Range-Doppler processing can then be applied on the received signals in order to extract the position and velocity of a target. By considering a target at delay τ_0 with a Doppler ν_0 , the received pulse train is

$$r(t) = A_r \sum_{n=0}^{N_p-1} u(t - \tau_0 - nT_r) e^{2i\pi\nu_0 t} + w(t). \quad (2.34)$$

A common assumption is that the Doppler has a minimal impact on the phase during the duration of a simple pulse and this will only shift the phase of the signal from one pulse to the next [45]. Therefore, it is possible to write $e^{2i\pi\nu_0 t} \approx e^{2i\pi\nu_0 nT_r}$ for $t \in [nT_r, nT_r + T]$. According to this hypothesis, the first step of the Range-Doppler processing consists in applying the matched filter for each pulse n of the train to obtain the range compression as expressed below:

$$y(\tau) = A_r \sum_{n=0}^{N_p-1} e^{2i\pi\nu_0 nT_r} \int_{-\infty}^{+\infty} u(t - \tau_0) u^*(t - \tau) dt + \sum_{n=0}^{N_p-1} \int_{-\infty}^{+\infty} w(t) u^*(t - \tau) dt. \quad (2.35)$$

The second step enables to determine the target Doppler shift by testing all possible hypotheses of ν_d , which yields a computation similar to the ambiguity function. This output can be written

as

$$y(\tau, \nu_d) = A_r \sum_{n=0}^{N_p-1} e^{-2i\pi(\nu_d - \nu_0)nT_r} \int_{-\infty}^{+\infty} u(t - \tau_0)u^*(t - \tau)dt + w_{RD}(\tau, \nu_d), \quad (2.36)$$

where w_{RD} represents the filtered white noise at the output of the Range-Doppler processing. Obviously, the maximum of this function is attained for the pair $(\tau, \nu_d) = (\tau_0, \nu_0)$. The output of such processing is shown in figure 2.11 for two targets with a pulse train of $N_p = 100$ chirps with a duration of $T = 10\mu\text{s}$, a bandwidth of $B = 100\text{MHz}$ and a PRI of $T_r = 10T$.

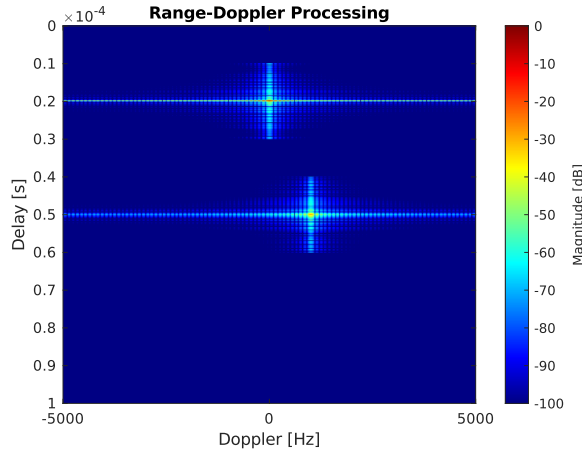


Figure 2.11: Output of the Range-Doppler processing for two simulated targets with a chirp pulse train. One target is stationary at a delay of $\tau = 20\mu\text{s}$, while the second is at a delay of $\tau = 50\mu\text{s}$ with a Doppler of $\nu_d = 1\text{kHz}$.

2.2 The World of Bats

Because the dual work of this thesis requires to have knowledge on both radar and bats, the following section deals with this little mammal and their exceptional ability: the echolocation.

2.2.1 Introduction to Bats and Echolocation

Bats of the order *Chiroptera*⁴ are mammals just like us. One main difference, which sets them apart from the other mammals is that they learned to fly by their own. Bats represent a fifth of the 6,500 known mammal species with more than 1,300 bat species worldwide [46] and are the second largest order of mammals, after the rodents. As shown in figure 2.12 by Professor Batty, bats have adapted to most of the terrestrial habitats and climatic zones, while exploiting a great variety of food sources, including insects and other arthropods, small vertebrates, fruits, leaves, nectar, flowers, pollen, and even blood (do not worry, only 3 species are known to be

4. For the distinguished Hellenist, $\chi\epsilon\iota\rho=kheir$ for the hand and $\pi\tau\acute{\epsilon}\rho\omicron\nu=pteron$ for wings.

hematophagous, and they have no taste for human blood). Consequently, they play a huge ecological role, acting as predators and regulating insect populations, as efficient pollinators, and as prey for larger predators, such as owls.

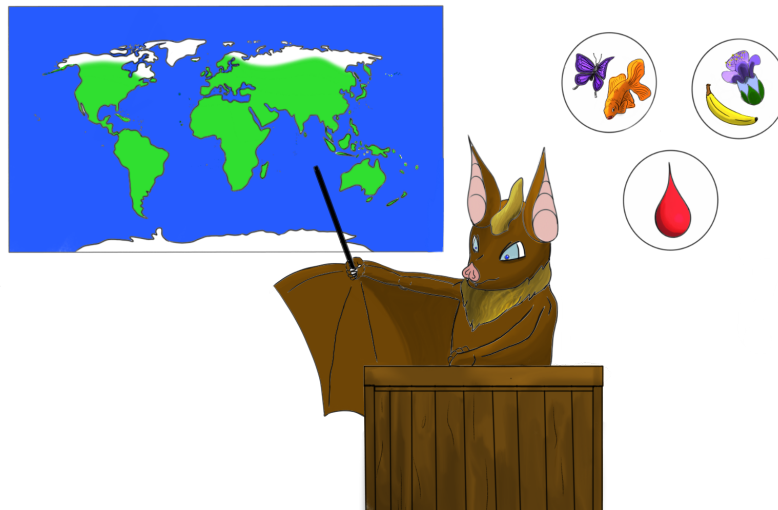


Figure 2.12: The worldwide distribution of bat species and their diet explained by Professor Batty. Bats can be found in the green areas.

Beyond their dietary habits, another noteworthy aspect of bats is their incredible capacity to navigate using ultrasonic sounds. This biological sonar, often referred to as echolocation, consists of emitting high-frequency signals in the range of 20kHz to 100kHz and above, waiting for the returning echoes to detect, characterise and localise the reflecting objects. For bats, this system is used for orientation in space but also for hunting preys and feeding themselves as shown with Batty looking for a (Batty-)meal⁵ in figure 2.13. The logic is similar to the one explained in figure 2.1 for the radar case, but this time the emitted and received signals are sound waves.

Ecology & Conservation

Insectivorous bats are capable of consuming their own body weight in insects each night, which can represent thousands of insects. They play an important role in regulating insect populations, including disease-carrying pests like mosquitoes. Additionally, some bats are also effective pollinators and without them, certain varieties of tropical fruits, such as bananas, mangoes, and agave would not exist [46]. The protection of bats is thus of primary importance.

5. credits for this joke: Abigael Taylor.

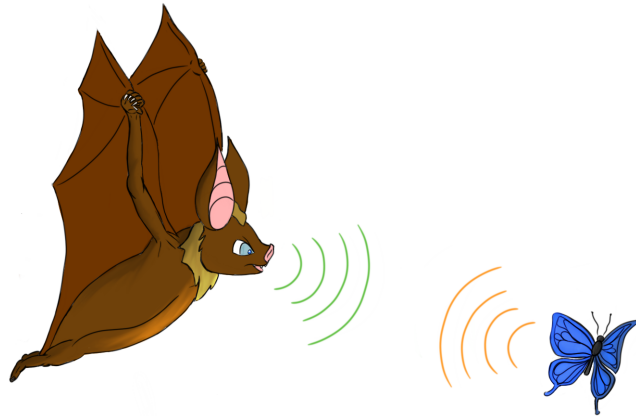


Figure 2.13: Overview of the echolocation hunting framework.

To realise such a task, bats generate ultrasonic vocalisations within the larynx through the use of vocal chords adapted for the generation of such frequencies [47][48]. Subsequently, the sound is emitted through their own biological "antenna". In some species, this "antenna" is nothing else than their mouth, whereas in others the ultrasounds are emitted through the nostrils, thanks to a lance-shaped nose, the noseleaf, characteristic of bats belonging to the *Phyllostomidae*, *Hipposideridae* and *Rhinolophidae* families. This distinction at the emission is illustrated in figures 2.14(a) and 2.14(b) with two pictures of representative species for each "antenna". Finally, the returning echo is received by the ear and processed by the whole auditory system [49], which translates the delay to distance. The strength of the echo indicates the size of the prey, while the Doppler effect measures its speed.



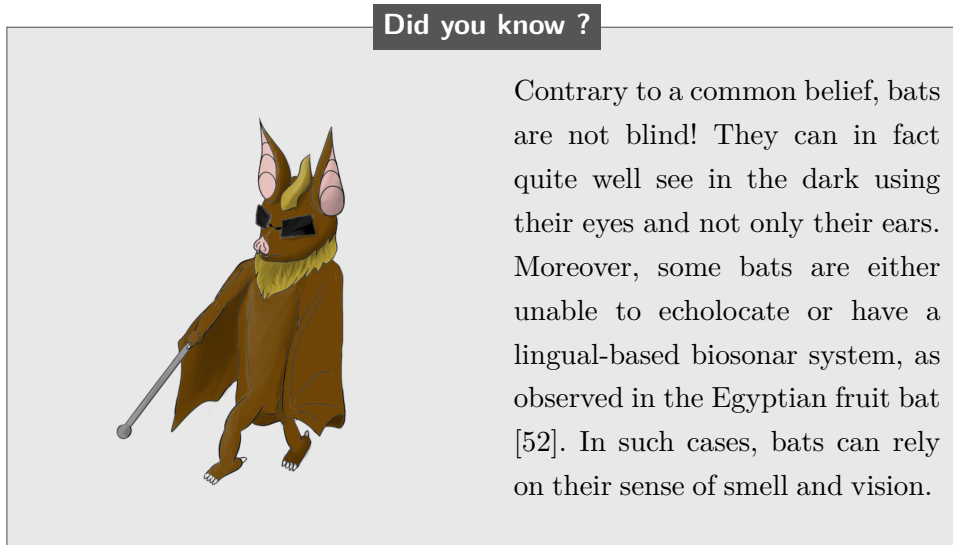
(a) Portrait of *Nyctalus Noctula* by Mnolf, Photo taken in Rum, Austria, CC BY-SA 3.0 [50].



(b) Portrait of *Rhinolophus ferrumequinum* by Prof. emeritus Hans Schneider (Geyersberg), CC BY-SA 3.0 [51].

Figure 2.14: Example of species with different "antennas". The common noctule, on the left, emits ultrasounds through its mouth, whereas the greater horseshoe bat emits through its noseleaf.

As a consequence, and in the light of the aforementioned scheme in figure 2.1, the analogy with radar should be evident, were it not for the fact that for them, echolocation is the result of millions of years of biological evolution. The echolocation (and bats of course) is the keystone of this thesis and the next paragraphs will try to portray the major and essentials aspects of this biological sonar. The following information should make it clear why the study of bats and echolocation is appealing for radar applications.



2.2.2 Bats Waveforms

Given that both radar and bats emit frequency modulated waveforms, which is the basis of this thesis, it is of particular interest to study the waveforms of bats. The following discussion will demonstrate that radar have much to learn in this domain.

First of all, echolocation calls can be divided into two types of signals: narrowband and broadband waveforms [12][13]. On one hand, narrowband components describe either quasi-constant frequency (QCF) signals with little frequency modulated segments of only a few kHz between the onset and end of the signal (shallow modulation) or long constant frequency (CF) elements with slight portions of frequency modulation of a few kHz at the beginning and end of the pulse. On the other hand, broadband signals comprise a downward frequency modulated (FM) waveform of a large bandwidth (steep modulation). A classification of these signals can be made according to their bandwidth. For narrowband signals, the most prominent harmonic sweeps over less than half an octave⁶, whereas in broadband signals, it covers more than half an octave [12]. Figure 2.15 summarises the main categories of bat echolocation pulses.

6. In acoustics, an octave is the interval between one musical pitch and another at twice the frequency. For example, a note with a frequency of 440Hz is one octave above at 880Hz and one octave below at 220Hz.

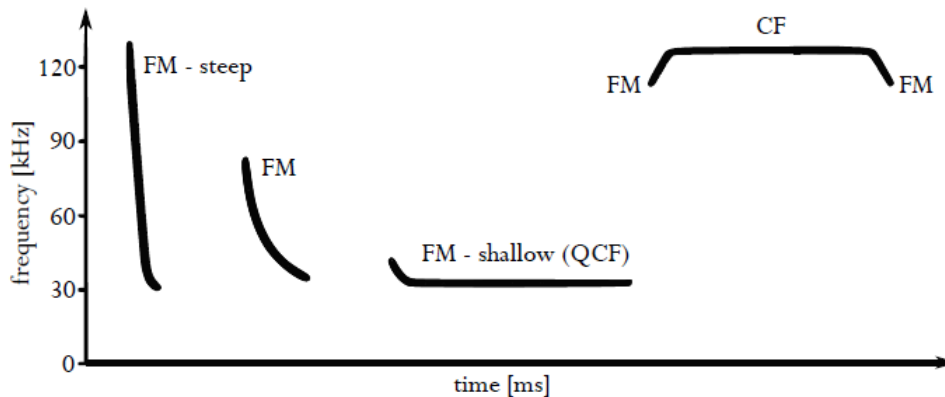


Figure 2.15: Main categories of bat echolocation pulses (From [13], CC BY-NC-SA 3.0).

The diversity of waveforms observed among bats appears to be significant, as each species has adapted to several factors and has thus developed its own waveform. First, each species has its own foraging mode, with some bats capable of catching prey in the air (aerial mode), others gleaning their food from solid surfaces (gleaning mode) and some engaged in fishing (trawling mode) [7][12]. This adaptation is thus directly linked to their diet. Moreover, each species is confronted with different hunting environments and therefore different clutter conditions [7]. Bats hunting in open spaces will not be bothered by clutter but require a long-range detection of prey. They will use relatively long (8 to 25ms) shallowly frequency modulated signals for detection. By approaching buildings, in the vicinity of forest edges or above water, other species must contend with a background-cluttered space, the edge spaces. Echolocation signals in this configuration are shorter, 3 to 10ms in average and can be more steeply modulated. Finally, some bats evolve in highly cluttered spaces, called the narrow spaces, such as forests [7]. Various species use a flutter detecting method by sending long CF-FM signals, while others can use FM signals for active or passive gleaning. In passive gleaning, bats rely on prey generated cues and echolocation only serves to guide the approach to the prey site [7].

Besides an extraordinary adaptation, bats also possess an excellent control over their emission parameters. They are capable of rapidly varying the pulse duration, the bandwidth, the interpulse duration, and the curvature of their waveforms. This flexibility is particularly evident when foraging, as illustrated by the schemes in figures 2.16. These are examples of hunting echolocation sequences from two bats with different kinds of waveforms, which can be divided into three phases. The initial phase, which is the search phase, is characterised by the bat probing its environment and searching for a potential prey. Then comes the approach phase as soon as a prey is detected. The emission parameters are modified in order to avoid overlap between outgoing and returning signals by slowly decreasing the interval between pulses and by decreasing their durations. Finally, the terminal phase, often called the terminal buzz, marks the conclusion

of the sequence and precedes the capture, which may or may not be successful.

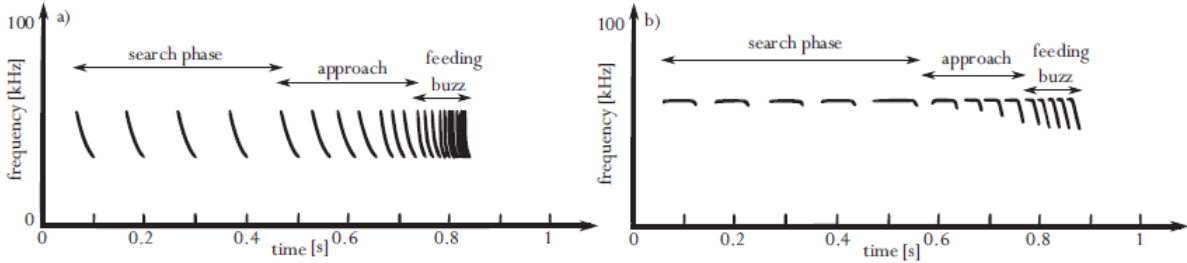


Figure 2.16: Echolocation sequence of a FM (a) and CF (b) bats emitted during prey pursuit (From [13], CC BY-NC-SA 3.0).

2.2.3 Bats Processing

The waveforms and the global mechanism of echolocation being described, one might wonder how bats process the delay and Doppler information like it was described for radar. The acuity of the bat echolocation has been evaluated on repeated occasions, with numerous articles on the subject [53][54]. Moreover, the complexity of the bat auditory system could be the subject of a thesis in itself. To correctly apprehend how bats translate the information contained in echoes, a brief overview of the auditory pathway will be given, accompanied by a model of the auditory computations. The Spectrogram Correlation And Transformation receiver (SCAT) is a computational model of the bat auditory system, which was proposed by Saillant [27]. It is constituted of three blocks: the cochlear, temporal and spectral blocks. The SCAT represents a monaural (relative to one ear) version of the auditory system and underlying neural response in FM bats (based on a particular species, *Eptesicus fuscus*, also known as big brown bat). It simulates the auditory reception and processing of bats and could provide an insightful first look at the bat processing.

The Reception

The mammalian ear presented in figure 2.17 is composed of three distinct parts: the outer, middle and inner ears. The first two will not be discussed here, but they play an important role in localising the direction of a sound source and especially in transmitting the sound to the inner ear [13]. The latter one, the inner ear, comprises the semicircular canals, which are responsible for dynamic balance, and the cochlea, which is responsible for the sense of hearing. The cochlea is a sophisticated sound receiver and frequency analyser composed of three canal ducts in parallel [13]. Sound waves propagate from the base to the apex of this spiral-shaped organ according to their frequency content. The lower the frequency the further it travels within the cochlea. It is responsible for converting the sound and its frequency content into an electrical

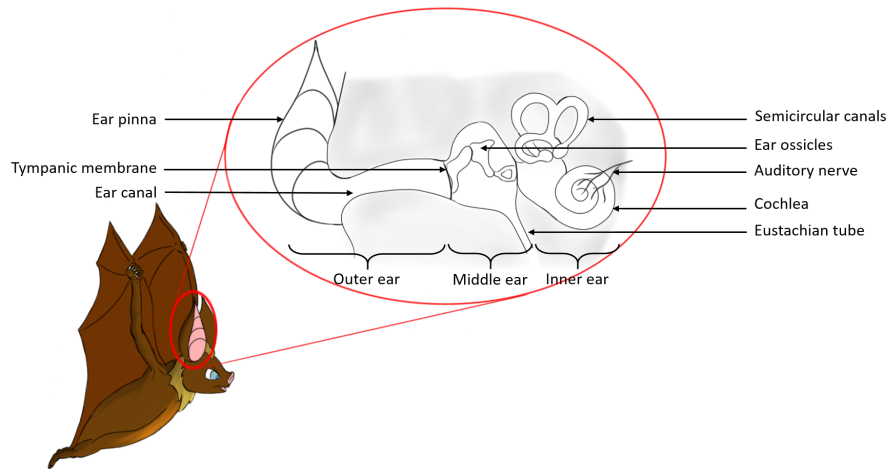


Figure 2.17: Anatomical point of view of Batty's ear.

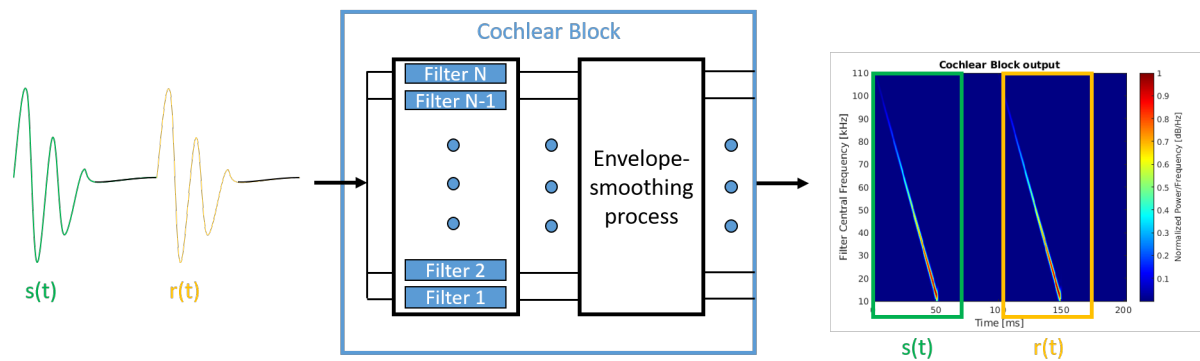


Figure 2.18: Overview of the cochlear block and its output as modelled by the SCAT. Butterworth filter hyperbolically spaced are implemented and the envelope-smoothing process is skipped in this case.

signal, which is transmitted to the auditory nerve cells. The signal is thus broken up into parallel frequency bands, which in a signal processing framework would be equivalent to a filter bank. This is precisely how the cochlea is modelled in the SCAT thanks to parallel band-pass filters arranged according to the tonotopic⁷ organisation of bats cochlea (in other words, the spatial arrangement of how sounds of different frequency are processed in the brain). As evidenced by the different versions of the SCAT, the implemented filters are various, with Butterworth filters in [27] or gammatone filters in [55] for example. At the filter level, the signal undergoes an envelope-smoothing process [27] to simulate bat neural responses. It is often implemented thanks to a rectifier followed by a low-pass filter [27][55] or an amplitude extractor as in [10]. The output of this cochlear block corresponds to a spectrogram-like format of the waveform as shown

7. For the distinguished Hellenist, $\tau\omicron\nu\omicron\varsigma=tono$ for frequency and $\tau\omicron\pi\omicron\varsigma=topos$ for place.

in figure 2.18, which can be further analysed thanks to the central auditory system. The linear appearance at the output of the cochlear block is due to the spacing of the filter channels, which respect the hyperbolic frequency scale of the bat’s cochlea and its waveform in this example. The filters spacing is also a tunable parameter often chosen as linear or hyperbolic in the literature. For complementary information and precise implementation examples, the SCAT version in [55] and [10] are highly recommended.

The Temporal Processing

To accurately determine the range of its prey, a bat will compare the echoes to its own emission. This stage can be explained by the temporal block from the SCAT also designated as the spectrogram correlation block [27]. This block represents the delay-tuned neurons responsible for target ranging in the auditory system of bats. The response is based on the cochlear output and estimates the time delay between a call and the received echo. This is achieved through a set of tapped delay lines that implement a cross-correlation-like function between the call and the received echo. It produces a "dechirping" of the signal by adding the right delays between the signal and its echo to each frequency channel. The activity in each filter channels is then summed up and followed by a peak detection or threshold detection to decide where lies the target. In summary, bats perform a matched filter of their own kind to localise a potential target. The scheme in figure 2.19 depicts the neural response and the result of the bat matched filter.

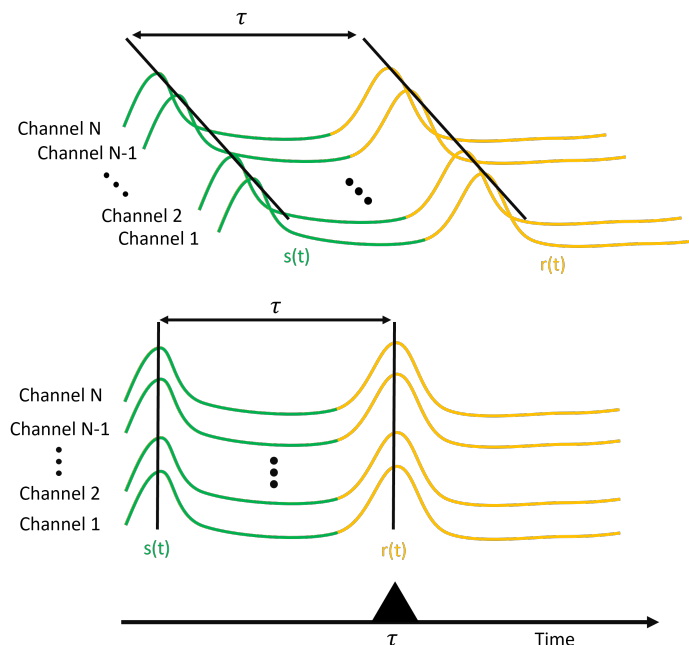


Figure 2.19: Descriptive scheme of the temporal block mechanism.

The Spectral Processing

The final block of the SCAT is the spectral block or spectrogram transformation block [27], which is designed for the extraction of the fine structure of the target in the presence of highly overlapping echoes. It completes the temporal block when the delay between high overlapping echoes can not be resolved. To achieve such a task, the spectral block analyses each target detected by the temporal block. When echoes overlap, it creates peculiar interference patterns, called glints in [55] and in bat biological processing. These interference patterns can be detected by observing the suppression or amplification of the power of the output of some filters channel in the cochlear output. Again, the processing of such patterns also has different implementations according to the SCAT version, with inverse cosine transformation in [27] or an inversion of the frequency spacing of interference to find the glint delay in [55] for example.

In summary, the auditory processing in bats can be described as follows: the cochlea decomposes the signal into parallel frequency channels and feeds them to the nervous system. The central auditory system then performs a kind of cross-correlation to localise the target. Of course, there are much more information extracted in the processing but this first approach is sufficient for the subject of this thesis. A computational model of this system, the SCAT, can be declined in various forms and there are some discussions about its different blocks and their implementation [56], but in the overall this model helps understanding how bats process a part of the information necessary to catch their prey.

What about the Doppler?

In the same way radar signals are prone to Doppler effect, bats have to deal with this phenomenon too. Some preys, such as flying insects, exhibit a characteristic Doppler signature due to their wing-beat frequencies [57]. Moreover, bats flight also induces Doppler effect, which results in their signal being Doppler shifted. In response, a majority of species belonging to the CF bats family, such as the horseshoe bat presented earlier in figure 2.14(b), dispose of a compensation mechanism. By emitting CF-FM signals like the one presented in figure 2.20, bats like the horseshoe bat can compensate for the flight-induced Doppler shift. By lowering their call frequency, they keep the echo frequency within the best frequency range for the bat hearing, the auditory fovea [58]. They are also able to detect and classify fluttering insects based on amplitude and frequency modulations caused by their movements

With regard to FM bats, their signals are more Doppler tolerant, which means that they are less affected by the Doppler effect [13]. However, the range-Doppler coupling can be argued to be a source of error in bat echolocation, as underlined in [59]. A variety of strategies is employed by FM bats to counteract this coupling and in particular the control of their different emission parameters have a strong influence on their success. Besides pulse design, the hypothesis of a Linear Error Correction system (LEC) has been formulated in [60], which could help bat being

tolerant to Doppler shifts by compensating the altered received signals in the frequency domain. Other research [28] has indicated that FM bats could have the same capacity as CF bats, to discriminate flying insects, thanks to the Doppler effect, after receiving different echoes from stationary and fluttering parts of the prey [57][17].

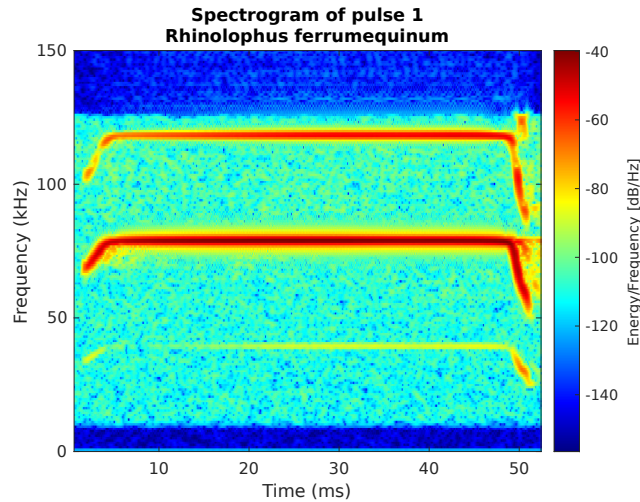


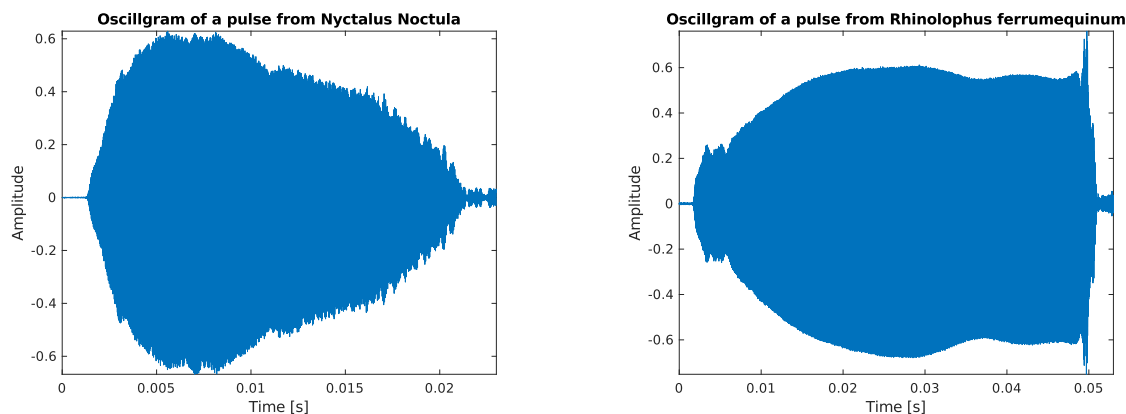
Figure 2.20: Pulse of a greater horseshoe bat [61].

Harmonics and Amplitude Modulation

One may have notice in the previous figure, that the pulse of the greater horseshoe bat exhibits a harmonic structure. In other words, the emitted sound is composed of three harmonics, each with a distinct energy level. The lowest frequency harmonic is often designated as the fundamental, while the other are harmonics, whose frequencies are integer multiples of the fundamental. In the case of the greater horseshoe bat, the second harmonic, at 83kHz here, is prominent, whereas in a majority of bat species, it will be the fundamental. The number of harmonics depends on the species and the emission. A pulse may be composed of a single fundamental or the combination of two to even four harmonics, as observed in the case of the mustached bat [62]. The purpose of these harmonics is still under debate and many hypotheses have been investigated. The use of harmonics could help in the differentiation of targets from the clutter [34]. This assumptions has even been studied for radar application in spaceborne radar for geophysical exploration [35]. Another possibility is that harmonics help bats in distinguishing their calls from those of conspecifics (members of the same species) and subspecies [63]. Furthermore, the neuronal activity at the reception may also be linked to harmonics, as evidenced in [62], where the combinations of harmonics influenced the neuronal response.

Another aspect of bat signals is the amplitude modulation. Figures 2.21(a) and 2.21(b) show the oscillogram of pulses from the common noctule and the greater horseshoe bat, where the

amplitude modulation is clearly visible in both cases. Bats are able to control the amplitude of their signal as one of the numerous emission parameters. The glints, mentioned earlier in the auditory processing, not only consists of frequency modulations but also of amplitude modulations. The wing movements of insects can induce changes in the amplitude modulation of the returning signal, which can be informative on the insect species. Moreover, foraging bats can analyse the returned intensity to determine the target characteristics like its size [13].



(a) Pulse of a common noctule [14].

(b) Pulse of a greater horseshoe bat [61].

Figure 2.21: Example of the amplitude modulation observable in bat echolocation with real signals.

2.3 Conclusion

This introductory chapter comes to an end. The first section is fundamental but obviously a naive first approach to the concept of radar. It is evident that a comprehensive understanding of radar systems necessitates a more nuanced approach that encompasses a multitude of functions. Moreover, the scene covered by the radar, which can be more or less complex (buildings, vegetation,...), the wave propagation theory or the radar signature of targets are among the various parameters to be taken into account. Nevertheless, the basis given here should help to understand the radar concept and lay the foundation for the rest of the thesis. Concerning the bats, the same observation could be made because a mere introduction is not sufficient to explore everything researchers have found until now. Their extraordinary capacities do not stop at their waveforms and the neural process behind the auditory system is a complex mechanism still investigated. However, this should help to understand why their waveforms are of interest for radar and for this thesis. Therefore, reproducing bats waveform and capacities will be the focus of the next chapter.

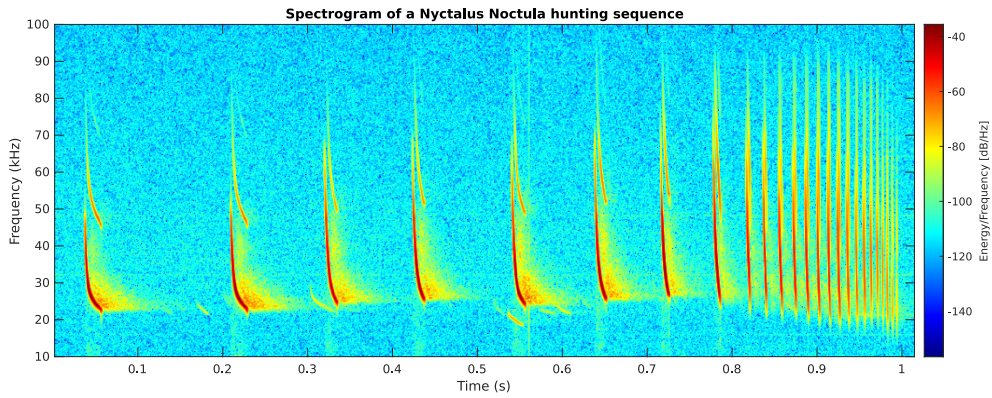
FROM BATS TO RADAR

Now that the basics have been established, the relationship between the echolocation and the radar should be clearer. The main objective of this thesis is now to be addressed, namely the proposal of a bio-inspired radar waveform. First, the study of a range of authentic bat signals is conducted in order to better understand their emission parameters and the manner in which they construct their signals. In conjunction with the extensive existing literature on bats, a new bio-inspired function capable of reproducing bat signals can then be introduced: the Parsons waveform. Afterwards, its capabilities as a radar function are evaluated through the application of classical radar processing techniques presented earlier like the matched filter. Throughout this chapter, the performance of the Parsons waveform are assessed, notably through the Cramér-Rao Lower Bounds (CLRB) computation, in comparison with the radar waveforms presented in the introductory chapter, thereby highlighting the advantages and drawbacks of the latter. Finally, real measurements are analysed to observe the true functional abilities of the bat-inspired waveform.

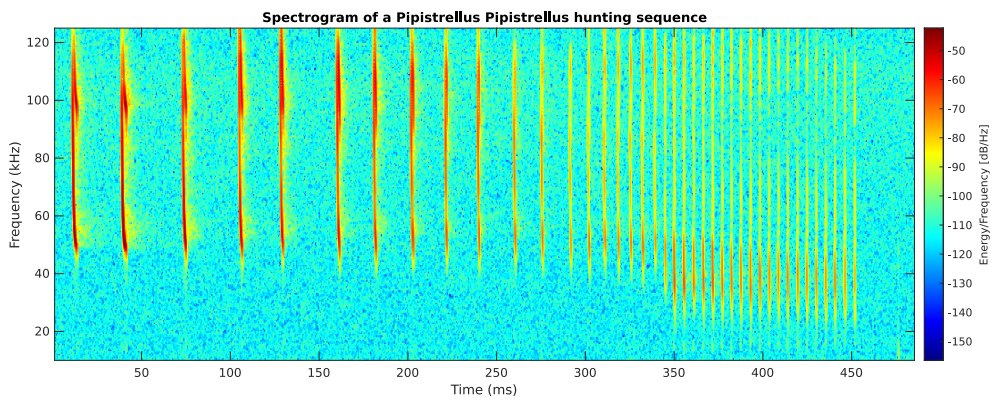
3.1 Becoming a Bat

3.1.1 Listen to the Bats

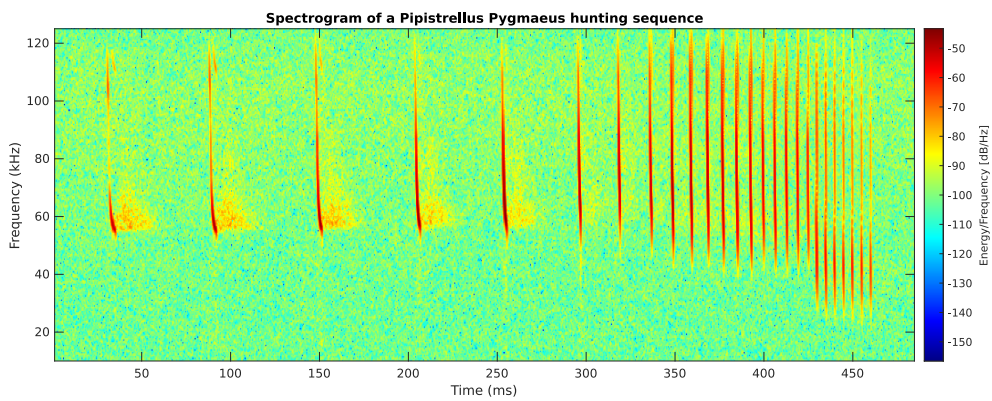
The introductory section on bat waveforms (section 2.2.2) provided an insight into the variety of waveforms observed in the bat repertoire. This diversity highlights the complexity of designing an appropriate function to accurately mimic bat waveforms. In this context, the initial step towards a bio-inspired function is to analyse authentic bat signals in conjunction with the relevant literature. The waveforms used by bats for foraging are of particular interest in the present case of study, and especially the frequency modulated signals. Compared to continuous frequency modulated signals, the flexibility of frequency modulated bat signals appears very attractive. For this very reason, three real bat hunting sequences from three different species, presented in figures 3.1(a) to 3.1(c), have been examined. The first one, in figure 3.1(a), is emitted by a representative of the species *Nyctalus noctula*, also known as the common noctule. This is an insectivorous bat that forages predominantly in open spaces by emitting curvilinear narrowband and shallowly modulated search signals with quite long duration ranging from 8 to 25ms [7].



(a) *Nyctalus noctula* hunting sequence [14].



(b) *Pipistrellus pipistrellus* hunting sequence [64].



(c) *Pipistrellus pygmaeus* hunting sequence [65].

Figure 3.1: Spectrogram of authentic hunting sequences from three different bat species recorded in Germany by Raimund Specht [14][64][65]. The pulse trains are sampled at 250kHz and contain respectively 25, 40 and 26 pulses.

Following the detection of a prey, the signals becomes more broadband, usually sweeping down from 60 to 20kHz with a decreasing duration and pulse interval [7][15]. The calls frequently contain two to three harmonics, with the first being the most energetic. The second pulse train, in figure 3.1(b), and the third pulse train, in figure 3.1(c), are hunting sequences emitted by two bats of the genus¹ *Pipistrellus*. The *Pipistrellus pipistrellus*, or common pipistrelle, and the *Pipistrellus Pygmaeus*, or soprano pipistrelle, are two species belonging to the edge space guild [7] that emit frequency-modulated signals to hunt insects. These cryptic species² of pipistrelle can be differentiated by the end frequency of their emission [67]. In fact, their search-phase signals are 3 to 5ms in duration and exhibit a first harmonic that sweeps down from approximately 110kHz to 45kHz for the common pipistrelle and 55kHz for the soprano pipistrelle [68][69]. A second harmonic can also be observed.

The three presented pulse trains being hunting sequences, the approach and terminal buzz phases evoked in figure 2.16 in the preceding chapter can be distinguished. Due to a lack of information, the detection may have occurred before the recording started, thus preventing us from the observation of a complete search phase. Nevertheless, the analysis of the temporal and frequency parameters described below may indicate that the first two or three pulses for the common noctule in figure 3.1(a) and pipistrelle soprano in figure 3.1(c) could be search signals. The analysis of these hunting sequences highlighted the incredible control that bats have over their emission parameters, as already mentioned in the introductory chapter. Whether it is the pulse duration, the bandwidth, the Pulse Repetition Interval (PRI) or the curvature of their waveforms, bats are able to adapt their calls in a very short amount of time, one second or even half a second in these examples. Figures 3.2(a) and 3.2(b) illustrate this ability by displaying the first and thirteenth pulses of the common noctule pulse train.

Being able to emulate synthetic versions of these signals required a comprehensive analysis of the natural hunting sequences and the extraction of their emission parameters. This study was divided into three stages. The initial phase consisted in the isolation of each pulse to better extract the temporal and frequency parameters. In order to obtain the most accurate estimation of the onset and end of each pulse, a change point detection algorithm, known as the Cumulative Sum (CuSum) [29], was computed. It allowed the hunting sequences to be sliced with highly satisfactory results, hence giving access to the duration and the PRI of each pulses. The CuSum algorithm computation will be investigated in Chapter 5. For our bats, the CuSum algorithm facilitates a precise analysis of each pulses, by detecting the onset and end of each signal. It gives access to the temporal parameters, but the bandwidth, comprising the starting and ending frequencies, remains to be estimated. The second stage of the analysis is then to separate the harmonics and to determine their Instantaneous Frequencies (IF). To realise this separation,

1. taxonomic rank regrouping species with several similar characteristics [66]. E.g. *Panthera leo*, the lion, and *Panthera onca*, the jaguar, are two species within the genus *Panthera*.

2. defines species known to be distinct but that can not be reliably distinguished by morphology.

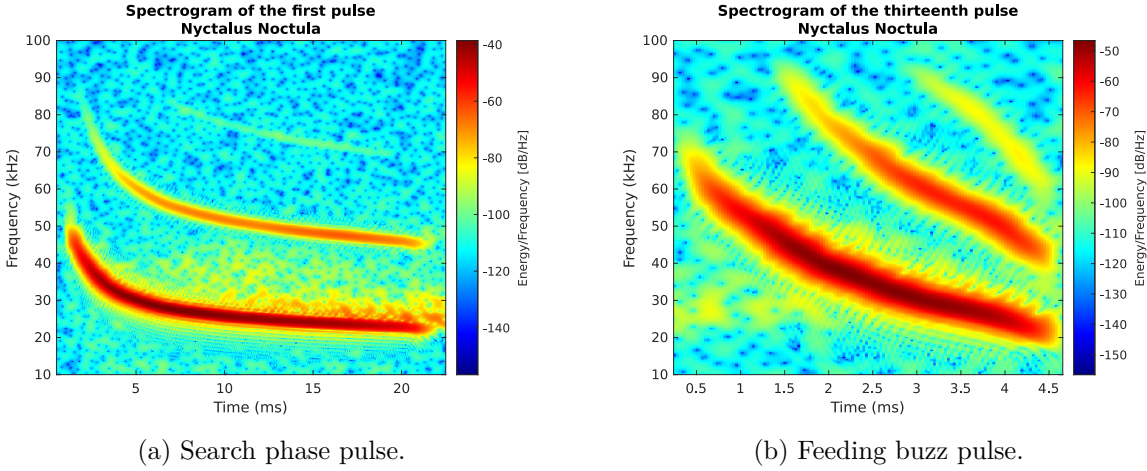


Figure 3.2: Spectrogram of the first and thirteenth pulse of the *Nyctalus noctula* hunting sequence [14]. The pulse duration is greatly reduced as the bat approaches a target while the bandwidth broadens. The PRI, which can be observed in figures 3.1(a) to 3.1(c), decreases as well. Moreover, the quasi-constant frequency portion is eliminated to get a more linearly frequency modulated signal. This indicates the switch between the Doppler and target characteristics estimation process and the will to improve the range resolution.

the Fourier Synchrosqueezed Transform (FSST) [70], a frequency reallocation technique, has been computed and combined with an algorithm for the extraction of maximum energy ridges from a time-frequency matrix. This processing technique, detailed in the appendix B, enables to retrieve the harmonics among a single pulse and to separate them for analysis. The results are illustrated in figures 3.3(a) and 3.3(b), where the two harmonics of the first pulse in the common noctule pulse train are isolated. It should be noted that once isolated, the CuSum can be also computed on the second harmonic to extract its onset and end, given that its duration is often shorter than that of the first harmonic. The red vertical lines indicate the temporal estimation of the onset and end for each harmonic made with the CuSum. The extraction of bat signal parameters can then be used for their synthesis.

3.1.2 A Function to Mimic them all

Understanding how bat signals are constructed and being able to reproduce them are of interest in the context of this thesis, as well as in the field of biology, where it can contribute to the classification of species. This was the aim of the authors of [16], where eight mathematical parametric functions, including the HFM function, were studied to approximate the frequency-time course of echolocation calls from diverse bat species. The objective was to identify species according to their emission parameters and the shape of their echolocation calls. Among the considered functions, the exponential-2 decay, henceforth referred to as the Parsons function

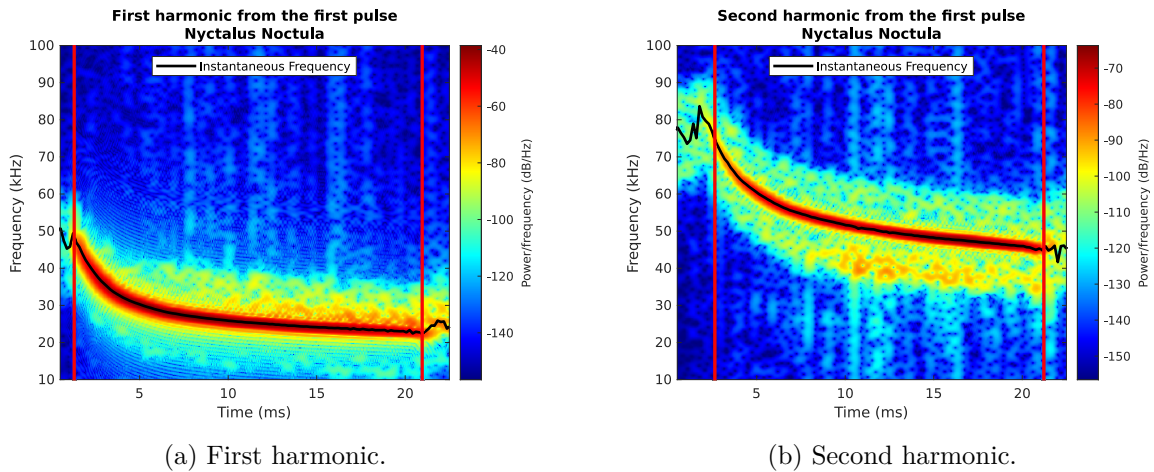


Figure 3.3: Result of the harmonic isolation through the application of the FSST and a ridge extraction algorithm on the first pulse of the common noctule signal [14]. The IF of each harmonic is superimposed with black lines.

(in reference to the author's name [16]), appeared as a promising candidate for a bio-inspired waveform. Indeed, this function was identified as one of the best to fit signals from several bat species [16], particularly the three species presented earlier. The corresponding instantaneous frequency³ and the transmitted signal are defined by

$$f(t) = \frac{f_0}{f_0 - af_1} \left[(f_0 - f_1) \left(\frac{af_1}{f_0} \right)^{\frac{t}{T}} + (1 - a)f_1 \right], \quad (3.1)$$

$$u(t) = \frac{1}{\sqrt{T}} \text{Rect} \left\{ \frac{t}{T} \right\} e^{\frac{2i\pi f_0}{f_0 - af_1} \left[\lambda \beta^{\frac{t}{T}} + (1-a)f_1 t \right]}, \quad (3.2)$$

where $\lambda = \frac{(f_0 - f_1)T}{\ln(\beta)}$ and $\beta = \frac{af_1}{f_0}$ with f_0 the starting frequency, f_1 the ending frequency and T the pulse duration. The particularity of the Parsons function resides in the parameter a , which enables the adjustment of the hyperbolic curvature. This decay parameter comes with certain conditions when considering $f_0 > f_1$ [16]:

- ✶ $a = 0$, the time-frequency course describes a vertical frequency-modulated component followed by a constant-frequency component.
- ✶ $a < \frac{f_0}{f_1}$ the sweep is convex and approximates a chirp when a gets closer to the ratio $\frac{f_0}{f_1}$.
- ✶ $a > \frac{f_0}{f_1}$ the sweep is concave.

Figure 3.4 illustrates the behaviour of the Parsons function regarding these different conditions. It should be noted that decreasing sweeps ($f_0 > f_1$) are considered in this example.

³ In order to ensure that the equation is dimensionally homogeneous, the exponent t , as defined in [16], is replaced by the ratio $\frac{t}{T}$.

The last two conditions on a are inverted with increasing sweeps ($f_0 < f_1$). Therefore, this parameter a enables the Parsons function to compose countless waveforms at a fixed duration and bandwidth.

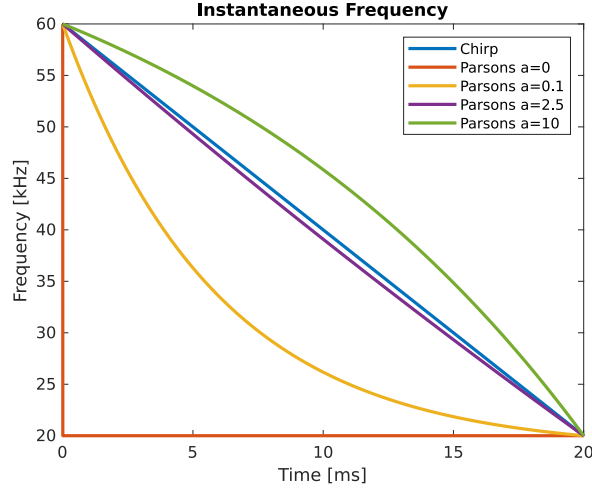


Figure 3.4: Instantaneous frequencies of Parsons functions with varying curvatures ($\frac{f_0}{f_1} = 3$ with $f_0 = 60\text{kHz}$, $f_1 = 20\text{kHz}$ and $T = 20\text{ms}$).

By employing a curve-fitting approach, the Parsons waveform can then be used to mimic the authentic signals presented in the preceding paragraphs, as investigated in [16]. The Root-Mean-Square Error (RMSE) between the instantaneous frequencies of the previously extracted harmonics (figures 3.3(a) and 3.3(b)) and those obtained with the Parsons function when a is varying can be minimised to identify the values of a for which the Parsons function provides the more accurate approximation of the real IF. As a reminder, the RMSE is defined as the square root of the Mean Square Error (MSE), where \hat{X} is an estimator of a parameter X :

$$\text{RMSE} = \sqrt{\mathbb{E}((\hat{X} - X)^2)}. \quad (3.3)$$

This approach is depicted with an example on the first pulse of the common noctule. Figure 3.5(a) displays the RMSEs obtained for the instantaneous frequencies of each harmonic as a function of the parameter a . The minimal values obtained for each harmonic thus correspond to the optimal parameter value a , and, by extension, to the Parsons function that best describes each harmonic. The results are presented in figure 3.5(b) with the approximated harmonics. The black vertical lines represent the estimated onset and end of each harmonic computed with the CuSum, which define the starting and ending frequencies. Consequently, each harmonic can be replicated by a Parsons function, which enables the complete emulation of bat signals. The original pulse from the common noctule, represented once more in figure 3.5(c), is therefore recreated in figure 3.5(d) by combining the Parsons functions representing each harmonic. To

enhance visualisation and provide a more accurate representation of the reality, the synthetic version presents an amplitude modulation (see appendix C) similar to that of the real pulse in figure 3.5(c). It should be noted that the third harmonic discernible in figure 3.5(c) has not been analysed, given its insufficient energy level.

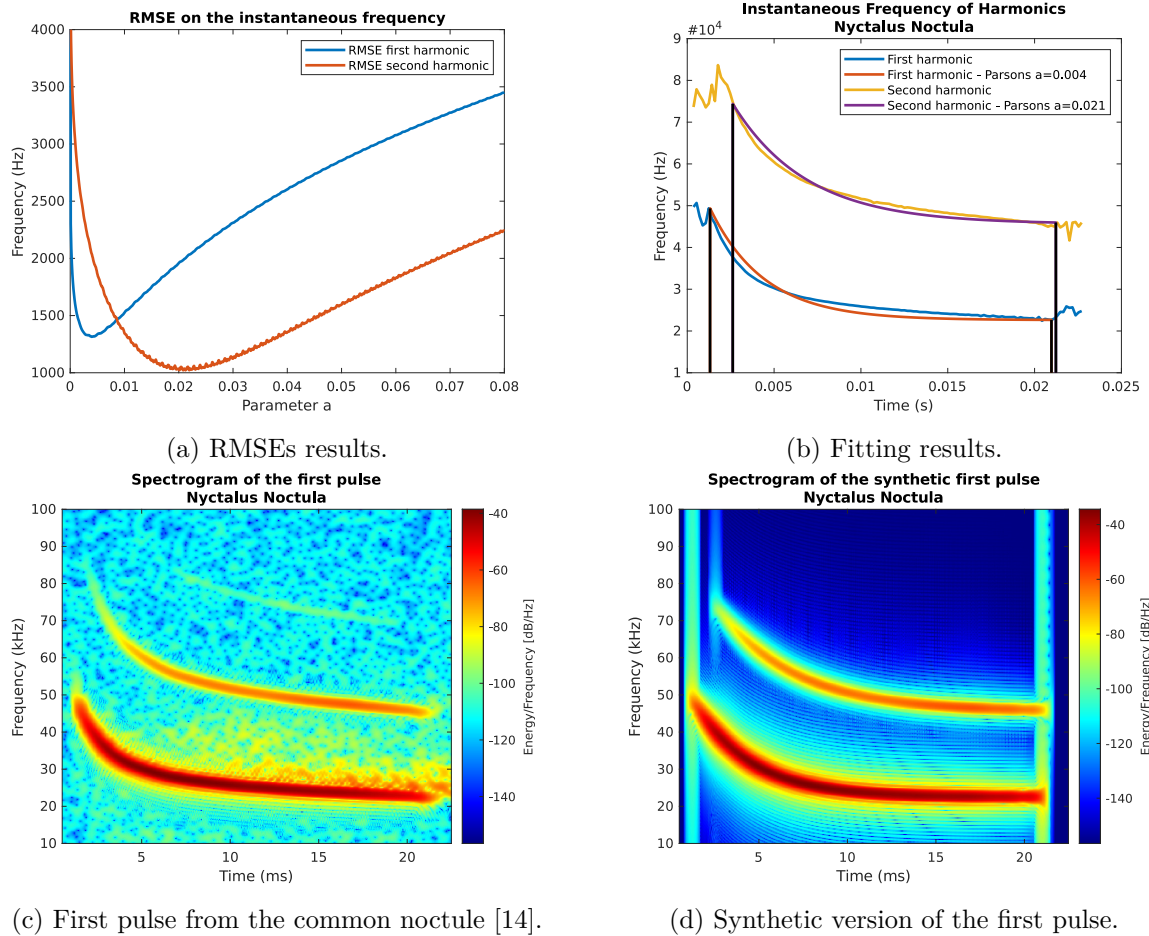


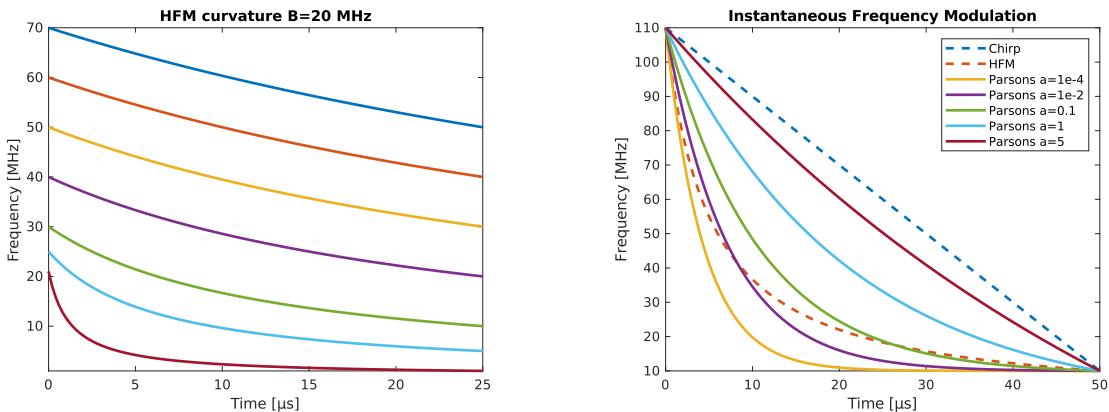
Figure 3.5: The mimicking of bat signals achieved with the Parsons function.

Obviously, results were demonstrated with a single pulse of the common noctule. However, the process has also been validated with several pulses from the common noctule and the two other species. It showed that the Parsons waveform enables to mimic bat waveforms with a high degree of accuracy as evidenced in [16]. The bio-inspiration aspect of the research is thus completed but the question remains as to whether the bio-inspired waveform is effective for radar applications.

3.2 First Steps as a Radar Waveform

3.2.1 The Parsons Waveform: a Function with Curves

The Parsons waveform has been identified as a promising potential bio-inspired radar waveform. However, in the section 2.1.2, the HFM function was presented as the classical bat-inspired radar waveform [8]. To tell the major difference between the two functions, one has to examine the curvature of the instantaneous frequency in relation to the emission parameters, taking into account the desired bat-like plasticity. Concerning the HFM function, this has been investigated in [20] and it was demonstrated that the hyperbolic curvature of the HFM function depends on its temporal and frequency parameters, especially the ending frequency, f_1 . Figure 3.6(a) shows the impact of f_1 on the curvature of the instantaneous frequency for the HFM waveform. This renders the HFM function less flexible than the bat’s capacities. Besides, the approximation of bat calls by the HFM function was deemed inadequate in [16]. In contrast, the Parsons function disposes of the parameter a , which, as explained above, allows to change its curvature at a fixed duration and bandwidth. This therefore offers an additional degree of flexibility in the waveform design in comparison to the HFM function. Moreover, as evidenced by the findings in [16] and the preceding analysis, the Parsons waveform design is more closely aligned with the capabilities of bats. Figure 3.6(b) depicts this plasticity by comparing Parsons function with the chirp and the HFM function at various values of a . Despite its capacity to accurately represent bat waveforms, the suitability of the Parsons function as a radar waveform requires further investigation.



(a) Change in curvature as a function of f_1 for the HFM function ($T = 25\mu\text{s}$, $B = 20\text{MHz}$). (b) Instantaneous frequencies of Parsons functions with varying curvatures ($T = 50\mu\text{s}$, $B = 100\text{MHz}$).

Figure 3.6: Comparisons between the flexibility of the HFM and Parson functions.

3.2.2 Behaviour towards Classical Radar Processing

All along this section, the response of the Parsons, the HFM and the Chirp waveforms to classical radar processing are compared. The objective is to investigate the capacity of the Parsons function as a radar waveform.

MF and MMF

The first step of this analysis concerns the response of the Parsons waveform to the matched filter. Figure 3.7 illustrates the output of the matched filter for different Parsons functions. The primary observation is that, compared to the chirp, the hyperbolic waveforms (Parsons and HFM) exhibit noticeable higher sidelobe levels. The mainlobe also appears to broaden as the curvature of the signal increases, with the HFM mainlobe and its sidelobes becoming almost indistinguishable in this example. This expansion of the mainlobe is linked to the quasi-constant frequency behaviour of the signal. In fact, the instantaneous frequencies, represented in figure 3.6(b), which exhibit a notable curvature, sweep over a narrow bandwidth for approximately half or more of the signal duration. This result, frequently described in bat-related literature, is attributed to the fact that quasi-constant frequency modulated signals are more appropriate for detection solely rather than precise ranging [18]. Moreover, the combination of CF and FM signals could be an advantage with the first modulation for target/velocity detection and the second one for target range resolution [17]. This is typically the kind of signals used by the greater horseshoe bats for example (see figure 2.20). It is also noteworthy that the Parsons function displays considerable flexibility in its response to the matched filter, depending on the

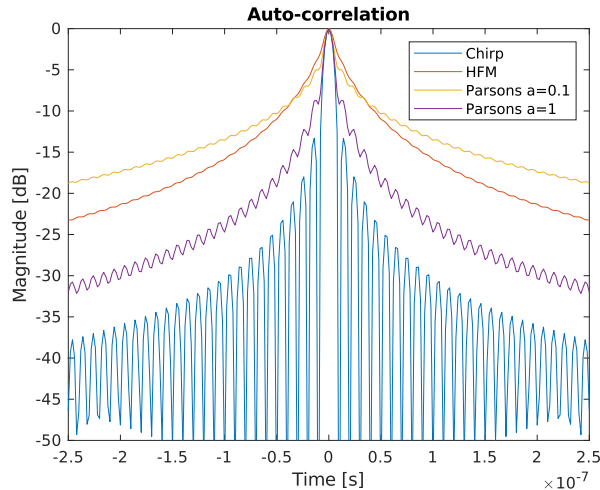
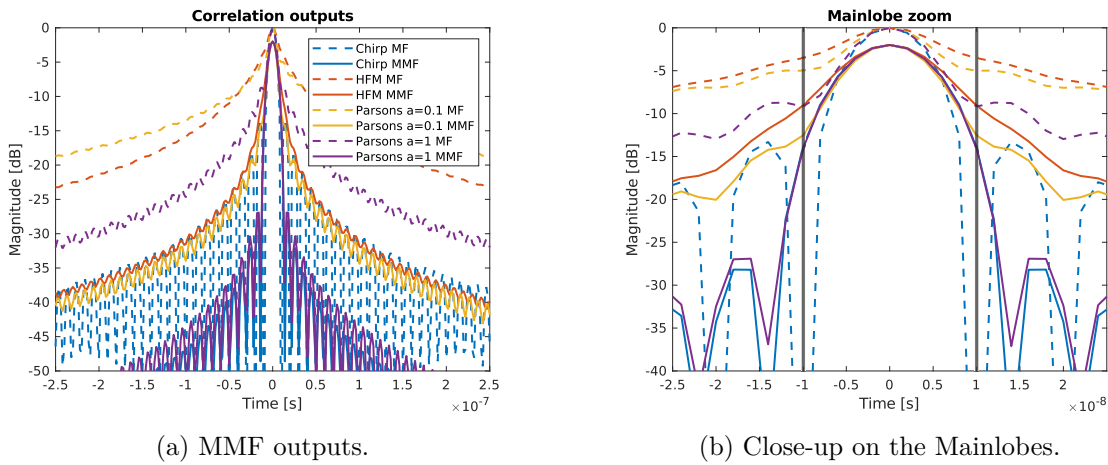


Figure 3.7: Comparison of auto-correlations between the Chirp, HFM and Parsons waveforms ($T = 50\mu\text{s}$, $B = 100\text{MHz}$).

value of the parameter a . The output approaches that of a chirp as a increases towards the ratio $\frac{f_0}{f_1}$. The Parsons waveform allows for quite precise control of the matched filter response and the sidelobe levels through the parameter a . The Parsons function thus offers an adaptability that is comparable to that observed in bat signals.

Nevertheless, the high sidelobe level associated with the curvature of the Parsons waveform could be problematic for radar applications, as it could mask targets with weak responses. This is where the MisMatched Filter (MMF) enters the field as a possible solution for sidelobes mitigation. The MMF of each waveform has been calculated to optimise the ISLR and figures 3.8(a) displays the MMF outputs in comparison to the previous MF responses. The result for



(a) MMF outputs.

(b) Close-up on the Mainlobes.

Figure 3.8: Behaviour comparison between the Chirp, HFM and Parsons waveforms processed by the MMF for the optimisation of the ISLR ($T = 50\mu\text{s}$, $B = 100\text{MHz}$, $K_q = N = 25,001$ samples, $\beta_q = 2\text{dB}$). The legend is the same for both figures but not displayed in the second one for a better readability.

the chirp has already been discussed in section 2.1.3 and can be compared with the MMFs of the Parsons and HFM functions. For both hyperbolic functions, the MMF can be readily calculated. The ISLRs and PSLRs values have been measured for a fixed mainlobe width (equals to $\frac{2F_s}{B} = 10$ samples here and represented with the black vertical lines in figure 3.8(b)) to ensure the comparison between the MF and MMF outputs. The values are presented in the Table 3.1. As a first observation, the relatively high sidelobe level linked to the curvature can be effectively mitigated by the MMF for both the Parsons and the HFM waveforms. Regarding the mainlobe width, the Parsons waveform with $a = 1$ and the chirp suffer a broadening by a factor of 1.1 and 1.2, respectively. In contrast, the HFM and Parsons ($a = 0.1$) waveforms exhibit a narrower mainlobe by a factor of 0.7 and 0.9, respectively. This can be explained by comparing the spectrum of the waveforms and their MMFs presented in the figure 3.9. The initial mainlobe width linked to the quasi-constant frequency behaviour of the more curved functions (HFM and

Parsons with $a = 0.1$) is narrower because the spectrum of the MMF is flattened, resulting in a rounded spectrum and a reduction in the impact of the quasi-constant frequency component. For the chirp and Parsons ($a = 1$) waveforms, the opposite logic can be applied as their spectrum becomes more rounded. Overall, the Parsons waveforms present an improved behaviour with a mismatched filter, as the sidelobe levels are reduced to a level approaching that of a chirp.

s_i	MF-ISLR [dB]	MMF-ISLR [dB]	MF-PSLR [dB]	MMF-PSLR [dB]
Chirp	-9.7	-15.1	-13.3	-26.2
HFM	2.4	-5.4	-21.7	-18.9
Parsons $a = 0.1$	4.5	-7	-5	-17.1
Parsons $a = 1$	-2.6	-15	-8.7	-24.9

Table 3.1: ISLRs and PSLRs calculated from the MF and MMF outputs of the different waveforms. The positive values obtained for the ISLRs of the HFM and the first Parsons waveforms are due to the sidelobes energy being superior to that of the mainlobe.

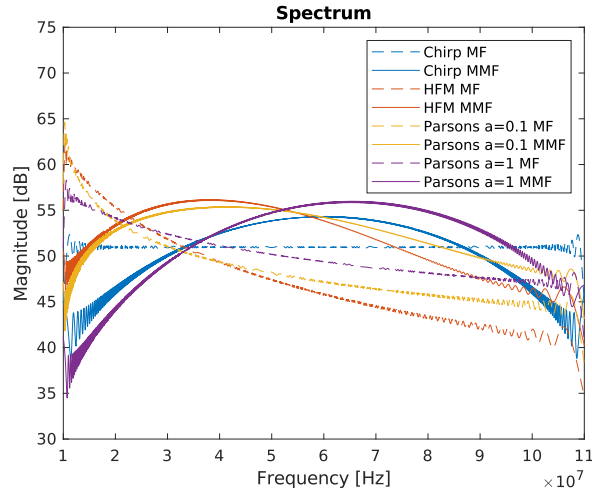


Figure 3.9: Comparison between the spectrum of the presented waveforms and the spectrum of their MMFs ($T = 50\mu\text{s}$, $B = 100\text{MHz}$).

Ambiguity Function

Logically, the next step in the study of the Parsons waveform is to investigate the impact of the Doppler on the output of the MF by looking at its Ambiguity Function (AF). The AF of

the Parsons waveform can be written as

$$\begin{aligned}
 \chi(\tau, \nu_d) &= \int_{-\infty}^{+\infty} u(t)u^*(t + \tau)e^{2i\pi\nu_d t} dt, \\
 &= \frac{1}{T} \int_0^{T-\tau} e^{\frac{2i\pi f_0}{f_0 - af_1} [\lambda\beta^{\frac{t}{T}} + (1-a)f_1 t]} e^{\frac{-2i\pi f_0}{f_0 - af_1} [\lambda\beta^{\frac{t+\tau}{T}} + (1-a)f_1(t+\tau)]} e^{2i\pi\nu_d t} dt, \\
 &= \frac{1}{T} e^{\frac{-2i\pi f_0}{f_0 - af_1} (1-a)f_1 \tau} \int_0^{T-\tau} e^{\frac{2i\pi f_0}{f_0 - af_1} \lambda \left(1 - \beta^{\frac{\tau}{T}}\right) \beta^{\frac{t}{T}}} e^{2i\pi\nu_d t} dt.
 \end{aligned} \tag{3.4}$$

The integral is solved for $\tau > 0$ by considering the symmetry property of the AF:

$$|\chi(-\tau, -\nu_d)| = |\chi(\tau, \nu_d)|. \tag{3.5}$$

The change of variable $x = \beta^{\frac{t}{T}}$ can help pursue the calculations. If t varies from 0 to $T - \tau$ then x goes from 1 to $\beta^{\frac{T-\tau}{T}}$. Moreover, by using the equality $e^{b \ln(y)} = y^b$, the following derivation $\frac{dx}{dt} = \frac{\ln \beta}{T} \beta^{\frac{t}{T}}$ is obtained. Therefore, the ambiguity function becomes

$$\begin{aligned}
 \chi(\tau, \nu_d) &= \frac{1}{\ln \beta} e^{\frac{-2i\pi f_0}{f_0 - af_1} (1-a)f_1 \tau} \int_1^{\beta^{\frac{T-\tau}{T}}} \frac{1}{x} e^{\frac{2i\pi f_0}{f_0 - af_1} \lambda \left(1 - \beta^{\frac{\tau}{T}}\right) x} e^{2i\pi\nu_d \frac{T}{\ln \beta} \ln x} dx, \\
 &= \frac{1}{\ln \beta} e^{\frac{-2i\pi f_0}{f_0 - af_1} (1-a)f_1 \tau} \int_1^{\beta^{\frac{T-\tau}{T}}} e^{\frac{2i\pi f_0}{f_0 - af_1} \lambda \left(1 - \beta^{\frac{\tau}{T}}\right) x} x^{2i\pi\nu_d \frac{T}{\ln \beta} - 1} dx.
 \end{aligned} \tag{3.6}$$

We define the following parameters

$$\alpha_1 = \frac{2i\pi f_0}{f_0 - af_1} \lambda \left(1 - \beta^{\frac{\tau}{T}}\right), \tag{3.7}$$

$$\alpha_2 = 2i\pi\nu_d \frac{T}{\ln \beta} - 1, \tag{3.8}$$

such that the integral part of (3.6) becomes

$$I = \int_1^{\beta^{\frac{T-\tau}{T}}} e^{\alpha_1 x} x^{\alpha_2} dx. \tag{3.9}$$

Again, a change of variable is operated. Let $u = -\alpha_1 x$, so $x = -\frac{u}{\alpha_1}$ and $\frac{du}{dx} = -\alpha_1$, the integral then writes as

$$I = \int_{-\alpha_1}^{-\alpha_1 \beta^{\frac{T-\tau}{T}}} e^{-u} \left(-\frac{u}{\alpha_1}\right)^{\alpha_2} \frac{du}{-\alpha_1} = \left(-\frac{1}{\alpha_1}\right)^{\alpha_2+1} \int_{-\alpha_1}^{-\alpha_1 \beta^{\frac{T-\tau}{T}}} e^{-u} u^{\alpha_2} du. \tag{3.10}$$

According to the definition of an upper incomplete gamma function given by [21]

$$\Gamma(\alpha_\Gamma, u) = \int_u^\infty e^{-t} t^{\alpha_\Gamma-1} dt, \tag{3.11}$$

then

$$I = \left(-\frac{1}{\alpha_1}\right)^{\alpha_2+1} \left(\Gamma\left(\alpha_2 + 1, -\alpha_1\beta^{\frac{T-\tau}{T}}\right) - \Gamma(\alpha_2 + 1, -\alpha_1)\right). \quad (3.12)$$

Note that the upper incomplete gamma function is known to be holomorphic⁴ with respect to both u and α_Γ , for all α_Γ and $u \neq 0$ [71][72]. The following step is based on the relation between the incomplete gamma function and the generalised exponential integral [21], which writes

$$E_{-\alpha_2}(-\alpha_1 x) = (-\alpha_1 x)^{-\alpha_2-1} \Gamma(\alpha_2 + 1, -\alpha_1 x). \quad (3.13)$$

The integral can then be solved using the generalised exponential integral by writing

$$I = \left(\beta^{\frac{T-\tau}{T}}\right)^{\alpha_2+1} E_{-\alpha_2}\left(-\alpha_1\beta^{\frac{T-\tau}{T}}\right) - E_{-\alpha_2}(-\alpha_1), \quad (3.14)$$

and the ambiguity function for the Parsons waveform is thus expressed by

$$\chi(\tau, \nu_d) = \frac{1}{\ln \beta} e^{\frac{-2i\pi f_0}{f_0 - a f_1} (1-a) f_1 \tau} \left[\left(\beta^{\frac{T-\tau}{T}}\right)^{\alpha_2+1} E_{-\alpha_2}\left(-\alpha_1\beta^{\frac{T-\tau}{T}}\right) - E_{-\alpha_2}(-\alpha_1) \right]. \quad (3.15)$$

It is important to note that with this equation, the delay cut at $\tau = 0$ can not be obtained as the exponential integral definition excludes the origin and $\alpha_1 = 0$ under this condition. This is consistent with the fact that the upper incomplete gamma function is defined for $u \neq 0$ as stated earlier. Nevertheless, the mathematical definition obtained for the ambiguity function can still be verified for $\tau \neq 0$ as illustrated in figures 3.10(a) and 3.10(b). Figure 3.10(a) gives the Doppler cut obtained with the theoretical formula (orange dashes) compared to the autocorrelation of the Parsons function with $a = 1$ (blue solid line). The results show an almost perfect agreement between the theory and the simulations, as the RMSE is less than 0.6dB for $\tau \in \left[0, \frac{T}{2}\right]$ and increases to 3.5dB for $\tau \in [0, T]$. The same result can be observed in figure 3.10(b), where the range cut is shown for $\nu_d = 20\text{kHz}$.

Figures 3.11(a) to 3.11(d) display the Ambiguity Functions for the chirp, the HFM waveform and two Parsons functions ($a = 0.1$ and $a = 1$). The superiority of the chirp, in terms of Doppler tolerance, is evident based on the increased sidelobe levels observed in the response of the HFM and the Parsons function, which gives this peculiar "bow tie" aspect, with wings that are more or less shrunk depending on the curvature. Nevertheless, Figures 3.11(c) and 3.11(d) demonstrate that the Doppler tolerance of the Parsons function can be controlled by the parameter a . The Parsons waveform, due to its increased agility compared to the HFM waveform, offers new possibilities in waveform design but its performance still needs to be evaluated. The AF is the basis for assessing the capacity of a waveform in a radar context. To this end, it can be used to calculate the Cramér-Rao Lower Bounds (CLRB) presented hereafter.

4. designates a complex-valued function of one or more complex variables, which is complex differentiable in a neighbourhood of each point in its domain.

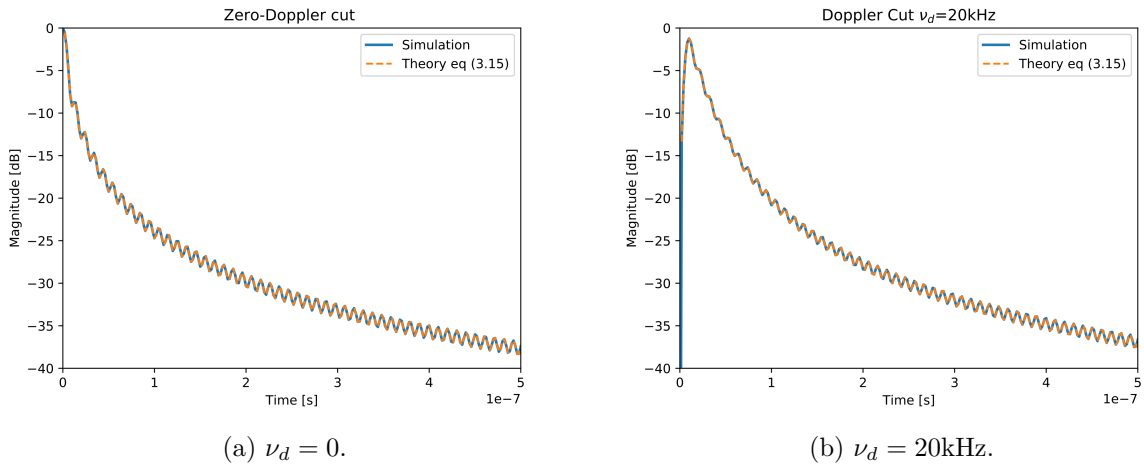


Figure 3.10: Doppler cut of the AF for the Parsons waveform ($T = 50\mu\text{s}$, $B = 100\text{MHz}$, $a = 1$).

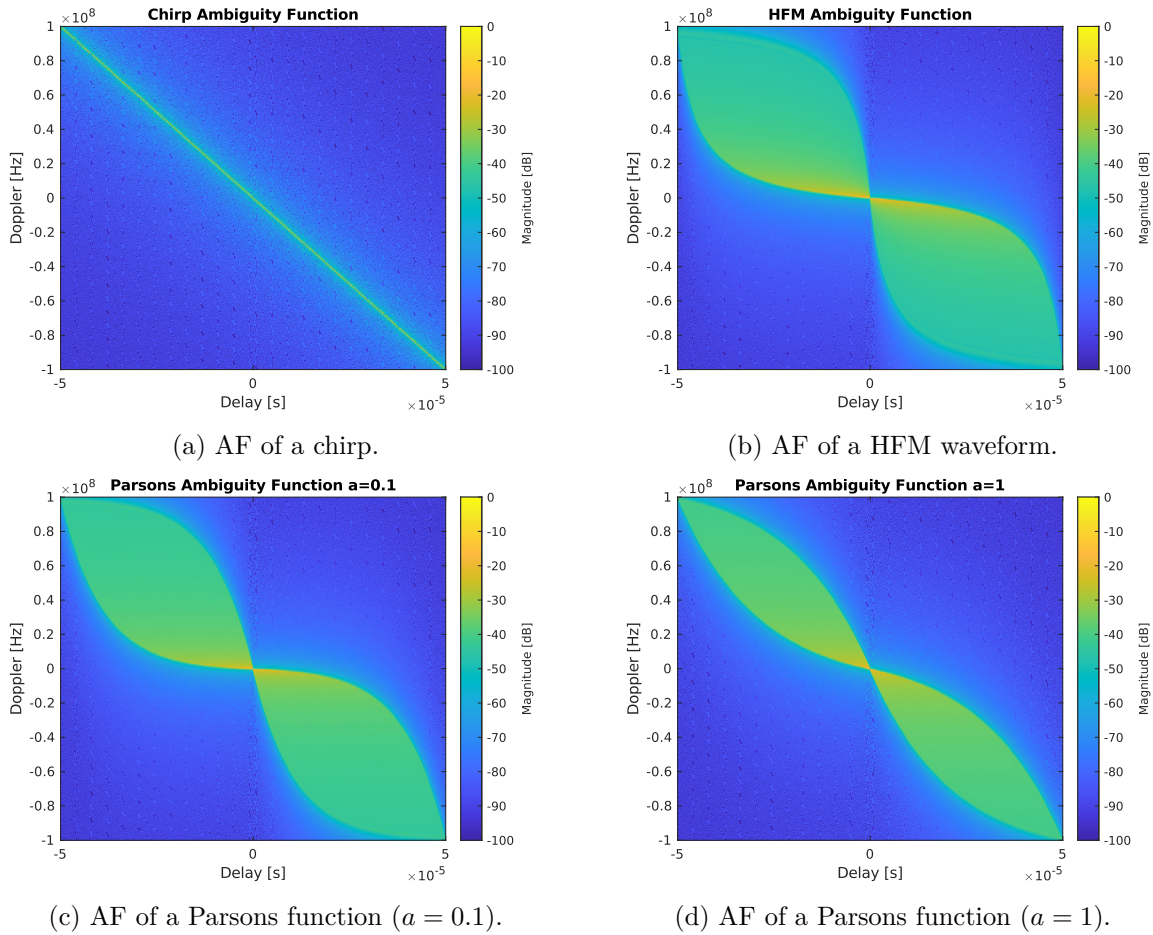


Figure 3.11: Ambiguity Functions of various waveforms ($T = 50\mu\text{s}$, $B = 100\text{MHz}$).

3.2.3 The Cramér-Rao Lower Bat Bound

Mathematical formulation

The Cramér-Rao Lower Bound define a lower bound on the variance of an unbiased estimator. In the case of radar waveforms, it is relevant to evaluate the accuracy of the joint-estimator of delay τ and Doppler ν_d . These bounds are derived from the Fisher Information matrix [22][23] as

$$CRLB(\tau) = -\frac{\mathbf{J}_{AF}(2, 2)}{\text{SNR } \det(\mathbf{J}_{AF})}, \quad (3.16)$$

$$CRLB(\nu_d) = -\frac{\mathbf{J}_{AF}(1, 1)}{\text{SNR } \det(\mathbf{J}_{AF})}, \quad (3.17)$$

where SNR represents the Signal-to-Noise Ratio and \mathbf{J}_{AF} is the matrix of the second order derivatives of the squared amplitude of the AF that can be written as follows:

$$\mathbf{J}_{AF} = \begin{pmatrix} \frac{\partial^2 |\chi(\tau, \nu_d)|^2}{\partial \tau^2} & \frac{\partial^2 |\chi(\tau, \nu_d)|^2}{\partial \tau \partial \nu_d} \\ \frac{\partial^2 |\chi(\tau, \nu_d)|^2}{\partial \nu_d \partial \tau} & \frac{\partial^2 |\chi(\tau, \nu_d)|^2}{\partial \nu_d^2} \end{pmatrix} \Bigg|_{\tau, \nu_d=0} \quad (3.18)$$

To calculate the elements of \mathbf{J}_{AF} , the following equations can be calculated [20][22]:

$$\frac{\partial^2 |\chi(\tau, \nu_d)|^2}{\partial \tau^2} = 2\text{Real} \left\{ \chi^*(\tau, \nu_d) \frac{\partial^2 \chi(\tau, \nu_d)}{\partial \tau^2} \right\} + 2 \left| \frac{\partial \chi(\tau, \nu_d)}{\partial \tau} \right|^2, \quad (3.19)$$

$$\frac{\partial^2 |\chi(\tau, \nu_d)|^2}{\partial \tau \partial \nu_d} = 2\text{Real} \left\{ \chi^*(\tau, \nu_d) \frac{\partial^2 \chi(\tau, \nu_d)}{\partial \tau \partial \nu_d} \right\} + 2\text{Real} \left\{ \frac{\partial \chi^*(\tau, \nu_d)}{\partial \nu_d} \frac{\partial \chi(\tau, \nu_d)}{\partial \tau} \right\}, \quad (3.20)$$

$$\frac{\partial^2 |\chi(\tau, \nu_d)|^2}{\partial \nu_d \partial \tau} = 2\text{Real} \left\{ \chi^*(\tau, \nu_d) \frac{\partial^2 \chi(\tau, \nu_d)}{\partial \nu_d \partial \tau} \right\} + 2\text{Real} \left\{ \frac{\partial \chi(\tau, \nu_d)}{\partial \nu_d} \frac{\partial \chi^*(\tau, \nu_d)}{\partial \tau} \right\}, \quad (3.21)$$

$$\frac{\partial^2 |\chi(\tau, \nu_d)|^2}{\partial \nu_d^2} = 2\text{Real} \left\{ \chi^*(\tau, \nu_d) \frac{\partial^2 \chi(\tau, \nu_d)}{\partial \nu_d^2} \right\} + 2 \left| \frac{\partial \chi(\tau, \nu_d)}{\partial \nu_d} \right|^2. \quad (3.22)$$

The detailed calculations of CLRb for the chirp and the HFM are not discussed in this manuscript but can be found in [20]. Their respective \mathbf{J}_{AF} matrices are still given in Appendix D. This section focuses on the calculation of the CLRb for the Parsons function following the same logic as the one proposed in [20] and described below. Let

$$u(t) = e^{\frac{2i\pi f_0}{f_0 - a f_1} \left[\lambda \beta^{\frac{t}{T}} + (1-a)f_1 t \right]}, \quad (3.23)$$

The Ambiguity Function of the Parsons waveform can be written as

$$\chi(\tau, \nu_d) = \frac{1}{T} \int_0^{T-\tau} \text{Rect} \left\{ \frac{t}{T} \right\} u(t) \text{Rect} \left\{ \frac{t+\tau}{T} \right\} u(t+\tau) e^{2i\pi \nu_d t} dt. \quad (3.24)$$

The first stage consists in deriving eq. (3.24) with respect to ν_d

$$\frac{\partial \chi(\tau, \nu_d)}{\partial \nu_d} = \frac{1}{T} \int_0^{T-\tau} u(t) u^*(t + \tau) 2i\pi t e^{2i\pi \nu_d t} dt, \quad (3.25)$$

$$\frac{\partial^2 \chi(\tau, \nu_d)}{\partial \nu_d^2} = \frac{1}{T} \int_0^{T-\tau} -u(t) u^*(t + \tau) 4\pi^2 t^2 e^{2i\pi \nu_d t} dt. \quad (3.26)$$

Therefore, evaluating these derivatives for $(\tau, \nu_d) = (0, 0)$ gives

$$\left. \frac{\partial \chi(\tau, \nu_d)}{\partial \nu_d} \right|_{\tau, \nu_d=0} = \frac{1}{T} \int_0^T 2i\pi t dt = i\pi T, \quad (3.27)$$

$$\left. \frac{\partial^2 \chi(\tau, \nu_d)}{\partial \nu_d^2} \right|_{\tau, \nu_d=0} = \frac{1}{T} \int_0^T -4\pi^2 t^2 dt = -\frac{4}{3}\pi^2 T^2. \quad (3.28)$$

By observing that $\chi^*(\tau, \nu_d)|_{\tau, \nu_d=0} = 1$ and by replacing eq. (3.27) and (3.28) in eq. (3.22), a first element of the \mathbf{J}_{AF} matrix is obtained as

$$\left. \frac{\partial^2 |\chi(\tau, \nu_d)|^2}{\partial \nu_d^2} \right|_{\tau, \nu_d=0} = 2\text{Real} \left\{ -\frac{4}{3}\pi^2 T^2 \right\} + 2|i\pi T|^2 = -\frac{2}{3}\pi^2 T^2. \quad (3.29)$$

Because the derivatives of the ambiguity function with respect to ν_d do not depend on the waveform design, the previous result is the same for any type of waveform with unit energy and rectangular amplitude modulation. The derivatives of the AF with respect to τ are obtained by applying the chain rule $\frac{\partial f(u)}{\partial u} \frac{\partial u}{\partial x}$, leading to

$$\frac{\partial u^*(t + \tau)}{\partial \tau} = -\frac{2i\pi f_0}{f_0 - af_1} e^{-\frac{2i\pi f_0}{f_0 - af_1} \left[\lambda \beta^{\frac{t+\tau}{T}} + (1-a)f_1(t+\tau) \right]} \times \left[\lambda \frac{\ln(\beta)}{T} \beta^{\frac{t+\tau}{T}} + (1-a)f_1 \right], \quad (3.30)$$

$$\begin{aligned} \frac{\partial^2 u^*(t + \tau)}{\partial \tau^2} &= -\frac{4\pi^2 f_0^2}{(f_0 - af_1)^2} e^{-\frac{2i\pi f_0}{f_0 - af_1} \left[\lambda \beta^{\frac{t+\tau}{T}} + (1-a)f_1(t+\tau) \right]} \times \left[\lambda \frac{\ln(\beta)}{T} \beta^{\frac{t+\tau}{T}} + (1-a)f_1 \right]^2 \\ &\quad - \frac{2i\pi f_0}{f_0 - af_1} e^{-\frac{2i\pi f_0}{f_0 - af_1} \left[\lambda \beta^{\frac{t+\tau}{T}} + (1-a)f_1(t+\tau) \right]} \times \lambda \frac{\ln^2(\beta)}{T^2} \beta^{\frac{t+\tau}{T}}. \end{aligned} \quad (3.31)$$

The first order derivative with respect to τ is obtained by the following equation (Proof in Appendix D)

$$\frac{\partial \chi(\tau, \nu_d)}{\partial \tau} = \frac{1}{T} \int_0^{T-\tau} u(t) \frac{\partial u^*(t + \tau)}{\partial \tau} e^{2i\pi \nu_d t} dt - \frac{1}{T} u(T - \tau) u^*(T) e^{2i\pi \nu_d (T-\tau)}, \quad (3.32)$$

and by inserting eq. (3.23) and (3.30) in (3.32), we get

$$\begin{aligned} \left. \frac{\partial \chi(\tau, \nu_d)}{\partial \tau} \right|_{\tau, \nu_d=0} &= \frac{-2i\pi f_0}{T(f_0 - af_1)} \int_0^T \left[\lambda \frac{\ln(\beta)}{T} \beta^{\frac{t}{T}} + (1-a)f_1 \right] dt - \frac{1}{T} \\ &= \frac{-2i\pi f_0}{T(f_0 - af_1)} [\lambda(\beta - 1) + (1-a)f_1 T] - \frac{1}{T}. \end{aligned} \quad (3.33)$$

Concerning the second order derivative with respect to τ , it can be written as (Proof in Appendix D)

$$\begin{aligned} \frac{\partial^2 \chi(\tau, \nu_d)}{\partial \tau^2} &= \frac{1}{T} \int_0^{T-\tau} u(t) \frac{\partial^2 u^*(t+\tau)}{\partial \tau^2} e^{2i\pi\nu_d t} dt - \frac{1}{T} u(T-\tau) \left. \frac{\partial u^*(t+\tau)}{\partial \tau} \right|_{t=T-\tau} e^{2i\pi\nu_d(T-\tau)} \\ &\quad - \frac{1}{T} u^*(T) \frac{\partial u(T-\tau)}{\partial \tau} e^{2i\pi\nu_d(T-\tau)} \\ &= c' - a' - b', \end{aligned} \quad (3.34)$$

where a' , b' and c' evaluated at $(\tau, \nu_d) = (0, 0)$ give respectively

$$a'|_{\tau, \nu_d=0} = \frac{-2i\pi f_0}{T(f_0 - af_1)} \left[\lambda \frac{\ln(\beta)}{T} \beta + (1-a)f_1 \right], \quad (3.35)$$

$$b'|_{\tau, \nu_d=0} = \frac{-2i\pi f_0}{T(f_0 - af_1)} \left[\lambda \frac{\ln(\beta)}{T} \beta + (1-a)f_1 \right], \quad (3.36)$$

$$\begin{aligned} c'|_{\tau, \nu_d=0} &= \frac{-2i\pi f_0}{T(f_0 - af_1)} \left[\lambda \frac{\ln(\beta)}{T} (\beta - 1) \right] \\ &\quad - \frac{4\pi^2 f_0^2}{T(f_0 - af_1)^2} \left[\lambda^2 \frac{\ln(\beta)}{2T} (\beta^2 - 1) + (1-a)^2 f_1^2 T + 2\lambda(\beta - 1)(1-a)f_1 \right]. \end{aligned} \quad (3.37)$$

Therefore, eq. (3.34) writes

$$\begin{aligned} \left. \frac{\partial^2 \chi(\tau, \nu_d)}{\partial \tau^2} \right|_{\tau, \nu_d=0} &= -\frac{4\pi^2 f_0^2}{T(f_0 - af_1)^2} \left[\lambda^2 \frac{\ln(\beta)}{2T} (\beta^2 - 1) + (1-a)^2 f_1^2 T + 2\lambda(\beta - 1)(1-a)f_1 \right] \\ &\quad + \frac{2i\pi f_0}{T(f_0 - af_1)} \left[\lambda \frac{\ln(\beta)}{T} (\beta + 1) + 2(1-a)f_1 \right], \end{aligned} \quad (3.38)$$

Then, equation (3.19) leads to

$$\begin{aligned} \left. \frac{\partial^2 |\chi(\tau, \nu_d)|^2}{\partial \tau^2} \right|_{\tau, \nu_d=0} &= -\frac{8\pi^2 f_0^2}{T(f_0 - af_1)^2} \left[\lambda^2 \frac{\ln(\beta)}{2T} (\beta^2 - 1) + (1-a)^2 f_1^2 T + 2\lambda(\beta - 1)(1-a)f_1 \right] \\ &\quad + \frac{8\pi^2 f_0^2}{T^2(f_0 - af_1)^2} [\lambda(\beta - 1) + (1-a)f_1 T]^2 + \frac{2}{T^2} \\ &= \frac{8\pi^2 f_0^2}{T^2(f_0 - af_1)^2} \lambda^2 (\beta - 1) \left[\beta - 1 - \frac{\ln(\beta)}{2} (\beta + 1) \right] + \frac{2}{T^2}. \end{aligned} \quad (3.39)$$

Because the anti-diagonal terms in eq. (3.20) and (3.21) are equal, only the calculation of eq. (3.20) is detailed. The second order derivative of the AF with respect to ν_d and τ can be easily derived from eq. (3.32) which gives

$$\frac{\partial^2 \chi(\tau, \nu_d)}{\partial \tau \partial \nu_d} = \frac{1}{T} \int_0^{T-\tau} u(t) \frac{\partial u^*(t+\tau)}{\partial \tau} 2i\pi t e^{2i\pi \nu_d t} dt - \frac{1}{T} u(T-\tau) u^*(T) 2i\pi (T-\tau) e^{2i\pi \nu_d (T-\tau)}. \quad (3.40)$$

Then,

$$\begin{aligned} \left. \frac{\partial^2 \chi(\tau, \nu_d)}{\partial \tau \partial \nu_d} \right|_{\tau, \nu_d=0} &= \frac{4\pi^2 f_0}{T(f_0 - af_1)} \int_0^T t \left[\frac{\lambda \ln(\beta)}{T} \beta^{\frac{t}{T}} + (1-a)f_1 \right] dt - 2i\pi \\ &= \frac{4\pi^2 f_0}{(f_0 - af_1)} \left[\lambda\beta - \frac{\lambda}{\ln(\beta)}(\beta - 1) + \frac{T(1-a)f_1}{2} \right] - 2i\pi. \end{aligned} \quad (3.41)$$

From eq. (3.27), (3.33) and (3.41), the anti-diagonal terms can be written as

$$\begin{aligned} \left. \frac{\partial^2 |\chi(\tau, \nu_d)|^2}{\partial \tau \partial \nu_d} \right|_{\tau, \nu_d=0} &= \left. \frac{\partial^2 |\chi(\tau, \nu_d)|^2}{\partial \nu_d \partial \tau} \right|_{\tau, \nu_d=0} \\ &= \frac{4\pi^2 f_0}{(f_0 - af_1)} \left[2\lambda\beta - \left(\frac{2}{\ln(\beta)} + 1 \right) (\beta - 1)\lambda \right]. \end{aligned} \quad (3.42)$$

Finally, the matrix (3.43) is obtained from eq.(3.29), (3.39) and (3.42) for the Parsons waveform:

$$\mathbf{J}_{AF, Parsons} = \left(\begin{array}{cc} \frac{8\pi^2 f_0^2 \lambda^2 (\beta-1)}{T^2 (f_0 - af_1)^2} \left[\beta - 1 - \frac{\ln(\beta)}{2} (\beta + 1) \right] & \frac{4\pi^2 f_0}{(f_0 - af_1)} \left[2\lambda\beta - \left(\frac{2}{\ln(\beta)} + 1 \right) (\beta - 1)\lambda \right] \\ + \frac{2}{T^2} & \\ \frac{4\pi^2 f_0}{(f_0 - af_1)} \left[2\lambda\beta - \left(\frac{2}{\ln(\beta)} + 1 \right) (\beta - 1)\lambda \right] & - \frac{2}{3} \pi^2 T^2 \end{array} \right) \Bigg|_{\tau, \nu_d=0} \quad (3.43)$$

Simulation Analysis

The matrix $\mathbf{J}_{AF, Parsons}$ provides access to the CLRB defined in eq. (3.16) and (3.17) for the Parsons waveform. Nevertheless, the comparison with the linear chirp for a unique pulse with rectangular amplitude is not possible due to the coupling between delay and Doppler [20] leading to undefined CLRB. They can still be estimated if we consider a decoupling by calculating the following expressions [22]

$$CRLB(\tau) = -\frac{1}{\text{SNR } \mathbf{J}_{AF}(1, 1)}, \quad (3.44)$$

$$CRLB(\nu_d) = -\frac{1}{\text{SNR } \mathbf{J}_{AF}(2, 2)}. \quad (3.45)$$

Since $\mathbf{J}_{AF}(2, 2)$ is independent of the waveform, the CLRB over Doppler in a single pulse configuration are equal and are thus not displayed. Figure 3.12 displays the corresponding CLRB for the different waveforms considered in this study. The resulting lower bounds of Parsons waveforms for different values of the parameter a are satisfactory for radar purpose, as they match the capacity of the chirp. The flexibility of the Parsons function is once again visible in the manner in which the CLRB change according to the curvature. These CLRB are close to that of a HFM waveform ($a = 0.01$) or akin to a chirp ($a = 3.12$).

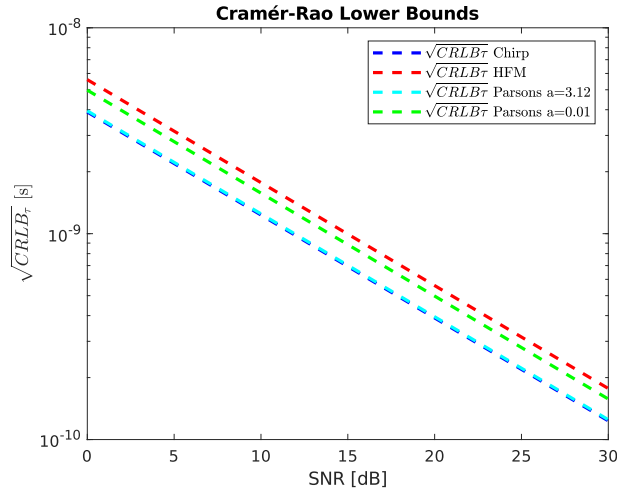


Figure 3.12: CLRB for delay τ for a unique pulse as a function of SNR for various waveforms.

To validate the CLRB calculation, Monte-Carlo simulations have been computed with the chirp, the HFM function and different Parsons waveforms. The simulations were realised with 10^5 runs for varying SNR in the range $[0, 30]$ dB, where the Root-Mean-Square Error (RMSE) over the estimated delay was computed with the Matched Filter (MF). Figure 3.13 illustrates the results with the CLRB plotted as dashed lines and the RMSE for the different waveforms

as solid lines. For all the waveforms, the observed precision is close to their respective CLRB for SNR larger than 15dB. Moreover, the estimation capacities for the Parsons function are still verified and quite satisfying because the curvature of the function (parameter a) is linked to the accuracy in delay estimation. The Parsons function flexibility offers better or similar results compared to the HFM function at fixed temporal and frequency parameters and can compete with the chirp in terms of performances.

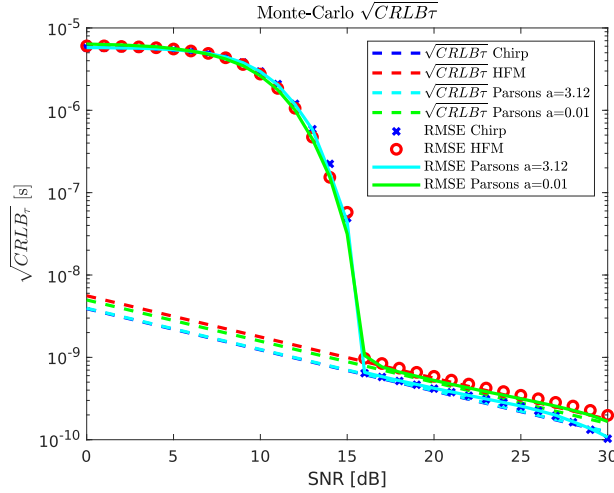


Figure 3.13: CLRB and RMSE for delay τ , for a single pulse and Monte-Carlo simulations results with different waveforms as function of the SNR.

The calculation of CLRB can be extended to the case of a pulse train. The calculations in [20] show that for a given Pulse Repetition Interval, T_r , and a train of N_p pulses, the matrix of the second derivatives of the squared amplitude of the ambiguity function can be written as

$$\mathbf{J}_{AF, N_p} = \begin{pmatrix} \frac{\partial^2 |\chi(\tau, \nu_d)|^2}{\partial \tau^2} & \frac{\partial^2 |\chi(\tau, \nu_d)|^2}{\partial \tau \partial \nu_d} \\ \frac{\partial^2 |\chi(\tau, \nu_d)|^2}{\partial \nu_d \partial \tau} & \frac{\partial^2 |\chi(\tau, \nu_d)|^2}{\partial \nu_d^2} - \frac{2}{3} \pi^2 T_r^2 (N_p^2 - 1) \end{pmatrix} \Bigg|_{\tau, \nu_d=0} \quad (33)$$

The CLRB over the delay τ are thus calculated and plotted in figure 3.14 along with the RMSE obtained with Monte-Carlo simulations. The results are quite similar to the uncoupled estimation seen before.

In order to complete the description, the Ziv-Zakai bound of the chirp is also plotted along with the A Priori and Sampling Bounds [24]. The A Priori bound represents an upper bound for low SNR equal to $\frac{T^2}{12}$ and it is linked to the fact that the peak output of the MF can be anywhere in the noisy signal response. The Sampling Bound indicates a lower bound established with respect to the sampling frequency $\frac{1}{12F_s^2}$. In this case $F_s = 2GHz$, in order to obtain a clear result at high SNRs. The Ziv-Zakai Bound is defined to provide a better representation of the

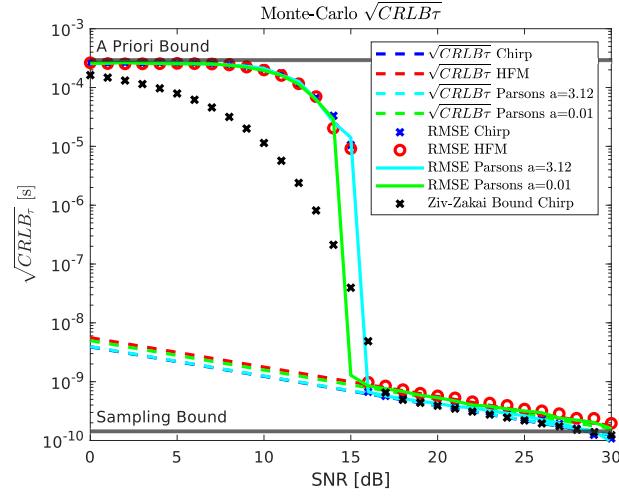


Figure 3.14: CLRB and RMSE for delay τ , for pulse train of various waveforms as function of the SNR ($T_r = 10T$, $N_p = 10$).

feasible precision at every SNR, by combining the behaviour of the A Priori upper bound at low SNR and the behaviour of the CLRB at high SNR [24].

With the CLRB, the radar capacities of the Parsons function in terms of estimation have been assessed and the results are quite satisfying, as the Parsons function have similar accuracy with the chirp, while its flexibility offers an advantage.

3.3 Real Data Experiments

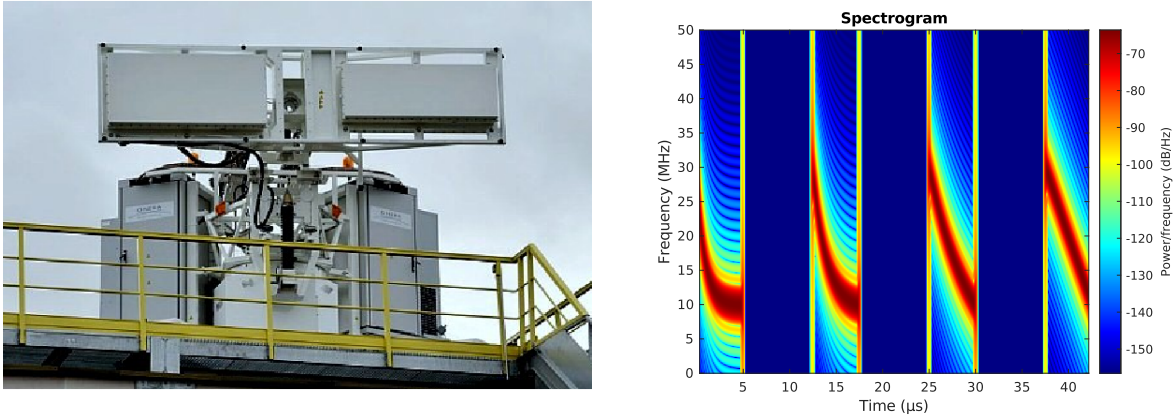
In this section, real tests with the Parsons function are analysed to complement the simulations. Thanks to the ONERA facilities and the radar HYCAM, it has been possible to emit Parsons waveforms with varying curvatures and to observe the real behaviour of the bio-inspired function.

3.3.1 Experiment Framework

To begin with, let's present HYCAM and the experiment parameters. HYCAM is a ground-based radar from the ONERA [25][26] that operates in the S-band (2 to 4 GHz). Figure 3.15(a) portrays HYCAM with its two antennas mounted on a turret, as it stands over the ONERA Palaiseau. Due to its geographical position and the rotating turret, its two antennas, a transmit antenna and a receive antenna, are able to track targets over a large region. This radar is employed in a variety of radar projects and serves as a robust testbed for the experimentation of novel radar concepts that require real data, as it is the case in this thesis.

In the present, HYCAM was used for the transmission of intertwined waveforms, as those

presented in figure 3.15(b). Three distinct Parsons functions with varying parameter a and a chirp are successively emitted in order to track the trajectory of aircrafts departing from Orly airport. Two sets of parameters summarised in the Table 3.2 were employed. Each waveform lasts $T = 5\mu\text{s}$ and is separated from the next waveform by an interpulse of $T_p = 50\mu\text{s}$. It follows that the same waveform is repeated every $T_r = 200\mu\text{s}$. The analysis of a set of data is presented to assess the real capacities of the Parsons waveform.



(a) HYCAM with its antennas in horizontal position <https://www.onera.fr/en/demr-research-units>. (b) Example of the waveforms transmitted with HYCAM ($B = 20\text{MHz}$).

Figure 3.15: Conditions of the real experiments. The interpulse in the right figure is not representative of the true parameter to ensure a better visualisation.

Parameters	Value
Bandwidth B	$[2, 20]\text{MHz}$
Sampling frequency F_s	$[5, 25]\text{MHz}$
Pulse duration T	$5\mu\text{s}$
Interpulse T_p	$50\mu\text{s}$
PRI T_r	$200\mu\text{s}$
Parsons parameter a	$[0.01, 0.1, 1]$

Table 3.2: Emission parameters.

3.3.2 Data Processing

The data analysed here concerned the tracking of an Airbus A-320 (HEX code 440128) departing from Orly airport on 31st May 2024. The plane trajectory, together with the position of HYCAM, is illustrated in figure 3.16. The aircraft was illuminated for a period of two minutes

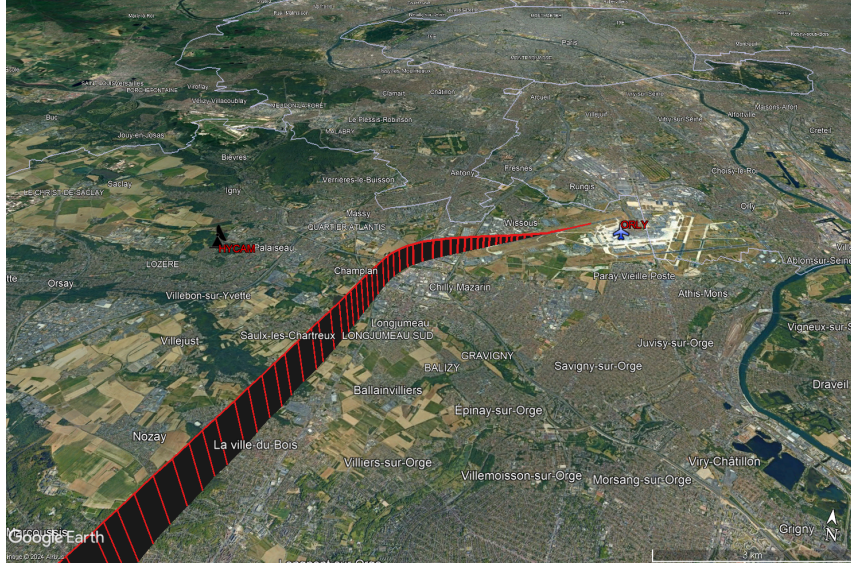


Figure 3.16: Trajectory of the Airbus A-320 (Hex code 440128) in red with the position of HYCAM and Orly. Image obtained with Google Earth Pro.

with the different waveforms having a bandwidth of $B = 20\text{MHz}$. This implies that at least 600,000 pulses were emitted for each waveform.

To correctly process the received data, two major parameters have to be considered. Firstly and because the waveforms are intertwined, the reception of a single specific waveform is only possible for a duration of $50\mu\text{s}$, which implies a range ambiguity of 7,5km. Secondly, the transmit and receive antennas are situated in close proximity to one another, which induces a coupling effect. In other words, the initial $T = 5\mu\text{s}$ of the reception period corresponds to the emitted signal and must be ignored. In order to ensure a good readability of the data, the first $10\mu\text{s}$ are ignored. The suppression of the polluting coupling results in a blind distance of 1,5km, which does not impede the study since the aircraft progresses at greater distances. In light of the aforementioned considerations, the received signals and their spectrum can be illustrated in figures 3.17(a) to 3.17(d). These figures display oscillograms of the received normalised amplitude and spectrum for one of the Parsons waveforms and the chirp. For comparison, the reference signal is also plotted particularly in regard to the obtained spectrum. The typical hyperbolic and rectangular behaviour of both waveforms are clearly distinguishable.

The signal processing that follows is the range compression followed by Doppler processing, which yields the Range-Doppler map described in the introductory chapter (section 2.1.3). This is conducted with either the matched filter (MF) or the mismatched filter (MMF). The parameters employed for the computation of the MMFs are $K_q = N = 1250$ samples and $\beta_q = 2\text{dB}$. An example of each output is illustrated in figures 3.18(a) and 3.18(b) for a Parsons waveform, with the target located at 6.1km. It is evident that the Range-Doppler maps exhibit high responses

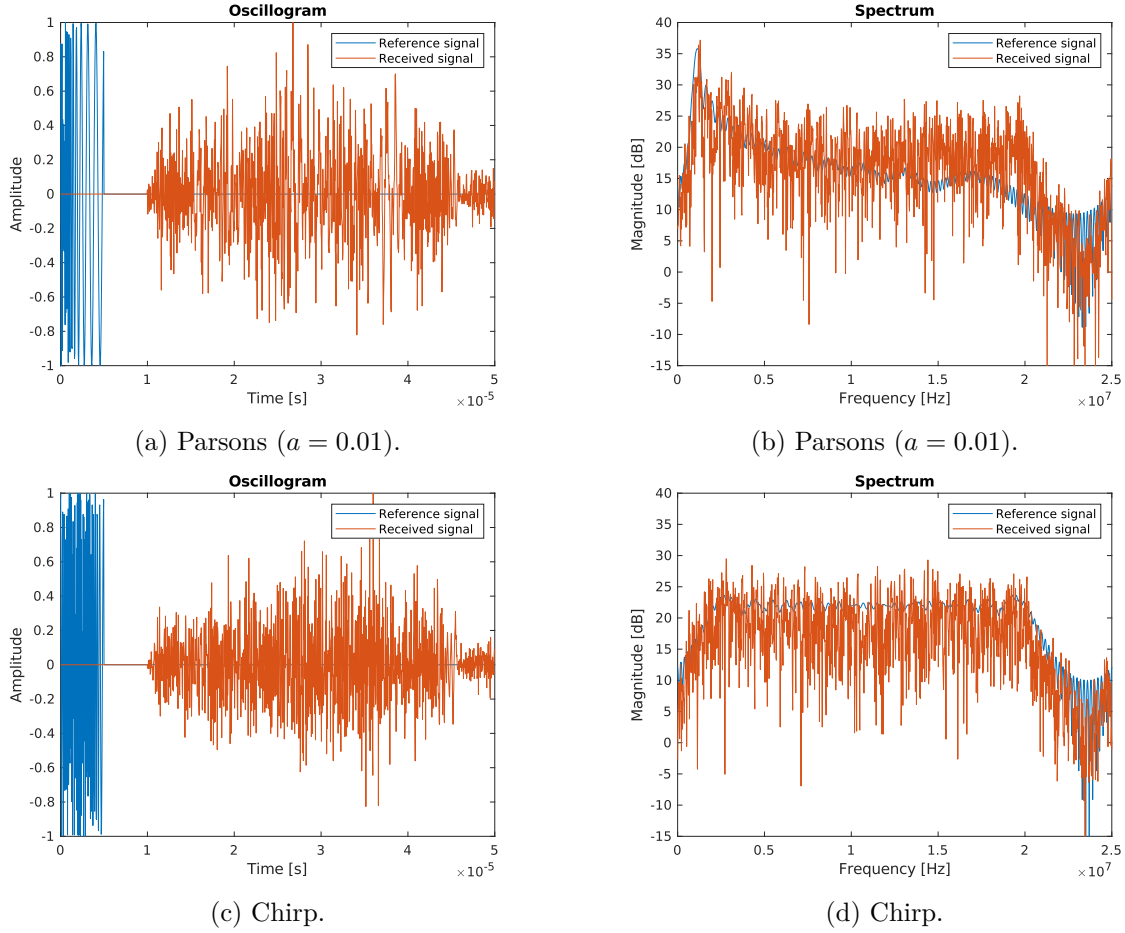


Figure 3.17: Received data for the Airbus A-320 with two of the emitted waveforms.

in the zero-Doppler region, which can be attributed to the environmental clutter. This responses linked to trees, buildings and even the rain can hinder the detection of the target. To enhance the readability of the Range-Doppler maps, an Extensive Cancellation Algorithm (ECA) [73] can be implemented. This performs a projection of the range-compressed data onto a subspace that is orthogonal to the disturbance subspace, which in this case is the Doppler region around the zero-Doppler. The problem can be written as

$$\hat{\Omega} = \arg \min_{\Omega} \|\mathbf{y} - \mathbf{X}\Omega\|^2, \quad (3.46)$$

where \mathbf{X} is a matrix of size $N_p \times N_{\nu_d}$ that combines the Doppler hypotheses to be rejected and the range compressed data are denoted \mathbf{y} . The values of N_p and N_{ν_d} correspond to the number of pulses and the number of rejected Doppler hypotheses, respectively. The solution of the problem

(3.46) is given by

$$\hat{\Omega} = (\mathbf{X}^H \mathbf{X})^{-1} \mathbf{X}^H \mathbf{y}. \quad (3.47)$$

Therefore, the range compressed data after clutter rejection can be expressed as

$$\mathbf{y}_{eca} = \mathbf{y} - \mathbf{X}(\mathbf{X}^H \mathbf{X})^{-1} \mathbf{X}^H \mathbf{y}. \quad (3.48)$$

Thanks to the ECA, the Range-Doppler maps presented in figures 3.19(a) and 3.19(b) are obtained. The target response is more clearly visualised, while the clutter has been effectively rejected. The sidelobes no longer spread in the Doppler axis compared to the figures 3.18(a) and 3.18(b).

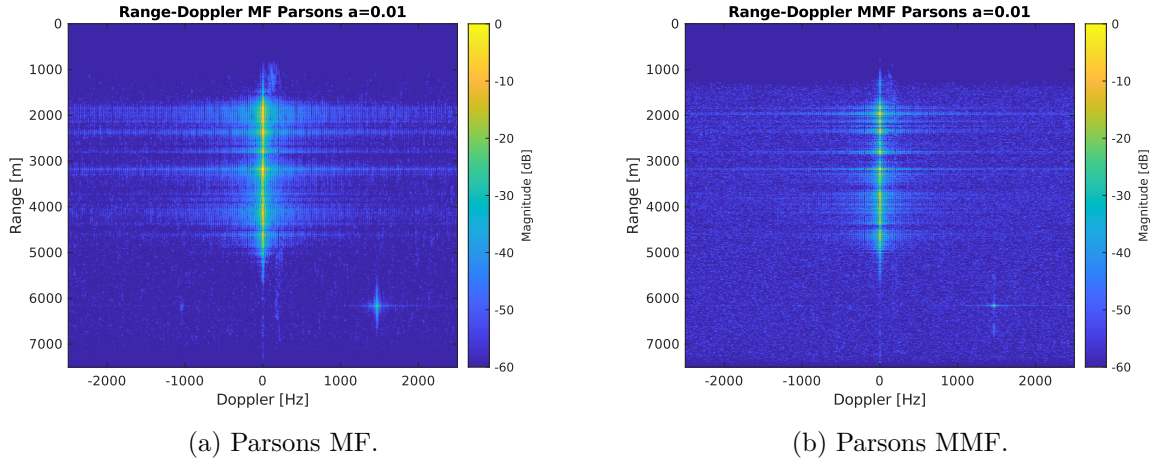


Figure 3.18: Range-Doppler maps of the aircraft for a Parsons waveform ($a = 0.01$).

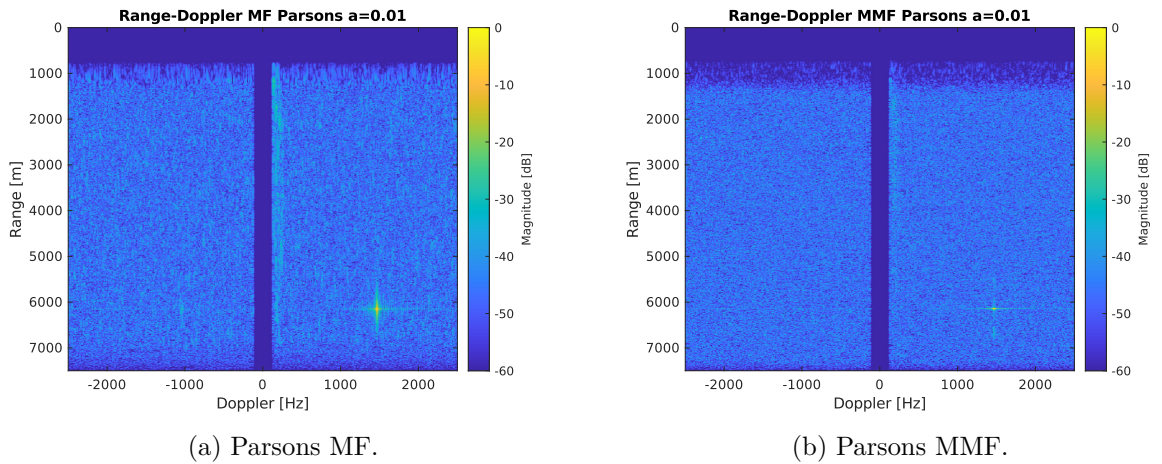


Figure 3.19: Range-Doppler maps of the aircraft for a Parsons waveform ($a = 0.01$) after clutter rejection.

3.3.3 Data Analysis

Now that the data have been processed correctly, the actual response of the Parsons waveform can be evaluated. Figures 3.20(a) to 3.20(d) illustrate the Range-Doppler maps obtained for each waveform with a zoom on the target of interest. As in the previous analysis, the response of the

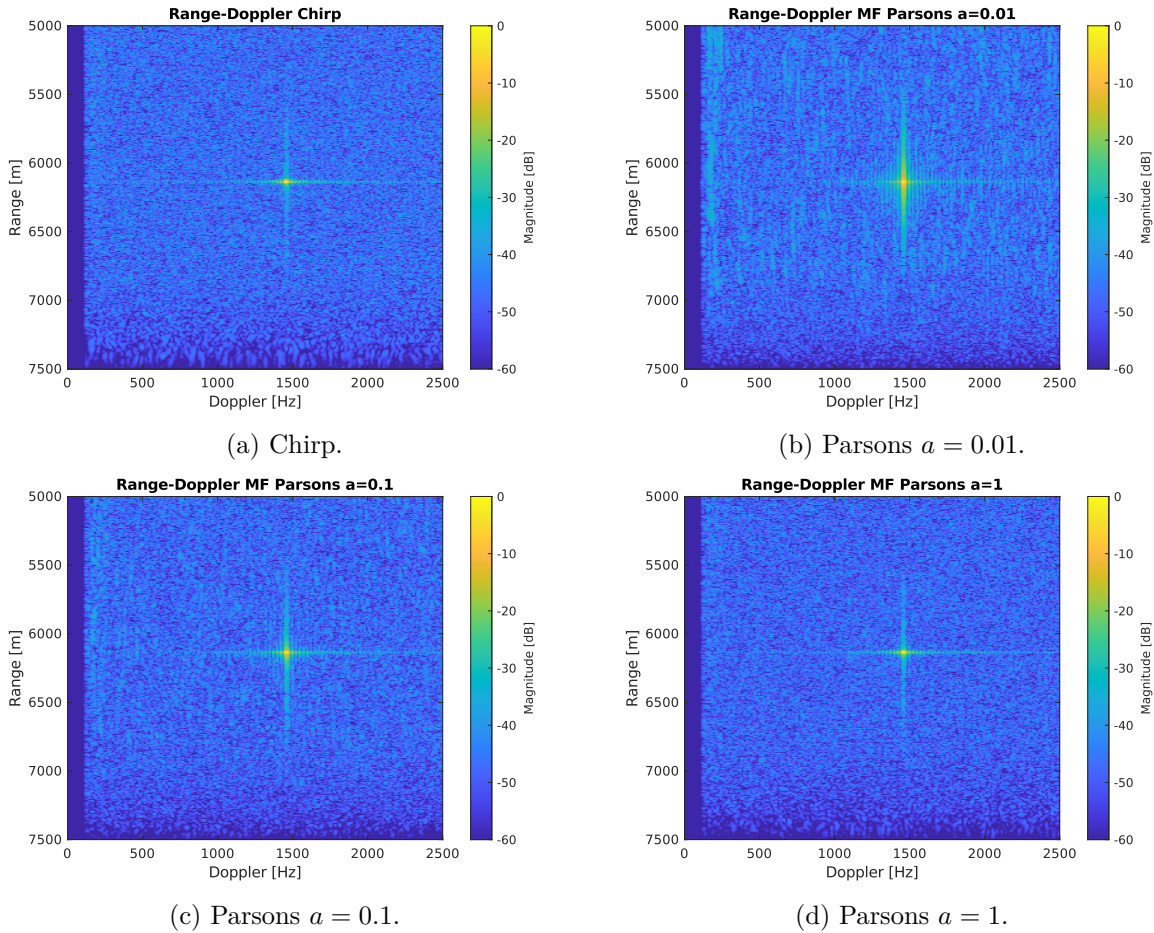


Figure 3.20: Range-Doppler maps of the aircraft for the different waveforms after clutter rejection.

Parsons waveform depends on the parameter a . A pronounced curvature induces a broadening of the mainlobe, as evidenced in figure 3.20(b). In fact, the target signature is more spread out along the range axis compared to the others. Nevertheless, the target is clearly detected with each of the waveforms. Regarding the sidelobes behaviour, the calculation of the MMF for each Parsons waveform yields the figures 3.21(a) to 3.21(c). The three new Range-Doppler maps related to the Parsons waveforms exhibit improved sidelobe levels and a target response close to that of a chirp. The corresponding range profiles are provided in figures 3.22(a), 3.22(b) and 3.22(c) with the chirp response plotted for comparison. Taking into account the different

figures and the results obtained, the behaviour of the Parsons waveform thus observed is in accordance with the simulations. The matched filter and the Range-Doppler processing outputs are both linked to the curvature of the waveform and the setting of the parameter a , but both can be improved with the MMF. Moreover, the capacity in terms of delay estimation given by the CLRB is also verified.

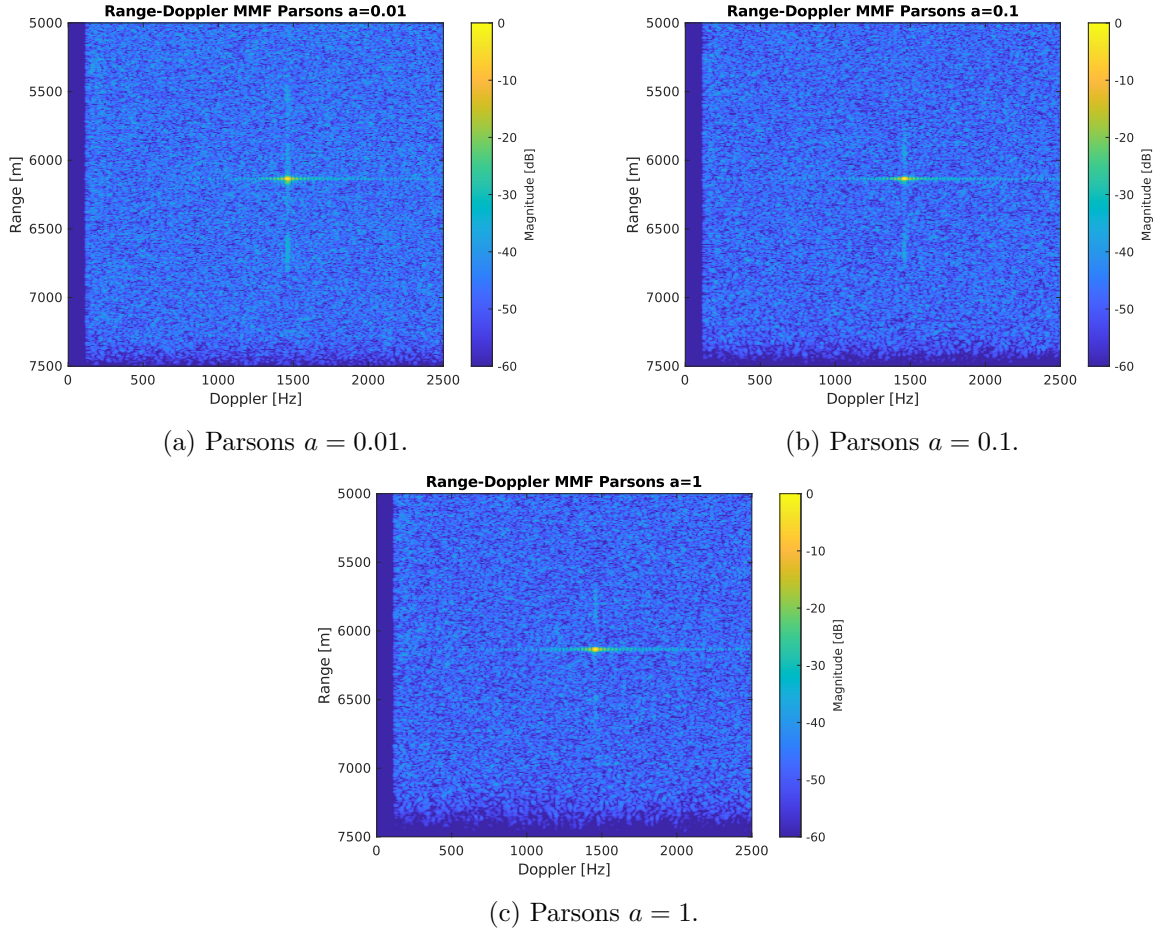


Figure 3.21: Range-Doppler maps of the aircraft computed with the MMF for the Parsons waveforms after clutter rejection.

An interesting result that can be observed when the plane is progressing, leaving the radar behind him, is the Doppler signature of one of its reactor. Illustrated in figure 3.23(a), there is a second peak observable in the negative Doppler values of the Doppler profile obtained at the estimated range of the target. This can also be distinguished in the Range-Doppler map in figure 3.23(b).

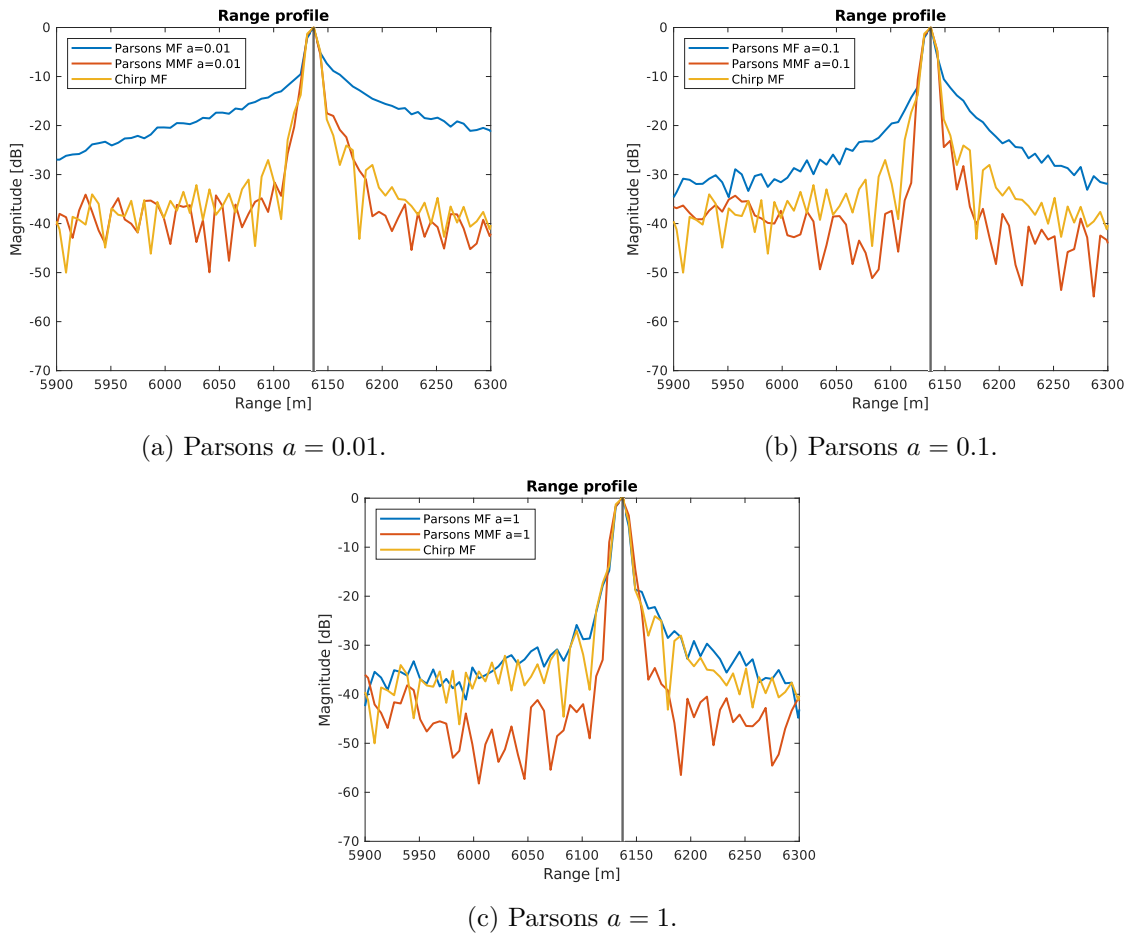


Figure 3.22: Range cut of the aircraft response for the Parsons waveforms.

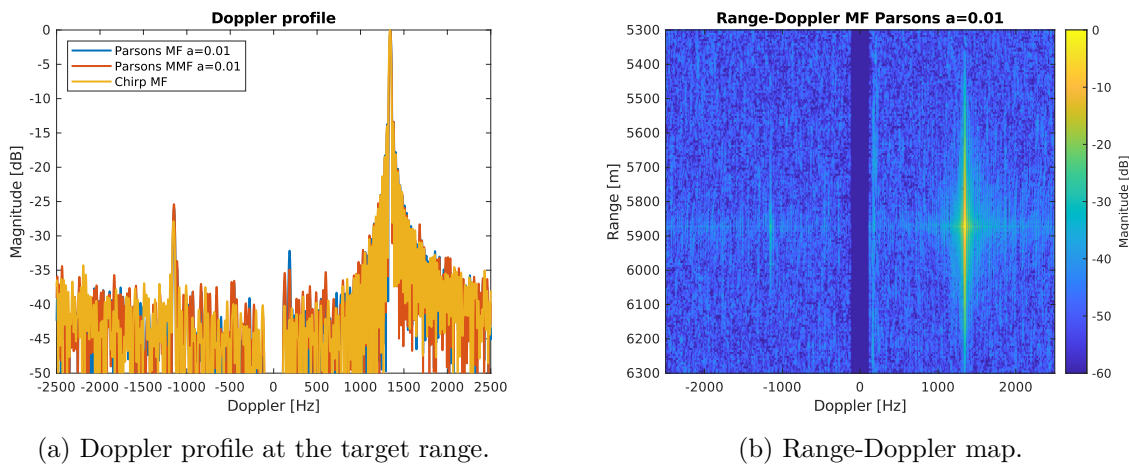


Figure 3.23: Observation of the response linked to the reactor of the aircraft.

3.4 Conclusion

In this chapter, the path to a bat-inspired radar began with an understanding of bat signal design, thanks to the study of authentic bat hunting sequences. This led to the introduction of a bio-inspired waveform capable of mimicking such signals: The Parsons waveform. This function approaches the flexibility observed in bat waveform design thanks to the parameter a , which drives the curvature of the instantaneous frequency sweep. Its radar capacities were then investigated and in comparisons with the chirp and the HFM, the Parsons waveform has nothing to envy to the classical radar waveforms. In fact, the bio-inspired function showed a valuable potential as a radar waveform with significant performances illustrated with the CLRB along with different simulations as well as real experiments using the classical radar processing techniques.

THE PARSONS WAVEFORM IN A RADAR FRAMEWORK

Now that the capacity to create our own bat-inspired signal is within our grasp, the plasticity of the Parsons waveform can be implemented in a concrete radar framework. This is precisely the aim of this chapter, which describes two cases of bio-inspired radar applications. The first one implements the bio-inspired waveform in order to address one of the main challenges for the radar community: the spectrum management. The application of the Parsons function in a multistatic framework is presented, accompanied by evidence asserting its efficiency in such a configuration. A second use of the Parsons waveform is then investigated, by combining it with a SCAT adapted to radar. The underlying objective is to estimate the Doppler shift at the reception in order to compensate it and correct the delay misestimation.

4.1 MultisBatic Application

4.1.1 The Multistatic Principle

The first chapter introduced how a single radar works (see chapter 2), but what if you consider several (two or more) radars operating, whether in a transmitting or receiving mode, within a shared area of coverage and separated by large distances when compared to the antenna sizes, as illustrated in figure 4.1? This defines a multistatic radar system according to the IEEE Standard Radar Definitions [74]. Compared to a monostatic configuration (co-located transmitter and receiver) or a bistatic configuration (transmitter and receiver separated by a distance), a multistatic radar system allows for the observation of targets from multiple different transmitter-receiver pairs [75]. These different point of views of a singular target facilitate enhanced target recognition. Another advantage with such a configuration is the improvement in terms of resolution and parameter estimation [75]. Nevertheless, in a multistatic layout, the received signal for each radar becomes more complex because it combines the response of the target to several transmitted signals. Consequently, interference mitigation represents a major challenge in the design of transmitted waveforms for a multistatic framework. The objective is to minimise the impact of one radar on another through a careful waveform design. In addition, the

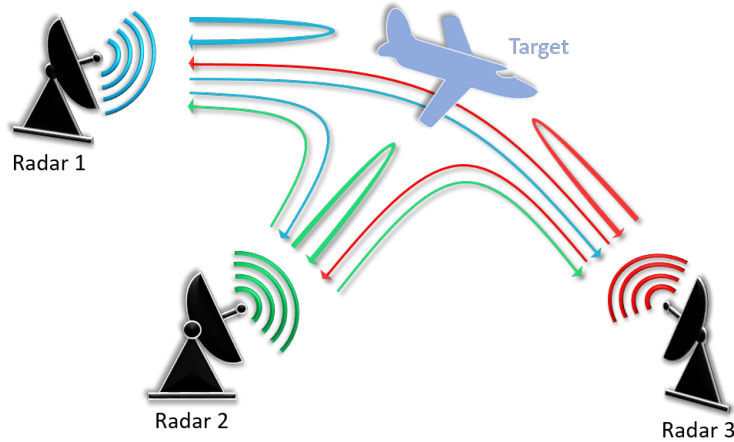


Figure 4.1: Scheme of a multistatic radar configuration. Each radar emits a distinct signal, which is then reflected back by the target in varying directions. Consequently, each arrow represents a back-scattered signal, which complicates the reception for each radar.

increasing spectral congestion, coupled with the necessity for enhanced or at least maintained capabilities, such as a finer resolution, drive the radar community to find innovative solutions in order to efficiently use the available spectral resources [3], and represent additional constraints for multistatic radar system design.

Waveform diversity is one of the study axis largely exploited in the past years to address the aforementioned issues [4]. In particular, the design of waveforms is of great interest for multistatic configuration and multi-beam radar systems. The primary objective in these cases is to identify radar waveforms with valuable autocorrelation properties, which allows the control of the sidelobe level. Additionally, it is essential to ensure good orthogonality between the different considered waveforms to allow multiple systems to operate simultaneously without mutual negative impact. Concerning the orthogonality requirement and the reduction of mutual interferences, a number of options are available, such as Time-Division Multiplexing (TDM), Frequency-Division Multiplexing (FDM) or Code-Division Multiplexing (CDM), each with its advantages and disadvantages [76]. FDM involves a multi-band functioning, which definitely does not address the issue of spectrum congestion. In TDM, each radar emits alternatively its own waveform, thus avoiding overlap between transmissions. As a consequence, the capabilities of the radar antennas are not fully used [76]. Regarding CDM, the Doppler intolerance is frequently highlighted and investigated [77][78]. A different approach is to use existing waveforms while widening the waveform diversity by adjusting temporal and frequency parameters. This axis is explored in [6], where the author evaluates the orthogonality and Doppler tolerance of different sets of Piecewise Linear Frequency Modulated (PLFM) waveforms.

In order to pursue the biomimicry track and in light of its demonstrated value as a radar

waveform, the Parsons waveform and its flexibility could potentially benefit a multistatic configuration. In particular, the aim of this section is to transmit several signals within the same frequency band, while maintaining satisfying radar performance. The performance of systems transmitting the proposed waveform or different chirp-based waveforms is assessed by measuring the isolation level to assure the orthogonality between waveforms, Doppler tolerance and sidelobe levels. Afterwards, improvements in the sidelobe levels of the considered waveforms are discussed with the application of the mismatched filter and its influence on the isolation properties and Doppler tolerance.

4.1.2 A Simulated Multistatic Environment

To evaluate the efficacy of the Parsons function in a multistatic environment, its use in conjunction with different chirp modulations is observed. The considered chirps are issued from [6], where the author compared several sets of PLFM waveforms triplets, or in other words, combinations of LFM subchirps. The objective was to incorporate at least two Parsons waveforms to enhanced the waveform diversity, and therefore the number of available transmitters, while maintaining the radar performance. The studied configuration corresponds to the first set presented in [6], where an up-chirp, a down-chirp and a combination of up- and down-chirp were confronted. All the waveforms share the same pulse duration, $T = 50\mu\text{s}$, and the same bandwidth, $B = 100\text{MHz}$, which results in a constant time-bandwidth product of $BT = 5000$. The sampling frequency is set to $F_s = 300\text{MHz}$. Note that the starting frequency, f_0 , is 110MHz . Figure 4.2 illustrates the frequency evolution for the up-down-chirp, up-chirp, down-chirp, Parsons down- and up-sweep, which are often designated respectively by the following symbols \wedge , \nearrow , \searrow , \smile and \frown in the remainder of this section for ease of reading.

The Parsons function appears as a promising candidate for such a configuration, as it combines the hyperbolic modulation properties [20] with a greater flexibility. A visible benefit for a multistatic configuration, is the existence of several different Parsons waveforms within the same bandwidth and duration thanks to the parameter a . This offers a certain degree of adaptability to a variety of configurations. However, the known disadvantages discussed in the chapter 3 of such a frequency modulation are the relatively high sidelobe levels linked to the curvature of the instantaneous frequency and a lower Doppler tolerance in narrowband processing compared to a linear modulation (chirp) [20]. The implementation of the Parsons function should not be detrimental to the radar capabilities by causing the masking of low-energy targets or misestimation of target range due to Doppler shifts. In order to optimise the response of the bio-inspired waveform, the mismatched filter presented in chapter 2 could be a potential solution to mitigate the sidelobe level and improve target detection.

The following study thus consists of evaluating the isolation between the different waveform pairs, the Doppler tolerance of the Parsons function and the effect of the mismatched filter on

the sidelobe level but also regarding the isolation.

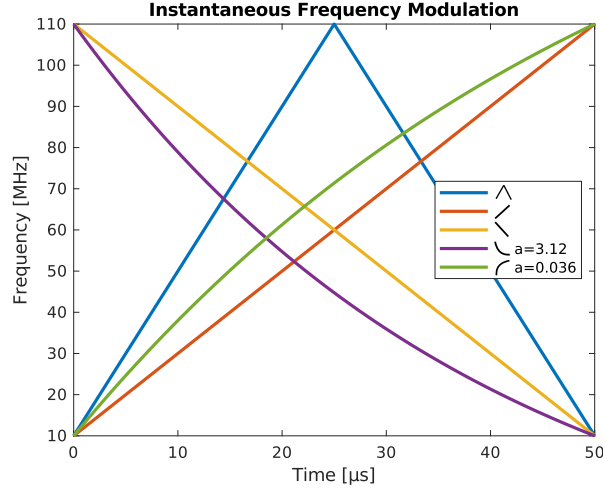


Figure 4.2: The simulated multistatic environment through the instantaneous frequencies of the considered waveforms ($B = 100\text{MHz}$, $T = 50\mu\text{s}$) [79].

4.1.3 Radar Processing and Evaluation

Mismatched Filter Parameters

The MMF has already been described in the introductory chapter (see section 2.1.3), but let us recall that the optimisation problem under study writes

$$\begin{aligned}
 & \min_{\mathbf{q}} \|\mathbf{F}\mathbf{y}\|_2^2, \\
 & s.t. \mathbf{s}^H \mathbf{q} = \mathbf{s}^H \mathbf{s}, \\
 & \mathbf{q}^H \mathbf{q} \leq 10^{\frac{\beta_q}{10}} \mathbf{s}^H \mathbf{s}.
 \end{aligned} \tag{4.1}$$

The parameters of the problem are set as follows: the filter length is $K_q = N$ (where N is the length of the signal) and the Loss-in-Processing Gain (LPG) is fixed to $\beta_q = 2\text{dB}$. Regarding the filter length, it has been demonstrated that selecting $K_q > 3N$ does not necessarily improve the performance and is linked to increased computational time [80].

The MMF problem stated in (4.1) is convex and can be solved efficiently with the adapted software such as the CVX toolbox, a Matlab package [81]. Because the optimisation procedure is iterative, the computation can become costly for increasing problem size [19]. Even though the computation can be done offline, an algorithm based on a primal-dual approach [5] is used to calculate the MMFs in order to improve the computational time, when optimising the ISL criterion. For instance, for $N = 1501$ samples, computation takes in average a few seconds,

whereas a conventional convex solver like the CVX toolbox, can take up to 45 minutes to provide the same results.

Performance Metrics

Since the beginning of this section, the terms orthogonality and isolation have been mentioned and may require a brief explanation. When working in a multistatic environment with multiple transmissions in a shared bandwidth, orthogonality or quasi-orthogonality among waveforms is strongly advised. The principle of orthogonality between two waveforms indicates how much they correlate with each other. Let us consider the cross-correlation function of two signals s_i and s_j

$$\chi_{i,j}(\tau, \nu_d) = \int s_i^*(t) s_j(t + \tau) e^{2i\pi\nu_d t} dt. \quad (4.2)$$

The isolation $I_{i,j}$ between s_i and s_j is defined as the ratio between the peak of the amplitude of the autocorrelation function and the cross-ambiguity function [6]

$$I_{i,j}(\tau, \nu_d) = \left| \frac{\chi_{i,i}(0, 0)}{\chi_{i,j}(\tau, \nu_d)} \right| = \left| \frac{\chi_{j,j}(0, 0)}{\chi_{j,i}(-\tau, \nu_d)} \right|. \quad (4.3)$$

The minimum isolation level is then

$$I_{min_{i,j}} = \frac{|\chi_{i,i}(0, 0)|}{\max_{\tau, \nu_d} |\chi_{i,j}(\tau, \nu_d)|}. \quad (4.4)$$

This level provides an insight on how an echo from a target illuminated by a transmitter j will interfere with another transmitter i . The lower the isolation level is, the closer to orthogonality the waveforms are. The figure 4.3(a) plots the auto-correlation of the up-chirp and the figure 4.3(b), its cross-correlation with the down-chirp. In this configuration the isolation level is $I_{min} = 37.44\text{dB}$.

Another useful metric when considering targets with a certain velocity is the filter mismatch loss due to the Doppler shift, which can be evaluated as [6]

$$M_i(\nu_d) = \frac{\max_{\tau} |\chi_{i,i}(\tau, \nu_d)|}{|\chi_{i,i}(0, 0)|}. \quad (4.5)$$

This feature measures the loss in decibels that can be observed in the output of the MF or the MMF. It is generally degraded when considering orthogonal waveforms obtained with phase coding and constant for the chirp.

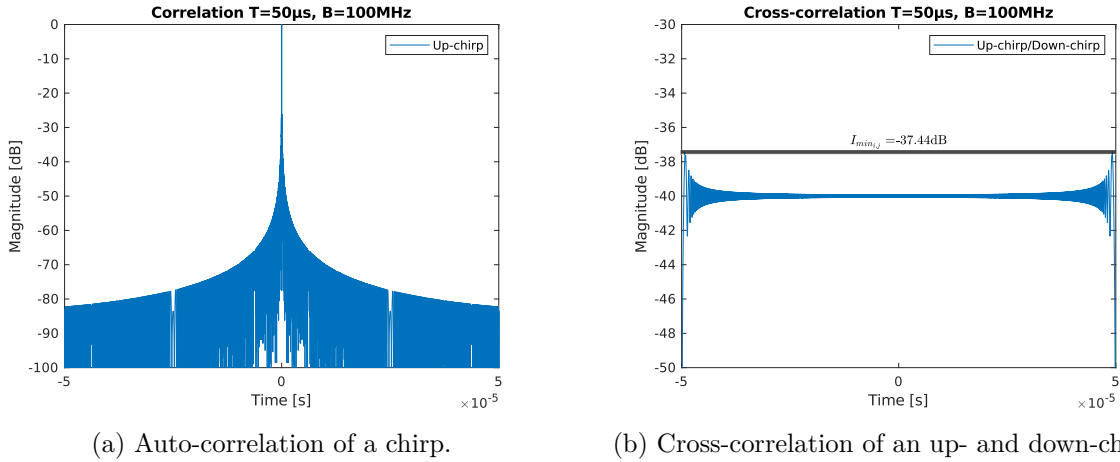


Figure 4.3: Auto-correlation (left) and cross-correlation of up- and down-chirps ($T = 50\mu\text{s}$, $B = 100\text{MHz}$). Here, isolation corresponds to the maximum cross-correlation.

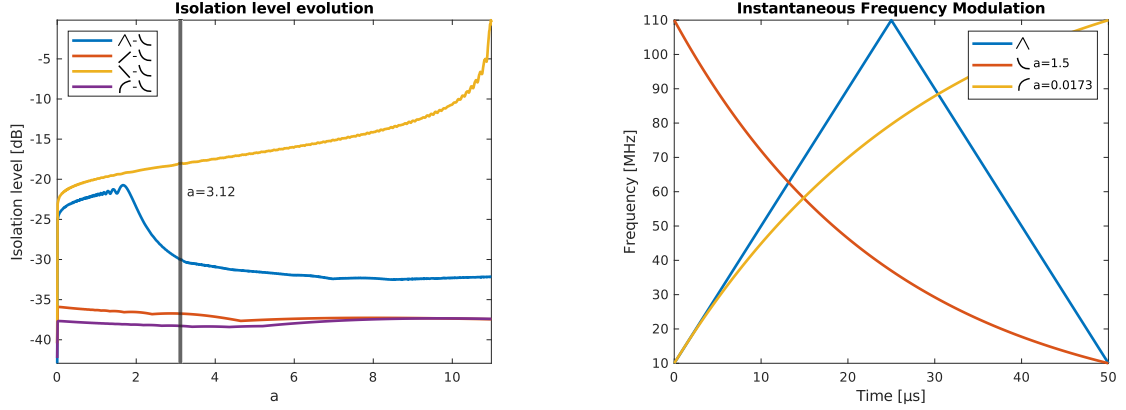
4.1.4 Simulation Results

The Isolation Level

To begin with, the orthogonality of the set of waveforms presented in figure 4.2 is evaluated through the isolation level of each pair of waveforms. With regard to the Parsons function, notice in Figure 4.2 that the parameters a shown for both the up- and down-sweep have been set to optimise the isolation level with respect to the other functions. Parameters are selected to favour the isolation between both Parsons waveforms and the up-down-chirp pairs with a desired isolation level close to 30dB and the objective not to reduce the isolation between Parsons and chirp waveforms with slopes of the same sign too much.

Figure 4.4(a) illustrates the process for selecting the parameters a , with the isolation level plotted as a function of the parameter a for the different waveforms cross-correlated with the Parsons down-sweep. This figure shows that the pairs $\setminus\setminus$ and $\wedge\setminus$ are more critically impacted by the choice of a . Indeed, the closer a gets to the ratio $\frac{f_0}{f_1} = 11$, the closer the Parsons down-sweep is to a down-chirp. Consequently, the degree of isolation level decreases as the two waveforms become increasingly correlated. Concerning the $\wedge\setminus$ pair, the behaviour of the Parsons waveform implies a more subtle response. When a is low, which implies a pronounced curvature, the initial portion of the Parsons down-sweep correlates more with the initial part of the down-chirp component because the two waveforms share a number of intersection points in the time-frequency-space. The phenomenon is illustrated in figure 4.4(b). For a visual representation, the aforementioned intersection points are illustrated with the Parsons up-sweep and the up-chirp component of the up-down chirp signal as the problem is symmetric. It is then visible that the portion until $10\mu\text{s}$ will correlate in this case. As the Parsons waveform approaches a chirp, the

whole signal becomes more linear and correlates less with this portion of the up-down chirp as the number of intersection points decreases. The explanations presented in this paragraph can also be applied to the Parsons up-sweep as the results are analogous.



(a) Isolation level as function of a between the Parsons down-sweep and other waveforms [79]. (b) Instantaneous frequencies of Parsons waveform and the up-down-chirp.

Figure 4.4: (a) Evolution of the isolation level between a Parsons function and other chirp-based waveforms ($B = 100\text{MHz}$, $T = 50\mu\text{s}$). (b) Illustration of the cross-correlation behaviour of $\wedge - \searrow$ and $\wedge - \swarrow$ pairs.

Table 4.1 provides a summary of the isolation levels $I_{i,j}$ obtained with each pair of waveforms (s_i, s_j) . A result given in [82] and verified in [6] showed that the isolation level improves with the time-bandwidth product BT but also that up- and down-chirps exhibited the best isolation performance. The second assertion remains true for the Parsons up- and down-sweep, as the isolation between them is 38.27dB, but is also preserved for Parsons and chirp waveforms with opposed slopes, their isolation values being of 36.74dB and 37.4dB. Figure 4.5(a) shows the cross-correlations output for the Parsons down-sweep. Signals with opposite frequency rates exhibit a relatively flat cross-correlation, hence a higher isolation level. It is then observable that the highest cross-correlation values, i.e. the lowest isolation levels, are effectively due to the down-chirp portion (for the blue curve) or the entire signal (yellow curve) sweeping with a decreasing rate, similar to the Parsons down-sweep.

Obviously, Parsons and chirp waveforms sweeping in the same way exhibit lower isolation levels, which could be improved ($> 20\text{dB}$) by considering a higher time-bandwidth [82]. This is supported by the figure 4.5(b), which depicts the evolution of the isolation level of this two pairs of waveforms as a function of the parameter a and the time-bandwidth product BT . In Figure 4.5(b), the pulse duration T is varied from $10\mu\text{s}$ to $100\mu\text{s}$ with a fixed bandwidth of $B = 100\text{MHz}$, which gives a BT varying between 10^3 and 10^4 . The pair $\searrow - \searrow$ in particular shows a strong link with the time-bandwidth product for relatively low values of a . Note that the light blue and yellow lines in Figure 4.4(a) can be extracted from the top and bottom

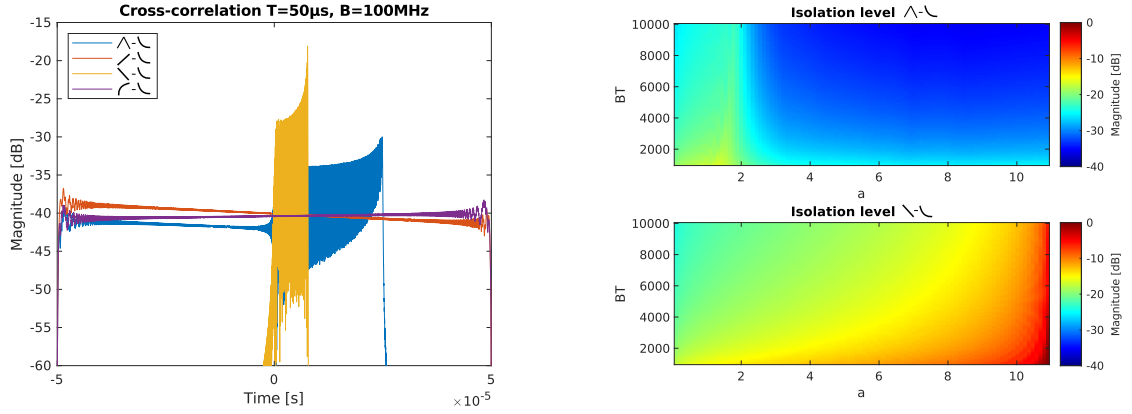
s_i	s_j	$I_{i,j}$ [dB]	$I_{q_i,j}$ [dB]	I_{i,q_j} [dB]
\wedge	\swarrow	32.13	30.09	33.02
\wedge	\searrow	32.13	30.09	33.02
\wedge	\smile	30	29.45	30.90
\wedge	\frown	29.96	25.01	31.73
\swarrow	\searrow	37.44	37.79	37.79
\swarrow	\smile	36.74	38.21	37.21
\swarrow	\frown	17.19	15.95	15.94
\searrow	\smile	18.09	17.05	17.03
\searrow	\frown	37.4	38.05	37.66
\smile	\frown	38.27	37.22	37.67

Table 4.1: Isolation levels for different pair of waveforms. The third column represents the isolation level between a pair (s_i, s_j) . The fourth and fifth columns account respectively for the isolation level between the pair (q_i, s_j) and (s_i, q_j) , where q_i and q_j are the MMF of the corresponding waveform [79].

surfaces respectively for $BT = 5000$. Overall, the isolation level investigation is encouraging and the Parsons function exhibits valuable orthogonality properties regarding chirp waveforms, thus confirming its application as an additional option for waveform diversity.

The MMF and its Contributions

The hyperbolic behaviour of the Parsons function leads to high sidelobe levels, as illustrated earlier in Figure 3.7. Therefore, the use of the MMF could be of interest, should the orthogonality be sufficiently preserved. The isolation levels obtained using the MMF, calculated for each waveform, are provided in Table 4.1. The fourth column indicates the isolation level, $I_{q_i,j}$, between the MMF of one waveform, q_i , and a second waveform, s_j ($j \neq i$), whereas the fifth column indicates the isolation level, I_{i,q_j} , between the first waveform, s_i , and the MMF of the second waveform, q_j . The variations of isolation levels between the first and the two other columns can be attributed to the redistribution of energy within the spectrum of the computed MMFs. Figures 4.6(a) and 4.6(b) depict the spectrum of the waveforms used in this investigation and of their MMFs spectra respectively. It is then noticeable that the energy distribution of each waveform has been modified, which may influence the cross-correlations. This will have a negligible impact on the isolation level of waveforms with opposite frequency rates as confirmed by the values given in Table 4.1. In contrast, it can also increase the energy coupling in the time-frequency domain like for the pair $\wedge - \frown$, where approximately 5dB are lost with the MMF of the up-down chirp. Indeed, the spectrum of this MMF is close to the one of the Parsons up-sweep. It

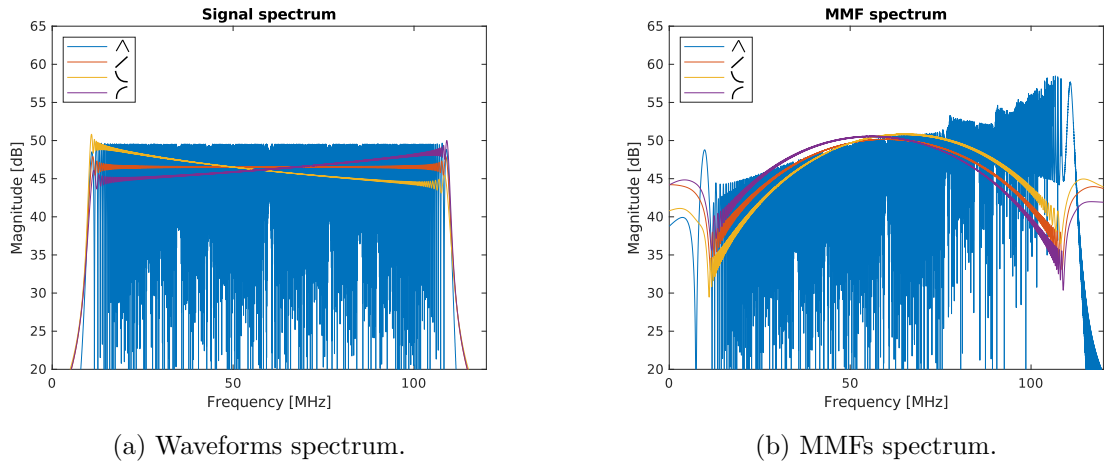


(a) Cross-correlation output for the Parsons down-sweep with different waveforms.

(b) Isolation level as function of BT and a [79].

Figure 4.5: (a) Isolation levels summarised in Table 4.1 for the Parsons down-sweep. (b) Isolation level for two pair of waveforms $\wedge - \setminus$ and $\setminus - \setminus$ for varying BT and a ($B = 100\text{MHz}$, $T \in [10; 100]\mu\text{s}$, $a \in [0; 11]$).

may be important to consider these results when computing the MMF of a waveform. However, the results are encouraging as the variations between $I_{i,j}$ and $I_{q_i,j}$ or I_{i,q_j} are on average only 1dB. This indicates that the MMF manages to preserve the orthogonality of the set.



(a) Waveforms spectrum.

(b) MMFs spectrum.

Figure 4.6: Comparison between the spectrum of the investigated waveforms and the spectrum of their MMFs.

The primary objective of the MMF, namely the sidelobe level reduction, is then to be investigated. Table 4.2 gives the ISLR and PSLR values obtained with the matched and mismatched filters for each waveform. These results demonstrate that for the Parsons function, the MMF yields promising results at a level quite similar to that obtained for the chirp. Figure 4.7 il-

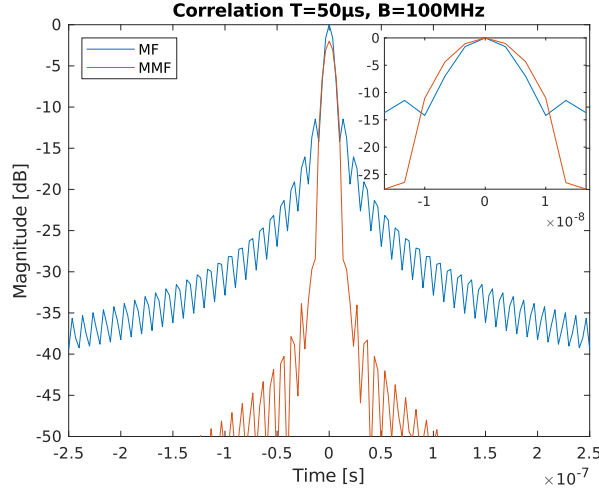


Figure 4.7: Outputs of the Matched Filter and Mismatched Filter minimising the ISL criterion for the Parsons down-sweep ($a = 3.12$). A zoom on the mainlobe illustrates the widening of the mainlobe operated with the MMF (LPG compensated) [79].

illustrates these improvements for the Parsons down-sweep with a zoom on the mainlobe. The LPG is compensated in the zoom to better appreciate the difference in width. The resolution degradation is by a factor of 1.3 measured 3dB below the mainlobe peak.

\mathbf{s}_i	ISLR $_i$ [dB]	ISLR $_{q_0}$ [dB]	PSLR $_i$ [dB]	PSLR $_{q_0}$ [dB]
\wedge	-1.84	-3.61	-13.7	-21.52
\nearrow	-9.7	-13.02	-13.7	-32.21
\searrow	-9.7	-13.02	-13.7	-32.21
\smile	-6.54	-13.01	-11.45	-31.88
\frown	-7.34	-13.02	-12.32	-32.01

Table 4.2: ISLRs and PSLRs calculated from the MF and MMF outputs of the different waveforms [79].

The possibility of designing the MMF to optimise both autocorrelation and cross-correlation properties has been studied but the performance were not sufficient compared to the optimisation of the autocorrelation alone. In fact, this result has been documented in [19] for mismatched filters applied to MIMO radar. If two signals, s_i and s_j , are considered, the problem (4.1) could be written as follows:

$$\begin{aligned}
 & \min_{\mathbf{q}} \|\mathbf{F}\mathbf{y}_{i,i}\|_2^2 + \|\mathbf{I}\mathbf{y}_{i,j}\|_2^2, \\
 & s.t. \mathbf{s}_i^H \mathbf{q} = \mathbf{s}_i^H \mathbf{s}_i, \\
 & \mathbf{q}^H \mathbf{q} \leq 10^{\frac{\beta_q}{10}} \mathbf{s}_i^H \mathbf{s}_i,
 \end{aligned} \tag{4.6}$$

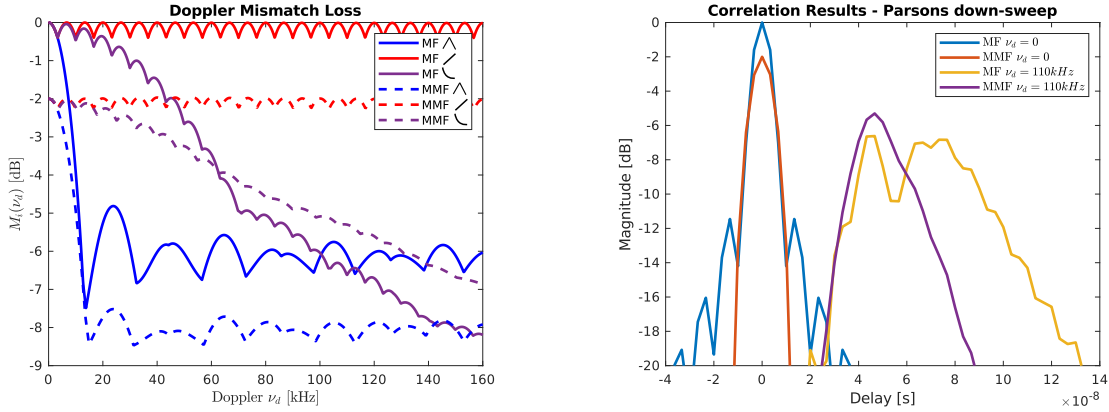
where $\mathbf{y}_{i,j} = \mathbf{\Lambda}_q^*(\mathbf{s}_j)\mathbf{q}$ and \mathbf{I} is the identity matrix. The PSLRs obtained from this optimisation problem are considerably lower than those achieved through a simple optimisation (4.1). For instance, optimising the MMF for an up-chirp and its cross-correlation with the Parsons up-sweep yields a PSLR = 21.49dB, which is a loss of 10.72dB compared to the PSLR in Table 4.2. Moreover, the gain in isolation is only of 1.48dB. This has been verified for all the possible waveform pairs shown in this set, and would be an unsuitable approach in any case.

The Doppler Tolerance

The next objective of the study is to examine the influence of the Doppler effect on the Parsons function. The linear chirp is appreciated for its Doppler tolerance at narrowband frequencies, whereas the hyperbolic chirp is less tolerant [20]. Figure 4.8(a) shows the Doppler mismatch loss experienced by the up-down chirp, the up-chirp and the Parsons down-sweep ($\wedge, /, \searrow$) for Doppler varying from 0 to 160kHz (only positive Doppler values are plotted, but the behaviour is symmetrical). The solid lines correspond to the outputs of the MF and the dashed lines correspond to the outputs of the MMF. With regard to the chirp waveforms, the Doppler mismatch loss has already been documented in [6] but it is visible that with the MMF, apart from the 2dB LPG, the behaviour remains globally similar and the mismatch loss is still valuable. For the Parsons function, the MMF can mitigate the Doppler mismatch effect at high Doppler. This is due to the narrowing of the mainlobe achieved by the mismatched filter, as can be seen in Figure 4.8(b). Moreover, the mismatch loss observed for both the MF and MMF of the Parsons down-sweep are better than the mismatch loss obtained with \wedge for a large range of Doppler. Note that the Parsons up-sweep ($a = 0.036$) gives similar results. The ripple effect discernible in figure 4.8(a) for each mismatch loss is attributable to the sampling frequency. As the Doppler induces a delay shift in the correlation output, the maximum is likewise shifted and may fall between two sampling points.

4.1.5 Discussion

The above observations demonstrate the potential of bio-inspired waveforms for radar applications and in particular for multistatic configurations. The orthogonality between the Parsons function and other waveforms has been validated through significant isolation level. Although the Parsons function is a hyperbolic-like modulation and therefore less Doppler tolerant than the usual chirp, it offers a control of its tolerance and isolation level thanks to the parameter a . It is thus more flexible than the classic HFM function, especially in a fixed bandwidth configuration, and has valuable capabilities, comparable to those of the chirp. The implementation of the MMF has once again demonstrated its value for the Parsons waveform. It reduces the sidelobe level, hence increasing the target detection, while maintaining the orthogonality of the evaluated waveforms set. On the Doppler side, compared to the up-down chirp, the Parsons



(a) Doppler Mismatch Loss for different waveforms as function of Doppler.

(b) MFs and MMFs outputs for a Parsons down-sweep ($a = 3.12$) in different Doppler configurations.

Figure 4.8: Doppler mismatch loss results with different waveforms of the set. The Parsons up-sweep and the down-chirp (\swarrow and \nwarrow) are not represented but the results are similar to that of their inverted versions [79].

waveform still demonstrated a much higher resilience to Doppler mismatch loss. Moreover, the MMF may help mitigating this loss on certain range of Doppler. The difficulty when facing Doppler with a hyperbolic-like function such as the Parsons function (or the HFM) is to handle the Continuous Frequency (CF) component as stated in Chapter III. In fact, a hyperbolic-like function can be seen as the sum of a Frequency Modulated (FM) component and a CF second part. The latter is more predominant as the curvature of the frequency modulation increases, masking the FM response and thus affecting the output of the MF or the MMF. This effect was discussed in [59] and it was shown that a filter bank model like the Spectrogram Correlation And Transformation receiver (SCAT) [27] could be more robust to this CF component.

4.2 Doppler Estimation

In addition to the classical radar processing techniques employed thus far, is it possible that the combination of a waveform and a processing method both bio-inspired may offer new perspectives for radar? The idea here is to combine the Parsons waveform with a bio-inspired processing approach for a Doppler estimation application. Still related to bat, the SCAT (Spectrogram Correlation and Transformation receiver) [27] can take advantage of the hyperbolic behaviour of the Parsons function to estimate the Doppler of a target, thereby correcting range misestimation. This section presents an exploratory work based on this hypothesis, together with simulations to support the discussion.

4.2.1 The Concept

The SCAT, a computational model of the bat auditory system, and the ability of bats to estimate Doppler were introduced in the first chapter (sections 2.2.3 and 2.2.3). In particular, it is known that bats using constant frequency signals are able to sense the Doppler shift induced by their flight and the fluttering targets. Concerning the Parsons function, it has been shown that the curvature emphasises the effect of the constant frequency portion of the signal. Driven by the parameter a , a strong curvature produces QCF signals where the quasi-constant frequency portion of the signal hinders the MF output. Instead of relying only on the delay estimation, mostly linked to the frequency modulated part of the waveform, the Parsons waveform may be of interest for Doppler estimation. In the same way that FM bats, such as the common noctule, use QCF search signals to detect and estimate the Doppler of a potential target [18], the Parsons function may offer the same capabilities for radar. Using the cochlear block of the SCAT, the sensitivity around the constant frequency component in strongly hyperbolic Parsons waveform could be useful for evaluating the Doppler of targets. This can help discriminate between target and clutter and correct for the misestimation of delay.

As a reminder, the cochlear block of the SCAT mimics the cochlea (hence the name) thanks to a bank of M parallel band-pass filters with centre frequencies f_i , $i = 0, \dots, M - 1$ and bandwidth B_i usually arranged in a linear or hyperbolic scale. For this study, $M = 2001$ Butterworth filters are considered each with a bandwidth of $B_i = 1MHz$. The filters are hyperbolically spaced between 10 and 110MHz, which means that the centre periods of the filters are linearly spaced. Figure 4.9(a) represents the obtained filter bank, where the hyperbolic spacing of the filters can be observed. The output of the cochlear block is similar to that of a spectrogram as outlined in figure 4.9(b). The SCAT is often computed for its ranging performances and its ability to resolve close targets [27][55]. A radar version has even been documented in [10], nevertheless, the Doppler information is not often investigated. In response, the fine frequency segmentation offered by the hyperbolic spacing in the cochlear filter bank could be used as an advantage, since

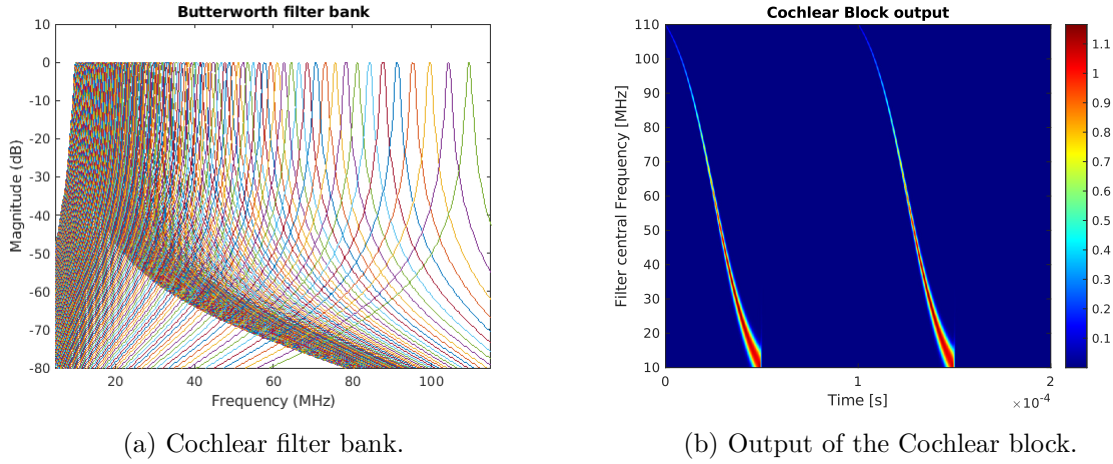


Figure 4.9: Illustration of the hyperbolically arranged filters in the cochlear block (one tenth of the filters are represented for clarity). The output of the cochlear block is given for a Parsons waveform ($B = 100\text{MHz}$, $T = 50\mu\text{s}$ and $a = 0.1$) and its echo delayed by $\tau = 50\mu\text{s}$.

the frequency region related to the CF component should be more sensitive to Doppler. The spectrum obtained with the cochlear block can be observed in figure 4.10(a) and compared with the classic spectrum obtained with a fast Fourier transform in figure 4.10(b). In both cases, the maximum energy is obtained around the end frequency, which thus appears to be more sensitive to the Doppler shift. The hyperbolic behaviour typical of the Parsons waveform is preserved within the cochlear block and the resulting spectrum. Moreover, such an observation would not be possible with the flat spectrum of a chirp.

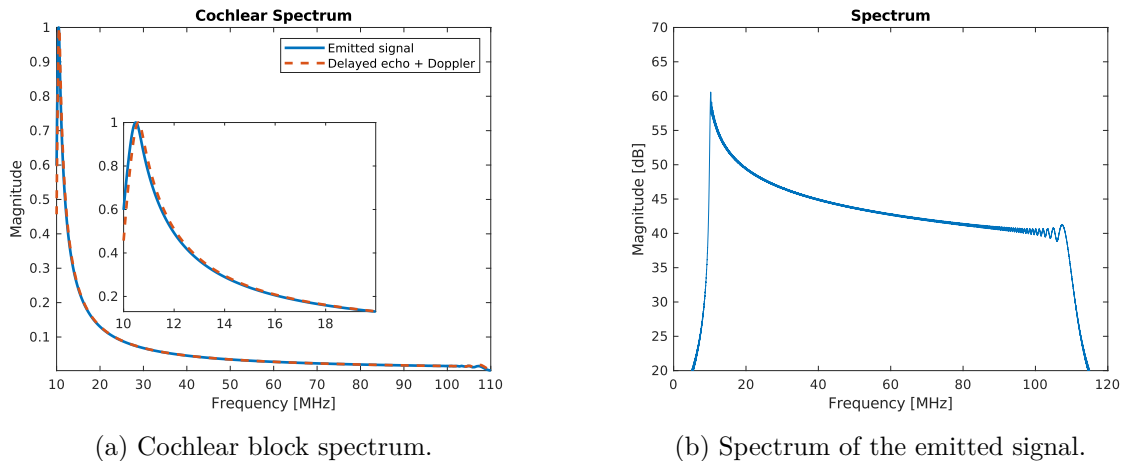


Figure 4.10: Comparison between the cochlear spectrum and the Fourier spectrum. The output of the cochlear block is given for a Parsons waveform ($B = 100\text{MHz}$, $T = 50\mu\text{s}$ and $a = 0.1$) and its echo delayed by $\tau = 50\mu\text{s}$.

Two Doppler estimators are thus evaluated based on the cochlear spectrum behaviour. Figure 4.11 depicts the process with an overview of the estimators along with a noisy version to visualise the impact of noise. The first estimator $\hat{\nu}_{d,1}$ estimates the frequency offset between the two signals by observing the difference in the first couple of frequency to get the same amplitude level in both spectrum.

$$\hat{\nu}_{d,1} = \arg \min_{\nu_d} ||S(f, 0) - S(f, \nu_d)||^2, \quad (4.7)$$

where S designates a spectrum. In the example illustrated in figure 4.11, the difference is measured at an amplitude close to 0.6. The second estimator $\hat{\nu}_{d,2}$ estimates the Doppler from the difference between the magnitude peak in the spectrum of the original signal and its echo.

$$\hat{\nu}_{d,2} = \arg \max_f |S(f, 0)| - \arg \max_f |S(f, \nu_d)|. \quad (4.8)$$

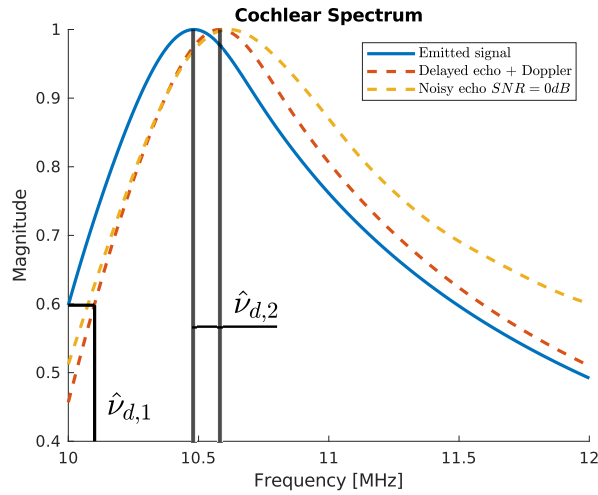


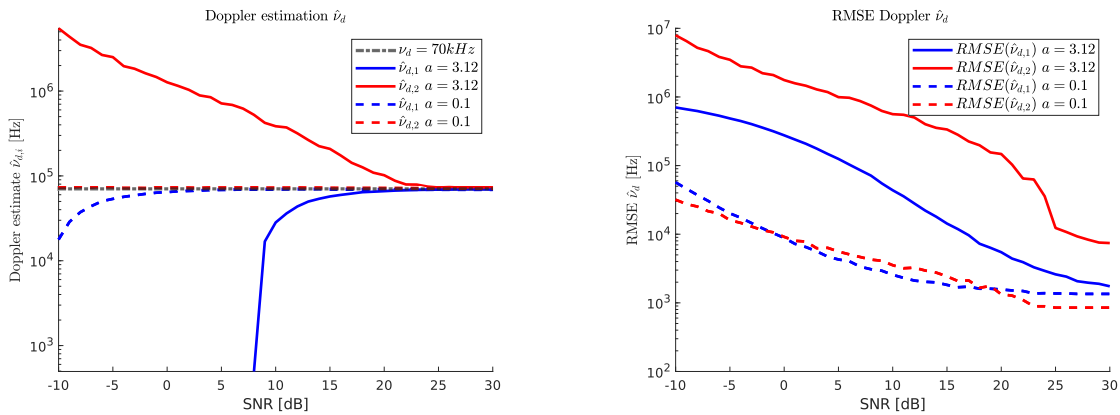
Figure 4.11: Doppler estimators based on the cochlear spectrum of a signal and its echo.

4.2.2 Simulations and Results

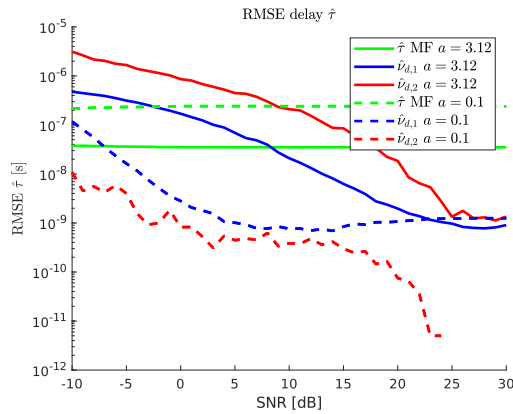
In order to evaluate the Doppler estimation with the bio-inspired waveform and the cochlear block, Monte-Carlo simulations have been computed at varying SNR with 500 trials each. Two Parsons function with a duration of $T = 50\mu\text{s}$ and a bandwidth of $B = 100\text{MHz}$ are being compared. The first one is close to a chirp with an almost linear behaviour ($a = 3.12$) and the second Parsons function has a more pronounced curvature ($a = 0.1$).

The resulting estimations are plotted in figure 4.12(a) for the two Parsons waveforms with $a = 3.12$ in solid lines and $a = 0.1$ in dashed lines. The true Doppler is $\nu_d = 70\text{kHz}$. First observations, the more curved or hyperbolic the waveform, the more precise is the estimation of

Doppler at low SNRs. This comes from the fact that the energy of the signal is concentrated in the final frequency portion, which is less drown in the noise as the curvature of the instantaneous frequency increases. For the Parsons waveform with $a = 3.12$, it seems that the estimator $\hat{\nu}_{d,1}$ is better than the second estimator $\hat{\nu}_{d,2}$ at lower values of SNR ($<20\text{dB}$). This could be linked to its spectrum, because with $a = 3.12$, the instantaneous frequency is more linear and thus the QCF component does not have a sufficient energy to assure a valuable estimation. Concerning the other waveform, the results appears inverted for $\text{SNR} < 0\text{dB}$. This observations is confirmed in figure 4.12(b), where the RMSE on the Doppler estimation is plotted. Overall, the Doppler estimation is valuable as we can approach an error close or inferior to 1kHz.



(a) Doppler estimates as function of the SNR. (b) RMSE on the Doppler estimates as function of the SNR.



(c) RMSE on the corrected delay with two Parsons waveforms for varying SNR.

Figure 4.12: Results of the Monte-Carlo simulations for the Doppler estimation. The true Doppler is $\nu_d = 70\text{kHz}$.

This Doppler estimation not only provides an information on the target velocity but can also help to reduce the error in the delay estimation. The figure 4.12(c) illustrates the RMSE on the

delay estimation for the MF before (green colour plot) and after correction with the estimated Doppler. Again the two Parsons waveforms and their estimators are compared. The given results show a clear improvement in the delay estimation. Note that for the second estimator for $a = 0.1$, the line stops at 25dB because the error is null and the plot scale is set to logarithmic. Overall, the simulations show a real possibility in a Doppler estimator based on the Parsons function and the SCAT.

4.3 Conclusion

This concludes the chapter on the application of the Parsons waveform in different radar frameworks. The multistatic use of the Parsons waveform shows that biomimicry has the potential to contribute significantly to the solution of the spectrum management challenge, while offering a concrete application of the Parsons signal. Although, we are a long way from the capacity of bats to evolve by hundreds in close vicinity, the Parsons waveform can increase the waveforms diversity and thus the number of users. The next step would be to test it in real conditions to check the reliability of the results. Furthermore, the capabilities of the bat-inspired waveform are really significant, particularly when combined with known radar processing like the Mismatched Filter, which confirms the results of the previous chapter. On another note, the combination with a bio-inspired processing like the SCAT could be really valuable to use the Parsons function to its full potential. In fact, the Doppler estimation investigated could reduce the error in delay estimation. Moreover, this would be another step towards a bat-inspired radar system. Obviously, further research is needed and only real tests can validate the hypothesis observed here, but the simulations showed an interesting potential.

THE CUSUM: AN ALGORITHM TO DETECT THE PRESENCE OF AN UNKNOWN SIGNAL

As promised, the final chapter is entirely dedicated to the Cumulative Sum (CuSum) algorithm. Introduced in the Chapter 3, the extraction of pulses within bat echolocation signal led to the implementation of this particular change point detection algorithm. Initially computed for this preliminary study on bat signals, the results obtained were sufficiently satisfying and promising to justify extending the application of the CuSum algorithm to radar purposes. This chapter details the motivation behind the choice of the CuSum as an algorithm for the detection of unknown radar signals. The mathematical and statistical background are then furnished to finally appreciate the functioning of the CuSum. The explanations of its operational principle, and applications to both simulated and real data are thus presented.

5.1 Story of an Algorithm

5.1.1 CuSum begins

As previously stated in the Chapter 3, the analysis of bat waveforms required the examination of their signals, in particular hunting sequence as the one displayed in figure 5.1. Doing such a study with only a visual approximation based on spectrograms and extracted instantaneous frequencies worked in the first place but this remained a coarse approximations. Also, this task would deserve being automated. Therefore, the necessity arose for an algorithm capable of extracting pulse-by-pulse bat signals in order to correctly retrieve temporal and frequency parameters and to facilitate the analysis. Hence, appears the great saviour: the CuSum algorithm.

The initial inspiration came from the work of Cobos in [83]. In this paper, the author attempts to detect and spatially localise an acoustic source of interest using a Wireless Acoustic Sensor Networks (WASN) and the CuSum algorithm. But what does this algorithm represent? The Cumulative Sum algorithm, or logically abbreviated to CuSum, was firstly introduced by Page [29]. It is among the most commonly used algorithms in change point detection theory,

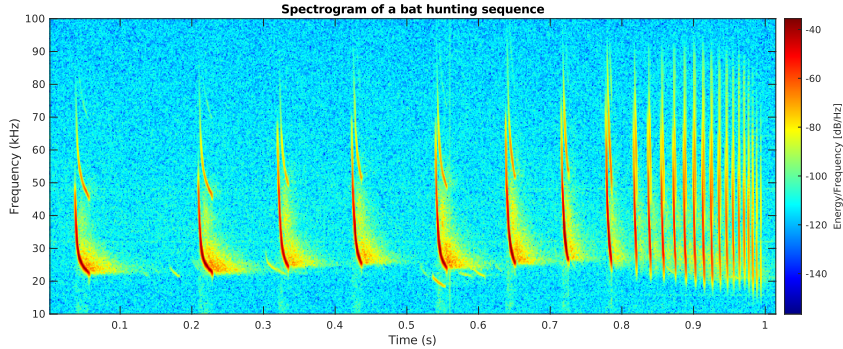


Figure 5.1: Example of a real hunting sequence from *Nyctalus Noctula* [14]. This illustrates the kind of signal that have been investigated and the need to extract each pulse for relevant parameters estimation.

where the objective is to identify one or several *abrupt changes*¹ in the intrinsic characteristics of a considered object [30]. Such a goal can be encountered in several fields of application, including industrial monitoring, the prediction of natural catastrophic events (such as earthquakes and tsunami) and, in the present case, signal processing and pattern recognition. However, the elementary problem of change point detection is the detection of a single change point, while in the studied situation, given that all signals have a beginning and an end, the algorithm must find the onset and the end of a pulse in order to perform a complete detection. A comprehensive explanation of the algorithm and its generalisation to our problem will be provided in the statistical section later on.

For now, keep in mind that, the CuSum algorithm tries to differentiate between portions of the signal containing noise only and those with a signal of interest, namely a pulse. A preliminary, naive and simple implementation of the algorithm has been computed in accordance with the approach outlined in [83] to detect the onsets and ends of isolated pulses in bat signals. At this stage, the detection was conducted on the filtered envelope of pulses that had already been roughly extracted, which means that the detection was simplified. With this first implementation, the CuSum algorithm showed an interesting efficiency to detect and facilitate the extraction of unknown pulses without preliminary information on the signal. Moreover, its simplicity and processing speed appeared attractive for further investigation. Figure 5.2 illustrates the result obtained with an ulterior version of the algorithm, where the first pulses of the hunting sequence previously presented are now detected.

Because the literature about the application of this algorithm to signal detection in radar processing is scarce, the idea came to investigate the use of this algorithm in this framework. The objective is then the detection of unknown signals, which means without prior knowledge,

1. As Basseville observed in [30], abrupt changes do not designate changes with large magnitude. On the contrary, in the change point detection theory, the objective is typically to identify small changes.

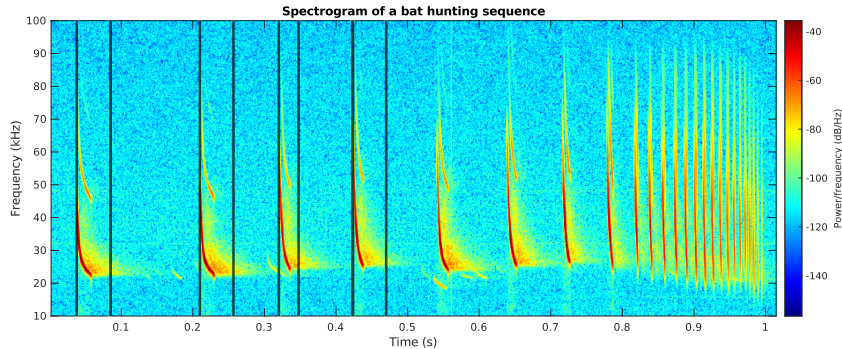


Figure 5.2: Example of a real hunting sequence from *Nyctalus Noctula* [14] where the first pulses are detected and can be extracted thanks to the CuSum algorithm (for the sake of clarity, the subsequent detections are not shown in this illustration). The black vertical lines represent the estimated onset and end of each pulse.

using a single antenna, and the estimation of the Time of Arrival (TOA) but also the emission parameters such as the duration or bandwidth with the change point detection logic.

5.1.2 CuSum and Radar

To better understand the motivations behind this desire to further investigate the CuSum algorithm for radar applications, note that the growing number of users and applications, combined with the implementation of new types of waveforms (what a coincidence...) has led to an increase need for tools that can effectively detect and recognise a range of signals with unknown parameters in the presence of noise. In this context, the ability to accurately and rapidly localise and identify a received signal is often a crucial requirement. Concerning radar applications, the detection of unknown signals can help provide countermeasures, avoid interference and localise potential threats and hostile emissions.

For known signals, a matched filter is typically used. However, it requires prior knowledge of the transmitted signal. In the case of unknown signals, alternative methods must thus be considered, and there are numerous possibilities. The most traditional approach is the energy detection [84]. Usually, a network of antennas is also a good way to detect and localise signals of interest [85]. Recently, the combination of time-frequency methods (Short-Time Fourier Transform, Wigner-ville Distribution or Continuous Wavelet Transform) with machine learning has been expanding. Time-frequency methods offer the advantage of dissociating superimposed signals in time by studying their two-dimensional versions. It also helps to concentrate the energy of the signals embedded in noise. The main idea proposed in [86][87] is the construction of a mask around the detected component using time-frequency methods while the recognition is processed by a convolutional neural network. Nevertheless, these methods can potentially encounter resolution issues, which may impair the accuracy of the parameter estimations. In the present case,

and following the results obtained from the study of bat signals, the CuSum algorithm appeared as attractive in terms of simplicity, efficiency and processing speed for a detection framework. It will be demonstrated that the logic behind the algorithm is very intuitive and the resultant detection is of quality. Besides, the detection speed of the CuSum in a multiple change point detection case is optimal [88].

The principle of the CuSum investigation in this chapter is to apprehend the detection of an unknown signal as a change point detection problem. In the context of radar applications, change detection is mostly encountered when attempting to detect modifications in a time-series of Synthetic Aperture Radar (SAR) images. For instance, in [89], the author used the Cumulative Sum algorithm as a detection method for deforestation monitoring to counter cloud cover loss. As a method based on statistics, the CuSum is designed to detect any type of variation that impacts the trend of a time-series and thereby it is less affected by seasonal variability of vegetation and cloud cover. Similarly, the CuSum has been employed to detect non-stationarity in the clutter, which, when combined with machine learning can help updating the emission parameters of a radar system and improve the target detection [90][91]. Concerning Cognitive Radio, the CuSum algorithm can find some applications as a spectrum sensing tool [92]. Additionally, the CuSum has been used in maritime [93] or aerial [94] manoeuvre detection. Nevertheless, these applications refer to geospatial applications rather than signal detection methods. More recently, the CuSum algorithm has been proposed to assist in distinguishing the Pulse Repetition Interval (PRI) variations and work modes for Multi-Function Radars (MFRs) [95] but in the context of radar signal detection, the available literature on this subject is scarce. It thus appeared that the application of a CuSum algorithm to the detection of unknown signals seemed appealing and could represent a novel and innovative contribution to the literature in this field.

5.2 Behind the Sum

Now that the objective is clearly defined, the (why so) serious part is about to begin: the description of the implementation of the algorithm. How does it work ? What are the mathematics and statistics behind the CuSum ? All relevant information will be presented in the subsequent paragraphs and in the referenced literature.

5.2.1 Statistical Framework

The goal of the CuSum algorithm is to identify moments when the probability distribution of a time-series changes. Therefore, the algorithm searches for changes in mean or variance in the signal. To begin, let us consider the elementary problem of change point detection: the detection of a single change point, which in our case corresponds to the search for the onset of a signal. Later, it is easily generalised to the detection of several successive change points. Statistically,

the received data may be modelled as a discrete process $x[n]$, $n \in \llbracket 0, N \rrbracket$, with a given probability density function (PDF), $p(x[n], \theta)$, θ being a deterministic parameter vector with two possible values, θ_0 and θ_1 , corresponding to the two possible hypotheses

$$\begin{aligned} H_0 : \theta &= \theta_0, \text{ Only observation noise is present.} \\ H_1 : \theta &= \theta_1, \text{ The signal is present.} \end{aligned}$$

Under each hypothesis, the joint probability density functions on the $N + 1$ samples write as

$$p_{x|H_0} = \prod_{n=0}^N p(x[n], \theta_0), \quad (5.1)$$

$$p_{x|H_1} = \prod_{n=0}^{\tau-1} p(x[n], \theta_0) \prod_{n=\tau}^N p(x[n], \theta_1), \quad (5.2)$$

where $\tau \in \llbracket 0, N - 1 \rrbracket$ is the sought change point. This configuration means that for $n < \tau$, the samples contain noise only. Following the detection theory and the Neyman-Pearson theorem, the Log-Likelihood Ratio (LLR) test, Δ_x , is the test that maximises the probability of detection [96], thus optimal to decide between the two hypotheses with a comparison to a threshold η :

$$\Delta_x = \ln \left(\frac{p_{x|H_1}}{p_{x|H_0}} \right) \underset{H_0}{\overset{H_1}{\gtrless}} \eta. \quad (5.3)$$

Due to the impossibility of computing this LLR because θ_0 , θ_1 and τ are unknown, a Generalised Log-Likelihood Ratio (GLLR) is defined by taking the Maximum-Likelihood estimates of each unknown (ML estimates). Let $\hat{\theta}_0$ and $\hat{\theta}_1$ be the ML estimates of θ_0 and θ_1 under H_0 and H_1 hypotheses respectively for fixed τ . The ML estimate $\hat{\tau}$ of τ is then the value maximising the likelihood $p(x_{0:N-1} | \tau, \hat{\theta}_0, \hat{\theta}_1)$, where $x_{0:N-1} = (x_0, x_1, \dots, x_{N-1})$. It can be checked that the GLLR writes

$$g[N] = \sum_{n=\hat{\tau}}^N \ln \left(\frac{p(x[n], \hat{\theta}_1)}{p(x[n], \hat{\theta}_0)} \right). \quad (5.4)$$

Let the Instantaneous LLR (ILLR) at time n be defined by

$$s[n] = \ln \left(\frac{p(x[n], \hat{\theta}_1)}{p(x[n], \hat{\theta}_0)} \right). \quad (5.5)$$

According to [29], the Cumulative Sum of s from 0 to N is then

$$g[N] = \sum_{n=0}^N s[n] - \min_{1 \leq \hat{\tau} \leq N} \sum_{n=0}^{\hat{\tau}-1} s[n]. \quad (5.6)$$

The previous equation indicates that the algorithm tries to find a minimum in the sum from which the next samples will have a sufficient change in slope. The decision function being compared to a positive threshold η , it can be written [30]

$$g[N] = \max(g[N - 1] + s[N], 0). \quad (5.7)$$

This is the basis of the CuSum algorithm and figure 5.3 illustrates the behaviour of the CuSum for the detection of a single change point.

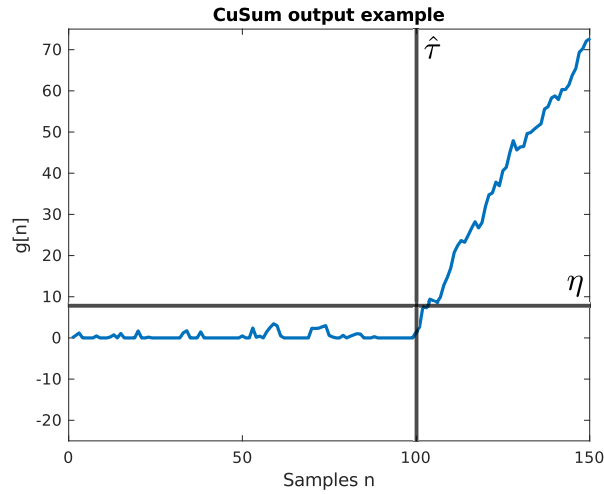


Figure 5.3: Example of the CuSum result for the detection of a single change point located at $\tau = 100$.

5.2.2 Signal Distribution in the Radar Framework

The sum behind the algorithm thus described, the signal distribution and the different PDF models are described along with the calculation of their LLR. The objective is to understand how the signal behave accordingly to the CuSum hypotheses and to choose the best corresponding distribution.

As stated before, the hypothesis H_0 describes portions with noise only and the hypothesis H_1 , the portions containing signal of interest embedded in noise. Usually, noise is described as a random variable following a complex-valued normal distribution with zero mean $\mu_0 = 0$ and a known variance $\mathbb{E}[|x[n]|^2] = \sigma_0^2$ corresponding to the noise power. Its density is given by:

$$p(x[n], \theta_0) = \frac{1}{\pi\sigma_0^2} e^{-\frac{|x[n]|^2}{\sigma_0^2}}. \quad (5.8)$$

Concerning the signal, a familiar approach in a radar framework would be to consider the signal

as an unknown but deterministic variable. In that case, we assume that, in the presence of noise, the signal follows a Gaussian probability density function with a certain unknown mean μ_1 , where μ_1 is the noise-free signal, and a variance $\sigma_1^2 = \sigma_0^2$ (meaning that the variance only comes from the noise):

$$p(x[n], \theta_1) = \frac{1}{\pi\sigma_0^2} e^{-\frac{|x[n]-\mu_1|^2}{\sigma_0^2}}. \quad (5.9)$$

After estimation of $\hat{\mu}_1 = x[n]$, the GLLR defined with respect to the deterministic approach leads to a classical energy detection scheme where (5.5) becomes:

$$s[n] = \frac{|x[n]|^2}{\sigma_0^2}. \quad (5.10)$$

Obviously, the Cumulative Sum using this ILLR would be constantly increasing as n increases, leading to difficulties finding the change points with the ML estimates $\hat{\tau}$. The deterministic approach alone is thus not appropriate to correctly compute the CuSum. A solution could be to use a slope detection, another detection algorithm with the disadvantage of being time-consuming when used to find several change points because of the number of hypotheses to be tested [97]. A second strategy could be to use the Akaike Information Criterion (AIC) [98], which adds a penalty to the log-likelihood of the deterministic ILLR. The classical energy detection scheme (5.10) then becomes:

$$s[n] = 2\frac{|x[n]|^2}{\sigma_0^2} - 2C. \quad (5.11)$$

Here, $C = 2$ is the AIC penalty, corresponding to the number of parameters of our model (real and imaginary part of the signal). The detection of the onset of a chirp is considered. Figure 5.4 illustrates the CuSum results for the deterministic case with or without the AIC penalty term. As expected, the non-penalised deterministic case results in an ever-increasing CuSum value. This behaviour, compared to that presented earlier in figure 5.3, prevents the detection of a local minimum (here assumed to occur at $\tau = 1000$). For high enough SNR, the AIC penalty enables the CuSum to exhibit a strong change of slope along with the possibility to determine a minimum. Nevertheless, the detection is nearly impossible at low SNR because the AIC penalty is not sufficient. Hence, even with the AIC penalty, the deterministic model leads to an unsatisfying test statistic, thus another approach has to be considered. From now on, the signal is modelled as a **random variable**, with independent and identically distributed (iid) samples. Obviously, it is difficult to assume a particular distribution for every possible signal, in particular when looking for unknown signals and the task becomes even more difficult when several signals with various parameters are mixed together.

Because the data are complex-valued time series and the variable considered in the CuSum is the magnitude $r = |x| = \sqrt{\Re(x)^2 + \Im(x)^2}$ (see Appendix E.1), the choice has been made

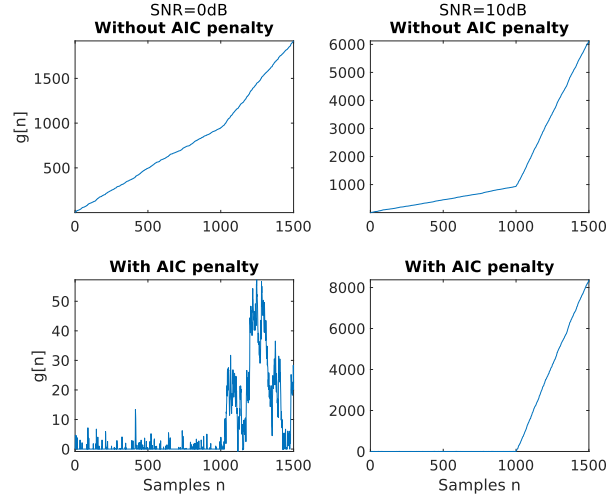


Figure 5.4: CuSum outputs for the deterministic case without (top) and with (bottom) the AIC penalty for the detection of the beginning of a chirp located at $\tau = 1000$ samples. The left column represents a low SNR case, while the right column depicts a high SNR case.

to consider the Rayleigh-Rice (RR) distribution. This choice is driven by the fact that the RR distribution model is often associated with complex signals embedded in Gaussian noise [32]. Under H_1 , where the data contain both the signal of interest and the polluting noise, the Rice distribution [31] seems to be a judicious choice. In particular, noisy complex signals with constant amplitude² ν write $x[n] = \nu e^{i\varphi[n]} + w[n]$ with the phase $\varphi[n] \sim \mathcal{U}[0, 2\pi]$ and the noise $w[n] \sim \mathcal{CN}(0, \sigma_0^2)$, leading to $r[n] = |x[n]| \sim \text{Rice}\left(\nu, \frac{\sigma_0^2}{2}\right)$. Its density is given by:

$$p(r[n], \theta_1) = \frac{2r[n]}{\sigma_0^2} e^{-\frac{(r[n]^2 + \nu^2)}{\sigma_0^2}} I_0\left(\frac{2r[n]\nu}{\sigma_0^2}\right), \quad (5.12)$$

where I_0 is the zeroth order modified Bessel function. On the other hand under H_0 , where the data contain only noise ($\nu = 0$), the signal is Rayleigh distributed, $r[n] \sim \text{Rayleigh}\left(\frac{\sigma_0^2}{2}\right)$. Its PDF writes as

$$p(r[n], \theta_0) = \frac{2r[n]}{\sigma_0^2} e^{-\frac{r[n]^2}{\sigma_0^2}}. \quad (5.13)$$

Then, from (5.5), the ILLR becomes

$$s[n] = -\frac{\nu^2}{\sigma_0^2} + \ln\left(I_0\left(\frac{2r[n]\nu}{\sigma_0^2}\right)\right). \quad (5.14)$$

Justification and explanations about the Rice and Rayleigh distributions particularities are available in the appendices E.2 and E.3.

2. This assumption is true for a wide variety of radar signals, such as chirp or phase codes.

Another option has been found in the literature, in the case where no particular distribution is assumed, Tartakovsky in [99] proposed a more general ILLR of linear-quadratic form. Letting $y[n] = \frac{|x[n]| - \mu_0}{\sigma_0}$ denote the centred scaled observation at time n , with μ_0 and σ_0 the mean and variance in the H_0 hypothesis, the ILLR in [99] writes

$$s[n] = C_1 y^2[n] + C_2 y[n] - C_3, \quad (5.15)$$

where

$$C_1 = \frac{1 - q_\sigma^2}{2}, \quad C_2 = \delta q_\sigma^2, \quad C_3 = \frac{\delta^2 q_\sigma^2}{2} - \ln q_\sigma, \quad (5.16)$$

with $q_\sigma = \frac{\sigma_0}{\sigma_1}$, $\delta = \frac{\mu_1 - \mu_0}{\sigma_0}$. Obviously, μ_1 and σ_1 are the mean and variance in the H_1 hypothesis.

5.3 Everything has a Beginning and an End

5.3.1 The CuSum Logic for Pulse Detection

The previous chapter described the mathematical and statistical background behind the CuSum. As precise as the theory can be, an illustrative example would be very welcome to really understand what happens in practice. This paragraph thus explains how the CuSum operates, with a focus on our specific case of application, to complete the recent underlying statistical knowledge.

The main objective of the algorithm is to detect and extract unknown signals. The signal in our investigation, whether it is bats or radar signals, is characterised by an onset and an end, which logically induces that the extracted parameters concern both endpoints. Page [29] and later Basseville [30] described a two-sided CuSum algorithm made to detect a positive or negative change in θ . This results in the consideration of an alternative hypothesis, designated as H_2 , and the termination of the algorithm upon the identification of either H_1 or H_2 . Our case of investigation is a bit different since the objective is to detect the switch back and forth between H_0 (parts with noise only) and H_1 (parts where a signal is present). In other words, the onset of a signal is identified by the transition from H_0 to H_1 , while the inverse is synonymous with the end of a signal. Detecting the end of a signal can simply be seen as the opposite problem presented in equation (5.7) and the search for a maximum followed by a decreasing slope, signifying a return to the H_0 hypothesis.

A picture is worth a thousand words, therefore consider a pulse train composed of 10 pulses of the signal displayed in figure 5.5. The Pulse Repetition Interval is set to $T_r = 10T$, with T being the pulse duration. The CuSum algorithm is computed to detect the 10 pulses.

The output of the algorithm is presented in figure 5.6(a) with a zoom-in view of one pulse detection in figure 5.6(b) to show the behaviour of the algorithm during the threshold crossing. Logically (and because it was set like this) the CuSum begins with the search of an onset. The

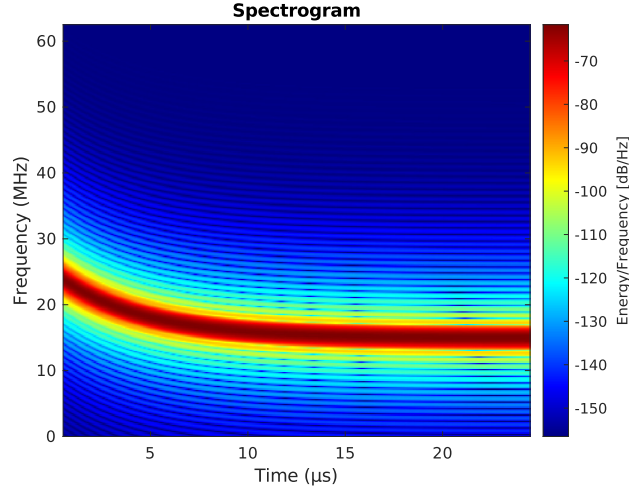
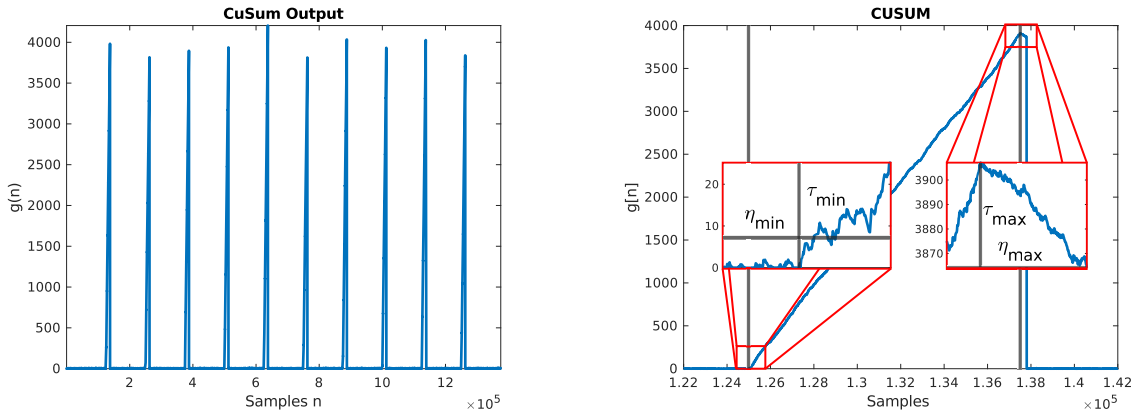


Figure 5.5: Spectrogram of a Parsons waveform ($B = 10\text{MHz}$, $T = 25\mu\text{s}$ and $a = 5.10^{-3}$).



(a) CuSum result on a pulse train with 10 pulses. (b) Behaviour of the CuSum around one pulse.

Figure 5.6: CuSum output on a pulse train (SNR= 0dB).

algorithm computes the sum until it crosses a threshold, η_{min} , synonymous with a registered change point (a minimum), at time τ_{min} , associated with the *potential* beginning of a signal. Note that the term used is *potential* because at this point the detection can be either accurate or erroneous. In both cases, the algorithm switches to the search of the end (maximum), at time τ_{max} , of this potential signal. If the onset detection was correct, like presented in figure 5.6(b), the sum should increase linearly until a point where a maximum is reached. If this maximum is, in fact, the end of the signal, the sum should then decrease until it reaches a certain threshold, η_{max} , below the maximum reached to validate the new change point. The sum is then reset to zero and the algorithm starts a new onset search. On contrary, if the onset detection was a false positive, the sum will still be calculated according to equation (5.6), but it will not exhibit a

sufficiently increasing behaviour because it is a pure noise part. Therefore, the algorithm will find a maximum rather quickly, or the sum will be automatically reset to zero, as in equation (5.7). The search for an onset resumes and the algorithm follows this pattern until the end of the studied signal.

5.3.2 Thresholds settings

The CuSum algorithm and its behaviour are now clearer, but one last point remains: the threshold settings in order to be able to take a decision about the minima and maxima. Deciding how to set them is always a challenging task. A preliminary implementation with constant thresholds showed that it was not adapted to our situation. This is due to the fact that the CuSum has to identify two different change points, the start and the end of a pulse, which are associated with a minimum and a maximum. Therefore, two thresholds based on the estimation of the noise in the signal and adapted to the search for a minimum or a maximum have been implemented.

First, the minimum threshold set up is presented. Because it is linked to the detection of the onset, the underlying desire is to avoid false detection. It is synonymous with false alarm, which means validating the hypothesis H_1 while still being under the hypothesis H_0 . This threshold must thus be sufficiently high to avoid false alarms, but not too much to avoid missed detection. The threshold is designed to be an Empirical Constant Threshold (EC-Threshold), inspired by the definition given in [100]. Because the false alarms occur during the H_0 hypothesis, the minimum threshold is therefore linked to the noise behaviour under this hypothesis. Considering the parameters of the studied signal, σ_0^2 and ν , along with the chosen distribution models (RR or Tartakovsky), the CuSum algorithm is computed for L simulated noise series of M samples:

$$g_i^j = \max(g_{i-1}^j + s_i^j, 0), \text{ where } j \in \llbracket 1, L \rrbracket \text{ and } i \in \llbracket 1, M \rrbracket. \quad (5.17)$$

Then the maximum or local score of each series, $m^j = \max g^j$, is saved and the threshold is set as

$$\eta_{min} = q_{1-M\alpha}[m_{1 \leq j \leq L}^j], \quad (5.18)$$

where α is the false alarm rate and $q_{1-M\alpha}$ represents the quantile³ of order $(1 - M\alpha)$. According to this equation, the threshold, η_{min} , is the value such that the cumulative distribution function of the maximum series $m_{1 \leq j \leq L}^j$ is $P(m_{1 \leq j \leq L}^j \leq \eta_{min}) = 1 - M\alpha$. In other words, the probability that a local score $m_{1 \leq j \leq L}^j$ will take a value less than or equal to η_{min} is of $(1 - M\alpha)$. It is important to note that α can not exceed $\frac{1}{M}$ in that case [100]. The false alarm rate α will be defined in the next section with the corresponding performance indicators. Figures 5.7(a) and

3. In statistics and probability, quantiles are values dividing the range of a probability distribution (or sorted observations) into continuous intervals with equal probabilities.

5.7(b) give an example of the setting of threshold η_{min} with $L = 100$ noise series of $M = 10,000$ samples and a false alarm rate $\alpha = 10^{-5}$ (left) and $\alpha = 5 \cdot 10^{-5}$ (right). With regard to the preceding explanation, the threshold in figure 5.7(a) is set such that the probability that a maximum simulated value is less than or equal to η_{min} is of 90%. In figure 5.7(b), this probability decreases to 50%. Obviously, the higher the false alarm rate is, the more false alarms you get due to a lower threshold.

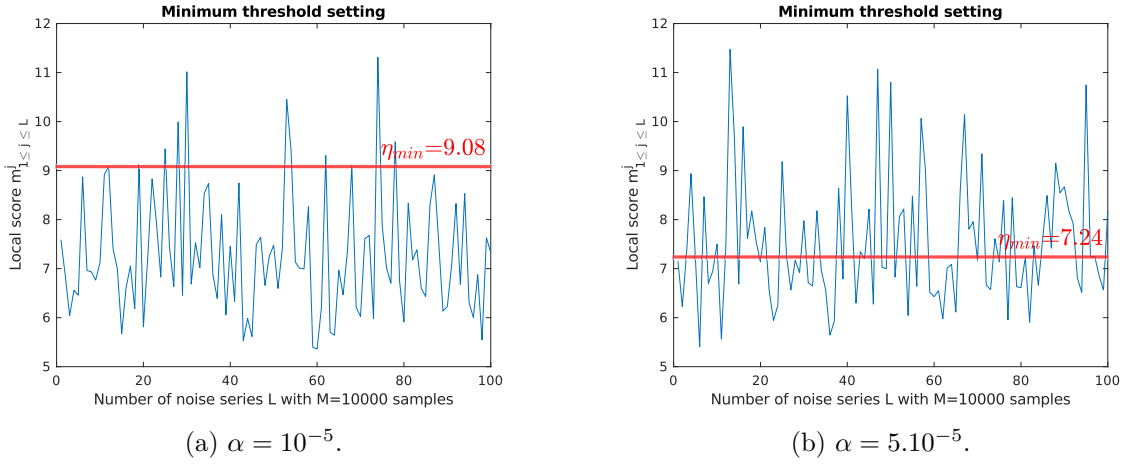


Figure 5.7: Minimum threshold setting for two values of α .

Once the onset has been identified, the detection is complete when the end is identified thanks to a second threshold. This threshold must be set high enough to avoid abruptly cutting a pulse into pieces, but not too much in order to find a potential end and keep going on the search for other pulses. Since the maximum is associated with the end of a pulse, what follows is supposedly only noise. Under the hypothesis H_0 , it can be demonstrated, by calculating the CuSum with equation (5.6), that the sum $g[N]$ constantly decreases, following a linear behaviour. It is therefore possible to describe the typical CuSum output related to noise only by a slope factor a_w . Again, thanks to the L simulated noise series of M samples, the CuSum algorithm is computed according to equation (5.6). For each noise series, a slope factor $a_{w,j}$ can be evaluated. Figure 5.8 gives an example of this slope estimation with the CuSum output for a noise series $j \in \llbracket 1, L \rrbracket$ with $M = 10,000$ samples. Once a slope factor has been estimated for each noise series, the average slope factor a_w can be calculated. The maximum threshold, linked to the detection of the end of a signal, can then be obtained by multiplying this average slope factor by K samples. The choice of K will be shown to have an impact on the mean delay for the end detection.

$$\eta_{max} = K a_w. \quad (5.19)$$

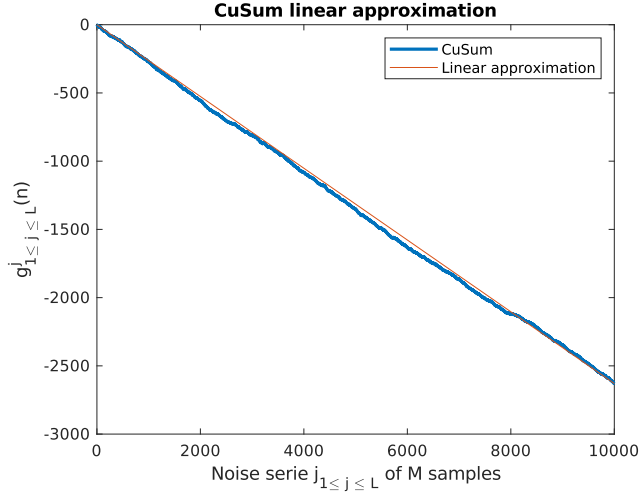


Figure 5.8: Linear approximation of the CuSum output under the noise only hypothesis (H_0).

5.3.3 Performance indicators

To assess the performance of the CuSum algorithm and to characterise its response, some indicators issued from the CuSum literature [30] need to be defined.

First of all, the False Alarm Rate (FAR), α , has already been mentioned in the definition of the minimum threshold. It represents the ratio between the number of false alarms (number of false detections or false positives) and the total number of alarms or detections. If the algorithm is well designed, the measured FAR, $\hat{\alpha}$, should tend towards α . Directly related to the FAR is the Mean Time Between False Alarms (MTBFA), which is the average time before the first false alarm or between false alarms⁴. It is given by

$$\text{MTBFA} = \frac{1}{\alpha}. \quad (5.20)$$

The impact of the thresholds can also be measured thanks to a Mean Delay for Detection D_d . Firstly, when searching for a possible onset, the CuSum can easily find an instant $\hat{\tau}$ corresponding to a local minimum in the sum, but it needs some time to confirm this minimum as a possible onset. This delay, which corresponds to the Mean Delay for detection, designated as $D_{d,start}$, represents the duration over which the algorithm tries to find a value exceeding the threshold η_{min} . If no other minimum is found along the computation, the instant $\hat{\tau} + n_d$ where the threshold is exceeded confirms the instant $\hat{\tau}$ as a change point and $D_{d,start} = n_d$. Figures 5.9(a) and 5.9(b) illustrate the minimum threshold in action with a case of false alarm and a true detection. The algorithm is searching for Parsons waveforms similar to the one presented in figure 5.5. The

4. In [30], the Mean Time Between False Alarms and the Mean Time Before First Alarm are considered to be the same.

thresholds are set with $L = 100$ simulated noise series of $M = 10,000$ samples according to a false alarm rate of $\alpha = 5.10^{-5}$ and a threshold multiplier of $K = 200$ samples. In each figure the first red vertical line situates the instant $\hat{\tau}$ and the second one the instant $\hat{\tau} + n_d$ corresponding to the instant of validation. In the false onset detection, $\hat{\tau} = 86,708$ and the algorithm validates the estimation after a delay of $n_d = 29$ samples. In the correct detection case, the onset is estimated at $\hat{\tau} = 125,000$ with a confirmation delayed of $n_d = 28$ samples.

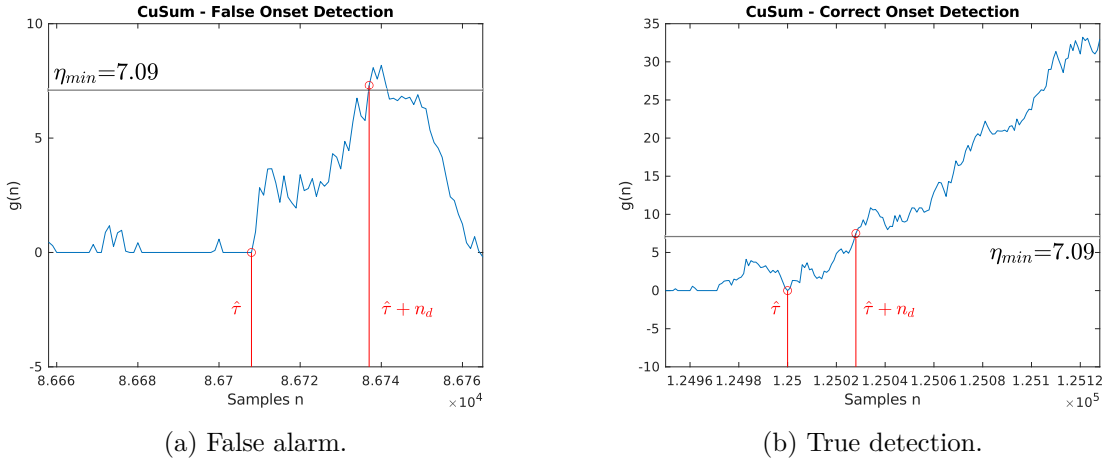


Figure 5.9: Minimum threshold application in the case of a false alarm and a true detection.

The same logic can be applied with the maximum threshold, this time by computing $D_{d,end}$. The figure 5.10 illustrates this case on a correct end identification. In the case of false alarms, the sum will usually be reset to zero before it reaches the maximum threshold. Concerning this example, the algorithm needs $n_d = 206$ samples to validate $\hat{\tau} = 137,456$.

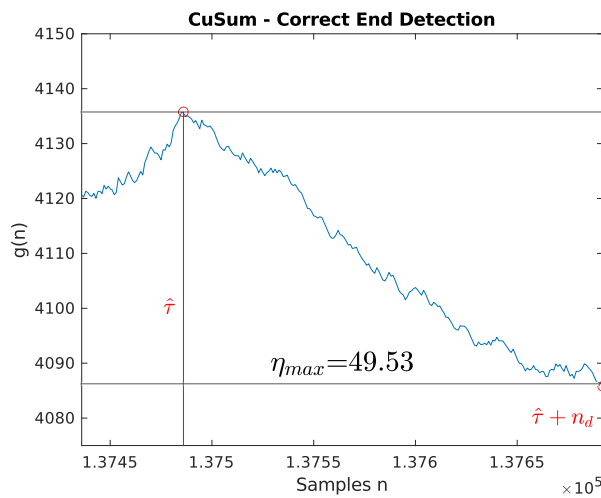


Figure 5.10: Maximum threshold application in the case of a true detection.

Last but not least, the Root Mean Square Error (RMSE) (see equation (3.3) for the mathematical definition) is an efficient indicator to evaluate the estimation of the pulse duration T , the PRI and also the time delay for pulse onset and end.

5.4 CuSum at Work

The CuSum algorithm thus detailed, its implementation on both simulated and real data is documented in the following paragraphs.

5.4.1 Simulations

For the simulation part, consider pulse trains of $N_p = 20$ temporally disjoint Chirp or Parsons pulses with unit amplitude and the following sets of parameters. The singular parameters are inspired from our dear bats, two bat species in particular, *Nyctalus Noctula* (first set) and *Pipistrellus Pipistrellus* (second set).

- Bandwidth $B_1 = 26.73\text{MHz}$ or $B_2 = 68.96\text{MHz}$,
- Pulse duration $T_1 = 19.66\mu\text{s}$ or $T_2 = 2.56\mu\text{s}$,
- Pulse Repetition Interval $Tr = 10T_i$, $i \in [1, 2]$,
- Parsons curvature parameter $a_1 = 4.10^{-3}$ or $a_2 = 3.78.10^{-2}$.

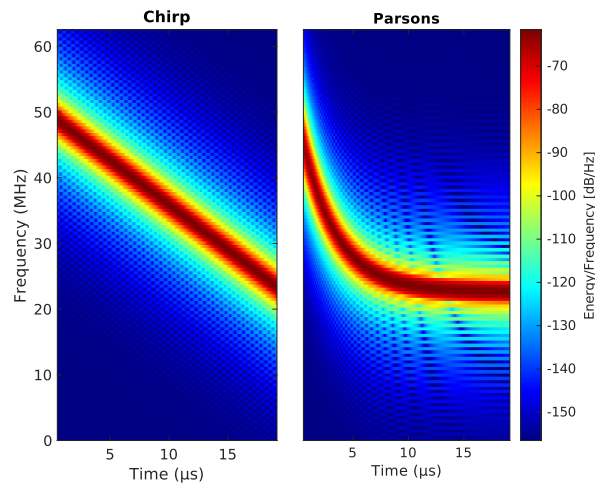
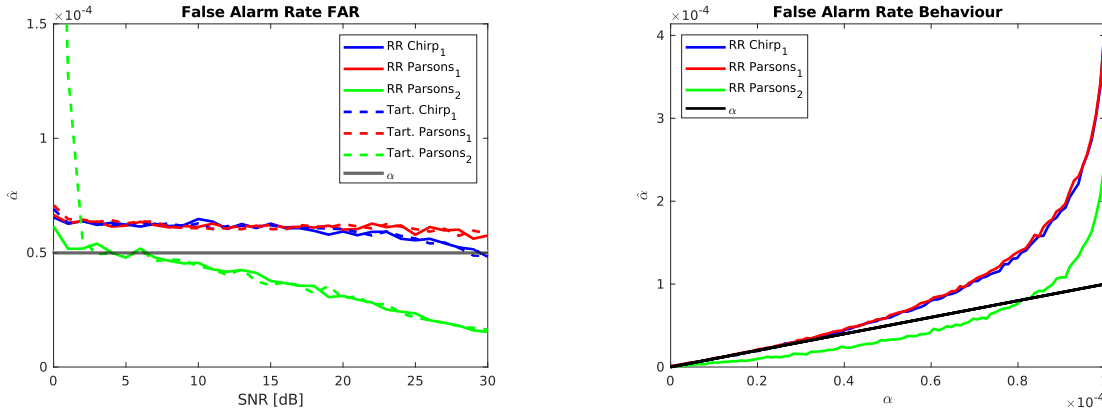


Figure 5.11: Spectrograms of a Chirp and a Parsons pulse with the first set of parameters ($B_1 = 26,73\text{MHz}$ and $T_1 = 19,66\mu\text{s}$).

Figure 5.11 shows the kind of pulses used in the simulations that the CuSum algorithm is tasked with identifying within a noisy recording. The algorithm has been tested for varying SNRs (0 to 30dB with 100 simulations at each SNR), for the different configurations described above. The simulations were conducted for the Rayleigh-Rice (RR) and the Tartakovsky (Tart.)

distribution models with the two sets of parameters. The CuSum was computed for a false alarm rate $\alpha = 5 \times 10^{-5}$ and thresholds set from $L = 100$ noise series of $M = 10,000$ samples, with $K = 200$ samples for the maximum threshold definition. The sampling frequency is $F_s = 500\text{MHz}$.

Figure 5.12(a) illustrates that the measured FAR is close to the desired α for the Chirp and Parsons pulse trains with the first set of parameters. Nevertheless, $\hat{\alpha}$ always exceeds the implemented FAR α for this set of parameters. This observation has been investigated through Monte-Carlo simulations, with 100 trials conducted using the same parameters but this time as function of α (SNR fixed at 20dB). Figure 5.12(b) displays the results, where it can be observed that the estimated FAR has effectively a tendency to exceed the tolerated α starting from a certain value (approximately $\alpha = 0.4$ for the first set). This result is linked to the EC-Threshold, which, as explained in [100], gives the lowest detection delay but always exceeds the implemented α . In the case of the Parsons pulse train with the second set of parameters,



(a) Estimated FAR as function of the SNR. (b) Estimated FAR as function of α (SNR= 20dB).

Figure 5.12: Results of the Monte-Carlo simulations for the estimated FAR $\hat{\alpha}$.

the deviations are more pronounced. In this instance, the measured FAR is lower, which is not erroneous, but rather an underestimation due to the insufficient number of samples, which is almost eight times less samples than the number of samples obtained for the pulse trains with the first set of parameters. This can be explained by the MTBFA. As said in the previous section, according to [100] the MTBFA is the inverse of α . Therefore, in our case, a false alarm should occur on average every 20,000 samples. With the second set of parameters, there are only 11,556 samples between consecutive pulses. In consequence, the noise portions are insufficiently long for the CuSum to make a detection mistake, particularly at high SNR, and the false alarm rate α is not calibrated for this set of parameters. To obtain a FAR similar to that obtained with the first set, α should be set higher. Besides the false detections, the number of missed detections is also measured. The results indicate that at very low SNR ($< 5\text{dB}$), the algorithm may miss a few pulses from time to time. Nevertheless, the average number of missed detections

is approximately zero, which demonstrates the excellent performance of the CuSum algorithm. The only extreme value obtained with the Tartakovsky model and the second set of parameters (green dashed line in figure 5.12(a)) is due to an increase in the number of false alarms, which goes hand in hand with more missed detections (10 in average). This is due to the Tartakovsky model being less adapted to low SNR as the sum becomes increasingly linear similarly to the deterministic model in figure 5.4.

The next performance indicator to be evaluated is the mean decision delay, D_d , for the detection of the onset and end points of a pulse, shown in figures 5.13(a) and 5.13(b) respectively. For a better visualisation, the y-axis is on a logarithmic scale. It can be observed that it does

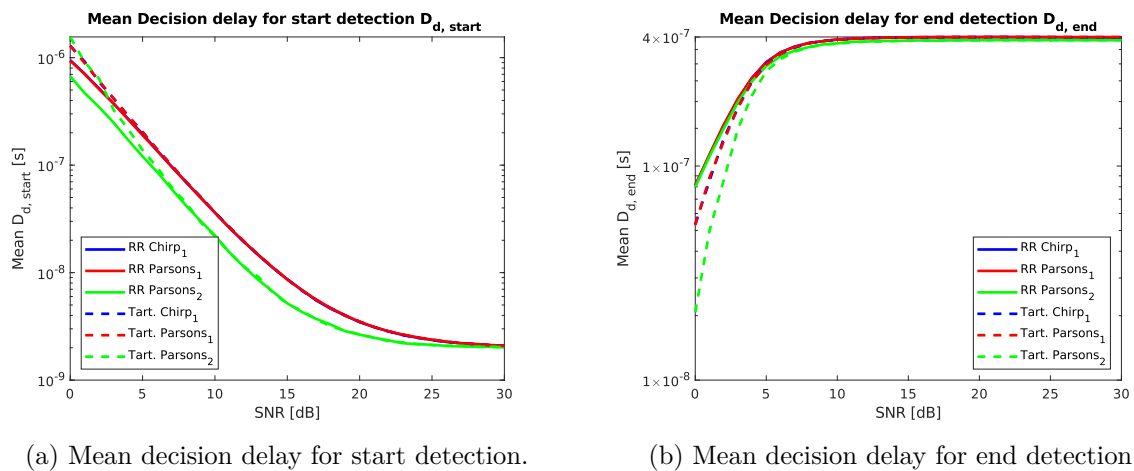


Figure 5.13: Results of the Monte-Carlo simulations for the mean delays of detection as a function of the SNR.

not matter whether a RR distribution or an unknown signal distribution with the Tartakovsky model is considered. While there may be a small advantage for the RR distribution at very low SNR, the two distributions yield similar results overall. Looking at the evolution of these mean decision times, it can be seen that the higher the SNR, the shorter the mean decision time to detect the onset of a signal. As the noise has less and less impact on the signal, the CuSum value increases faster after the beginning of a pulse, rapidly exceeding the threshold. On the contrary, the mean time decision for the end detection increases due to the threshold definition. Defined by equation (5.19), at high SNR, the algorithm requires the K samples to reach the maximum threshold and make a decision. Consequently, the mean time decision is pushed towards $\frac{K}{F_s} = 4 \times 10^{-7}$ s in the presented simulations. The selection of K is therefore of significance in order to correctly estimate the end (and thus the duration) of a signal. In this case, the value of the parameter K was set constant at $K = 200$ samples for every SNR, but it could be adapted as the noise impact is estimated with the slope factor. The mean decision time could thus be corrected according to the SNR. Another interesting aspect could be to have

a sufficiently large K , which involves a longer mean time decision for the end detection, but ensures that the end of the signal is caught.

The last indicator checked is the RMSE on the pulse duration, which requires a correct estimation of both the onset and the end of a pulse. Here again, it is visible in figure 5.14 that the distribution does not play a significant role. Moreover, the algorithm demonstrates satisfactory overall accuracy for each type of pulse train. Regarding the PRI, similar results are obtained which demonstrates the capacity of the CuSum algorithm to correctly retrieve every temporal features of unknown signals.

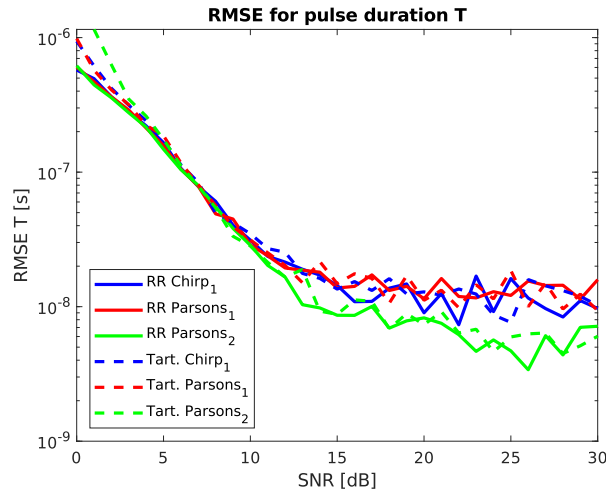


Figure 5.14: Results of the Monte-Carlo simulations for the RMSE as a function of the SNR.

To conclude on these simulations, the CuSum algorithm shows a valuable efficiency in terms of detection and parameter extraction. The results pointed out that the correct detection and estimation of the onset and the end of a pulse are strongly dependent on the allowed false alarm rate α and the number K of samples before making a decision regarding the end of the signal. Because the post processing can easily get rid of the false alarms by assuming a minimal duration for the detected pulses, the false alarm rate could be set higher compared to the value chosen here even if it induced more false alarms. The temporal features extraction of signals without any prior knowledge are really accurate, while being promptly computed. This confirmed the motivations to apply the CuSum in the detection of unknown radar signals.

5.4.2 Real Data

The CuSum showed its capacities on simulated signals but does it perform as well when confronted with real signals?

Chirps everywhere The first real signal to be examined is a series of 13 pulse trains, each comprising 10 up- or down-chirps (with the exception of the final train, which contains only 9 pulses), exhibiting a range of parameters outlined in the Table 5.1 below. It should be noted that the bandwidth is either positive or negative in order to indicate the frequency sweep behaviour and thus the type of chirp (up or down respectively). This signal is a record of a HF radar signal prior to propagation and is thus almost free of noise, as it originates from a closed loop at the emission⁵. Figure 5.15 displays an extract of this signal, representing pulses 8 to 13 from the first two pulse trains.

Pulse train	T [ms]	PRI [ms]	B [kHz]
1	4.8	19.1	41.9
2	3.8	15	-35.8
3	3.5	14.2	20.8
4	4.6	18.2	40.5
5	3.5	13.9	-37.5
6	4.1	16.5	43.5
7	4.3	17.1	29.8
8	4.4	17.5	-29.9
9	4.5	18.2	-17
10	3.5	14.1	-30.3
11	3.6	14.6	31.7
12	3.3	13.3	-32.5
13	4.5	17.9	19.7

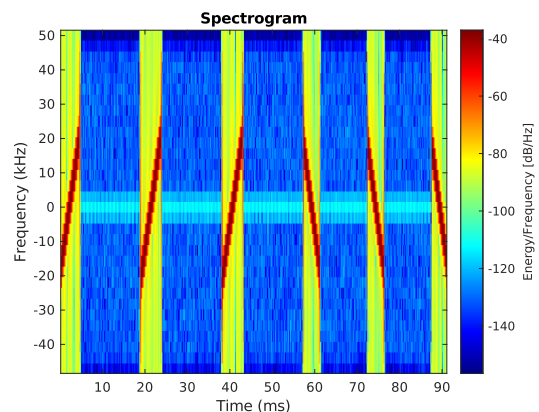


Table 5.1: Parameters of the pulse trains.

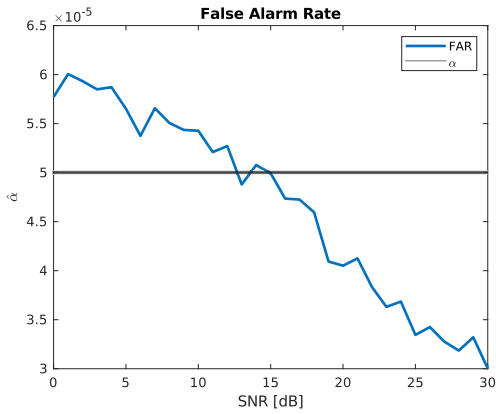
Figure 5.15: Spectrogram of pulses 8 to 13.

Monte-Carlo simulations have been conducted for varying SNRs ($\text{SNR} \in [0, 30]$ dB with 100 trials each), with the objective of evaluating the behaviour of the CuSum with such a signal. The parameters remain unchanged from the previous simulation, with $\alpha = 5 \times 10^{-5}$ and thresholds set from $L = 100$ noise series of $M = 10,000$ samples, with $K = 200$ for the maximum threshold. The sampling frequency is $F_s = 100$ kHz and the Rayleigh-Rice distribution model is applied.

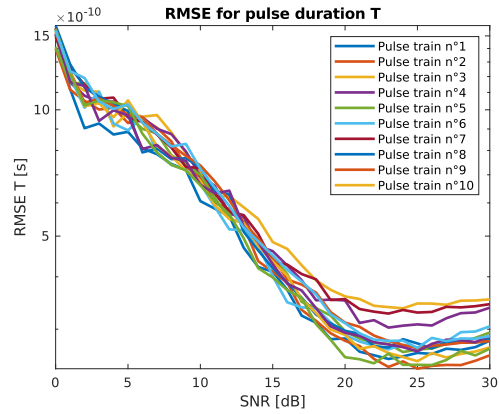
The initial observation concerns the FAR plotted in figure 5.16(a). The results seem to be analogous to those presented in the previous simulations, particularly with regard to the second set of parameters. Once again, the PRI are too short to get a substantial number of false alarms at high SNR. Nevertheless, the presented results and others obtained with a higher threshold

⁵ The emitted signal is stored in a closed loop for subsequent analysis, in case there are any differences between the desired emission and the actual emission.

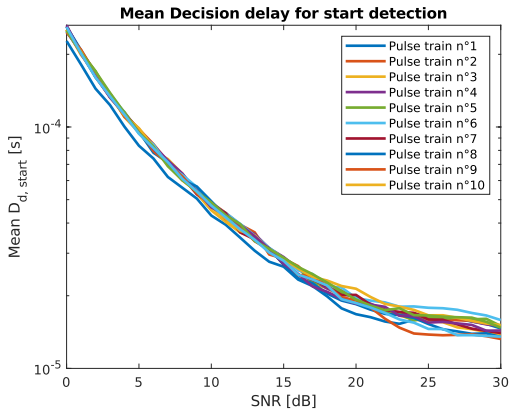
($\alpha = 5.10^{-3}$) yields the same capacity to detect the pulse of interest. The false alarm rate does not impair the CuSum in its detection process. Regarding the measured pulse duration for each pulse train, the RMSEs presented in figure 5.16(b) yield satisfying results. This is consistent with an accurate estimation of the onsets and ends of each pulse. Each pulse train is thus correctly retrieved and analysed thanks to the CuSum. A similar observation can be made about the RMSEs of the PRIs. Let remark that the signal presents almost three seconds of silence before



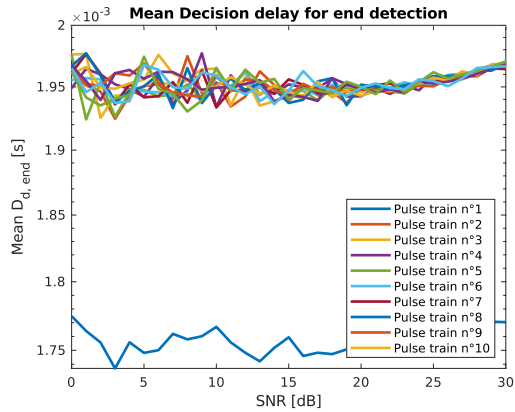
(a) FAR.



(b) RMSE for the pulse duration.



(c) Mean delay for start detection.



(d) Mean delay for end detection.

Figure 5.16: Results of the Monte-Carlo simulations with various performance indicators as function of the SNR for the 13 real pulse trains.

the first impulsion, which impact the estimation of the mean at high SNR. This misestimation of the distribution parameters at the beginning of the computation causes an offset in the detection of onsets and ends of a few samples. Rejecting these three seconds can improve the RMSEs results, however the parameter estimators bias pointed out here will be addressed in the next section. Lastly, the mean delay for detection of both onset and end are presented in figures 5.16(c) and 5.16(d). These figures demonstrate consistency with the observations made

on simulated data, exhibiting the same behaviours and quick decision time overall. With regard to the end detection, again the limit of $K = 200$ samples is reached for all of the pulse trains ($\frac{K}{F_s} = 2 \times 10^{-3}$ s).

This first real signal gives convincing results and shows that the CuSum algorithm has real capacities to detect signals embedded in noise, hence enabling a quite accurate parameters estimation. Nevertheless, this real signal is still too "clean" to really trouble the CuSum algorithm and to highlight its limits.

Congested radar signals The next radar signals are more complex. The figures 5.17(a), 5.17(b) and 5.17(c) display three different versions of pulse trains emitted by the Nostradamus radar⁶ and received by the ROS radar⁷. These signals have interacted with the ionosphere and

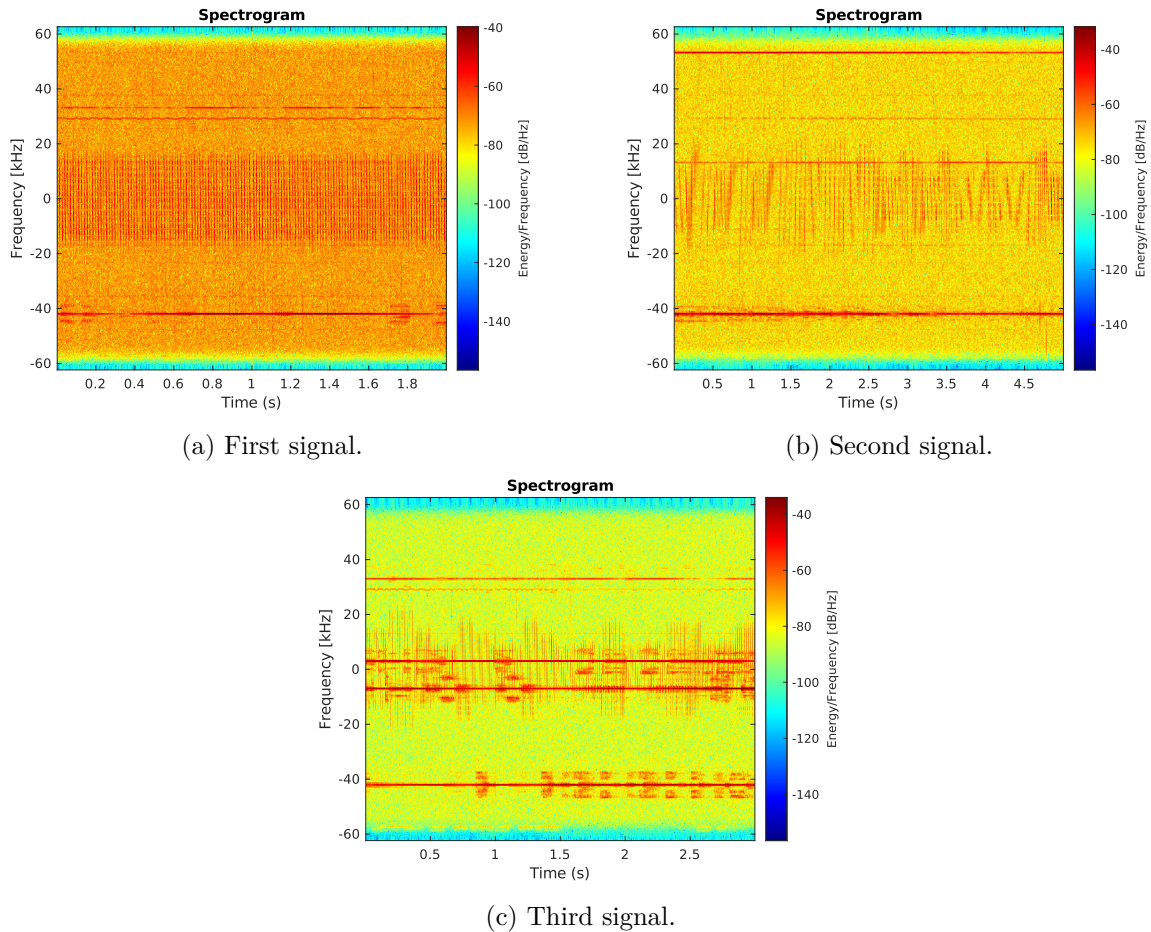


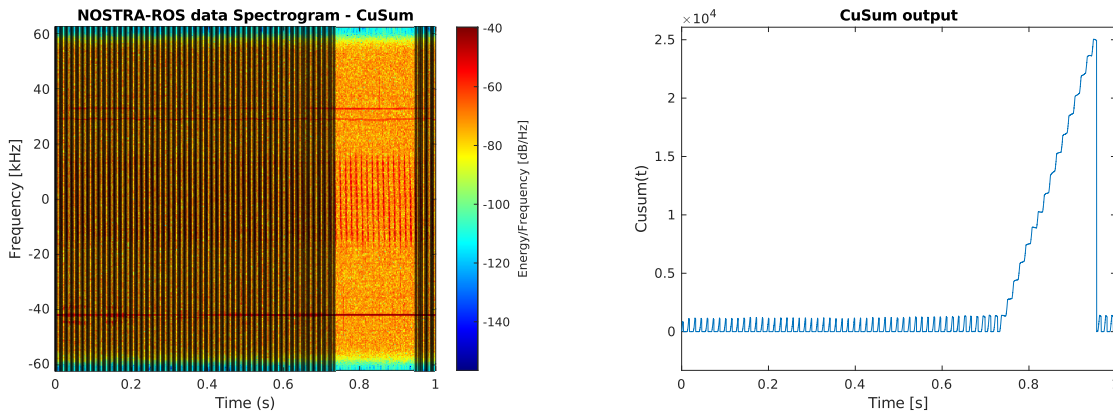
Figure 5.17: Spectrograms of NOSTRA-ROS radar signals received at different moment of the day.

6. Over The Horizon (OTH) radar with the ability to detect targets at very long range.

7. Surface Wave Radar (SWR) set up to monitor the Mediterranean sea.

the pulse trains are mixed with unknown interfering continuous frequencies at the reception. The sampling frequency is of $F_s = 125\text{kHz}$. From figure 5.17(a) to figure 5.17(c), the signals become increasingly polluted, thereby rendering the detection of radar signals challenging. Each signal is a succession of chirp pulse trains with various parameters as investigated earlier. However, the true TOA are not available and the objective here is solely the detection of pulses.

For the first signal, the CuSum algorithm has nearly no difficulties to retrieve the onset and end of pulses. Figures 5.18(a) and 5.18(b) illustrate this outcome for one second of the whole data set. The peculiar saw-tooth pattern exhibited by the CuSum is clearly visible in figure 5.18(b), which indicates the detection of the pulses. Nevertheless, it is possible that during a part of the signal, the CuSum may show a stairs-like behaviour. This is due to the incapacity to identify the end of a detected pulse before the next pulse onset. This result can be explained by the higher energy level of the constant frequency component around $CF = -42\text{kHz}$, which then becomes preponderant for the CuSum. A second run on this portion is sufficient to detect the missing pulses. Another solution could be to lower the maximum threshold to detect the missing pulses. This highlights a first limitation of our algorithm: considering the whole signal for parameters estimation smooths the overall behaviour and hinders the algorithm capacities as demonstrated. This motivates the design of a windowed CuSum presented later on.



(a) Part of the first signal with the detected pulses.

(b) CuSum output.

Figure 5.18: Results of the CuSum algorithm on the first signal.

The remaining two signals present a more challenging scenario due to the presence of constant frequencies that interfere with the reception. Their energy is such that the CuSum may fail to detect the relevant chirps. One potential solution is to initially filter the data in order to "clean" them. This phenomenon can be observed in the second signal in figures 5.19(a) and 5.19(b), where only the frequency band of interest has been kept, thus facilitating the CuSum computation. Concerning the third signal, the constant frequencies are polluting the frequency band of interest and can not be filtered out as easily. This analysis shows another limitation

of the CuSum algorithm when confronted with congested signal data. A potential solution has been quickly explored with a 2D-version of the CuSum and could be further investigated (see Appendices E.4).

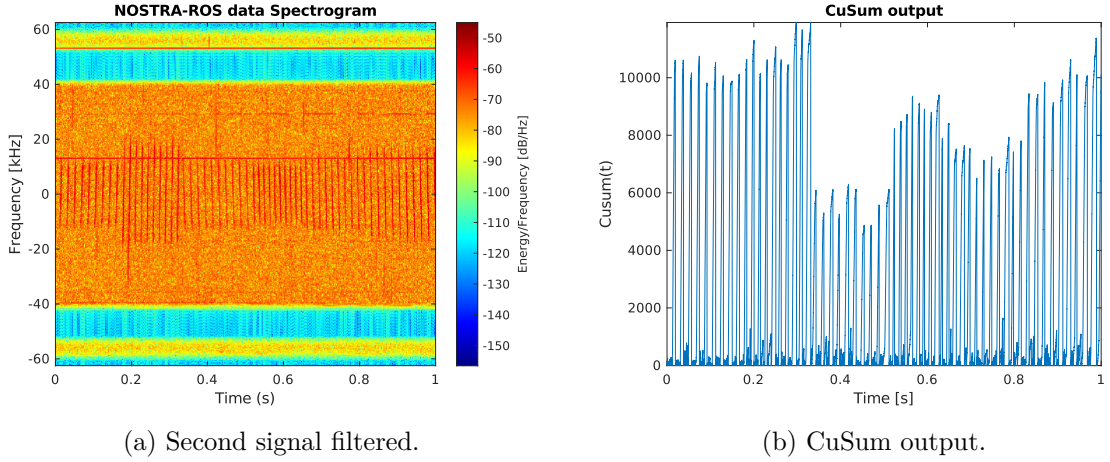


Figure 5.19: Results of the CuSum algorithm on the second filtered signal.

The CuSum algorithm demonstrates valuable and interesting results on both simulated and real data sets. It is evident that the threshold settings is of primary importance to ensure an accurate detection. However, the last observations showed that the actual version of the algorithm encounters limitations when facing congested signals. Another crucial aspect not yet discussed is the significant loss of results at very low SNR. Indeed, the detection results are really impacted at very low SNR and this could be somewhat improved by carefully looking at the parameters estimators used in the CuSum computations.

5.5 A Bias in the Estimator

The estimation of the signal distribution parameters are essential for the proper functioning of the CuSum algorithm. Unfortunately, some estimators proposed in the literature, in our case for the parameter ν , the amplitude of the signal, may be biased thus degrading the capacity of the CuSum. The following investigation describe these biased approaches and alternative solutions inspired from the Magnetic Resonance Imaging (MRI) literature.

5.5.1 Empirical estimator

To compute the CuSum, it is necessary to estimate the distribution parameters ν and $\frac{\sigma_0^2}{2}$. These parameters can be linked to the theoretical Rice distribution parameters, whose theoretical

mean \bar{r} and variance σ_r^2 are given by [32]

$$\bar{r} = e^{\frac{-\nu^2}{2\sigma_0^2}} \sqrt{\frac{\pi\sigma_0^2}{4}} \left[\left(1 + \frac{\nu^2}{\sigma_0^2}\right) I_0\left(\frac{\nu^2}{2\sigma_0^2}\right) + \frac{\nu^2}{\sigma_0^2} I_1\left(\frac{\nu^2}{2\sigma_0^2}\right) \right], \quad (5.21)$$

$$\sigma_r^2 = \langle M^2 \rangle - \bar{r}^2 = \sigma_0^2 + \nu^2 - \bar{r}^2, \quad (5.22)$$

where I_k is the k -th order modified Bessel function, $\bar{r} = \langle M \rangle$ and $\langle M^2 \rangle = \sigma_0^2 + \nu^2$ are the first and second moment of the Rice distribution. In an initial work [101], these parameters were obtained by computing the empirical mean, \hat{r} , and variance, $\hat{\sigma}_r^2$, of the observed signal. It can be argued that these estimators are justified at high SNR, given that the Rice distribution is very similar to a Gaussian distribution [32] (see Appendix E.3). However as SNR decreases, the Rice distribution strongly deviates from a Gaussian distribution. The average value \bar{r} defined in (5.21) and estimated by \hat{r} no longer coincides with the sought amplitude ν of the signal anymore, leading to biased parameter estimators and degraded detection results that our initial work did not take into account [101]. The objective of the next paragraphs is to compare different estimators to reduce the mentioned bias and to improve the estimation at low SNR.

5.5.2 Alternative estimators

In the MRI literature (see eg.[33][102]), the Rayleigh-Rice distribution is also often considered and is known to face the problem of biased estimators. To rectify this bias, a first alternative estimator was proposed in [102] where $\hat{\nu}$ was obtained via the following relation:

$$\hat{\nu}_1 = \sqrt{\hat{r}^2 - \frac{\sigma_0^2}{2}}. \quad (5.23)$$

This relation is derived from the behaviour of the Rice distribution at high SNR [102]. Nevertheless, this new estimator is shown later to overestimate the true amplitude at low SNR. Moreover, this estimator needs a prior estimation of the noise variance. Therefore, the authors of [33] proposed an alternative approach based solely on the computation of the mean \bar{r} and the variance σ_r^2 known as the Koay inversion technique. Consider the definition of the Rice variance given in equation (5.22). It is possible, by substituting $\Theta^2 = \frac{2\nu^2}{\sigma_0^2}$ and factoring out $\frac{\sigma_0^2}{2}$, to write

$$\sigma_r^2 = \langle M^2 \rangle - \bar{r}^2 = \xi(\Theta) \frac{\sigma_0^2}{2}, \quad (5.24)$$

where the correction factor, $\xi(\Theta)$, can then be expressed by

$$\xi(\Theta) = 2 + \Theta^2 - e^{-\frac{\Theta^2}{2}} \frac{\pi}{2} \left[\left(1 + \frac{\Theta^2}{2}\right) I_0\left(\frac{\Theta^2}{4}\right) + \frac{\Theta^2}{2} I_1\left(\frac{\Theta^2}{4}\right) \right]^2. \quad (5.25)$$

Assuming that by the method of moments the mean and variance of the magnitude are easily estimated, a fixed point formula of Θ can be obtain. From the relation between variances (5.24), the correction factor can also be expressed as

$$\xi(\Theta) = 2 + \Theta^2 - \frac{2\bar{r}^2}{\sigma_0^2}. \quad (5.26)$$

Replacing σ_0^2 by $\frac{2\sigma_r^2}{\xi(\Theta)}$, the fixed point formula is obtained:

$$\Theta = \sqrt{\xi(\Theta) \left[1 + \frac{\hat{r}^2}{\hat{\sigma}_r^2} \right] - 2} = h(\Theta). \quad (5.27)$$

By looking for the convergence of $|h(\Theta) - \Theta|$ to 0, the fixed point formula has a unique solution $\hat{\Theta}$ that can be found as long as the following inequality is verified

$$\frac{\hat{r}^2}{\hat{\sigma}_r^2} \geq \frac{\pi}{4 - \pi}. \quad (5.28)$$

This lower bound derives from the limit at very low SNR, where the Rice distribution approximates a Rayleigh distribution with parameter $\frac{\sigma_0^2}{2}$ and the theoretical mean and variance then become

$$\bar{r} = \sqrt{\frac{\sigma_0^2 \pi}{4}}, \quad (5.29)$$

$$\sigma_r^2 = \sigma_0^2 \left(1 - \frac{\pi}{4} \right). \quad (5.30)$$

This tendency is illustrated later on with yellow dashes in Figure 5.20. Finally, when $\hat{\Theta}$ is found and the correction factor is determined, a new estimator of the amplitude ν with reduced bias can be estimated by manipulating equation (5.26), leading to

$$\hat{\nu}_2 = \sqrt{\hat{r}^2 + (\xi(\hat{\Theta}) - 2) \frac{\sigma_0^2}{2}}, \quad (5.31)$$

or

$$\hat{\nu}_3 = \sqrt{\hat{r}^2 + \left(1 - \frac{2}{\xi(\hat{\Theta})} \right) \hat{\sigma}_r^2}, \quad (5.32)$$

depending whether the noise variance σ_0^2 is known or not. Note that the estimation of σ_0^2 can be done afterwards with equation (5.31) if $\hat{\nu}_3$ has been calculated.

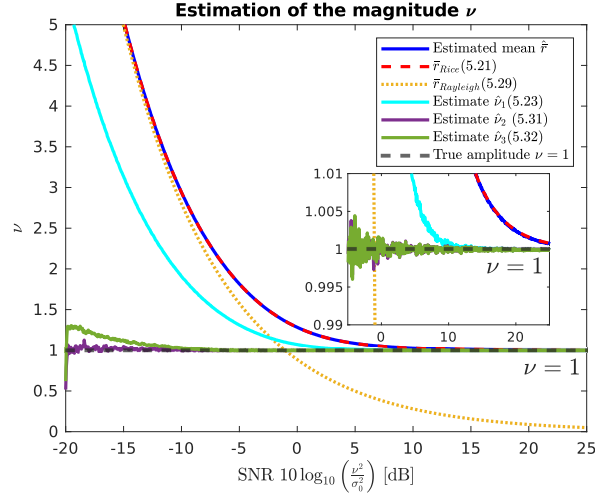


Figure 5.20: Estimation of the amplitude ν as a function of the SNR $= 10 \log_{10} \left(\frac{\nu^2}{\sigma_0^2} \right)$ (MC= 100 simulations).

5.5.3 Comparison of the estimators

Monte-Carlo (MC) simulations were computed for varying SNR with 100 trials at each SNR in order to observe the behaviour of the different estimators. Figure 5.20 presents the performances of the estimators of ν described above in the case of a unit amplitude chirp corrupted by noise. The dark blue line represents the estimated mean $\hat{\nu}$ of the magnitude while the theoretical value (5.21) is shown in red dashes. The black dashes represent the signal unit amplitude and the bias of the empirical mean at low SNR is therefore visible.

The first alternative estimator (5.23) is represented in cyan in Figure 5.20 and, as mentioned earlier, it offers a proper estimation for SNR > 10 dB but is still limited at lower SNRs. The estimates (5.31) and (5.32) are respectively represented by the purple and green lines. It is evident that at low SNR, both estimators provide highly accurate results as long as the Rice and Rayleigh distributions stay differentiated and the lower bound mentioned before is not attained (SNR < -10 dB). The fact that (5.23) approximates the estimator obtained with (5.31) or (5.32) can be explained by the limit of the correction factor ξ at high SNR which tends to 1. The Table 5.2 summarises the bias measurement of the different considered estimators for some SNRs varying from -5 dB to 25 dB.

Another way to look at the improvement made with the new estimator is to consider the Kolmogorov-Smirnov test (KS test) [104], which measures the distance between the empirical distribution function $F_n(r)$ of the signal and the Cumulative Distribution Function $F_{\hat{\nu}, \hat{\sigma}_0^2}(r)$ (CDF) of a hypothetical distribution

$$D_n = \sup |F_n(r) - F_{\hat{\nu}, \hat{\sigma}_0^2}(r)|. \quad (5.33)$$

SNR	-5dB	5dB	15dB	25dB
\hat{r}	8.2×10^{-1}	8.4×10^{-2}	7.8×10^{-3}	7.2×10^{-4}
Estimate $\hat{\nu}_1$ (5.23)	3.1×10^{-1}	8.2×10^{-3}	1.1×10^{-4}	7×10^{-5}
Estimate $\hat{\nu}_2$ (5.31)	2.6×10^{-4}	3.7×10^{-4}	1.7×10^{-4}	7.1×10^{-5}
Estimate $\hat{\nu}_3$ (5.32)	9.1×10^{-4}	1.2×10^{-4}	2×10^{-4}	1.1×10^{-4}

Table 5.2: Bias evolution of the estimators of ν [103].

The closer the hypothetical distribution is to the empirical distribution, the smaller the distance. Figure 5.21 gives a glimpse on the improvement made with the new estimator. Again in dark blue, the bias in the empirical estimator \hat{r} reverberates in the KS test. On the contrary, the robust estimators (purple and green lines) achieve a perfect fit with a Rice distribution visible in red dashes.

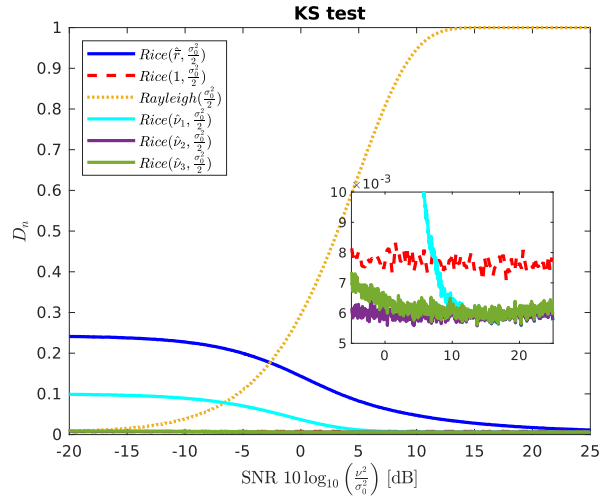


Figure 5.21: KS test for different estimates of amplitude (MC= 100 simulations).

The first observations show that the new estimators (5.31) and (5.32) are more robust and the latter one is even independent of the prior estimation of the noise variance. In the next section, the CuSum algorithm is tested with this new estimator to improve the detection performance at low SNR.

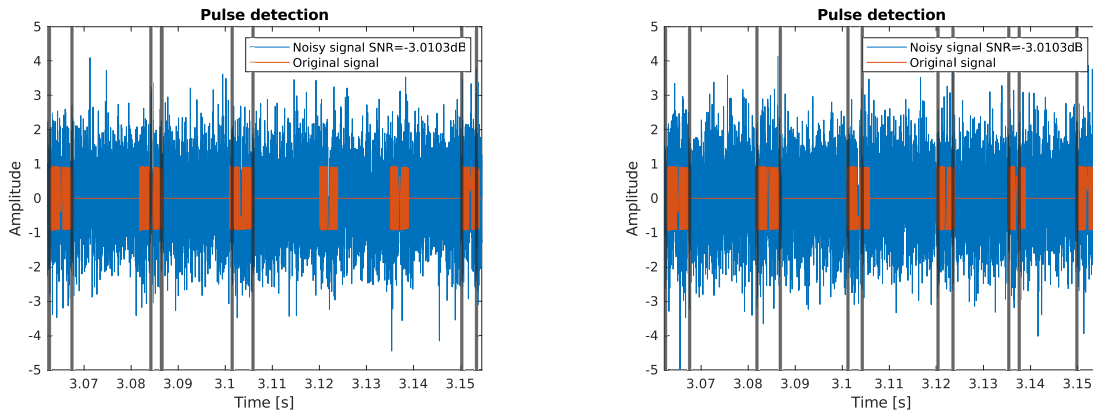
5.5.4 Improved CuSum

With a more robust estimator, the CuSum also needs to evolve. Compared to the version implemented and documented before, the CuSum algorithm in the following section is a Windowed-CuSum. Instead of estimating the distributions parameters over the whole signal, the estimation is done on a sliding window. The new estimator is thus calculated on each window

and the CuSum is computed with the evaluated parameters at each instant. The comparison with previous results from section 5.4 illustrates the improvements made at low SNR.

Simulated data The enhanced windowed version of the CuSum consists in evaluating the mean \bar{r} and variance σ_r^2 of the magnitude with a window centred around the considered sample. The algorithm estimates Θ to calculate the correction factor and to achieve reduced bias in the estimation of the amplitude ν . The CuSum was computed over a pulse train composed of 20 chirps with a duration of $T_1 = 19.66\mu\text{s}$, a bandwidth of $B_1 = 26.73\text{MHz}$ and a Pulse Repetition Interval of $T_r = 10T_1$. Noise was added to evaluate the results with Monte-Carlo simulations (100 iterations) for SNR varying from -10 to 10dB and window size varying from $0.5T_1$ to $1.5T_1$. With such a configuration, the improved CuSum was able to detect the 20 pulses until -6dB with a decreasing efficiency until -10dB whereas the previous CuSum version [101] missed every detection below -3dB . Parameters such as the duration T_1 or PRI were accurately evaluated (Root Mean Square Error of the order of 10^{-5} to 10^{-6}s) even at low SNR. The thresholds setting follows the methodology described in [101] with a false alarm rate $\alpha = 5 \times 10^{-5}$.

Real data The sequence of 13 pulse trains introduced in section 5.4.2 is again considered to illustrate the improvement achieved at very low SNR. Noise is added to the originally high SNR signal to get a low SNR (-3dB) and the first CuSum version [101] is compared to the enhanced version of this paper. It appears in Figure 5.22(a), that the first CuSum version may fail to detect some pulses and may be inaccurate regarding the onset and ending of detected pulses. Figure 5.22(b) illustrates the improvement achieved by the new estimator on the same portion of the signal. While some inaccuracies remain, the detection is overall better.



(a) Detection of pulses with the CuSum version in [101].

(b) Detection of pulses with the more robust estimator (5.32).

Figure 5.22: Illustration of the improvements made with the enhanced CuSum algorithm compared to previous work in [101].

Monte-Carlo simulations (100 iterations) were also conducted to observe the effect of window size. Figure 5.23 illustrates the number of missed detection against SNR with the previous and improved CuSum versions with two different windows. If the new estimator once again shows improvement at low SNR, its quality depends on both the window size and the SNR. The large window (10ms) seems better at low SNR than the shorter window (5ms) but should be avoided at higher SNR: a window that is too large can not accurately estimate the noise portion at high SNR which hinders the CuSum algorithm to have successive minima and maxima associated to the onset and end of pulses, causing the missed detection. The false alarm rate in this case is $\alpha = 9 \times 10^{-5}$.

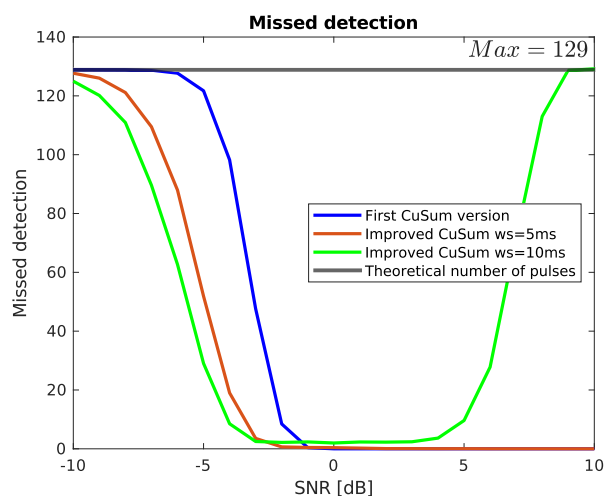


Figure 5.23: Number of missed detection with different window sizes (ws) as function of SNR (MC= 100 simulations) [103].

5.6 Conclusion

This concludes the chapter about the CuSum algorithm. The statistical approach brought by the change point detection framework and the CuSum algorithm has been really rewarding for the unknown signal detection problem. It can be a useful tool for segmenting data involving sounds generated by animals, where transmitted waveforms are not well known at the receiver side. In a radar context, the CuSum algorithm demonstrates interesting capacities in retrieving the onsets and ends of unknown radar signals without prior knowledge. The underlying principles (signal distribution, thresholds, performance indicators, etc) have been investigated and improved (parameters estimator) to propose an efficient radar CuSum approach.

CONCLUSION

6.1 Conclusion

The time has come to conclude three years of research on bio-inspired waveforms and their radar processing.

In order to address this issue, bats have been the primary focus of this work. The initial objective was to understand the manner in which bats construct their signals and to attempt to replicate them. This constituted a first approach to signal processing from both an acoustic and a biological point of view. An effective potential solution to mimic bat waveforms has been found in the Parsons function. Its flexibility, made possible with the single parameter a , enabled the mimicking of bat waveforms with a high degree of accuracy, thereby fulfilling the bio-inspired component of the project.

Obviously, the new waveform was directly put into test for radar applications through the evaluation of its capacities. The classical radar processing combined to a comparative analysis with known radar waveforms validated the potential of the Parsons function as a radar waveform. The ambiguity function and the Cramér-Rao Lower Bounds were calculated for this specific function. From simulations to real experiments, the Parsons function thus showed noteworthy precision capacities in estimation and a tangible efficiency in radar applications. Moreover, the application of the Parsons function in a multistatic radar framework proved to be efficient according to the simulations results. The bio-inspired waveform thus proposed can be considered as one solution to the spectrum management problematic, while maintaining valuable radar performance. In addition, a bio-inspired processing has also been briefly investigated to propose a Doppler estimation scheme adapted to the Parsons waveform.

Beside the bio-inspired waveform investigation, a change-point detection algorithm has been implemented. The algorithm, named CuSum, was initially chosen and adapted for the straightforward segmentation of the authentic bat sequences studied at the beginning of the thesis. Its capabilities were such that it was further studied for potential applications in a radar framework. While remaining in the domain of waveform analysis, it has been decided to apply the CuSum algorithm for the detection of unknown radar signals embedded in noise. To assess its performance, simulations and real signals were fed to the algorithm and the retrieval of the onset and end of unknown waveforms has been performed.

As a final conclusion, the Parsons function, a bat-inspired waveform, has been proposed for radar applications and proved its efficiency as a potential radar waveforms. Moreover, both the classical and bio-inspired processing are compatible with the bio-inspired waveform. Future work and research will now decide the fate of the Parsons function as a radar waveform.

6.2 Perspectives

In contrast with the title of the section 5.3 in the previous chapter, the research on bio-inspired radar and sonar is still in progress. The work presented in this thesis represents only a fragment of the research conducted in the field of bio-inspiration. The following points provide a non-exhaustive list of future studies that could complement and extend the scope of this thesis.

First of all, the impact of harmonics in a radar framework could be investigated. Section 2.2.3 introduced the use of harmonics in bat signals, and the literature on the subject indicates that these harmonics exert a significant influence on the capacities of bats. It may notably be used for clutter rejection [34] and ambiguities removal [35]. In addition, the ambiguity function and the Cramér-Rao Lower Bounds calculations may be of interest for such configurations.

The amplitude modulation also offers a valuable area of research, although radar systems are not yet particularly designed for such modulation. The amplitude modulation of emitted and received waveforms could be beneficial for target recognition, as it is for bats.

Another important factor to understand in the context of biomimicry is the brain and its functioning. As stated in [8], enhancing our comprehension of the mammalian brain, and in this case the bat brain, may inspire future research. In particular, the SCAT may be improved or the relationship between harmonics and their processing could be entirely understood. This is closely linked to the understanding of the different mammalian sensors for cognitive approach. Being able to vary the parameters of emission in a manner similar to that observed in bats during foraging could be highly advantageous for adaptation of the emission over time and for specific targets.

Regarding the proposed bio-inspired waveform in this thesis, further research could be carried on. The optimisation of the function could be investigated to better apprehend the sidelobe level with a solution other than the MMF. The Doppler mismatch loss evaluated in the multistatic configuration could be also better apprehended. The design of other functions is of course not to be put aside. For instance, it may be interesting to look at a polynomial approach or to use wavelets to design different bio-inspired functions. The use of the Parsons function for the multistatic configuration could be tested with real experiments to complement the simulations that have already been presented.

Regarding the CuSum algorithm, the research is still in progress. The limitations encountered with congested signals and very low SNR encourage further studies, like the 2D-CuSum

version presented in appendix E.4. Moreover, the threshold settings and the statistical background selected in this thesis could be put into question. For example, in situations where the Rayleigh-Rice distribution model is not valid, what would be the appropriate distribution model? Alternative approaches to threshold settings could be explored, in particular regarding the new windowed version presented in section 5.5.4.

To conclude this thesis and with respect to the ideas developed in this last chapter, I personally think that the following quote outlines perfectly the disguised advice a bat could give to a researcher on the bio-inspired radar.

“You think darkness is your ally. But you merely adopted the dark. I was born in it. Formed by it...”, Bane from the Dark Knight Rises.

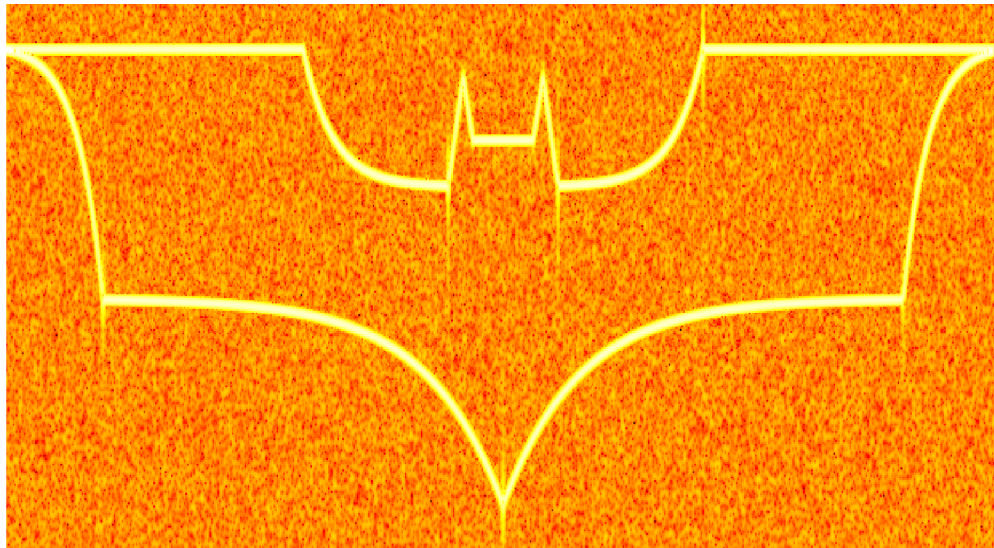


Figure 6.1: Batman logo made of Parsons waveforms.

Appendices

DOPPLER INVARIANCE

More details are available for instance in the original paper from Yang and Sarkar [105]. Consider the wideband case, then a target with a relative movement with respect to the radar induces a time-delay in the returning signal along with a Doppler compression (or expansion) of the originally transmitted waveform. The returning signal can then be written as

$$r(t) = \sqrt{\eta_d} u[\eta_d(t - \tau)], \quad (\text{A.1})$$

where $u(t)$ is the transmitted waveform, τ the delay and η_d the Doppler factor defined by

$$\eta_d = \frac{c - v_r}{c + v_r}, \quad (\text{A.2})$$

where c is the velocity of the signal and v_r the relative velocity between the target and the radar. Taking the example of the chirp, the returning signal becomes:

$$r(t) = \frac{\text{Rect}\left\{\frac{t}{T}\right\}}{\sqrt{T}} \sqrt{\eta_d} e^{2i\pi\eta_d f_0(t-\tau)} e^{2i\pi\gamma(\eta_d(t-\tau))^2}, \quad (\text{A.3})$$

and the derived instantaneous frequency is then

$$f_d(t) = \eta_d f_0 + 2\gamma\eta_d^2(t - \tau). \quad (\text{A.4})$$

According to [105], a Doppler invariant waveform should satisfies the following equation

$$f(t) = f_d(t - t_0), \quad (\text{A.5})$$

where t_0 is a constant time shift and $f(t)$ is the instantaneous frequency of the original waveform. Therefore for the chirp:

$$f_0 + 2\gamma t = \eta_d f_0 + 2\gamma\eta_d^2(t - \tau - t_0) \Rightarrow t_0 = \frac{f_0(\eta_d - 1) + 2\gamma t(\eta_d^2 - 1)}{2\gamma\eta_d^2} - \tau. \quad (\text{A.6})$$

The above equation indicates that for a chirp, t_0 is a function of time and the chirp is thus not Doppler invariant. In the case of a HFM waveform, the derived instantaneous frequency is

$$f_d(t) = \frac{f_0 \eta_d}{1 + \kappa \eta_d (t - \tau)}. \quad (\text{A.7})$$

The criterion then becomes

$$\frac{f_0}{1 + \kappa t} = \frac{f_0 \eta_d}{1 + \kappa \eta_d (t - \tau - t_0)} \Rightarrow t_0 = \frac{1 - \eta_d}{\kappa \eta_d} - \tau. \quad (\text{A.8})$$

In this case, t_0 is a constant under the hypothesis that v_r is constant. This means that the HFM waveform is Doppler invariant.

FSST AND RIDGES EXTRACTION

The analysis of bat signals, besides the need to extract each pulse thanks to the CuSum, also required the separation of each harmonic within a single pulse. In order to retrieve these harmonics, the Fourier Synchrosqueezed Transform (FSST) has been used in combination with a ridge extraction algorithm. Initially introduced for wavelet analysis [106][107], the synchrosqueezed transform is a frequency reallocation technique capable of extracting the harmonic components of a given signal. Based on the time-frequency space, like the spectrogram often used in this manuscript, it was then extended to the Fourier space [70]. The goal of the FSST is to "squeeze" the values in order to concentrate them around curves of instantaneous frequency, thereby providing a concentrated representation of multi-component signals. Moreover, this function is invertible, which allows for the reconstruction of each identified component. The following mathematical explanations of the FSST are derived from [70] and [108], where further detailed demonstrations are available. The signal under consideration can be expressed as a sum of K_H harmonic components

$$f(t) = \sum_{k=1}^{K_H} f_k(t) = \sum_{k=1}^{K_H} A_k(t)e^{2i\pi\varphi_k(t)}, \quad (\text{B.1})$$

where $A_k(t)$ and $\varphi_k(t)$ represent the signal amplitude and phase for each harmonic. The derivatives of the phases $\varphi_k(t)$ corresponds to instantaneous frequencies. As the FSST is based on the Short-Time Fourier Transform (STFT), it computes the following transform of the signal through a sliding window g

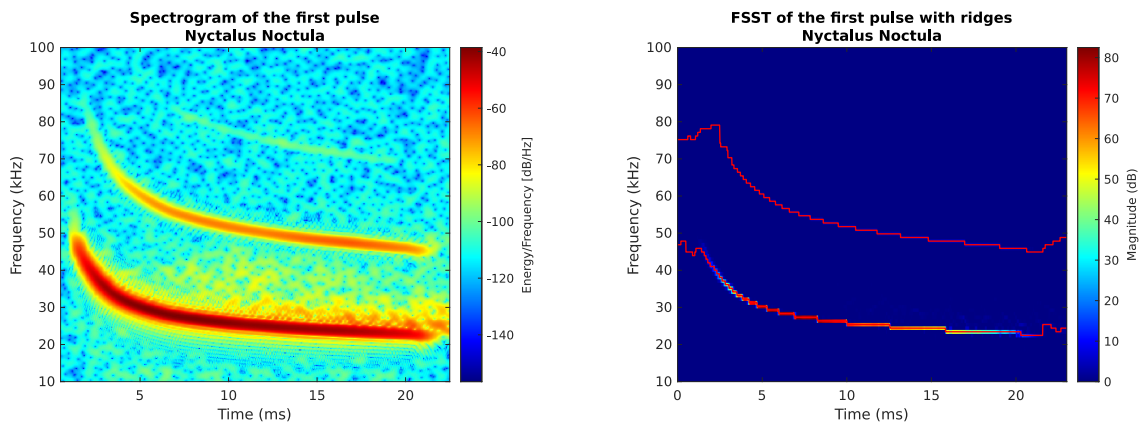
$$V_f^g(t, \eta) = \int_{\mathbb{R}} f(\tau)g(\tau - t)e^{-2i\pi\eta(\tau - t)}d\tau. \quad (\text{B.2})$$

This is the STFT with a modulation factor $e^{2i\pi\eta t}$ [70]. The FSST is then defined by

$$T_f(t, w) = \frac{1}{g(0)} \int_{\mathbb{R}} V_f^g(t, \eta)\delta(w - \hat{w}_f(t, \eta))d\eta, \quad (\text{B.3})$$

where δ is the Dirac function and $\hat{w}_f(\eta, t)$ is the local IF described by

$$\hat{w}_f(t, \eta) = \frac{1}{2i\pi} \frac{\partial_t V_f^g(t, \eta)}{V_f^g(t, \eta)}. \quad (\text{B.4})$$



(a) Original bat pulse [14].

(b) Output of the FSST with the extracted ridges.

Figure B.1: Results of the FSST process to separate two harmonics.

The operator ∂_t is the partial derivative with respect to t .

Combined with a penalised forward-backward greedy algorithm for the retrieval of the obtained ridges, the harmonics can be extracted using the inverse FSST. All of the aforementioned operations are available in the Signal Processing Toolbox from Matlab [109] with the function *fsst*, *ifsst* and *tfridge*. The outcome of this analysis is illustrated in figure B.1(b) in comparison to the original spectrogram of a bat pulse in figure B.1(a). The energy has been concentrated around the two harmonics, hence emphasising the related ridges. The retrieval of these ridges is presented in figures 3.3(a) and 3.3(b).

AMPLITUDE MODULATION AND GMM

Beyond the frequency modulation investigated in this thesis, the amplitude modulation has also been subject to a brief study. In order to replicate bat signals, both forms of modulation are to be taken into account. To recreate the amplitude modulation observed in authentic bat signals, a Gaussian Mixture Model (GMM) has been implemented.

Inspired from the work in [110] for speaker identification, the objective is to approximate the envelope of bat signals with a sum of M_G weighted Gaussian distributions. The Gaussian Mixture is given by

$$p(x|\lambda) = \sum_{i=1}^{M_G} p_i b_i(x), \quad (\text{C.1})$$

where x is the envelope vector from a bat signal in our case, $b_i(x)$ are the component probability densities and p_i are the mixture weights. The Gaussian mixture parameters are the mixture weights, the means and variances collectively represented by $\lambda = \{p_i, \mu_i, \sigma_i^2\}$ with $i = 1, \dots, M_G$. To estimate the best parameters, λ , for the GMM, a Maximum-Likelihood (ML) estimation is computed. For a sequence of T_G training vectors, $X = \{x_1, \dots, x_{T_G}\}$, the likelihood writes

$$p(X|\lambda) = \prod_{t=1}^{T_G} p(x_t|\lambda). \quad (\text{C.2})$$

Because direct computation is not feasible, the Expectation-Maximisation (EM) algorithm is employed in order to iteratively estimate the ML parameters. An initial model, designated as λ , is set to estimate a new model, $\hat{\lambda}$, such that $p(X|\hat{\lambda}) \geq p(X|\lambda)$. The new model replaces the initial model and the process is repeated until convergence is achieved. During each iteration, the mixture weights, the means, and the variances are calculated according to the following

formulas:

$$\hat{p}_i = \frac{1}{T_G} \sum_{t=1}^{T_G} p(i|x_t, \lambda), \quad (\text{C.3})$$

$$\hat{\mu}_i = \frac{\sum_{t=1}^{T_G} p(i|x_t, \lambda)x_t}{\sum_{t=1}^{T_G} p(i|x_t, \lambda)}, \quad (\text{C.4})$$

$$\hat{\sigma}_i^2 = \frac{\sum_{t=1}^{T_G} p(i|x_t, \lambda)x_t^2}{\sum_{t=1}^{T_G} p(i|x_t, \lambda)} - \hat{\mu}_i^2. \quad (\text{C.5})$$

Once the correct mixture has been obtained, results analogous to those presented in figures C.1(a) and C.1(b) may be achieved. In this example, the envelope of the first harmonic of the common noctule pulse illustrated in figure 3.2(a) is approximated thanks to a GMM of $M_G = 10$ components. Note that the synthetic envelope has been scaled to match the amplitude of the real one, hence the difference in amplitude between the two figures.

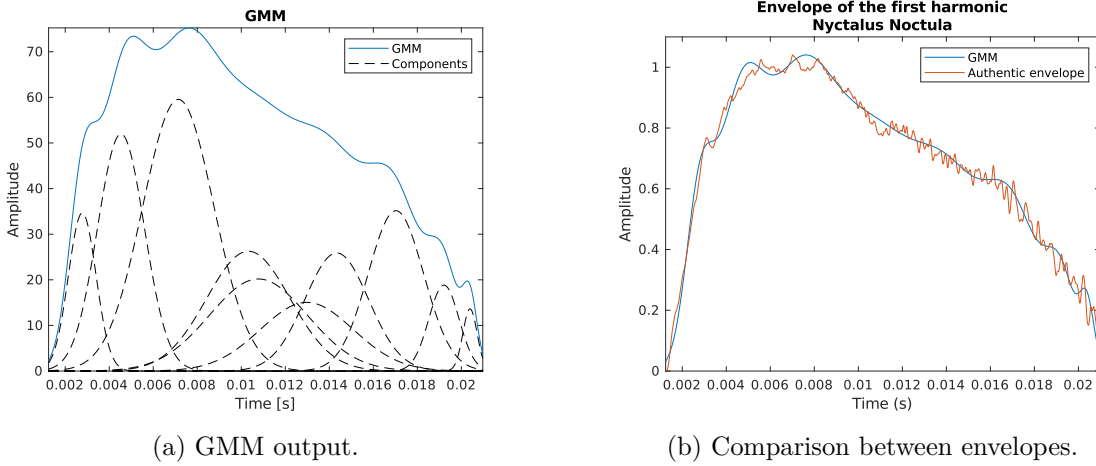


Figure C.1: Approximation of a real bat envelope [14] with a GMM.

CRLB ADDITIONAL RESSOURCES

This appendix furnishes details and results concerning the section 3.2.3, originally issued from [20].

Chirp - CRLB Matrix

$$\mathbf{J}_{AF, chirp} = \left(\begin{array}{cc} -\frac{2}{3}\pi^2\gamma^2T^2 + \frac{2}{T^2} & \frac{2}{3}\pi^2\gamma T^2 \\ \frac{2}{3}\pi^2\gamma T^2 & -\frac{2}{3}\pi^2T^2 \end{array} \right) \Bigg|_{\tau, \nu_d=0} \quad (\text{D.1})$$

HFM - CRLB Matrix

$$\mathbf{J}_{AF, HFM} = \left(\begin{array}{cc} \frac{-8\pi^2\alpha_h^2\kappa^2}{(1+\kappa T)} & \frac{8\pi^2\alpha_h}{T} \left(T - \frac{\ln(1+\kappa T)}{\kappa} \right) \\ + \frac{8\pi^2\alpha_h^2 \ln^2(1+\kappa T) + 2}{T^2} & -4\pi^2\alpha_h \ln(1 + \kappa T) \\ \frac{8\pi^2\alpha_h}{T} \left(T - \frac{\ln(1+\kappa T)}{\kappa} \right) & -\frac{2}{3}\pi^2T^2 \\ -4\pi^2\alpha_h \ln(1 + \kappa T) & \end{array} \right) \Bigg|_{\tau, \nu_d=0} \quad (\text{D.2})$$

Proof of the derivatives with respect to τ

$$\frac{\partial \chi(\tau, \nu_d)}{\partial \tau} = \frac{1}{T} \int_{-\infty}^{\infty} u(t) \text{Rect} \left\{ \frac{t}{T} \right\} \frac{\partial u^*(t + \tau) \text{Rect} \left\{ \frac{t + \tau}{T} \right\}}{\partial \tau} e^{2i\pi\nu_d t} dt, \quad (\text{D.3})$$

with

$$\frac{\partial u^*(t + \tau) \text{Rect} \left\{ \frac{t + \tau}{T} \right\}}{\partial \tau} = \frac{\partial u^*(t + \tau)}{\partial \tau} \text{Rect} \left\{ \frac{t + \tau}{T} \right\} + u^*(t + \tau) [\delta(t + \tau) - \delta(t - T + \tau)]. \quad (\text{D.4})$$

Then

$$\begin{aligned} \frac{\partial \chi(\tau, \nu_d)}{\partial \tau} &= \frac{1}{T} \int_{-\infty}^{\infty} u(t) \text{Rect} \left\{ \frac{t}{T} \right\} \left[\frac{\partial u^*(t + \tau)}{\partial \tau} \text{Rect} \left\{ \frac{t + \tau}{T} \right\} \right. \\ &\quad \left. + u^*(t + \tau) [\delta(t + \tau) - \delta(t - T + \tau)] \right] e^{2i\pi\nu_d t} dt, \end{aligned} \quad (\text{D.5})$$

which gives

$$\frac{\partial \chi(\tau, \nu_d)}{\partial \tau} = \frac{1}{T} \int_0^{T-\tau} u(t) \frac{\partial u^*(t + \tau)}{\partial \tau} e^{2i\pi\nu_d t} dt - \frac{1}{T} u(T - \tau) u^*(T) e^{2i\pi\nu_d (T - \tau)}. \quad (\text{D.6})$$

This result comes from the Dirac functions when evaluated at $t = 0$ and $t = T - \tau$ respectively.

The second derivatives with respect to τ writes as

$$\begin{aligned} \frac{\partial^2 \chi(\tau, \nu_d)}{\partial \tau^2} &= \frac{1}{T} \int_0^{T-\tau} u(t) \frac{\partial^2 u^*(t + \tau)}{\partial \tau^2} e^{2i\pi\nu_d t} dt \\ &\quad - \frac{1}{T} u(T - \tau) \left. \frac{\partial u^*(t + \tau)}{\partial \tau} \right|_{t=T-\tau} e^{2i\pi\nu_d (T - \tau)} \\ &\quad - \frac{1}{T} u^*(T) \frac{\partial u(T - \tau)}{\partial \tau} e^{2i\pi\nu_d (T - \tau)}, \\ &= c' - a' - b', \end{aligned} \quad (\text{D.7})$$

with

$$a' = \frac{1}{T} u(T - \tau) \left. \frac{\partial u^*(t + \tau)}{\partial \tau} \right|_{t=T-\tau} e^{2i\pi\nu_d (T - \tau)}, \quad (\text{D.8})$$

$$b' = \frac{1}{T} u^*(T) \frac{\partial u(T - \tau)}{\partial \tau} e^{2i\pi\nu_d (T - \tau)}, \quad (\text{D.9})$$

$$c' = \frac{1}{T} \int_0^{T-\tau} u(t) \frac{\partial^2 u^*(t + \tau)}{\partial \tau^2} e^{2i\pi\nu_d t} dt. \quad (\text{D.10})$$

CUSUM APPENDICES

E.1 Complex Signal Distribution

At a given time, the considered signal can be described as

$$x = re^{i\varphi} = \Re\mathbf{e}(x) + i\Im\mathbf{m}(x), \quad (\text{E.1})$$

where $\Re\mathbf{e}(x) = r \cos \varphi$ and $\Im\mathbf{m}(x) = r \sin \varphi$ and the phase $\varphi \sim \mathcal{U}[0, 2\pi]$. In [91], it is shown that the distribution of a circular complex signal depends only on the distribution of its amplitude r :

$$\begin{aligned} p(x) &= p(\Re\mathbf{e}(x), \Im\mathbf{m}(x)) \\ &= p(r, \varphi) |J_{r,\varphi}|^{-1} \\ &= \frac{1}{2\pi} p(r) \frac{1}{r}. \end{aligned} \quad (\text{E.2})$$

The matrix $|J_{r,\varphi}|$ is the determinant of the Jacobian matrix used for the polar-Cartesian coordinates transformation and defined as

$$|J(r, \varphi)| = \begin{vmatrix} \cos \varphi & -r \sin \varphi \\ \sin \varphi & r \cos \varphi \end{vmatrix} = r. \quad (\text{E.3})$$

E.2 Noise Distribution

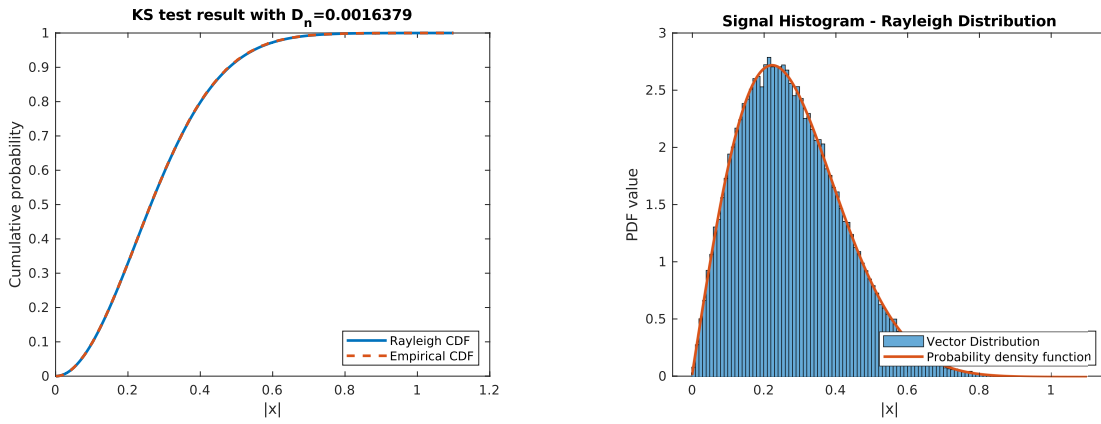
The CuSum algorithm considers the modulus of the received signal. Then, in the presence of a Gaussian circular noise where both the real and imaginary parts follow a normal distribution $\mathcal{N}(0, \frac{\sigma_0^2}{2})$, the noise variable $r = |x| = \sqrt{\Re\mathbf{e}(x)^2 + \Im\mathbf{m}(x)^2}$ is Rayleigh distributed ($r \sim \text{Rayleigh}(\frac{\sigma_0^2}{2})$) and its probability density function is given by:

$$p\left(r \mid \frac{\sigma_0^2}{2}\right) = \frac{2r}{\sigma_0^2} e^{-\frac{r^2}{\sigma_0^2}}. \quad (\text{E.4})$$

The corresponding CDF can be written

$$F_{Rayleigh} \left(r \mid \frac{\sigma_0^2}{2} \right) = 1 - e^{-\frac{r^2}{\sigma_0^2}}. \quad (\text{E.5})$$

The subsequent graphs are obtained using a noise vector with a variance of $\sigma_0^2 = 0.1$ (SNR=10dB). The KS test of the magnitude r under the Rayleigh hypothesis is plotted in figure E.1(a) along with its histogram in figure E.1(b). The KS test gives a distance of approximately 1.6×10^{-3} which consolidates the idea that the noise follows a Rayleigh distribution.



(a) Empirical and simulated CDF for a noise vector.

(b) Noise amplitude distribution.

Figure E.1: Verification of the compatibility between a Rayleigh distribution and a noise vector distribution.

The figure E.2 illustrates the results of the KS test for Monte-Carlo simulation (10,000 trials) for the real and imaginary parts with Gaussian distributions and for the magnitude with Rayleigh distribution. The dotted black lines represent the mean values of the mentioned results. Overall, the choice of the Rayleigh distribution for the pure noise component of a signal is validated through this simulations.

The variance and mean for a variable following a Rayleigh distribution of parameter $\frac{\sigma_0^2}{2}$ are given by:

$$\bar{r} = \sqrt{\frac{\sigma_0^2 \pi}{4}}, \quad (\text{E.6})$$

$$\sigma_r^2 = \sigma_0^2 \left(1 - \frac{\pi}{4} \right). \quad (\text{E.7})$$

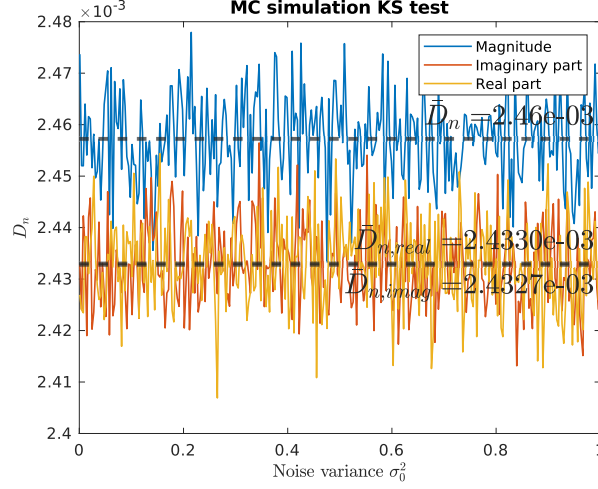


Figure E.2: Monte-Carlo simulation for a noise vector. Results of the KS tests for real part, imaginary part and magnitude.

E.3 Noisy Signal Distribution

A classic distribution to describe a noisy signal is the Rice distribution, named after its creator [31]. It is well explained in [32] with several references to applications (radar signals analysis, optical metrology, etc.). In the case of a signal embedded in noise, the real and imaginary parts of the noisy signal are assumed to be distributed according to normal independent distributions $\mathcal{N}\left(\nu \cos \varphi, \frac{\sigma_0^2}{2}\right)$ and $\mathcal{N}\left(\nu \sin \varphi, \frac{\sigma_0^2}{2}\right)$ respectively. The following mathematical development can be found in [111] and completes the example given by Rice [31] where only the real part is distorted. Consider a circular Gaussian variable, $y = y_r + iy_i$, observed in the presence of Gaussian circular noise, $w = w_r + iw_i$. The notations \cdot_r and \cdot_i represent respectively the real and imaginary parts of a considered variable in this discussion. The noisy signal is then described by the equation $x = y + w = x_r + ix_i = (y_r + w_r) + i(y_i + w_i)$. The PDFs for x_r and x_i are given by

$$p\left(x_{r,i} \middle| \frac{\sigma_0^2}{2}\right) = \frac{1}{\sqrt{\pi\sigma_0^2}} e^{-\frac{(y_{r,i} - x_{r,i})^2}{\sigma_0^2}}. \quad (\text{E.8})$$

In our case $r = |x| = \sqrt{(y_r + w_r)^2 + (y_i + w_i)^2} = \sqrt{(\nu \cos \varphi + w_r)^2 + (\nu \sin \varphi + w_i)^2}$, where ν and φ are the amplitude and phase of the noiseless signal. Then, conditional to (ν, φ) , the distribution of x writes

$$p\left(x_r, x_i \middle| \nu, \varphi, \frac{\sigma_0^2}{2}\right) = \frac{1}{\pi\sigma_0^2} e^{-\frac{(\nu \cos \varphi - x_r)^2}{\sigma_0^2}} e^{-\frac{(\nu \sin \varphi - x_i)^2}{\sigma_0^2}}, \quad (\text{E.9})$$

and in polar coordinates

$$p\left(r, \psi | \nu, \varphi, \frac{\sigma_0^2}{2}\right) = \frac{1}{\pi\sigma_0^2} e^{-\frac{(\nu \cos \varphi - r \cos \psi)^2}{\sigma_0^2}} e^{-\frac{(\nu \sin \varphi - r \sin \psi)^2}{\sigma_0^2}} J(r, \psi), \quad (\text{E.10})$$

where ψ is the phase of the noisy signal. The determinant of the Jacobian matrix is

$$|J(r, \psi)| = \begin{vmatrix} \cos \psi & -r \sin \psi \\ \sin \psi & r \cos \psi \end{vmatrix} = r. \quad (\text{E.11})$$

Integrating over a full ψ cycle, the PDF becomes

$$p\left(r | \nu, \varphi, \frac{\sigma_0^2}{2}\right) = \frac{r}{\pi\sigma_0^2} \int_0^{2\pi} e^{-\frac{(\nu^2 + r^2 - 2\nu r \cos(\psi - \varphi))}{\sigma_0^2}} d\psi, \quad (\text{E.12})$$

where φ is a constant unaffected by the noise, which can be dismissed as the integration is done over a full cycle. Combined with the zeroth order modified Bessel function of the first kind

$$I_0(z) = \frac{1}{2\pi} \int_0^{2\pi} e^{z \cos(\psi)} d\psi, \quad (\text{E.13})$$

the Rice PDF with parameters ν and $\frac{\sigma_0^2}{2}$ is obtained as

$$p\left(r | \nu, \frac{\sigma_0^2}{2}\right) = \frac{2r}{\sigma_0^2} e^{-\frac{(\nu^2 + r^2)}{\sigma_0^2}} I_0\left(\frac{2\nu r}{\sigma_0^2}\right). \quad (\text{E.14})$$

The Rician mean and variance for a variable with parameters (ν, σ^2) are expressed by the following formulas [32]:

$$\bar{r} = \sqrt{\frac{\pi\sigma^2}{2}} L_{1/2}\left(\frac{-\nu^2}{2\sigma^2}\right), \quad (\text{E.15})$$

$$\sigma_r^2 = 2\sigma^2 + \nu^2 - \frac{\pi\sigma^2}{2} L_{1/2}^2\left(\frac{-\nu^2}{2\sigma^2}\right), \quad (\text{E.16})$$

where $L_{1/2}(z) = e^{\frac{z}{2}} \left[(1-z)I_0\left(\frac{-z}{2}\right) - zI_1\left(\frac{-z}{2}\right) \right]$ is the Laguerre polynomial.

Since statistics are a small world, the Rice distribution is closely related to the Gaussian and Rayleigh distributions. In the following paragraphs, the SNR can be defined as the ratio $\frac{\nu}{\sigma}$, and it is known that for small values ($\text{SNR} = \frac{\nu}{\sigma} \ll 1$) the Rice distribution is approximated by a Rayleigh distribution since the noise predominates over the signal of interest (ν tends to zero). On the contrary, the higher the SNR ($\gg 1$) the closer the Rice distribution is to a Gaussian distribution. In the following discussions, a noisy chirp pulse ($T = 25\mu\text{s}$, $B = 10\text{MHz}$) with a

constant magnitude $\nu = 1$ is considered.

I want to be a Rayleigh distribution At low SNR, the noise has the high ground on the signal (It's over Anakin!) and the amplitude of the signal can be neglected ($\nu \simeq 0$), which gives $I_0(z) \xrightarrow{z \rightarrow 0} 1$. Therefore, the Rice distribution can be approximated by a Rayleigh distribution

$$p(r|\sigma^2) = \frac{r}{\sigma^2} e^{-\frac{r^2}{2\sigma^2}}. \quad (\text{E.17})$$

I want to be a Gaussian distribution On the other hand, high SNRs lead to a Gaussian approximation of the Rice distribution. The value $\frac{r\nu}{\sigma^2}$ is becoming large and an asymptotic expansion of the Rice distribution is given by [21]:

$$I_\alpha(z) = \frac{e^z}{\sqrt{2\pi z}} \left[1 - \frac{4\alpha^2 - 1}{8z} + \frac{(4\alpha^2 - 1)(4\alpha^2 - 9)}{2!(8z)^2} - \frac{(4\alpha^2 - 1)(4\alpha^2 - 9)(4\alpha^2 - 25)}{3!(8z)^3} + \dots \right]. \quad (\text{E.18})$$

Therefore, the PDF of the Rice distribution becomes

$$p(r|\nu, \sigma^2) = \frac{r}{\sigma^2} e^{-\frac{(\nu^2+r^2)}{2\sigma^2}} \frac{e^{\frac{\nu r}{\sigma^2}}}{\sqrt{2\pi \frac{\nu r}{\sigma^2}}} \left[1 + \frac{1}{8 \frac{\nu r}{\sigma^2}} + \frac{9}{2!(8 \frac{\nu r}{\sigma^2})^2} - \frac{225}{3!(8 \frac{\nu r}{\sigma^2})^3} + \dots \right], \quad (\text{E.19})$$

$$\rightarrow \frac{1}{\sqrt{2\pi\sigma^2}} e^{-\frac{(\nu+r)^2}{2\sigma^2}} \sqrt{\frac{r}{\nu}}, \text{ as } \frac{r\nu}{\sigma^2} \rightarrow \infty. \quad (\text{E.20})$$

Moreover, when the sample r is concentrated around ν ($|r - \nu| < \sigma$), then $\sqrt{\frac{r}{\nu}} \approx 1$, hence, the Gaussian distribution.

The two limit behaviour limits described here are illustrated in figure E.3. The KS tests for a chirp embedded in noise have been computed at varying SNR to check the distribution closer to that of the samples. It is then observable that the Rice distribution is clearly adapted to describe the distribution of a noisy signal at every SNR. Moreover, the Gaussian approximation at high SNR and the Rayleigh behaviour at low SNR are also verified as the corresponding KS curves draw near the one of the Rice distribution at the expected SNR.

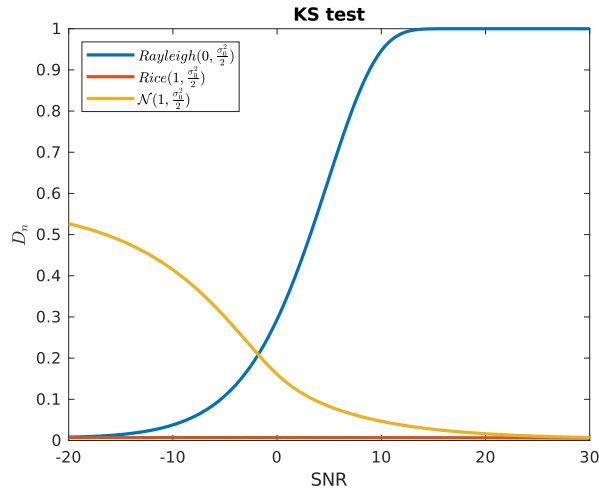
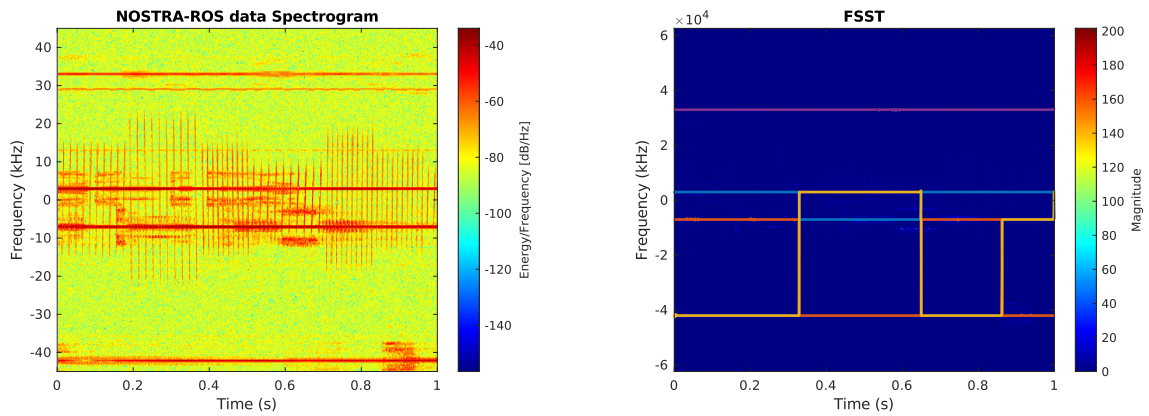


Figure E.3: Illustration of the behaviour of the Rice distribution as function of the SNR with KS tests (Monte-Carlo simulation with 1000 trials).

E.4 Towards a 2D-CuSum?

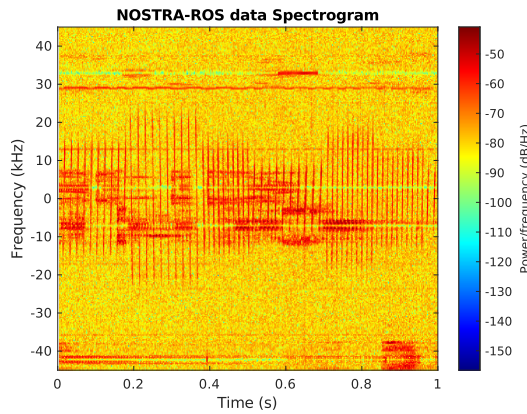
The investigation of real data showed that the CuSum algorithm has its limitation when confronted with congested signals like the one presented in figure E.4(a). A possible solution was thus explored through the examination of a two-dimensional version of the CuSum algorithm. Instead of computing the CuSum on the time series, the idea was to conduct the detection in the time-frequency space. This idea is further developed in this appendix on the signal presented in figure E.4(a). The Fourier Synchrosqueezed Transform (FSST) combined with the ridge extraction algorithm is applied in order to filter the prominent constant frequencies in a manner similar to that employed for bat signals when extracting the harmonics. Figures E.4(a) to E.4(c) illustrate the process. The energy of the constant frequencies being variable, the computation presents jumps in frequency and between ridges in figure E.4(b) because the maximum energy location changes. The ridges corresponding to the constant frequencies thus detected, their removal in the original signal can be done, which gives the filtered signal in figure E.4(c).

The objective is then to detect with the CuSum on the frequency axis at each instant t to obtain a result like in figure E.5(a), where an extract of the signal in figure E.4(c) is processed. A post-processing of the obtained detection can lead to a more accurate detection of the pulses like in figure E.5(b). This is an exploratory study that requires further investigation for application on congested signal analysis.



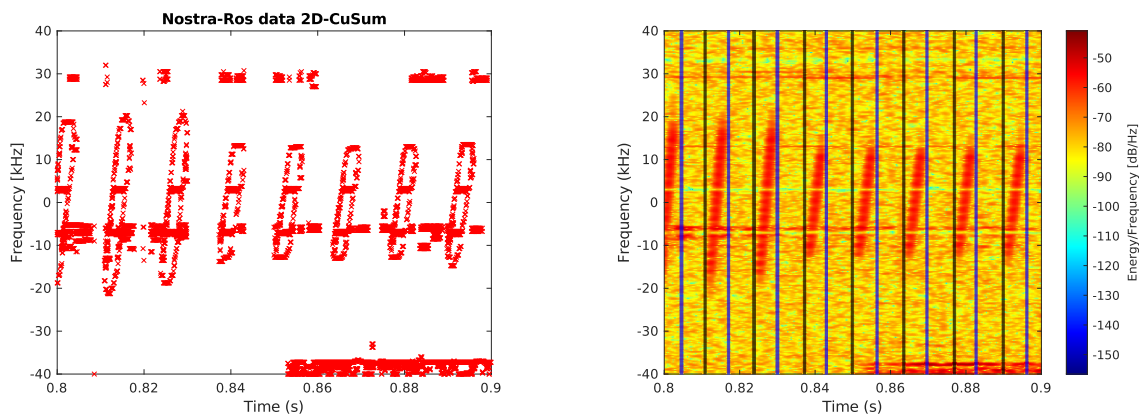
(a) Congested signal.

(b) FSST result.



(c) Congested signal with the removed ridges.

Figure E.4: FSST processing of the third NOSTRA-ROS signal in order to extract the polluting constant frequencies.



(a) Time-Frequency detection.

(b) Improved temporal detection.

Figure E.5: Illustration of the 2D-CuSum results.

BIBLIOGRAPHY

- [1] O. Blumtritt, H. Petzold, W. Aspray, and Center for the History of Electrical Engineering, Eds., *Tracking the history of radar: a publication of the IEEE-Rutgers Center for the History of Electrical Engineering and the Deutsches Museum*, ger. Piscataway, NJ: Dt. Museum, 1994, ISBN: 9780780399877.
- [2] M. I. Skolnik, *Introduction to radar systems*, 2d ed. New York: McGraw-Hill, 1980, ISBN: 9780070579095.
- [3] H. Griffiths, L. Cohen, S. Watts, *et al.*, “Radar Spectrum Engineering and Management: Technical and Regulatory Issues”, *Proceedings of the IEEE*, vol. 103, 1, pp. 85–102, Jan. 2015, ISSN: 0018-9219, 1558-2256. DOI: 10.1109/JPROC.2014.2365517.
- [4] S. D. Blunt and E. L. Mokole, “Overview of radar waveform diversity”, *IEEE Aerospace and Electronic Systems Magazine*, vol. 31, 11, pp. 2–42, Nov. 2016, ISSN: 0885-8985. DOI: 10.1109/MAES.2016.160071.
- [5] M.-E. Chatzitheodoridi, “Processing Optimization for Continuous Phase Modulation-based Joint Radar-Communication System : Application on Imaging Radar”, Phd thesis, Université Paris-Saclay, Feb. 2023.
- [6] L. Kocjancic, A. Balleri, and T. Merlet, “Numerical Characterisation of Quasi-Orthogonal Piecewise Linear Frequency Modulated Waveforms”, in *2019 Sensor Signal Processing for Defence Conference (SSPD)*, Brighton, United Kingdom: IEEE, May 2019, pp. 1–5, ISBN: 9781728105031. DOI: 10.1109/SSPD.2019.8751653.
- [7] A. Denzinger and H.-U. Schnitzler, “Bat guilds, a concept to classify the highly diverse foraging and echolocation behaviors of microchiropteran bats”, en, *Frontiers in Physiology*, vol. 4, 2013, ISSN: 1664-042X. DOI: 10.3389/fphys.2013.00164.
- [8] M. Vespe, G. Jones, and C. Baker, “Lessons for Radar”, en, *IEEE Signal Processing Magazine*, vol. 26, 1, pp. 65–75, Jan. 2009, ISSN: 1053-5888. DOI: 10.1109/MSP.2008.930412.
- [9] A. Balleri, “Biologically inspired radar and sonar target classification”, Phd thesis, University College London, Dec. 2010.
- [10] K. Georgiev, “Biologically inspired processing of radar and sonar target echoes”, Phd thesis, Cranfield University, Aug. 2017.
- [11] N. Levanon and E. Mozeson, *Radar signals*. Hoboken, NJ: J. Wiley, 2004.

-
- [12] H.-U. Schnitzler and E. K. V. Kalko, “Echolocation by Insect-Eating Bats”, en, *Bio-Science*, vol. 51, 7, p. 557, 2001, ISSN: 0006-3568. DOI: 10.1641/0006-3568(2001)051[0557:EBIEB]2.0.CO;2.
- [13] T. Gudra, J. Furmankiewicz, and K. Herm, “Bats Sonar Calls and its Application in Sonar Systems”, en, in *Sonar Systems*, N. Kolev, Ed., InTech, Sep. 2011, ISBN: 978-953-307-345-3. DOI: 10.5772/23199.
- [14] R. Specht, *Nyctalus Noctula original feeding sound*. Avisoft Biocoustics, 2009. [Online]. Available: <https://www.avisoft.com/batcalls/>.
- [15] L. A. Miller and H. J. Degn, “The acoustic behavior of four species of vespertilionid bats studied in the field”, en, *Journal of Comparative Physiology ? A*, vol. 142, 1, pp. 67–74, 1981, ISSN: 0340-7594, 1432-1351. DOI: 10.1007/BF00605477.
- [16] S. Parsons and G. Jones, “Acoustic identification of twelve species of echolocating bat by discriminant function analysis and artificial neural networks”, *Journal of Experimental Biology*, vol. 203, 17, pp. 2641–2656, Sep. 1, 2000, ISSN: 1477-9145, 0022-0949. DOI: 10.1242/jeb.203.17.2641.
- [17] J. A. Simmons, “Response of the Doppler echolocation system in the bat, *Rhinolophus ferrumequinum*”, en, *The Journal of the Acoustical Society of America*, vol. 56, 2, pp. 672–682, Aug. 1974, ISSN: 0001-4966. DOI: 10.1121/1.1903307.
- [18] B. Vogler and G. Neuweiler, “Echolocation in the noctule (*Nyctalus noctula*) and horseshoe bat (*Rhinolophus ferrumequinum*)”, en, *Journal of Comparative Physiology*, vol. 152, 3, pp. 421–432, 1983, ISSN: 0340-7594, 1432-1351. DOI: 10.1007/BF00606247.
- [19] O. Rabaste and L. Savy, “Mismatched filter optimization for radar applications using quadratically constrained quadratic programs”, *IEEE Transactions on Aerospace and Electronic Systems*, vol. 51, 4, pp. 3107–3122, 2015, ISSN: 0018-9251. DOI: 10.1109/TAES.2015.130769.
- [20] A. Balleri and A. Farina, “Ambiguity function and accuracy of the hyperbolic chirp: comparison with the linear chirp”, *IET Radar, Sonar & Navigation*, vol. 11, 1, pp. 142–153, Jan. 2017, ISSN: 1751-8792, 1751-8792. DOI: 10.1049/iet-rsn.2016.0100.
- [21] M. Abramowitz and I. A. Stegun, Eds., *Handbook of mathematical functions: with formulas, graphs, and mathematical tables* (Dover books on mathematics). New York, NY: Dover Publ, 2013, 1046 pp., ISBN: 9780486612720.
- [22] H. L. Van Trees, *Detection, estimation, and modulation theory. 3: Radar-Sonar signal processing and Gaussian signals in noise*. New York, NY: Wiley, 2001, 626 pp., ISBN: 9780471107934.
- [23] F. Le Chevalier, *Principles of Radar and Sonar Signal Processing*. Artech House, 2002.

-
- [24] M. A. Richards, *Fundamentals of radar signal processing*, Second edition. New York: McGraw-Hill Education, 2014, ISBN: 9780071798327.
- [25] P. Brouard, P. Dreuillet, A. Brun, L. Constancias, J. Peyret, and S. Attia, “HYCAM: a new S band surface radar testbed”, en, in *IET International Radar Conference 2013*, Xi’an, China: Institution of Engineering and Technology, 2013, pp. 0313–0313, ISBN: 9781849196031. DOI: 10.1049/cp.2013.0225.
- [26] M. Rozel, “Polarimetric detection of endo-clutter UAV in a low-grazing geometry”, Theses, Université Paris-Saclay, Oct. 2023.
- [27] P. A. Saillant, J. A. Simmons, S. P. Dear, and T. A. McMullen, “A computational model of echo processing and acoustic imaging in frequency-modulated echolocating bats: The spectrogram correlation and transformation receiver”, en, *The Journal of the Acoustical Society of America*, vol. 94, 5, pp. 2691–2712, Nov. 1993, ISSN: 0001-4966. DOI: 10.1121/1.407353.
- [28] A. Grossetête and C. F. Moss, “Target flutter rate discrimination by bats using frequency-modulated sonar sounds: Behavior and signal processing models”, en, *The Journal of the Acoustical Society of America*, vol. 103, 4, pp. 2167–2176, Apr. 1998, ISSN: 0001-4966, 1520-8524. DOI: 10.1121/1.421362.
- [29] E. S. Page, “Continuous inspection schemes”, *Biometrika*, vol. 41, 1, pp. 100–115, 1954, ISSN: 0006-3444, 1464-3510. DOI: 10.1093/biomet/41.1-2.100.
- [30] M. Basseville and I. V. Nikiforov, *Detection of abrupt changes: theory and application*. Englewood Cliffs, N.J: Prentice Hall, 1993, 528 pp., ISBN: 9780131267800.
- [31] S. O. Rice, “Mathematical Analysis of Random Noise”, *Bell System Technical Journal*, vol. 23, 3, pp. 282–332, 1944, ISSN: 00058580. DOI: 10.1002/j.1538-7305.1944.tb00874.x.
- [32] T. Yakovleva, “Nonlinear Properties of the Rice Statistical Distribution: Theory and Applications in Stochastic Data Analysis”, *Journal of Applied Mathematics and Physics*, vol. 07, 11, pp. 2767–2779, 2019, ISSN: 2327-4352, 2327-4379. DOI: 10.4236/jamp.2019.711190.
- [33] C. G. Koay and P. J. Basser, “Analytically exact correction scheme for signal extraction from noisy magnitude MR signals”, *Journal of Magnetic Resonance*, vol. 179, 2, pp. 317–322, 2006, ISSN: 10907807. DOI: 10.1016/j.jmr.2006.01.016.
- [34] M. E. Bates, J. A. Simmons, and T. V. Zorikov, “Bats Use Echo Harmonic Structure to Distinguish Their Targets from Background Clutter”, en, *Science*, vol. 333, 6042, pp. 627–630, Jul. 2011, ISSN: 0036-8075, 1095-9203. DOI: 10.1126/science.1202065.

-
- [35] L. Carrer and L. Bruzzone, “Solving for ambiguities in radar geophysical exploration of planetary bodies by mimicking bats echolocation”, en, *Nature Communications*, vol. 8, 1, p. 2248, Dec. 2017, ISSN: 2041-1723. DOI: 10.1038/s41467-017-02334-1.
- [36] A. Farina and G. Galati, “Surveillance radars: state of the art, research and perspectives”, in *Optimised Radar Processors*, ser. Radar, Sonar and Navigation, Institution of Engineering and Technology, 1987, pp. 161–178. DOI: 10.1049/PBRA001E_ch17.
- [37] G. Gilbert, “Historical Development of the Air Traffic Control System”, *IEEE Transactions on Communications*, vol. 21, 5, pp. 364–375, May 1973, ISSN: 0090-6778, 1558-0857. DOI: 10.1109/TCOM.1973.1091699.
- [38] R. Cowdery and W. Skillman, “Development of the airborne warning and control system (AWACS) radar”, *IEEE Transactions on Aerospace and Electronic Systems*, vol. 31, 4, pp. 1357–1365, Oct. 1995, ISSN: 0018-9251. DOI: 10.1109/TAES.1995.5930985.
- [39] C. Waldschmidt, J. Hasch, and W. Menzel, “Automotive Radar - From First Efforts to Future Systems”, *IEEE Journal of Microwaves*, vol. 1, 1, pp. 135–148, Jan. 2021, ISSN: 2692-8388. DOI: 10.1109/JMW.2020.3033616.
- [40] M. G. Amin, Ed., *Through-the-wall radar imaging*. Boca Raton, FL: CRC Press, 2011, ISBN: 9781439814765.
- [41] A. Sume, M. Gustafsson, M. Herberthson, *et al.*, “Radar Detection of Moving Targets Behind Corners”, *IEEE Transactions on Geoscience and Remote Sensing*, vol. 49, 6, pp. 2259–2267, Jun. 2011, ISSN: 1558-0644. DOI: 10.1109/TGRS.2010.2096471.
- [42] B.-H. Pham, O. Rabaste, J. Bosse, I. Hinostroza, and T. Chonavel, “GLRT Particle Filter for Non-Line of Sight Single Moving Target Tracking via Phased Array Radar”, in *2023 26th International Conference on Information Fusion (FUSION)*, Charleston, SC, USA: IEEE, Jun. 2023, pp. 1–7. DOI: 10.23919/FUSION52260.2023.10224179.
- [43] J. Kroszczyński, “Pulse compression by means of linear-period modulation”, *Proceedings of the IEEE*, vol. 57, 7, pp. 1260–1266, 1969. DOI: 10.1109/PROC.1969.7230.
- [44] C. Kiss, “Hyperbolic-FM (CHYPE)”, Army Missile Command, Redstone Arsenal, Alabama, AD-771 046, Tech. Rep., 1973.
- [45] F. Le Chevalier, *Principles of radar and sonar signal processing*. Boston: Artech House, 2002, 397 pp., ISBN: 9781580533386.
- [46] M. Taylor and M. D. Tuttle, *Bats: an illustrated guide to all species*, eng. Washington, DC: Smithsonian Books, 2018, ISBN: 978-1-58834-647-6.
- [47] P. E. Nachtigall and P. W. B. Moore, Eds., *Animal Sonar: Processes and Performance*, en. Boston, MA: Springer US, 1988, ISBN: 978-1-4684-7495-4. DOI: 10.1007/978-1-4684-7493-0.

-
- [48] M. B. Fenton, A. D. Grinnell, A. N. Popper, and R. R. Fay, Eds., *Bat Bioacoustics* (Springer Handbook of Auditory Research). New York, NY: Springer New York, 2016, vol. 54, ISBN: 9781493935253. DOI: 10.1007/978-1-4939-3527-7.
- [49] A. N. Popper, R. R. Fay, R. R. Fay, and A. N. Popper, Eds., *Hearing by Bats* (Springer Handbook of Auditory Research). New York, NY: Springer New York, 1995, vol. 5, ISBN: 9781461275770. DOI: 10.1007/978-1-4612-2556-0.
- [50] M. Nolf, “Noctule bat (*Nyctalus noctula*)”, *GFDL & CC ShareAlike 2.0*, 2006.
- [51] H. Schneider, “Große Hufeisennase”, *GFDL & CC ShareAlike 2.0*, 2006.
- [52] R. A. Holland, D. A. Waters, and J. M. V. Rayner, “Echolocation signal structure in the Megachiropteran bat *Rousettus aegyptiacus* Geoffroy 1810”, en, *Journal of Experimental Biology*, vol. 207, 25, pp. 4361–4369, Dec. 2004, ISSN: 1477-9145, 0022-0949. DOI: 10.1242/jeb.01288.
- [53] J. A. Simmons, “The resolution of target range by echolocating bats”, en, *The Journal of the Acoustical Society of America*, vol. 54, 1, pp. 157–173, Jul. 1973, ISSN: 0001-4966. DOI: 10.1121/1.1913559.
- [54] C. F. Moss and H.-U. Schnitzler, “Accuracy of target ranging in echolocating bats: acoustic information processing”, en, *Journal of Comparative Physiology A*, vol. 165, 3, pp. 383–393, 1989, ISSN: 0340-7594, 1432-1351. DOI: 10.1007/BF00619357.
- [55] C. Ming, S. Haro, A. M. Simmons, and J. A. Simmons, “A comprehensive computational model of animal biosonar signal processing”, en, *PLOS Computational Biology*, vol. 17, 2, L. J. Graham, Ed., e1008677, Feb. 2021, ISSN: 1553-7358. DOI: 10.1371/journal.pcbi.1008677.
- [56] A. Boonman and J. Ostwald, “A modeling approach to explain pulse design in bats”, en, *Biological Cybernetics*, vol. 97, 2, pp. 159–172, Jul. 2007, ISSN: 0340-1200, 1432-0770. DOI: 10.1007/s00422-007-0164-2.
- [57] G. von der Emde and D. Menne, “Discrimination of insect wingbeat-frequencies by the bat *Rhinolophus ferrumequinum*”, en, *Journal of Comparative Physiology A*, vol. 164, 5, pp. 663–671, Sep. 1989, ISSN: 0340-7594, 1432-1351. DOI: 10.1007/BF00614509.
- [58] H.-U. Schnitzler and A. Denzinger, “Auditory fovea and Doppler shift compensation: adaptations for flutter detection in echolocating bats using CF-FM signals”, en, *Journal of Comparative Physiology A*, vol. 197, 5, pp. 541–559, May 2011, ISSN: 0340-7594, 1432-1351. DOI: 10.1007/s00359-010-0569-6.

-
- [59] A. M. Boonman, S. Parsons, and G. Jones, “The influence of flight speed on the ranging performance of bats using frequency modulated echolocation pulses”, en, *The Journal of the Acoustical Society of America*, vol. 113, 1, pp. 617–628, Jan. 2003, ISSN: 0001-4966. DOI: 10.1121/1.1528175.
- [60] W. M. Masters and K. A. S. Raver, “Range discrimination by big brown bats (*Eptesicus fuscus*) using altered model echoes: Implications for signal processing”, en, *The Journal of the Acoustical Society of America*, vol. 107, 1, pp. 625–637, Jan. 2000, ISSN: 0001-4966, 1520-8524. DOI: 10.1121/1.428328.
- [61] M. Götttsche, *Rhinolophus ferrumequinum distress call*. Avisoft Bioacoustics, 2009. [Online]. Available: <http://www.avisoft.com/animal-sounds/#EugeneMcKeown>.
- [62] N. Suga, W. E. O’Neill, and T. Manabe, “Cortical Neurons Sensitive to Combinations of Information-Bearing Elements of Biosonar Signals in the Mustache Bat”, en, *Science*, vol. 200, 4343, pp. 778–781, May 1978, ISSN: 0036-8075, 1095-9203. DOI: 10.1126/science.644320.
- [63] T. Kingston and S. J. Rossiter, “Harmonic-hopping in Wallacea’s bats”, en, *Nature*, vol. 429, 6992, pp. 654–657, Jun. 2004, ISSN: 0028-0836, 1476-4687. DOI: 10.1038/nature02487.
- [64] R. Specht, *Pipistrellus pipistrellus original feeding sound*. Avisoft Biocoustics, 2009. [Online]. Available: <https://www.avisoft.com/batcalls/>.
- [65] R. Specht, *Pipistrellus pygmaeus original feeding sound*. Avisoft Biocoustics, 2009. [Online]. Available: <https://www.avisoft.com/batcalls/>.
- [66] International Commission on Zoological Nomenclature, W. D. L. Ride, International Trust for Zoological Nomenclature, Natural History Museum (London, England), and International Union of Biological Sciences, Eds., *International code of zoological nomenclature =: Code internationale de nomenclature zoologique*, engfre, 4th ed. London: International Trust for Zoological Nomenclature, c/o Natural History Museum, 1999, OCLC: ocm42516582, ISBN: 9780853010067.
- [67] G. Jones and E. M. Barratt, “*Vespertilio pipistrellus* Schreber, 1774 and *V. pygmaeus* Leach, 1825 (currently *Pipistrellus pipistrellus* and *P. pygmaeus*; Mammalia, Chiroptera): proposed designation of neotypes”, *The Bulletin of zoological nomenclature.*, vol. 56, pp. 182–186, 1999, ISSN: 0007-5167. DOI: 10.5962/bhl.part.23065.
- [68] A. Surlykke, V. Futtrup, and J. Tougaard, “Prey-capture success revealed by echolocation signals in pipistrelle bats (*Pipistrellus pygmaeus*)”, en, *Journal of Experimental Biology*, vol. 206, 1, pp. 93–104, Jan. 2003, ISSN: 1477-9145, 0022-0949. DOI: 10.1242/jeb.00049.

-
- [69] E. K. Kalko, “Insect pursuit, prey capture and echolocation in pipistrelle bats (*Microchiroptera*)”, en, *Animal Behaviour*, vol. 50, 4, pp. 861–880, 1995, ISSN: 00033472. DOI: 10.1016/0003-3472(95)80090-5.
- [70] G. Thakur and H.-T. Wu, “Synchrosqueezing-based recovery of instantaneous frequency from nonuniform samples”, *SIAM Journal on Mathematical Analysis*, vol. 43, 5, pp. 2078–2095, Jan. 2011, ISSN: 0036-1410, 1095-7154. DOI: 10.1137/100798818.
- [71] J. L. W. V. Jensen and T. H. Gronwall, “An Elementary Exposition of the Theory of the Gamma Function”, *The Annals of Mathematics*, vol. 17, 3, p. 124, Mar. 1916, ISSN: 0003486X. DOI: 10.2307/2007272.
- [72] A. Cuyt, V. B. Petersen, B. Verdonk, C. H. Waadeland, and W. B. Jones, *Handbook of continued fractions for special functions: with contributions by Franky Backeljauw, Catherine Bonan-Hamada ; verified numerical output Stefan Becuwe, Annie Cuyt*, eng. Dordrecht: Springer, 2010, ISBN: 9789048177752.
- [73] F. Colone, D. W. O’Hagan, P. Lombardo, and C. J. Baker, “A multistage processing algorithm for disturbance removal and target detection in passive bistatic radar”, *IEEE Transactions on Aerospace and Electronic Systems*, vol. 45, 2, pp. 698–722, 2009. DOI: 10.1109/TAES.2009.5089551.
- [74] *IEEE Standard for Radar Definitions*. DOI: 10.1109/IEEESTD.2017.8048479.
- [75] D. W. O’Hagan, S. R. Doughty, and M. R. Inggs, “Multistatic radar systems”, en, in *Academic Press Library in Signal Processing, Volume 7*, Elsevier, 2018, pp. 253–275, ISBN: 9780128118870. DOI: 10.1016/B978-0-12-811887-0.00005-5.
- [76] H. Sun, F. Brigui, and M. Lesturgie, “Analysis and comparison of mimo radar waveforms”, *2014 International Radar Conference*, pp. 1–6, 2014.
- [77] C. M. Schmid, R. Feger, C. Pfeffer, and A. Stelzer, “Motion compensation and efficient array design for tdma fmcw mimo radar systems”, *2012 6th European Conference on Antennas and Propagation (EUCAP)*, pp. 1746–1750, 2012. DOI: 10.1109/EuCAP.2012.6206605.
- [78] A. Pezeshki, A. R. Calderbank, W. Moran, and S. D. Howard, “Doppler resilient golay complementary waveforms”, *IEEE Transactions on Information Theory*, vol. 54, 9, pp. 4254–4266, 2008. DOI: 10.1109/TIT.2008.928292.
- [79] A. Torre, A. Taylor, D. Poullin, and T. Chonavel, “Bioinspired Waveform in a Multistatic Configuration”, *RADAR 2024*, Oct. 2024.
- [80] U. H. Tan, “Méthodologies de conception de formes d’onde pour radars sol. application au cas du radar mimo.”, Theses, Université Paris-Saclay, 2019.

-
- [81] M. Grant and S. Boyd, *CVX: matlab software for disciplined convex programming, version 2.1*, <http://cvxr.com/cvx>, Mar. 2014.
- [82] L. Kocjancic, A. Balleri, and T. Merlet, “Multibeam radar based on linear frequency modulated waveform diversity”, *IET Radar, Sonar & Navigation*, vol. 12, 11, pp. 1320–1329, 2018, ISSN: 1751-8792, 1751-8792. DOI: 10.1049/iet-rsn.2018.5029.
- [83] M. Cobos, J. J. Perez-Solano, S. Felici-Castell, J. Segura, and J. M. Navarro, “Cumulative-Sum-Based Localization of Sound Events in Low-Cost Wireless Acoustic Sensor Networks”, *IEEE/ACM Transactions on Audio, Speech, and Language Processing*, vol. 22, 12, pp. 1792–1802, Dec. 2014, ISSN: 2329-9290, 2329-9304. DOI: 10.1109/TASLP.2014.2351132.
- [84] H. Urkowitz, “Energy detection of unknown deterministic signals”, *Proceedings of the IEEE*, vol. 55, 4, pp. 523–531, 1967, ISSN: 0018-9219. DOI: 10.1109/PROC.1967.5573.
- [85] D. E. Hack, L. K. Patton, and B. Himed, “A unified detection framework for distributed active and passive RF sensing”, presented at the Asilomar Conference on Signals, Systems and Computers, 2013, pp. 449–453. DOI: 10.1109/ACSSC.2013.6810317.
- [86] M. Walencykowska, A. Kawalec, and K. Krenc, “An Application of Analytic Wavelet Transform and Convolutional Neural Network for Radar Intrapulse Modulation Recognition”, *Sensors*, vol. 23, 4, p. 1986, 2023, ISSN: 1424-8220. DOI: 10.3390/s23041986.
- [87] X. Ju, H. Zhu, G. Wang, X. Zou, M. Tan, and W. Song, “Radar signal recognition based on time-frequency feature extraction and convolutional neural network”, in *Second International Conference on Digital Society and Intelligent Systems (DSInS 2022)*, Chengdu, China: SPIE, 2023, p. 89, ISBN: 9781510663244. DOI: 10.1117/12.2673527.
- [88] G. V. Moustakides, “Optimal Stopping Times for Detecting Changes in Distributions”, *The Annals of Statistics*, vol. 14, 4, pp. 1379–1387, 1986. DOI: 10.1214/aos/1176350164.
- [89] B. Ygorra, F. Frappart, J. Wigneron, *et al.*, “Monitoring loss of tropical forest cover from sentinel-1 time-series: a CuSum-based approach”, *International Journal of Applied Earth Observation and Geoinformation*, vol. 103, p. 102532, 2021, ISSN: 15698432. DOI: 10.1016/j.jag.2021.102532.
- [90] M. Akcakaya, S. Sen, and A. Nehorai, “A Novel Data-Driven Learning Method for Radar Target Detection in Nonstationary Environments”, *IEEE Signal Processing Letters*, vol. 23, 5, pp. 762–766, May 2016, ISSN: 1070-9908, 1558-2361. DOI: 10.1109/LSP.2016.2553042.

-
- [91] Y. Xiang, M. Akcakaya, S. Sen, and A. Nehorai, “Target Detection via Cognitive Radars Using Change-Point Detection, Learning, and Adaptation”, *Circuits, Systems, and Signal Processing*, vol. 40, 1, pp. 233–261, Jan. 2021, ISSN: 0278-081X, 1531-5878. DOI: 10.1007/s00034-020-01465-z.
- [92] R. Budihal and H. S. Jamadagni, “Implementation and benchmarking of cusum algorithm for spectrum sensing under low snr regimes on anrc cognitive radio testbed”, in *2012 5th International Conference on New Technologies, Mobility and Security (NTMS)*, 2012, pp. 1–6. DOI: 10.1109/NTMS.2012.6208756.
- [93] A. Lamm and A. Hahn, “Detecting maneuvers in maritime observation data with cusum”, *2017 IEEE ISSPIT*, pp. 122–127, 2017. DOI: 10.1109/ISSPIT.2017.8388628.
- [94] H. Liu, Z. Zhou, and C. Lu, “Maneuvering Detection Using Multiple Parallel CUSUM Detector”, *Mathematical Problems in Engineering*, vol. 2018, pp. 1–17, 2018, ISSN: 1024-123X, 1563-5147. DOI: 10.1155/2018/5062184.
- [95] J. Bao, Y. Li, M. Zhu, and S. Wang, *Bayesian Non-parametric Hidden Markov Model for Agile Radar Pulse Sequences Streaming Analysis*, 2023. arXiv: 2302.04407 [eess.SP].
- [96] S. Kay, *Fundamentals of Statistical Signal Processing Volume II: Detection Theory*. Prentice Hall, 1998.
- [97] P. Fearnhead, R. Maidstone, and A. Letchford, “Detecting Changes in Slope With an L_0 Penalty”, *Journal of Computational and Graphical Statistics*, vol. 28, 2, pp. 265–275, 2019, ISSN: 1061-8600, 1537-2715. DOI: 10.1080/10618600.2018.1512868.
- [98] H. Akaike, “Information Theory and an Extension of the Maximum Likelihood Principle”, in *Breakthroughs in Statistics*, S. Kotz and N. L. Johnson, Eds., New York, NY: Springer New York, 1992, pp. 610–624, ISBN: 9780387940373. DOI: 10.1007/978-1-4612-0919-5_38.
- [99] A. G. Tartakovsky, A. S. Polunchenko, and G. Sokolov, “Efficient Computer Network Anomaly Detection by Changepoint Detection Methods”, *IEEE Journal of Selected Topics in Signal Processing*, vol. 7, 1, pp. 4–11, 2013, ISSN: 1932-4553, 1941-0484. DOI: 10.1109/JSTSP.2012.2233713.
- [100] N. Sahki, A. Gégout-Petit, and S. Wantz-Mézières, “Performance study of change-point detection thresholds for cumulative sum statistic in a sequential context”, *Quality and Reliability Engineering International*, vol. 36, 8, pp. 2699–2719, 2020, ISSN: 0748-8017, 1099-1638. DOI: 10.1002/qre.2723.
- [101] A. Torre, A. Taylor, D. Poullin, and T. Chonavel, “Parameters Extraction of Unknown Radar Signals Using Change Point Detection”, *IEEE Radar conference 2023*, Nov. 2023.

-
- [102] H. Gudbjartsson and S. Patz, “The rician distribution of noisy mri data”, *Magnetic Resonance in Medicine*, vol. 34, 6, pp. 910–914, 1995, ISSN: 0740-3194, 1522-2594. DOI: 10.1002/mrm.1910340618.
- [103] A. Torre, A. Taylor, D. Poullin, and T. Chonavel, “Improved Change Point Detection via Bias Reduction in Parameters Estimation”, in *EUSIPCO 2024*, LYON, France, Aug. 2024. [Online]. Available: <https://hal.science/hal-04757264>.
- [104] F. J. Massey, “The Kolmogorov-Smirnov Test for Goodness of Fit”, *Journal of the American Statistical Association*, vol. 46, 253, pp. 68–78, 1951, ISSN: 0162-1459, 1537-274X. DOI: 10.1080/01621459.1951.10500769.
- [105] J. Yang and T. K. Sarkar, “Doppler-invariant property of hyperbolic frequency modulated waveforms”, en, *Microwave and Optical Technology Letters*, vol. 48, 6, pp. 1174–1179, Jun. 2006, ISSN: 0895-2477, 1098-2760. DOI: 10.1002/mop.21573.
- [106] I. Daubechies, J. Lu, and H.-T. Wu, “Synchrosqueezed wavelet transforms: an empirical mode decomposition-like tool”, *Applied and Computational Harmonic Analysis*, vol. 30, 2, pp. 243–261, Mar. 2011, ISSN: 10635203. DOI: 10.1016/j.acha.2010.08.002.
- [107] I. Daubechies and S. Maes, “A nonlinear squeezing of the continuous wavelet transform based on auditory nerve models”, in *WAVELETS in Medicine and Biology*, A. Aldroubi and M. Unser, Eds., 1st ed., Routledge, Nov. 22, 2017, pp. 527–546, ISBN: 9780203734032. DOI: 10.1201/9780203734032-20.
- [108] T. Oberlin, “Analyse de signaux multicomposantes : contributions à la décomposition modale empirique, aux représentations temps-fréquence et au synchrosqueezing”, Thèses, Université de Grenoble, 2013.
- [109] I. The MathWorks, *Signal processing toolbox*, Natick, Massachusetts, United State, 2019. [Online]. Available: <https://www.mathworks.com/help/signal/>.
- [110] D. Reynolds and R. Rose, “Robust text-independent speaker identification using Gaussian mixture speaker models”, *IEEE Transactions on Speech and Audio Processing*, vol. 3, 1, pp. 72–83, Jan. 1995, ISSN: 10636676. DOI: 10.1109/89.365379.
- [111] A. Cárdenas-Blanco, C. Tejos, P. Irarrazaval, and I. Cameron, “Noise in magnitude magnetic resonance images”, *Concepts in Magnetic Resonance Part A*, vol. 32A, 6, pp. 409–416, Nov. 2008, ISSN: 15466086, 15525023. DOI: 10.1002/cmr.a.20124.

Titre : Formes d'onde et traitements bio-inspirés

Mot clés : biomimétisme, chauve-souris, écholocation, Forme d'onde, traitement radar.

Résumé : Cette thèse aborde le sujet de la diversité des formes d'onde afin d'apporter des réponses aux problématiques radar actuelles, telles que la congestion croissante du spectre électromagnétique ou encore le besoin constant de performances améliorées (ou du moins maintenues). En étudiant le principe d'écholocation utilisé par les chauves-souris et leurs formes d'onde, les potentiels atouts de ces signaux innés sont mis en exergue. Une forme d'onde bio-inspirée, la forme d'onde de Parsons, capable d'imiter la construction des signaux de chauves-souris avec une certaine flexibilité, a ainsi été proposée pour des applications radar. Tout au long de la thèse, la comparaison est faite entre la fonction de Parsons et des formes d'ondes radar classiques

(le chirp et la fonction hyperbolique) afin de mesurer le potentiel de cette forme d'onde bio-inspirée. En outre, ses réponses au traitement radar classique sont étudiées. En particulier, les bornes de Cramér-Rao ont été calculées pour quantifier l'efficacité de la forme d'onde dans l'estimation du délai et du Doppler. Des discussions sur des données simulées et réelles ont permis de valider la fonction de Parsons en tant que potentielle nouvelle forme d'onde radar. Pour aller plus loin, son implémentation dans des applications radar concrètes est étudiée. Enfin, à la suite de l'étude initiale sur les signaux de chauves-souris, un algorithme de détection de changement, le CuSum, est adapté et développé pour la détection de signaux radar inconnus.

Title: Bio-inspired waveforms and processing

Keywords: biomimicry, bat, echolocation, waveform, radar processing.

Abstract: This thesis addresses the issue of waveform diversity to answer current challenges in radar, such as the increasing spectral congestion or the need for improved (or at least maintained) capabilities. By studying the echolocation of bats and their waveforms, the potential assets of such innate waveforms have been highlighted. A bio-inspired waveform, the Parsons waveform, which is capable of mimicking the design of bat waveforms with a notable flexibility, has thus been proposed for use in radar applications. All along this thesis, the comparison is made between the Parsons function and classical radar waveforms (the chirp and the hyperbolic frequency modulation) in order to assess the potential of

the bio-inspired waveform. In addition, its responses to traditional radar processing have been studied. In particular, the Cramér-Rao lower bounds have been calculated to quantify the efficiency of the waveform in estimating delay and Doppler. Discussions on both simulated and real data have enabled the validation of the Parsons bio-inspired function as a potential new radar waveform. To further investigate this, its implementation in concrete radar applications is studied. Finally, following an initial study of bat signals, a change-point detection algorithm, namely the CuSum, is derived and developed for the detection of unknown radar signals.